

Kaoru Yamanouchi
Gustav Gerber
André D. Bandrauk
Editors

SPRINGER SERIES IN CHEMICAL PHYSICS 99

Progress in Ultrafast Intense Laser Science VI

 Springer

PUILS 

 **JILS**

Springer Series in
CHEMICAL PHYSICS

Series Editors: A. W. Castleman, Jr. J. P. Toennies K. Yamanouchi W. Zinth

The purpose of this series is to provide comprehensive up-to-date monographs in both well established disciplines and emerging research areas within the broad fields of chemical physics and physical chemistry. The books deal with both fundamental science and applications, and may have either a theoretical or an experimental emphasis. They are aimed primarily at researchers and graduate students in chemical physics and related fields.

Please view available titles in *Springer Series in Chemical Physics*
on series homepage <http://www.springer.com/series/676>

Kaoru Yamanouchi
Gustav Gerber
André D. Bandrauk

Editors

Progress in Ultrafast Intense Laser Science

Volume VI

With 128 Figures

 Springer

Editors

Professor Kaoru Yamanouchi

The University of Tokyo
Department of Chemistry
7-3-1 Hongo, Bunkyo-ku, Tokyo 113-0033, Japan
E-Mail: kaoru@chem.s.u-tokyo.ac.jp

Professor André D. Bandrauk

Université de Sherbrooke
Faculté des Sciences
Laboratoire Chimie Théorique
J1K 2R1 Sherbrooke Québec, Canada
E-Mail: andre.bandrauk@usherbrooke.ca

Professor Gustav Gerber

Physikalisches Institut, Universität Würzburg
Am Hubland, 97074 Würzburg, Germany
E-Mail: gerber@physik.uni-wuerzburg.de

Series Editors:

Professor A.W. Castleman, Jr.

Department of Chemistry, The Pennsylvania State University
152 Davey Laboratory, University Park, PA 16802, USA

Professor J.P. Toennies

Max-Planck-Institut für Strömungsforschung
Bunsenstrasse 10, 37073 Göttingen, Germany

Professor K. Yamanouchi

Department of Chemistry, The University of Tokyo
7-3-1 Hongo, Bunkyo-ku, Tokyo 113-0033, Japan

Professor W. Zinth

Universität München, Institut für Medizinische Optik
Öttingerstr. 67, 80538 München, Germany

Springer Series in Chemical Physics ISSN 0172-6218

ISBN 978-3-642-15053-1

e-ISBN 978-3-642-15054-8

DOI 10.1007/978-3-642-15054-8

Springer Heidelberg Dordrecht London New York

© Springer-Verlag Berlin Heidelberg 2010

This work is subject to copyright. All rights are reserved, whether the whole or part of the material is concerned, specifically the rights of translation, reprinting, reuse of illustrations, recitation, broadcasting, reproduction on microfilm or in any other way, and storage in data banks. Duplication of this publication or parts thereof is permitted only under the provisions of the German Copyright Law of September 9, 1965, in its current version, and permission for use must always be obtained from Springer. Violations are liable to prosecution under the German Copyright Law.

The use of general descriptive names, registered names, trademarks, etc. in this publication does not imply, even in the absence of a specific statement, that such names are exempt from the relevant protective laws and regulations and therefore free for general use.

Cover design: eStudio Calamar Steinen

Printed on acid-free paper

Springer is part of Springer Science+Business Media (www.springer.com)

Preface

We are pleased to present the sixth volume of Progress in Ultrafast Intense Laser Science. As the frontiers of ultrafast intense laser science rapidly expand ever outward, there continues to be a growing demand for an introduction to this interdisciplinary research field that is at once widely accessible and capable of delivering cutting-edge developments. Our series aims to respond to this call by providing a compilation of concise review-style articles written by researchers at the forefront of this research field, so that researchers with different backgrounds as well as graduate students can easily grasp the essential aspects.

As in previous volumes of PUILS, each chapter of this book begins with an introductory part, in which a clear and concise overview of the topic and its significance is given, and moves onto a description of the authors' most recent research results. All the chapters are peer-reviewed. The articles of this sixth volume cover a diverse range of the interdisciplinary research field, and the topics may be grouped into three categories: responses of molecules to ultrashort intense laser pulses (Chaps. 1 – 4), generation and characterization of attosecond pulses and high-order harmonics (Chaps. 5 – 8), and filamentation and laser–plasma interaction and their applications (Chaps. 9 – 11).

From the third volume, the PUILS series has been edited in liaison with the activities of Center for Ultrafast Intense Laser Science in the University of Tokyo, and JILS (Japan Intense Light Field Science Society), the latter of which has also been responsible for sponsoring the series and making the regular publication of its volumes possible. From the fifth volume, the Consortium on Education and Research on Advanced Laser Science, the University of Tokyo, has joined this publication activity as one of the sponsoring programs. The series has also collaborated since its inception with the annual symposium series of ISUILS (<http://www.isuils.jp>), which is designed to stimulate interdisciplinary discussion at the forefront of ultrafast intense laser science.

We take this opportunity to thank all the authors who have kindly contributed to the PUILS series by describing their most recent work at the frontiers of ultrafast intense laser science. We also thank the reviewers who have read the submitted manuscripts carefully. One of the co-editors (KY) thanks Ms. Chie Sakuta for her help with the editing processes. Last but not least, our gratitude goes out to Dr. Claus Ascheron, Physics Editor of Springer Verlag at Heidelberg, for his kind support.

We hope this volume will convey the excitement of Ultrafast Intense Laser Science to the readers, and stimulate interdisciplinary interactions among researchers, thus paving the way to explorations of new frontiers.

Tokyo
Würzburg
Sherbrooke
November 12, 2009

Kaoru Yamanouchi
Gustav Gerber
André D. Bandrauk

Contents

1	Laser-Induced Coulomb Explosion Ultrafast Imaging of Molecules	1
	C. Cornaggia	
1.1	Introduction	1
1.2	Experimental Procedures	4
1.3	Lifetimes of Dissociating States of N_2^{2+}	7
1.4	Double Ionization of H_2 at 10 and 40 fs	9
1.5	Coulomb Explosion of N_2 at 10 and 40 fs	13
1.6	Conclusion	16
	References	18
2	Quantum Switching of Magnetic Fields by Circularly Polarized Re-Optimized π Laser Pulses: From One-Electron Atomic Ions to Molecules	21
	Ingo Barth and Jörn Manz	
2.1	Introduction	22
2.2	Survey on Quantum Switching-on the Ring Currents and Magnetic Fields	25
2.3	Quantum Switching the Directions of Ring Currents and Magnetic Fields	36
2.4	Conclusions	37
	References	41
3	Alignment and Orientation of Hexapole State-Selected Molecules	45
	Arnaud Rouzée, Arjan Gijsbertsen, and Marc J.J. Vrakking	
3.1	Introduction	45
3.2	Molecules	48
3.3	Hexapole State Selection	50
3.4	Interactions with an Intense Laser Field	53
3.5	Numerical Example in Several Polar Molecules	55
3.6	Experimental Setup	59
3.7	Sign of the NO Dipole Moment	61

3.8	Impulsive Alignment and Orientation	62
3.8.1	Laser Field-Free Alignment	62
3.8.2	Laser Field-Free Orientation	65
3.8.3	Orientation and Alignment with Shaped Intense Laser Pulse	69
3.9	Conclusions and Remarks	71
	References	72
4	Quantum Interference in Ionization of Excited Molecules: X-Ray Emission Control and Dynamic Imaging	75
	Mikhail Yu. Emelin, Mikhail Yu. Ryabikin, and Alexander M. Sergeev	
4.1	Introduction	75
4.2	Attosecond Pulse Production from Electronically Excited Atoms and Molecules	76
4.2.1	Roles of Different Types of Transitions in HHG	77
4.2.2	Highly Efficient HHG from Excited Atoms and Molecules Using Continuum–Continuum Transitions	78
4.2.3	Single Attosecond Pulse Production: Bremsstrahlung vs. Recombination Radiation	78
4.3	Quantum Interference in Ionization of Stretched Molecules: Application to the X-Ray Emission Control	81
4.3.1	Numerical Results	81
4.3.2	Theory	84
4.4	Quantum Interference in Ionization of Stretched Molecules: Application to the Molecular Dynamic Imaging	87
4.5	Conclusions	87
	References	87
5	Single Isolated Attosecond Pulses Generation with Double Optical Gating	89
	Ximao Feng, Steve Gilbertson, Hiroki Mashiko, Sabih Khan, He Wang, Michael Chini, Yi Wu, and Zenghu Chang	
5.1	Introduction	89
5.2	Principle of Double Optical Gating	90
5.2.1	Two-Color Gating	91
5.2.2	Polarization Gating	91
5.2.3	DOG	93
5.2.4	GDOG	94
5.3	Carrier-Envelope Phase Stabilization of Oscillator, Amplifier and Hollow-Core Fiber Beams	96
5.4	Experimental Setup	98
5.4.1	DOG/GDOG Optics	99
5.4.2	XUV Grating Spectrometer	99
5.4.3	Attosecond Streak Camera	100

5.5	Results and Discussion	100
5.5.1	Study of Single Attosecond Pulse Generation with XUV Grating Spectrometer	101
5.5.2	Measurement with CRAB	103
5.6	Complete Reconstruction of Attosecond Bursts	106
5.7	Experimenting with Single Attosecond Pulses	107
5.8	Conclusion	109
	References	110
6	Toward the Generation of Isolated Attosecond Pulses in the Water Window	113
	Ruxin Li, Zhinan Zeng, Pu Zou, Yuxing Leng, Chunmei Zhang, and Zhizhan Xu	
6.1	Introduction	113
6.2	Generation of Isolated Attosecond Pulses in the Water Window	114
6.3	Generation of Tunable NIR Laser Pulses with Stabilized CEP	121
6.4	Conclusions	126
	References	126
7	High Harmonic Generation by Plasmonic Enhancement of Femtosecond Pulse Laser	129
	Seungchul Kim, In-Yong Park, Joonhee Choi, and Seung-Woo Kim	
7.1	Introduction	129
7.2	Geometrical Design of Bow-Tie Nanostructure	131
7.3	Fabrication of Bow-Tie Nanostructure	136
7.4	Experiments of High Harmonic Generation	138
7.5	Conclusion	142
	References	144
8	High-Order Harmonic Generation from Nanostructured Material Using the Laser-Plasma Method	145
	T. Ozaki, R.A. Ganeev, L.B. Elouga Bom, and J. Abdul-Hadi	
8.1	Introduction	145
8.2	Experimental Setup	146
8.3	Results	147
8.3.1	Silver Nanoparticles	147
8.3.2	Other Nanoparticles	151
8.3.3	C ₆₀ Fullerenes	153
8.4	Conclusions	159
	References	159

9	Filamentation in Ultrafast Laser Material Processing	161
	Wataru Watanabe, Takayuki Tamaki, Yasuyuki Ozeki, and Kazuyoshi Itoh	
9.1	Introduction	161
9.2	Filamentation	162
9.2.1	Filamentation and Supercontinuum Generation	162
9.2.2	Control of Multiple Filaments	162
9.3	Filamentation and Bulk Modifications	163
9.3.1	Filamentation and Bulk Modifications	163
9.3.2	Femtosecond Filamentary Track	164
9.4	Photonic Device Fabrication Using Filamentation	169
9.4.1	Fabrication of Waveguide Device	169
9.4.2	Fabrication of Diffractive Optical Element	172
9.4.3	Fabrication of Diffractive Optical Elements in Polymer Materials	174
9.5	Microwelding Using Filamentation	174
9.5.1	Femtosecond Laser Welding of Transparent Materials	174
9.6	Conclusion	179
	References	179
10	Plasma Electron Kinetics and Distribution Functions in Laser Fields	183
	Gaetano Ferrante and Roberto Luigi Oliveri	
10.1	Introduction	183
10.2	Theoretical Framework	185
10.3	Distribution Function in a Weak Field	187
10.3.1	Case $\alpha \geq 1$	190
10.3.2	Case $\alpha \ll 1$	191
10.3.3	Case of Arbitrary α	192
10.4	Distribution Function in a Strong Field	194
10.4.1	Analytical Investigations	194
10.4.2	Numerical Investigations	196
10.5	Main Results of Numerical Investigations	197
10.5.1	Characteristic Parameters and Their Behaviour in the Course of Laser–Plasma Interaction	197
10.5.2	Results of Selected Calculations. EDF Shape Evolution and Role of e–e Collisions	199
10.5.3	“Angular” Electron Distribution Function	203
10.6	Conclusions	206
	References	208
11	Ion Acceleration by Ultra-Intense Lasers: Analysis of Contrast Effects	211
	Alessandro Flacco and Dimitri Batani	
11.1	Laser Proton Acceleration	212
11.2	Laser Interaction with the Solid: Creation of a Preplasma	213

11.3	Effects Induced on the Front Surface	215
11.4	Effects Induced on the Back Surface	218
11.5	Laser-Produced Shocks and Proton Generation	220
11.6	Detailed Hydrodynamics Simulations	222
11.7	Two-Dimensional Effects and Proton Beam Deviation.....	224
11.8	Experimental Results.....	226
11.9	Conclusions.....	228
	References	229
Index	233

Contributors

J. Abdul-Hadi Institut National de la Recherche Scientifique, Énergie, Matériaux et Télécommunications, 1650 Lionel-Boulet, Varennes, QC, Canada J3X 1S2, ahadi@emt.inrs.ca

Ingo Barth Institut für Chemie und Biochemie, Freie Universität Berlin, Takustr. 3, 14195 Berlin, Germany
and
Kavli Institute for Theoretical Physics, University of California, Santa Barbara, CA 93106–4030, USA
and
Max-Born-Institut, Max-Born-Str. 2A, 12489 Berlin, Germany, barth@mbi-berlin.de

Dimitri Batani Università degli Studi di Milano-Bicocca, Piazza della Scienza 3, 20133 Milano, Italy, batani@mib.infn.it

L.B. Elouga Bom Institut National de la Recherche Scientifique, Énergie, Matériaux et Télécommunications, 1650 Lionel-Boulet, Varennes, QC, Canada J3X 1S2, elouga@emt.inrs.ca

Zenghu Chang J. R. Macdonald Laboratory, Department of Physics, Kansas State University, Manhattan, KS 66506, USA, zeChang@mail.ucf.edu

Michael Chini J. R. Macdonald Laboratory, Department of Physics, Kansas State University, Manhattan, KS 66506, USA, MChini@phys.ksu.edu

Joonhee Choi Ultrafast Optics for Ultraprecision Group, Korea Advanced Institute of Science and Technology (KAIST), Science Town, Daejeon, 305–701, South Korea, nguyjh@kaist.ac.kr

C. Cornaggia CEA IRAMIS, Service Photons, Atomes & Molécules, Saclay, Bâtiment 522, 91 191 Gif-sur-Yvette, France, christian.cornaggia@cea.fr

Mikhail Yu. Emelin Institute of Applied Physics of RAS, 46 Ulyanov Street, 603950 Nizhny Novgorod, Russia, emelin@ufp.appl.sci-nnov.ru

Ximao Feng J. R. Macdonald Laboratory, Department of Physics, Kansas State University, Manhattan, KS 66506, USA, xFeng@ksu.edu

Gaetano Ferrante Dipartimento di Fisica e Tecnologie Relative, Università di Palermo, Viale delle Scienze, 90128 Palermo, Italy, ferrante3@unipa.it

Alessandro Flacco Laboratoire d'Optique Appliquée (ENSTA-ParisTech, CNRS, École Polytechnique) Chemin de la Hunière, 91761 Palaiseau, France, alessandro.flacco@polytechnique.edu

R.A. Ganeev Institut National de la Recherche Scientifique, Énergie, Matériaux et Télécommunications, 1650 Lionel-Boulet, Varennes, QC, Canada J3X 1S2, rashid_ganeev@mail.ru
and
Scientific Association Akademprigor, Academy of Sciences of Uzbekistan, Akademgorodok, Tashkent 100125, Uzbekistan

Arjan Gijsbertsen FOM Instituut voor Atoom- en Molecuulfysica (AMOLF), Science Park 113, 1098 XG Amsterdam, The Netherlands, gijsbertsen@amolf.nl

Steve Gilbertson J. R. Macdonald Laboratory, Department of Physics, Kansas State University, Manhattan, KS 66506, USA, smg@phys.ksu.edu

Kazuyoshi Itoh Department of Material and Life Science, Graduate School of Engineering, Osaka University, 2-1, Yamadaoka, Suita, Osaka 565-0871, Japan, ito@mls.eng.osaka-u.ac.jp

Sabih Khan J. R. Macdonald Laboratory, Department of Physics, Kansas State University, Manhattan, KS 66506, USA, sabih@phys.ksu.edu

Seungchul Kim Ultrafast Optics for Ultraprecision Group, Korea Advanced Institute of Science and Technology (KAIST), Science Town, Daejeon, 305–701, South Korea, inter99@kaist.ac.kr

Seung-Woo Kim Ultrafast Optics for Ultraprecision Group, Korea Advanced Institute of Science and Technology (KAIST), Science Town, Daejeon, 305–701, South Korea, swk@kaist.ac.kr

Yuxing Leng State Key Laboratory of High Field Laser Physics, Shanghai Institute of Optics and Fine Mechanics, Chinese Academy of Sciences, Shanghai 201800, China, lengyuxin@siom.ac.cn

Ruxin Li State Key Laboratory of High Field Laser Physics, Shanghai Institute of Optics and Fine Mechanics, Chinese Academy of Sciences, Shanghai 201800, China, ruxinli@mail.shcnc.ac.cn

Jörn Manz Institut für Chemie und Biochemie, Freie Universität Berlin, Takustr. 3, 14195 Berlin, Germany
and
Kavli Institute for Theoretical Physics, University of California, Santa Barbara, CA 93106–4030, USA, jmanz@chemie.fu-berlin.de

Hiroki Mashiko J. R. Macdonald Laboratory, Department of Physics, Kansas State University, Manhattan, KS 66506, USA, mashiko@phys.ksu.edu

Roberto Luigi Oliveri Dipartimento di Fisica e Tecnologie Relative, Università di Palermo, Viale delle Scienze, 90128 Palermo, Italy, luigi.oliveri@difter.unipa.it

T. Ozaki Institut National de la Recherche Scientifique, Énergie, Matériaux et Télécommunications, 1650 Lionel-Boulet, Varennes, QC, Canada J3X 1S2, ozaki@emt.inrs.ca

Yasuyuki Ozeki Department of Material and Life Science, Graduate School of Engineering, Osaka University, 2-1, Yamadaoka, Suita, Osaka 565-0871, Japan, ozeki@mls.eng.osaka-u.ac.jp

In-Yong Park Ultrafast Optics for Ultraprecision Group, Korea Advanced Institute of Science and Technology (KAIST), Science Town, Daejeon, 305–701, South Korea, inyong@kaist.ac.kr

Arnaud Rouzée FOM Instituut voor Atoom- en Molecuulfysica (AMOLF), Science Park 113, 1098 XG Amsterdam, The Netherlands, A.rouzee@amolf.nl

Mikhail Yu. Ryabikin Institute of Applied Physics of RAS, 46 Ulyanov Street, 603950 Nizhny Novgorod, Russia, mike@ufp.appl.sci-nnov.ru

Alexander M. Sergeev Institute of Applied Physics of RAS, 46 Ulyanov Street, 603950 Nizhny Novgorod, Russia, ams@ufp.appl.sci-nnov.ru

Takayuki Tamaki Department of Control Engineering, Nara National College of Technology, 22, Yatacho, Yamatokoriyama, Nara 639-1080, Japan, tamaki@ctrl.nara-k.ac.jp

Marc J.J. Vrakking FOM Instituut voor Atoom- en Molecuulfysica (AMOLF), Science Park 113, 1098 XG Amsterdam, The Netherlands, vrakking@amolf.nl

He Wang J. R. Macdonald Laboratory, Department of Physics, Kansas State University, Manhattan, KS 66506, USA, HeWang@lbl.gov

Wataru Watanabe Photonics Research Institute, National Institute of Advanced Industrial Science and Technology, Higashi 1-1-1, Tsukuba, Ibaraki, 305-8565, Japan, wataru.watanabe@aist.go.jp

Yi Wu J. R. Macdonald Laboratory, Department of Physics, Kansas State University, Manhattan, KS 66506, USA, WuYi@phys.ksu.edu

Zhizhan Xu State Key Laboratory of High Field Laser Physics, Shanghai Institute of Optics and Fine Mechanics, Chinese Academy of Sciences, Shanghai 201800, China, zzxu@mail.shcnc.ac.cn

Zhinan Zeng State Key Laboratory of High Field Laser Physics, Shanghai Institute of Optics and Fine Mechanics, Chinese Academy of Sciences, Shanghai 201800, China, zhinan.zeng@mail.siom.ac.cn

Chunmei Zhang State Key Laboratory of High Field Laser Physics, Shanghai Institute of Optics and Fine Mechanics, Chinese Academy of Sciences, Shanghai 201800, China, feileiwuyu@siom.ac.cn

Pu Zou State Key Laboratory of High Field Laser Physics, Shanghai Institute of Optics and Fine Mechanics, Chinese Academy of Sciences, Shanghai 201800, China, pu.zou@tuwien.ac.at

Chapter 1

Laser-Induced Coulomb Explosion Ultrafast Imaging of Molecules

C. Cornaggia

Abstract Multiple ionization of small molecules leads to multifragmentation called Coulomb explosion. The atomic positions prior to the fragmentation event are determined from the multicharged fragments trajectories. Laser pulse durations have to be reduced to a few cycles in order to avoid any significant molecular stretching during multiple ionization. Pump–probe excitation schemes offer promising perspectives for straightforward ultrafast Coulomb explosion imaging of excited and ionized molecular species.

1.1 Introduction

Fragmentation has been used for years as an efficient and straightforward tool to retrieve the geometry and structural properties of physical systems. The related experimental techniques strongly depend on the targets under study, the excitation sources, and fragments detection schemes. Therefore, the fragmentation diagnostics appear to be specific of a particular field of experimental research such as particle, nuclear, or molecular physics. In atoms and molecules, fragmentation encompasses ionization and dissociation and may be triggered using various excitation sources such as ion, electron, and photon beams. The use of small laser systems is particular because the energy of near infrared and visible photons are well below the different fragmentation thresholds. Before discussing the necessary nonlinear coupling in order to reach these thresholds, let us emphasize the extraordinary achievements of laser physics in terms of power and ultrashort pulse duration of compact laser systems. Small laboratories have nowadays the possibility to study different fragmentation schemes of various objects from atoms to nanoparticles. In atoms and small molecules, the basic process is the electronic excitation leading to ionization.

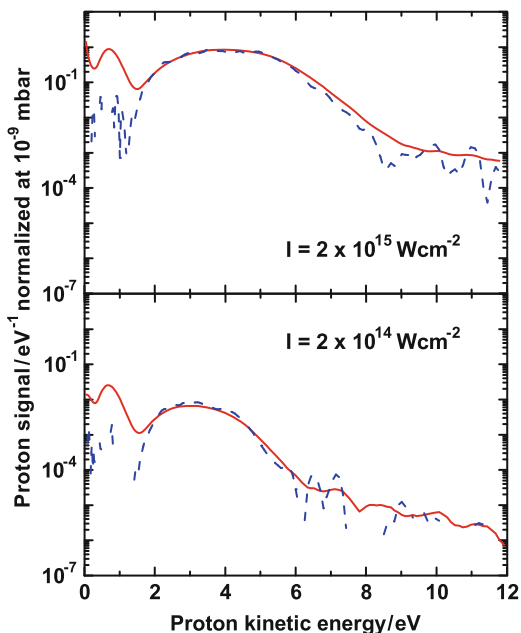
C. Cornaggia
CEA IRAMIS, Service Photons Atomes & Molécules
Saclay, bâtiment 522, F-91 191 Gif-sur-Yvette, France
e-mail: christian.cornaggia@cea.fr

From an energy point of view, the simultaneous absorption of several laser photons is necessary to overcome the ionization potential I_p . This process was labeled multiphoton ionization in the early days of strong-field laser physics [1, 2]. In the same time, Keldysh established the frontier between the multi-cycle multiphoton ionization and the single-cycle tunnel ionization introducing the well-known adiabaticity parameter $\gamma = \sqrt{I_p/2U_p}$ where U_p is the ponderomotive potential. The Keldysh parameter γ represents the ratio between the tunneling time through the potential barrier and the optical period. Therefore, tunnel ionization dominates in the strong field regime where $U_p \gg I_p$. This behavior was demonstrated experimentally by the pioneering experiments of Chin et al. using a CO₂ laser [3]. Moreover, tunnel ionization may be considered as the necessary first step for attosecond pulse generation in gases [4]. Indeed tunnel ionization may take less than a few hundreds of attoseconds. This time resolution may be only reached in accelerator-based experiments. For instance, in foil-induced Coulomb explosion of molecules, molecular ions are accelerated to a few percents of the velocity of light. Valence electrons are stripped away from the molecule when the ion beam crosses a thin foil with a thickness of around 5 nm. The stripping time is between 10 and 100 as. The resulting highly charged transient molecular ions instantaneously explode into multicharged atomic ions. The detection of these fragments allows one to image the positions of atoms within the molecule [5].

Laser-induced Coulomb explosion of molecules has been introduced in the late 1980s and early 1990s using picosecond and femtosecond amplified dye laser systems delivering intensities in the 10^{15} Wcm^{-2} range [6–8]. Having in mind the beam-foil-induced Coulomb explosion, the laser excitation time scales, i.e., the optical period and the pulse duration, are much longer than the attosecond time scale of accelerator-based experiments. In multiple ionization, an instantaneous tunneling of several electrons has not been observed yet. Non sequential double ionization occurs within one optical cycle following the rescattering mechanism at low laser intensity [9–13]. However, the dication final states are not Coulombic and present structures due to chemical binding at short internuclear distances. These states are not suitable for imaging the positions of atoms within the molecule. Coulomb explosion imaging requires higher charge states which lead to a nearly Coulombic repulsion between the fragments. For multiple ionization with final charge states larger than 4, the identification of rescattering non sequential processes remains difficult. In addition, the use of laser intensities in the 10^{15} Wcm^{-2} range noticeably increases the probability of sequential ionization over several optical cycles within the laser pulse. Therefore, the time resolution may be confidently taken as the pulse duration. In the future, high-contrast single-cycle pulses might open the door to controlled single-cycle multiple ionization events.

In foil-induced Coulomb explosion, the interaction time is much shorter than any rotational or vibrational nuclear motion time scale. This is not the case with femtosecond lasers with respect to vibrational motions. For instance, the vibrational periods of H₂, H₂⁺, and N₂ are, respectively, 7.6, 14.4, and 14.1 fs when one considers the lowest vibrational states. For pulse durations of several tens of femtoseconds, a noticeable nuclear dynamics may take place during multiple ionization.

Fig. 1.1 Proton spectra from H_2 recorded with 40-fs and 800-nm laser pulses at $2 \times 10^{14} \text{ Wcm}^{-2}$ and $2 \times 10^{15} \text{ Wcm}^{-2}$ using linearly polarized laser light. The full curves represent the total proton spectra. The dashed curves represent the covariance proton spectra from the $\text{H}^+ + \text{H}^+$ dissociation channel



For instance in H_2 , the first ionization step produces an ionic H_2^+ vibrational wave packet which oscillates back and forth during the laser pulse. In addition, the ionization of H_2^+ is strongly favored at large internuclear distances following Charge Resonance Enhanced Ionization. This important effect discovered by Bandrauk et al. involves a very efficient charge transfer coupling between the $1s\sigma_g$ ground electronic state and $2p\sigma_u$ first excited electronic state of H_2^+ induced by the laser field at large internuclear distances [14]. When the H_2^+ vibrational wave packet reaches this internuclear distance domain, the molecular ion is ionized with a very high probability.

Figure 1.1 represents two proton spectra recorded with 40-fs laser pulses at $2 \times 10^{14} \text{ Wcm}^{-2}$ and $2 \times 10^{15} \text{ Wcm}^{-2}$. The broad proton peak centered at around 3–4 eV comes from Charge Resonance Enhanced Ionization. An instantaneous two-electron emission would have produced a proton spectrum centered at 9.4 eV. This last process is dominated by Charge Resonance Enhanced Ionization by several orders of magnitude because the molecular ion vibrational wave packet has time to explore the enhanced ionization internuclear distance range within the laser pulse duration. Charge Resonance Enhanced Ionization has been shown to be a general effect in strong field molecular physics in symmetric as well as in nonsymmetric molecules [15, 16].

Even in the case of molecular bond stretching, laser-induced Coulomb explosion allows one to tackle the molecular geometry in a rather straightforward way in a few-minute experiment. For instance, Fig. 1.2 represents covariance maps recorded for fragmentation channels with three ions $\text{O}^+ + \text{C}^+ + \text{O}^+$ for CO_2 with a 130-fs pulse

duration and $O^+ + S^+ + O^+$ for SO_2 with a 50-fs pulse duration. The correlation locations of the central C^+ or S^+ ions with the terminal O^+ look very different in CO_2 and SO_2 . In particular, the elliptic shape observed in SO_2 comes from the bent geometry of this molecule [17]. In both cases, the extension of the correlation locations is due to vibrational wave packets and the corresponding nuclear motions which occur during multiple ionization [18]. As in the case of H_2 , the ion kinetic energy releases (KER) are smaller than the energies which are expected from an instantaneous Coulomb explosion. Here again, the pulse duration is long enough for bond stretching related to Charge Resonance Enhanced Ionization [19–22].

In addition to the examples given above, laser-induced Coulomb explosion has been used to study molecular orientation and rotational wave packets [23] and more generally the dynamics of small molecules in intense laser fields [24]. We give here a few examples from our experiments performed with small molecules. The first example reports measurements of lifetimes of excited states in the 100-fs range of the N_2^{2+} dication using 40-fs laser pulses [25]. This proof-of-principle experiment relies on the pump–probe excitation scheme which represents a decisive advantage of the laser excitation [26]. For Coulomb explosion of neutral molecules in their ground states, the pulse duration has to be reduced down to a few cycles because of the ultrafast molecular stretching during multiple ionization. Double ionization of H_2 will be considered since this molecule may be considered as a very simple ultrafast test system because of the light protons’ dynamics. We will show that few-cycle pulses allow one to identify non sequential rescattering double ionization without any ambiguity in comparison with longer pulses [27]. However, proton spectra recorded with 10-fs laser pulses do not image the ground vibrational state of H_2 because of the ultrafast dynamics of the intermediate H_2^+ ions. Charge Resonance Enhanced Ionization does not have enough time for a noticeable effect with such pulses. A 10-fs pump–probe scheme permits to retrieve this phenomenon [28]. Finally, Coulomb explosion of N_2 using 10- and 40-fs laser pulses will be presented [29]. Little stretching takes with 10-fs pulses. This observation opens the way to ultrafast imaging of neutral and excited molecular species.

1.2 Experimental Procedures

Multiple ionization experiments require femtosecond laser pulses with energies up to several hundreds of microjoules and tight focusing, e.g., focal distances of the order of 100 mm at $f/10$. A peak intensity in the 10^{15} Wcm^{-2} intensity range is sufficient in order to reach charge states up to 6–8 in molecules such as N_2 or CO_2 . We use a kilohertz titanium:sapphire laser chain which can deliver pulse energies up to 600 μJ with one regenerative amplifier stage based on chirped pulse amplification. Gain narrowing in the amplifier prevents one to exploit the full emission spectral bandwidth of titanium:sapphire. The pulse duration is 40 fs. Therefore, an external compressor stage had to be built in order to generate few-cycle laser pulses. The method is to broaden the laser spectrum in a nonlinear medium using

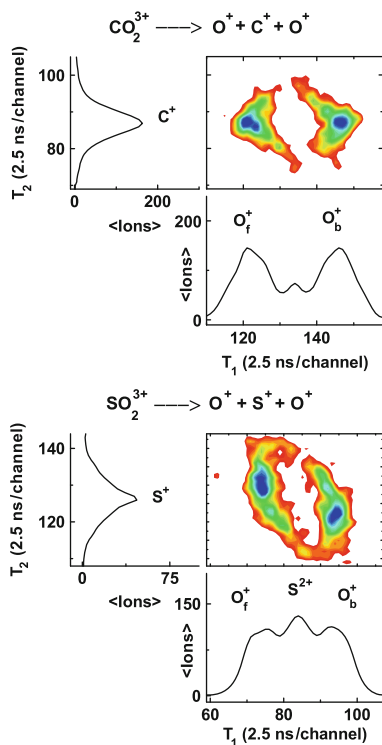


Fig. 1.2 Covariance maps recorded with CO_2 and SO_2 using, respectively, 130- and 50-fs linearly polarized laser pulses. For each molecule, correlations are plotted between the central C^+ or S^+ ion and the external O^+ ions. The corresponding time-of-flight spectra are plotted on the *left* and *bottom* graphs. The *elliptical shape* of the SO_2 map is due to the bent geometry of this molecule. The relatively large extensions of the correlation locations are due to nuclear motions

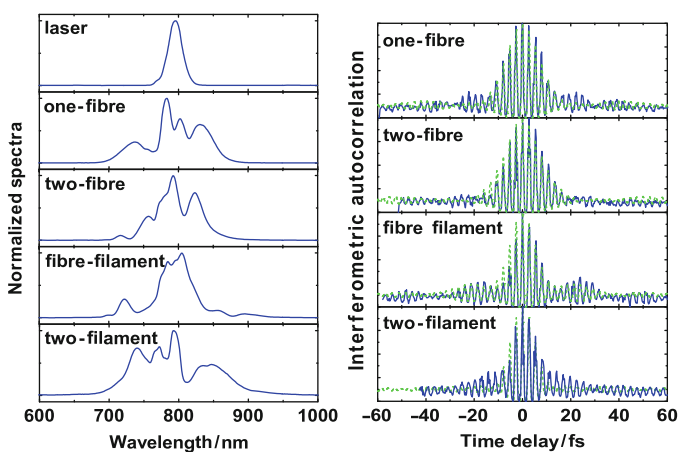


Fig. 1.3 Measured spectra and interferometric autocorrelations recorded with different compressor schemes. The *dashed curves* in the *right panels* are the calculated interferometric autocorrelations using the measured spectra and assuming a constant spectral phase

self-phase-modulation. In addition, an important condition is to get a spatial homogeneous broadening with respect to the transverse section of the laser beam. A decisive breakthrough was achieved by Nisoli et al. who introduced the hollow fiber technique [30]. The nonlinear medium is a noble gas such as neon or argon which can withstand much higher laser intensities than the bulk medium of the previously used fibres. The gas takes place in the hollow fiber which works as a wave guide for homogeneous spectral broadening. Using this technique with argon gas and a fiber of length 700 mm and inner diameter 250 μm , a spectrum spanning over 200 nm is generated with an initial spectral bandwidth of 27 nm at full-width-half-maximum. The pulse is recompressed down to 10 fs with a set of commercial chirped mirrors. The available energy at 10 fs is 200 μJ for an input energy of 600 μJ . Experiments presented here were performed with this set-up.

Filamentation was introduced a few years ago by Hauri et al. as an alternative to the hollow fiber wave guide [31]. In this case, the set-up is simpler since it merely involves a long tube filled with gas as the non linear medium. The laser beam propagation is guided by the focusing-defocusing pattern of filamentation. Figure 1.3 presents some measured spectra and the corresponding autocorrelations using both techniques with argon gas [32]. In the case of filamentation, two cells for two different filaments and the associated recompression chirped mirrors were necessary in order to get sufficient spectral broadening. The best results were recorded with the two-filament set-up. However, noticeable wings appear in the autocorrelation signal and could not be removed using our chirped mirrors.

Coulomb explosion experiments are based on the detection of multicharged atomic ions. Different time-of-flight mass spectrometers may be used in order to identify the fragments and to measure their initial momenta. Usually, the Wiley–McLaren configuration is preferred in order to get a linear relationship between the time of flight and the projection of the initial momentum along the time-of-flight tube axis for a mass-resolved fragment [33, 34]. Techniques based on the angle discrimination and/or the laser polarization dependence allow one to get the modulus of the momentum and hence the initial kinetic energy release (KER) of the ion [35].

Here, the fragmentation channels are identified using covariance mapping introduced by Frasinski et al. [36]. In general, several fragmentation events are detected per laser shot even with pressures in the 10^{-9} mbar range. In that case, coincidence techniques cannot be used. Covariance mapping consists in measuring the fluctuations of the signals on a shot-to-shot basis. Correlated signals only occur when fragments come from the same fragmentation channel. For instance in Fig. 1.1, the proton spectra from the $\text{H}^+ + \text{H}^+$ channel are given by the dashed curves which come from the recorded covariance map [34]. The weakness of the covariance signals for protons with energies below 2 eV allows one to identify these protons as coming from the singly charged $\text{H}^+ + \text{H}$ fragmentation channel since they are not correlated to any other proton.

In order to conclude this brief experimental section, let us mention new powerful position-sensitive detection schemes of Coulomb explosion such as Coincidence Momentum Imaging [37] or COLTRIMS [38] that will benefit from the fast progress of ultrashort high-repetition-rate lasers.

1.3 Lifetimes of Dissociating States of N_2^{2+}

Molecular dications exhibit lifetimes which range from seconds to femtoseconds due to the interplay between chemical bonding at short internuclear distances and Coulomb repulsion of singly charged fragments at large distances. These ion species and their properties play an important role in planetary ionospheres and interstellar clouds [39]. The N_2^{2+} dication has been studied using a variety of experimental techniques and exhibits a rich electronic structure due to low lying excited electronic states above the $X^1\Sigma_g^+$ ground state [40, 41]. As a proof-of-principle experiment, the dissociation lifetimes of N_2^{2+} ions produced by a femtosecond laser pulse are measured using a pump-probe scheme represented in Fig. 1.4. The experiment is performed with 40-fs laser pulses. The first pulse is commonly denoted the pump pulse. The studied dissociation pathways are determined using covariance mapping and are respectively $N^+ + N^+ + 8.6\text{ eV}$, $N^+ + N^+ + 10\text{ eV}$, and $N^{2+} + N + 2\text{ eV}$. This last channel is determined from N_2^{2+} ions which do not correlate to any other

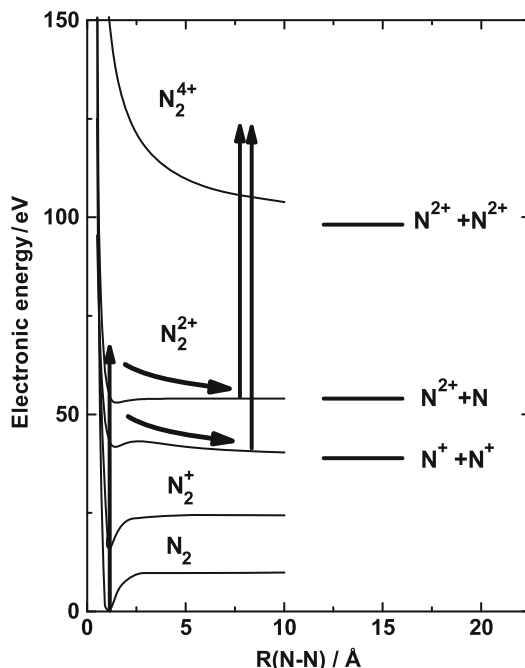


Fig. 1.4 Pump-probe excitation scheme in N_2 . The pump laser pulse double-ionizes the neutral molecule in order to produce the excited N_2^{2+} dication which decays into the $N^+ + N^+$ and $N^{2+} + N$ fragmentation channels. A time-delayed second laser pulse removes two additional electrons from the dissociating doubly charged molecule and leads to the $N^{2+} + N^{2+}$ fragmentation channel. The temporal dynamics of the dissociating N_2^{2+} dication is measured from the kinetic energy release (KER) of the $N^{2+} + N^{2+}$ channel as a function of the time delay between the pump and probe pulses

charged fragments. Concerning the $N^+ + N^+$ dissociation channels, the measured kinetic energies are in good agreement with the high-resolution experiment of Lundqvist et al. [40]. In order to measure the dissociation lifetimes, the dissociation has to be stopped at different times by a second laser pulse denoted here the probe pulse. The probe pulse removes 2 more electrons from the dissociating molecule. The experiment consists in measuring the KER of the resulting $N^{2+} + N^{2+}$ fragmentation channel as a function of the pump–probe time delay. The dissociation time is extracted from the data of Fig. 1.5 using the following procedure.

The method is aimed at measuring dissociation times from the equilibrium internuclear distance R_e , where the excitation takes place, up to a distance R_c where the potential curves of the corresponding $N^+ + N^+$ and $N^{2+} + N$ are exactly known. This distance R_c can safely be taken as $R_c = 5 \text{ \AA}$ since chemical binding is no more effective for larger distances. For distances $R > 5 \text{ \AA}$, the potential curves of the $N^+ + N^+$ and $N^{2+} + N$ fragmentation channels are, respectively, $U(R) = 1/R$ and $U(R) = 0$ in atomic units. The time taken to reach an internuclear distance R_f larger than R_c is given by

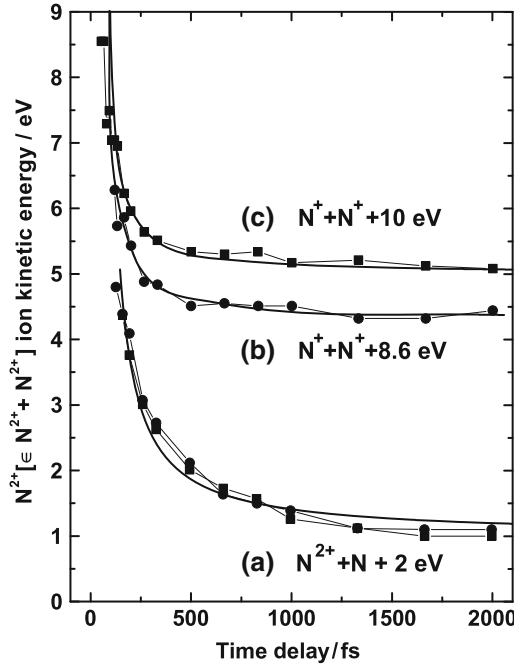


Fig. 1.5 Kinetic energies of the N^{2+} ions from the $N^{2+} + N^{2+}$ probe fragmentation channel as a function of the time delay between the pump and probe pulses. The square and bullet points are experimental data. The full lines represent fits from the model explained in the text: (a) N^{2+} ions coming from the double ionization of the $N^{2+} + N + 2 \text{ eV}$ fragmentation channel, (b) N^{2+} ions coming from the double ionization of the $N^+ + N^+ + 8.6 \text{ eV}$ fragmentation channel, and (c) N^{2+} ions coming from the double ionization of the $N^+ + N^+ + 10 \text{ eV}$ fragmentation channel

$$t(R_e \rightarrow R_f) = t(R_e \rightarrow R_c) + \int_{R_c}^{R_f} \frac{dR}{v(R)}, \quad (1.1)$$

where the velocity $v(R) = \sqrt{2[E - U(R)]/\mu}$ is a function of the KER E , here 2, 8.6, or 10 eV, and of the reduced mass μ . In order to measure the unknown time $t(R_e \rightarrow R_c)$, the probe pulse is applied at time $t(R_e \rightarrow R_f)$ after the excitation pump pulse. The corresponding energy $E_{\text{probe}}[t(R_e \rightarrow R_f)]$ of the $\text{N}^{2+} + \text{N}^{2+}$ imaging fragmentation channel is

$$E_{\text{probe}}[t(R_e \rightarrow R_f)] = E + U_{\text{probe}}(R_f) - U(R_f), \quad (1.2)$$

where $U_{\text{probe}}(R)$ is the potential curve of the probe fragmentation channel. Beyond $R_c = 5 \text{ \AA}$, the potential energy of $\text{N}^{2+} + \text{N}^{2+}$ is purely Coulombic $U_{\text{probe}}(R) = 4/R \text{ a.u.}$ Therefore, the only parameter of the model is the time $t(R_e \rightarrow R_c)$.

The fits of the experimental curves given in Fig. 1.5 give $t(1.1 \rightarrow 5 \text{ \AA}) = 80 \pm 20 \text{ fs}$ for both $\text{N}^+ + \text{N}^+$ channels and $t(1.1 \rightarrow 5 \text{ \AA}) = 120 \pm 20 \text{ fs}$ for the $\text{N}^{2+} + \text{N}$ channel. These dissociation times are larger than the pulse duration. This is an a posteriori validation of the method although shorter pulses are highly desirable in order to increase the temporal resolution. Assuming a quasi-Coulombic dissociation of the $\text{N}^+ + \text{N}^+$ channels for $R < R_c$, i.e. $U(R) = \alpha/R$ where the parameter α is given by the dissociation energy $E = U(R_e) = \alpha/R_e$, the dissociation times $t(1.1 \rightarrow 5 \text{ \AA})$ are smaller than 40 fs for both $\text{N}^+ + \text{N}^+$ channels.

The larger measured dissociation times are to be assigned to chemical bindings in N_2^{2+} which slow down the dissociation process even for purely dissociative states. The high density of states of N_2^{2+} may require a more resolvable excitation pulse than our pump pulse in order to select a particular spectral range of N_2^{2+} . Several schemes may be proposed including harmonic generation. Valence double photoionization with a single photon might be possible although the corresponding cross section is very weak. This type of experiment may require laser systems with very high repetition rates.

1.4 Double Ionization of H_2 at 10 and 40 fs

The ultrafast dynamics of H_2 and H_2^+ molecules and the charge transfer transition $1s\sigma_g \rightarrow 2p\sigma_u$ in H_2^+ give rise to a rich set of phenomenon such as Bond Softening, Bond Hardening, or Charge Resonance Enhanced Ionization [14, 24]. Single ionization of H_2 is expected to produce a vibrational wave packet in H_2^+ since the equilibrium internuclear distance $R_e^+ = 1.052 \text{ \AA}$ of the molecular ion is larger than the equilibrium distance $R_e = 0.741 \text{ \AA}$ of the neutral molecule. Therefore, double ionization may take place while the ion internuclear distance moves. Non sequential double ionization processes are mainly due to rescattering-induced double ionization. The instantaneous ejection of both electrons in a very short time window in comparison with the laser optical period has not been observed yet using laser pulses

in the near infrared-visible optical range. Sequential double ionization results from the single ionization of H_2^+ with no correlations with the first ejected electron. It may occur several optical cycles after the first ionization step when the laser intensity is increased. The time delay between both ionization events is encoded in the proton spectrum which gives the internuclear range where the second ionization occurs. Indeed the proton spectrum and the internuclear distance distribution are linked by the $E = 1/R$ transformation where E and R are, respectively, the total KER and the internuclear distance in atomic units.

Figure 1.6 presents proton spectra recorded at $8 \times 10^{13} \text{ Wcm}^{-2}$ in linear polarization and $1.6 \times 10^{14} \text{ Wcm}^{-2}$ in circular polarization with 40-fs pulse durations. The laser intensities are kept lower than the saturation ionization intensity of H_2 in order to prevent any depopulation of the neutral molecule ground state. Using linear polarization and 40-fs laser pulses, this saturation intensity is around $2 \times 10^{14} \text{ Wcm}^{-2}$. Here, the total proton spectra are represented in order to get the total proton yield. From covariance mapping, we know that protons with energies below 2 eV come from the $\text{H}^+ + \text{H}$ fragmentation channel. These protons are not correlated to any double ionization event as it can be seen in Fig. 1.1.

No fast protons are detected in both polarizations. Although rescattering only occurs in linear polarization, no difference is detected between linear and circular polarizations. At energies above 2 eV, both spectra are dominated by Charge Resonance Enhanced Ionization with a maximum of $\sim 3 \text{ eV}$. The $1\sigma_g-2p\sigma_u$ transition matches the photon energy at $R = 2.5 \text{ \AA}$ at 800 nm. At this distance, the ionization of H_2^+ gives a proton energy of 2.9 eV. At 40 fs, the vibrational nuclear wave packet of H_2^+ has enough time to reach the internuclear range where enhanced ionization takes place. The associated very large probability leads to proton spectra which are dominated by this effect [14]. Concerning the similar heights of proton spectra in both polarization states, no particular conclusion can be drawn because of the strong angular discrimination of the ion spectrometer. The laser intensities are set in order to get the same electric field strength in both polarizations.

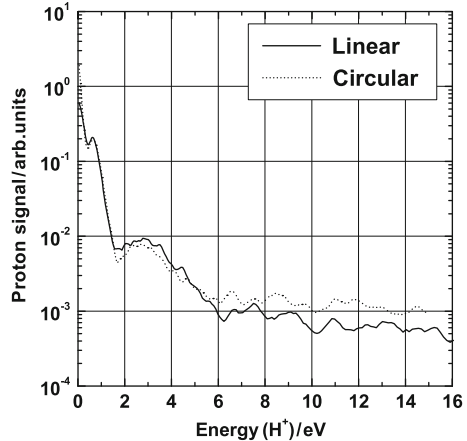


Fig. 1.6 Proton KER spectra recorded from H_2 using 40-fs laser pulses. *Full curve*: linear polarization and $8 \times 10^{13} \text{ Wcm}^{-2}$. *Dotted curve*: circular polarization and $1.6 \times 10^{14} \text{ Wcm}^{-2}$

Figure 1.7 presents proton spectra recorded with the same laser intensities but with 10-fs pulses. The saturation ionization intensity of the neutral molecule is higher with few-cycle pulses than with 40-fs laser pulses. In linear polarization, the enhancement of the proton signal up to 13 eV is a clear signature of ultrafast non sequential double ionization. Moreover, the absence of this enhancement in circular polarization signs the rescattering origin of high-energy protons. Instantaneous double ionization should be independent of the polarization state. The dashed curves represent proton spectra which might be expected from an instantaneous double ionization of H_2 with a maximum around 9.4 eV and single ionization of H_2^+ with a maximum around 6.7 eV. These spectra are calculated assuming that the molecules are in their ground vibrational state and using the $E = 1/R$ transformation with the associated normalization, where E and R are, respectively, the total KER and the internuclear distance in atomic units. The extension of the experimental spectrum over the range of both calculated spectra shows the ultrafast dynamics of the nuclear wave packet during the rescattering process. Such a behavior has been reported in high-order harmonic generation which follows the same rescattering dynamics [42,43]. Varying the pulse duration from 30 fs down to 8 fs, Alnaser et al. have been able to distinguish the first electronic wave packet return from the third one and their respective contributions to the proton spectra. However, Légaré et al. using 8.6 fs pulses and a similar detection scheme do not report such a detailed rescattering pattern but a pronounced Charge Resonance Enhanced Ionization peak [44] that is not reported in reference [38] and does not appear here in Fig. 1.7. The

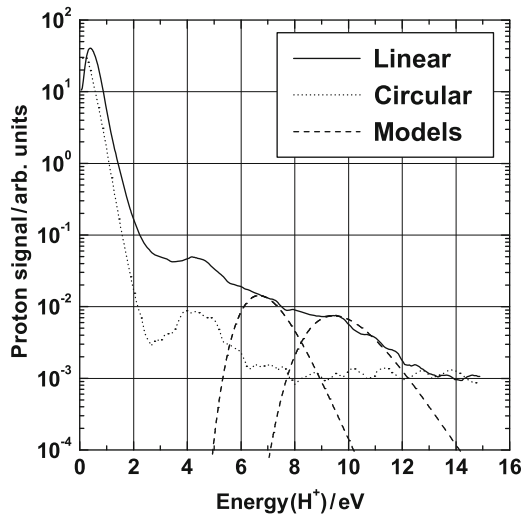


Fig. 1.7 Proton KER spectra recorded from H_2 using 10-fs laser pulses. *Full curve*: linear polarization and $8 \times 10^{13} \text{ Wcm}^{-2}$. *Dotted curve*: circular polarization and $1.6 \times 10^{14} \text{ Wcm}^{-2}$. The *dashed curves* centered at 6.7 and 9.4 eV represent the proton spectra expected from, respectively, the instantaneous ionization of $(X^2 \Sigma_g^+, v^+ = 0) H_2^+$ ions and instantaneous double ionization of $(X^1 \Sigma_g^+, v = 0) H_2$ molecules

similarities and differences between spectra recorded with sub-10 fs laser pulses indicate the high sensitivity of double ionization in H_2 regarding ultrashort pulses.

In Fig. 1.7, there are humps at 4.5 eV which correspond to sequential ionization in both polarizations. The energy range of these humps is significantly larger than the energy range around 3 eV of Charge Resonance Enhanced Ionization in Fig. 1.6. Within 10 fs, the molecular ion nuclear wave packet does not have time to explore the enhanced ionization distance range. As the laser intensity is increased, sequential ionization is expected to dominate the double ionization dynamics. In Fig. 1.8, the sequential ionization broad structure between 4.5 and 6 eV is shifted toward higher energies as the laser intensity gets higher. Indeed the time delay between the first and second electron ejections decreases as the laser intensity is increased because of the steeper leading edge of the pulse at higher intensities [29]. In the same time, the relative rescattering probability decreases because single ionization is saturated and sequential ionization dominates the overall dynamics. Rescattering is detected at relatively low intensities around $5 \times 10^{13} \text{ Wcm}^{-2}$. The corresponding electron maximum energy is $3.17U_p = 9.5 \text{ eV}$ when it recollides the H_2^+ ion core. This energy is well below the ionization potential of H_2^+ which is 29.9 eV for the ground vibrational level $v^+ = 0$. In consequence at low laser intensities, recollision cannot

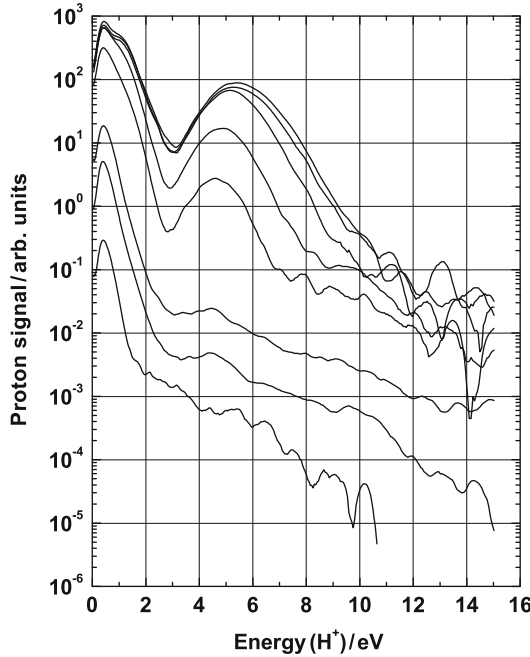
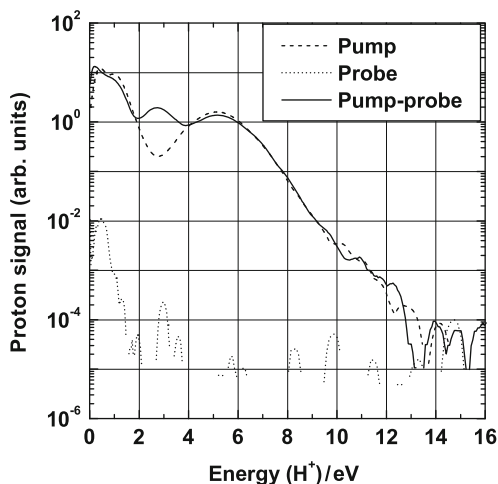


Fig. 1.8 Proton KER spectra recorded from H_2 using linearly-polarized 10-fs laser pulses. The spectra are normalized to the same H_2 pressure. From *top to bottom*, the laser intensities are, $1.5 \times 10^{15} \text{ Wcm}^{-2}$, $8.7 \times 10^{14} \text{ Wcm}^{-2}$, $4.7 \times 10^{14} \text{ Wcm}^{-2}$, $2.7 \times 10^{14} \text{ Wcm}^{-2}$, $1.5 \times 10^{14} \text{ Wcm}^{-2}$, $7.8 \times 10^{13} \text{ Wcm}^{-2}$, $5.6 \times 10^{13} \text{ Wcm}^{-2}$, and $3.1 \times 10^{13} \text{ Wcm}^{-2}$

Fig. 1.9 Proton spectra recorded from H_2 using 10-fs pump, probe, and pump-probe laser excitation schemes. *Dashed curve*: pump pulse at $1.4 \times 10^{15} \text{ Wcm}^{-2}$. *Dotted curve*: probe pulse at $3.4 \times 10^{13} \text{ Wcm}^{-2}$. *Full curve*: same above pump and probe pulses where the probe pulse delay is 24 fs



eject directly the second electron but produces sufficient excitation of the ion core H_2^+ for a subsequent efficient field ionization leading to the ejection of the second electron. This behavior was observed with other molecules such as N_2 , CO_2 , and C_2H_2 [13].

Finally, we made a distinction between bare sequential double ionization and Charge Resonance Enhanced Ionization which are both sequential processes. The differences between both processes are illustrated in Fig. 1.9. The dashed curve is the proton spectrum recorded with a single 10-fs pulse at $1.4 \times 10^{15} \text{ Wcm}^{-2}$. The broad hump around 5.5 eV corresponds to bare sequential double ionization. The dotted curve is the proton spectrum recorded with a single 10-fs pulse but at a much smaller laser intensity $3.4 \times 10^{13} \text{ Wcm}^{-2}$. As expected from Fig. 1.8, the double ionization proton signal above 2 eV is very weak. When this weak pulse is delayed 24 fs after the main pulse, the pump-probe spectrum represented by the full curve exhibits a peak around 2.9 eV in addition to the broad peak. This new peak is the signature of Charge Resonance Enhanced ionization. Within 24 fs, the nuclear wave packet has time to explore the enhanced ionization distance range.

1.5 Coulomb Explosion of N_2 at 10 and 40 fs

Except for H_2 and its isotopes, Coulomb explosion imaging requires charge states higher than 2. Indeed molecular dications exhibit a dense pattern of non-Coulombic electronic states due to chemical binding forces. In general, the ionization sequence leading to the high charge states is difficult to identify in terms of sequential or non sequential multiple ionization. Therefore, the pulse duration remains the main indicator of time resolution. The optical period might be considered in the case of rescattering non sequential processes. However multi-cycle ionization events are not

to be completely excluded even for few-cycle laser pulses. A single-cycle multiple ionization sequence would demand carrier-envelope-phase-locked pulses with only one optical cycle in the pulse duration, i.e., within the full-width at half-maximum. The femtosecond contrast of such pulses should be very high in order to avoid any ionization in the foot of the leading edge of the pulse.

Here, we present results with recorded for the N_2 molecule with 10- and 40-fs laser pulses. The first interesting case is double ionization. The main difference with the H_2 molecule lies in the greater similarities between the $X^1\sigma_g^+$ electronic ground state of N_2 and $X^2\sigma_g^+$ electronic ground state of N_2^+ . For instance, the equilibrium internuclear distances, respectively, 1.098 and 1.116 Å for N_2 and N_2^+ , and the vibrational constants, respectively, 2,359 and 2,207 cm^{-1} for N_2 and N_2^+ , are much closer than in the case of H_2 . For these reasons, we do not expect a well developed nuclear wave packet as in the case of H_2 . For instance, the Franck–Condon factor between the ground vibrational state of N_2 and the ground vibrational state of N_2^+ is 90%. In consequence, the internuclear range is expected to be quite similar for double ionization using 10- or 40-fs pulses on the contrary to the H_2 situation. This behavior is illustrated in Fig. 1.10, which represents the energy spectra of N^+ ions belonging to the $N^+ + N^+$ fragmentation channel. The same structures are observed with both pulse durations. These structures are commented in Sect. 1.3 in terms of the dissociation lifetimes.

The situation is different for the ionization sequence leading to the N_2^{4+} transient molecular ion. In particular, the N_2^{3+} precursor transient molecular ion is expected to dissociate on a much shorter time scale than the N_2^{2+} dication discussed in Sect. 1.3. In N_2^{3+} , binding forces are now dominated by the Coulomb repulsion forces [45]. Therefore, the $N^{2+} + N^{2+}$ fragmentation channel from N_2^{4+} is a good

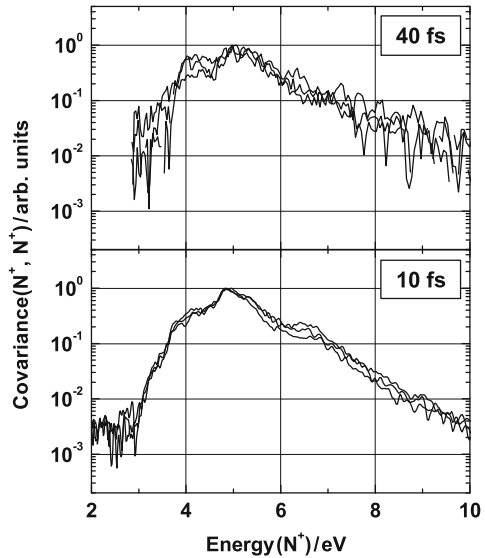


Fig. 1.10 Normalized covariance energy spectra of N^+ ions from the $N^+ + N^+$ fragmentation channel of N_2 recorded at 3 laser intensities $4 \times 10^{14} \text{ Wcm}^{-2}$, $8 \times 10^{14} \text{ Wcm}^{-2}$, $2 \times 10^{15} \text{ Wcm}^{-2}$, and with different pulse durations 40 and 10 fs

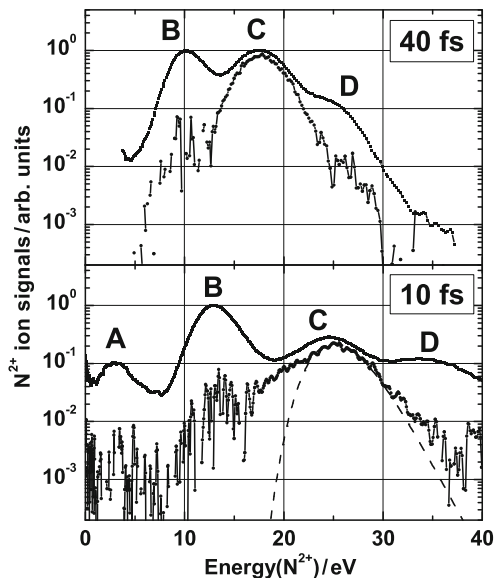


Fig. 1.11 Kinetic energy spectra of N^{2+} ions from N_2 recorded at $2 \times 10^{15} \text{ Wcm}^{-2}$ and 40 and 10 fs pulse durations. For each pulse duration, the *upper curves* represent spectra of all the detected N^{2+} ions. The labels A, B, C, and D represent respectively, N^{2+} ions coming from the (A) $\text{N}^{2+} + \text{N}$, (B) $\text{N}^{2+} + \text{N}^+$, (C) $\text{N}^{2+} + \text{N}^{2+}$, and (D) $\text{N}^{2+} + \text{N}^{3+}$ fragmentation channels. These channels are determined using covariance mapping. The *lower curves* represent the $(\text{N}^{2+}, \text{N}^{2+})$ covariance spectra that identify the $\text{N}^{2+} + \text{N}^{2+}$ without any ambiguity. The *dashed curve* in the bottom panel underneath the (C) $\text{N}^{2+} + \text{N}^{2+}$ covariance spectrum represents a fit of the energy spectrum assuming a Gaussian radial distribution of the internuclear distance following (1.3). See text for explanations

candidate in order to get an idea of the required pulse duration for Coulomb explosion. Figure 1.11 represents the N^{2+} kinetic energy spectra recorded at 10 and 40 fs using the same peak laser intensity $2 \times 10^{15} \text{ Wcm}^{-2}$. Structures labeled A, B, C, and D are associated to different fragmentation channels involving the N^{2+} ion. The $\text{N}^{2+} + \text{N}^{2+}$ fragmentation channel labeled C is identified by the covariance spectra represented by the lower curves. An important shift toward higher energies is observed when the pulse duration is reduced to 10 fs. Therefore, molecular explosion occurs at shorter internuclear distances. In addition, the relative branching ratio of the $\text{N}^{2+} + \text{N}^{2+}$ channel is weaker at 10 fs than at 40 fs as it can be seen from the heights of the B and C structures. This result is consistent with higher KER at 10 fs. Indeed, the multiple ionization thresholds scale as $1/R$ where R is the internuclear distance. Therefore, the N_2^{4+} threshold is higher at shorter internuclear distances and the corresponding ion yield is weaker than the ion yield obtained with longer pulses at larger internuclear distances.

For molecules in their ground vibrational state, the radial distribution $\chi^2(R)$ of the internuclear distance R may be approximated by a Gaussian

$$\chi^2(R) = \frac{1}{\sigma\sqrt{\pi}} \exp \left[- \left(\frac{R - R_e}{\sigma} \right)^2 \right], \quad (1.3)$$

assuming a perfect harmonic oscillator with $\sigma = \sqrt{\hbar/\mu\omega}$ where μ is the reduced mass and ω is the vibrational angular frequency. In the case of N_2 in the ground state $\text{X}^1\Sigma_g^+$, $v = 0$ the equilibrium distance is $R_e = 1.10 \text{ \AA}$ and the width is $\sigma = 0.045 \text{ \AA}$. The harmonic oscillator approximation is excellent because of the very large dissociation energy $D_0^0 = 9.759 \text{ eV}$ in comparison with the vibrational spacing $\hbar\omega_e = 0.29 \text{ eV}$. Equation (1.3) may be used in order to fit the measured ion energy spectrum with R_e and σ as fitting parameters. The relation between the energy spectrum $S(E)$ and the radial distribution $\chi^2(R)$ is $S(E) = \chi^2(R)|dR/dE|$ where the energy $E = 4/R$ is the Coulomb repulsion energy in atomic units. The dashed curve in the N^{2+} spectra at 10 fs of Fig. 1.11 represents such a fit. Although the procedure may not be rigorous because of the unknown multiple ionization pathway leading to $\text{N}^{2+} + \text{N}^{2+}$, the extracted internuclear distance $R_e^{\text{exp}} = 1.15 \pm 0.02 \text{ \AA}$ and width $\sigma^{\text{exp}} = 0.15 \pm 0.02 \text{ \AA}$ are significant of the laser experiment. The $\pm 0.02 \text{ \AA}$ error corresponds to the internuclear range where the fit is satisfactory. The extracted distance R_e^{exp} may be regarded as not too far from the tabulated equilibrium value R_e . However, the extracted width σ^{exp} is significantly larger than the zero-point vibrational internuclear range σ . Moreover in Fig. 1.11, the disagreement between the experimental data and the fit is much more pronounced in the low-energy wing of the covariance spectrum. Therefore, the large width σ^{exp} comes from the stretching of the molecular system during multiple ionization even for pulse durations as short as 10 fs.

Finally, the energies of the maxima of the $\text{N}^{2+} + \text{N}^{2+}$ spectra are plotted as a function of the laser intensity in Fig. 1.12. These energies increase with the intensity because of the steeper leading edge of the pulse at higher intensities. The same behavior is observed in H_2 in Fig. 1.8. When the peak laser intensity is increased, the time delays between multiple ionization events become smaller and the internuclear distance stretching is less pronounced. This intensity dependence of the KER shows the ultrafast dynamics of nuclear motions during multiple ionization. At high intensities, the measured energies are close to the repulsion energies for 10-fs pulses and may lead to the internuclear distance determination. Future experiments will demand even shorter pulse durations in order to get rid of the laser intensity dependence.

1.6 Conclusion

Laser-induced ultrafast Coulomb explosion imaging of molecules may be considered as a very simple imaging technique which requires a compact laser system, a pulse post-compression set-up, and a conventional ion time-of-flight spectrometer. Concerning the ultrafast laser source, the hydrogen molecule constitutes a

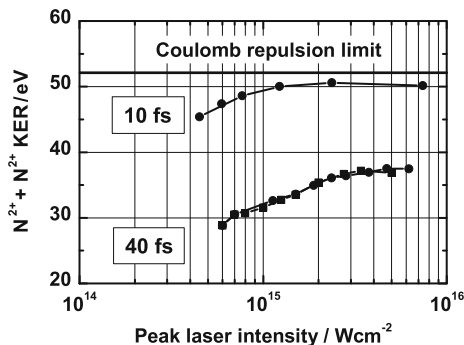


Fig. 1.12 KER of the $N^{2+} + N^{2+}$ fragmentation channel at 10 and 40 fs as a function of the laser intensity. These energies are the energies of the maxima of the corresponding KER spectra. The Coulomb repulsion energy is the electrostatic repulsion energy calculated at $R_e(N_2) = 1.098 \text{ \AA}$

remarkable benchmark for intense few-cycle laser pulses. In addition to non sequential double ionization and Charge Resonance Enhanced Ionization reported above, new effects such as auto-double-ionization may be observed in the future [46]. Sequential double ionization remains an interesting diagnostic for intense few-cycle pulses with intensities above the single ionization saturation intensity. Recently, a full-quantum non-Born-Oppenheimer model was developed and gives good agreements with the experimental data for 10-fs pulse durations [47]. This model predicts a high sensitivity of the proton spectra for pulse durations down to 1 fs. For heavier molecules such as N_2 , few-cycle pulses permit to multiple ionize the molecule without any significant stretching. The reduction of the pulse duration down to a few femtoseconds is highly desirable in order to freeze the nuclear motions and to avoid the pulse rise time effects reported here for N_2 . Finally, the pump-probe excitation scheme opens the door to ultrafast dynamics studies of excited and ionized molecular species. In addition to the reported experiment for N_2 , let us mention the real-time visualization of hydrogen migration in the acetylene-vinylidene dication isomerization reported by Hishikawa et al. [48]. These techniques may be of interest for the recently reported efficient ejection of H_3^+ ions from molecules which do not have any methyl group [49].

Results presented in this paper have been obtained in Saclay over the past few years. The work of undergraduate students E. Baldit, C. Beylerian, and C. Bondoux and graduate student S. Saugout as well as the technical assistance of M. Bougeard, D. Guyader, A. Fillon, and G. Le Chevallier are gratefully acknowledged. This research is supported by ANR (Agence Nationale de la Recherche, Projet Image Femto, décision d'aide No. ANR-07-BLAN-0162-01).

References

1. G.S. Voronov, N.B. Delone, *Sov. Phys. JETP Lett.* **1**, 66 (1965)
2. G.S. Voronov, N.B. Delone, *Sov. Phys. JETP* **23**, 54 (1966)
3. S.L. Chin, F. Yergeau, P. Lavigne, *J. Phys. B Atom. Mol. Opt. Phys.* **18**, L213 (1985)
4. P.M. Paul, E.S. Toma, P. Breger, G. Mullot, F. Augé Ph. Balcou, H.G. Muller, P. Agostini, *Science* **292**, 1689 (2001)
5. Z. Vager, R. Naaman, E.P. Kanter, *Science* **244**, 426 (1989)
6. L.J. Frasinski, K. Codling, P.A. Hatherly, J. Barr, I.N. Ross, W.T. Toner, *Phys. Rev. Lett.* **58**, 2424 (1987)
7. C. Cornaggia, J. Lavancier, D. Normand, J. Morellec, P. Agostini, J.-P. Chambaret, *Phys. Rev. A* **44**, 4499 (1991)
8. J.H. Posthumus, L.J. Frasinski, A.J. Gilles, K. Codling, *J. Phys. B Atom. Mol. Opt. Phys.* **28**, L349 (1995)
9. M. Yu Kuchiev, *Sov. Phys. JETP Lett.* **45**, 404 (1987)
10. K.J. Schafer, B. Yang, L.F. Di Mauro, K.C. Kulander, *Phys. Rev. Lett.* **70**, 1599 (1993)
11. P.B. Corkum, *Phys. Rev. Lett.* **71**, 1994 (1993)
12. B. Walker, B. Sheehy, L.F. Di Mauro, P. Agostini, K.J. Schafer, K.C. Kulander, *Phys. Rev. Lett.* **73**, 1227 (1994)
13. C. Cornaggia, Ph. Hering, *Phys. Rev. A* **62**, 023403 (2000)
14. T. Zuo, A.D. Bandrauk, *Phys. Rev. A* **52**, R2511 (1995)
15. S. Chelkowski, A.D. Bandrauk, *J. Phys. B Atom. Mol. Opt. Phys.* **28**, L723 (1995)
16. G. Lagmago Kamta, A.D. Bandrauk, *Phys. Rev. A* **76**, 053409 (2007)
17. C. Cornaggia, F. Salin, C. Le Blanc, *J. Phys. B Atom. Mol. Opt. Phys.* **29**, L749 (1996)
18. C. Cornaggia, *Phys. Rev. A* **54**, R2555 (1996)
19. A. Hishikawa, A. Iwamae, K. Hoshina, M. Kono, K. Yamanouchi, *Chem. Phys. Lett.* **282**, 283 (1998)
20. A. Hishikawa, A. Iwamae, K. Yamanouchi, *Phys. Rev. Lett.* **83**, 1127 (1999)
21. K. Zhao, W.T. Hill, *Phys. Rev. A* **71**, 013412 (2005)
22. W.A. Bryan, W.R. Newell, J.H. Sanderson, A.J. Langley, *Phys. Rev. A* **74**, 053409 (2006)
23. F. Rosca-Pruna, M.J.J. Vrakking, *Phys. Rev. Lett.* **87**, 153902 (2001)
24. J.H. Posthumus, *Rep. Prog. Phys.* **67**, 623 (2004)
25. C. Beylerian, C. Cornaggia, *J. Phys. B Atom. Mol. Opt. Phys.* **37**, L259 (2004)
26. A.H. Zewail, *J. Phys. Chem. A* **104**, 5660 (2000)
27. C. Beylerian, S. Saugout, C. Cornaggia, *J. Phys. B Atom. Mol. Opt. Phys.* **39**, L105 (2006)
28. S. Saugout, C. Cornaggia, *Phys. Rev. A* **73**, 041406 (2006)
29. E. Baldit, S. Saugout, C. Cornaggia, *Phys. Rev. A* **71**, 021403 (2005)
30. M. Nisoli, S. De Silvestri, O. Svelto, *Appl. Phys. Lett.* **68**, 2793 (1996)
31. C.P. Hauri, W. Kornelis, F.W. Helbing, A. Heinrich, A. Couairon, A. Mysyrowicz, J. Biegert, U. Keller, *Appl. Phys. B* **79**, 673 (2004)
32. C. Bondoux, C. Cornaggia, *J. Phys. B Atom. Mol. Opt. Phys.* **40**, 4463 (2007)
33. W.C. Wiley, I.H. McLaren, *Rev. Sci. Instrum.* **26**, 1150 (1955)
34. Ph. Hering, C. Cornaggia, *Phys. Rev. A* **59**, 2836 (1999)
35. A. Hishikawa, A. Iwamae, K. Hoshina, M. Kono, K. Yamanouchi, *Chem. Phys.* **231**, 315 (1998)
36. L.J. Frasinski, K. Codling, P.A. Hatherly, *Science* **246**, 973 (1989)
37. M. Ueyama, H. Hasegawa, A. Hishikawa, K. Yamanouchi, *J. Chem. Phys.* **123**, 154305 (2005)
38. A.S. Alnaser, X.M. Tong, T. Osipov, S. Voss, C.M. Maharjan, P. Ranitovic, B. Ulrich, B. Shan, Z. Chang, C.D. Lin, C.L. Cocke, *Phys. Rev. Lett.* **93**, 183202 (2004)
39. S.D. Price, *Int. J. Mass Spectrom.* **260**, 1 (2007)
40. M. Lundqvist, D. Edvardsson, P. Baltzer, B. Wannberg, *J. Phys. B Atom. Mol. Opt. Phys.* **29**, 1489 (1996)
41. M. Ahmad, P. Lablanquie, F. Penent, J.G. Lambourne, R.I. Hall, J.H.D. Eland, *J. Phys. B Atom. Mol. Opt. Phys.* **39**, 3599 (2006)
42. M. Lein, *Phys. Rev. Lett.* **94**, 053004 (2005)

- 43. S. Baker, J. Robinson, C.A. Haworth, H. Teng, R.A. Smith, C.C. Chirila, M. Lein, J.W.G. Tisch, J.P. Marangos, *Science* **312**, 424 (2006)
- 44. F. Légaré I.V. Litvinyuk, P.W. Dooley, F. Quéré, A.D. Bandrauk, D.M. Villeneuve, P.B. Corkum, *Phys. Rev. Lett.* **91**, 093002 (2003)
- 45. A.D. Bandrauk, D.G. Musaev, K. Morokuma, *Phys. Rev. A* **59**, 4309 (1999)
- 46. S. Saugout, C. Cornaggia, A. Suzor-Weiner, E. Charron, *Phys. Rev. Lett.* **98**, 253003 (2007)
- 47. S. Saugout, E. Charron, C. Cornaggia, *Phys. Rev. A* **77**, 023404 (2008)
- 48. A. Hishikawa, A. Matsuda, M. Fushitani, E.J. Takahashi, *Phys. Rev. Lett.* **99**, 258302 (2007)
- 49. K. Hoshina, Y. Furukama, T. Okino, K. Yamanouchi, *J. Chem. Phys.* **129**, 104302 (2008)

Chapter 2

Quantum Switching of Magnetic Fields by Circularly Polarized Re-Optimized π Laser Pulses: From One-Electron Atomic Ions to Molecules

Ingo Barth and Jörn Manz

Abstract Circularly polarized re-optimized π laser pulses may induce electronic and/or nuclear ring currents in model systems, from one-electron atomic ions till molecules which should have three-, four-, or higher-fold axes of rotations or reflection-rotations, in order to support doubly or more degenerate, complex-valued eigenstates which support these ring currents. The ring currents in turn induce magnetic fields. The effects are about two orders of magnitude larger than for traditional ring currents which are induced by external magnetic fields. Moreover, the laser pulses allow to control the strengths and shapes of the ring currents and, therefore, also the induced magnetic fields. We present a survey of the development of the field, together with new quantum simulations which document ultrafast switchings of magnetic fields. We discuss various criteria such as strong ring currents with small radii, in order to generate huge magnetic fields, approaching 1,000 T, in accord with the Biot–Savart law. Moreover, we consider various methods for monitoring the fields, and for applications, in particular ultrafast deflections of neutrons by means of quantum switching of the ring currents and induced magnetic fields.

I. Barth (✉)

Institut für Chemie und Biochemie, Freie Universität Berlin, Takustr. 3, 14195 Berlin, Germany
and

Kavli Institute for Theoretical Physics, University of California, Santa Barbara,
California 93106–4030, USA

and

Max-Born-Institut, Max-Born-Str. 2A, 12489 Berlin, Germany

e-mail: barth@mbi-berlin.de

J. Manz

Institut für Chemie und Biochemie, Freie Universität Berlin, Takustr. 3, 14195 Berlin, Germany
and

Kavli Institute for Theoretical Physics, University of California, Santa Barbara,
California 93106–4030, USA

e-mail: jmanz@chemie.fu-berlin.de

2.1 Introduction

Recent quantum dynamics simulations predict that circularly polarized laser pulses may induce stationary ring currents or time-dependent charge circulations in model systems, with applications from the hydrogen atom or one-electron atomic ions [1, 2] to molecules [3–13], see also [14, 15], circular carbon clusters [16], nanorings [17–20], and nanotubes [21]; for pioneering applications to Rydberg states see [22–27]. These ring currents and charge circulations in turn induce stationary [2, 4, 7–9, 28] and time-dependent [28] magnetic fields in the model systems, respectively. From a theoretical perspective, a stationary ring current is described in terms of a single complex stationary degenerate eigenfunction of the system, carrying angular momentum; different eigenstates correspond to different ring currents and, therefore, to different induced stationary magnetic fields [28]. As a rule, the corresponding stationary densities and charge distributions often have typical toroidal or near-toroidal shapes [2, 7–9, 11, 28]; exceptions from this rule (e.g., for ring-shaped molecules) are documented in [4, 28], see also Fig. 2.3b below. Recently, this characteristic signature has been observed experimentally in ionized states of atoms induced by well-designed circularly polarized laser pulses [29]. In contrast, charge circulations, i.e., non-stationary ring currents, are represented by time-dependent wave packets, which carry non-zero angular momentum, and corresponding time- and angle-dependent densities; again as a rule, the centers of these non-stationary densities and corresponding charge distributions move along toroidal or near-toroidal paths about the axis of symmetry (e.g., molecular axis) [10, 12, 28]; for exceptions from this rule (e.g., for ring-shaped molecules) see [3, 5, 6, 28]. These wave packets are also called “hybrid states” which are superpositions of at least one of the complex eigenfunctions which support ring currents, plus others which have different eigenenergies, e.g., the ground state.

The condition that laser-induced ring currents supporting magnetic fields are represented by complex eigenfunctions is essential because otherwise real eigenfunctions (or eigenfunctions which are real except for a phase factor) would yield zero flux/current densities, see e.g., [28, 30–32]. At the same time, this condition imposes the constraint of special symmetries for suitable model systems, i.e., they should support at least one, two- or higher-dimensional irreducible representation with corresponding doubly or more degenerate symmetry-adapted basis functions. This requirement is satisfied automatically for model systems which possess a principle axis of n -fold rotation or rotation–reflection, where $n \geq 3$, including the H atom and one-electron atomic ions ($n = \infty$) [1, 2], or linear molecules ($n = \infty$) [7–12] and nanorings ($n \approx \infty$) [17–20], or molecules which have, e.g., D_{nh} symmetry ($n \geq 3$) such as Mg-porphyrin ($n = 4$) [3–6] or benzene ($n = 6$); other possible symmetries include C_{nv} ($n \geq 3$), D_{nd} ($n \geq 2$), or tetrahedral (e.g., CH_4 , UH_4 , or more generally AB_4) or icosahedral molecules (e.g., C_{60}) or clusters. If the ideal symmetry of the system is just “weakly broken” such that it possesses near-degenerate states, it may still support temporary charge circulations [33, 34]. All other molecules do not allow excitations of ring currents (e.g., there are no stationary ring currents in molecules with D_{2h} symmetry such as ethylene, because

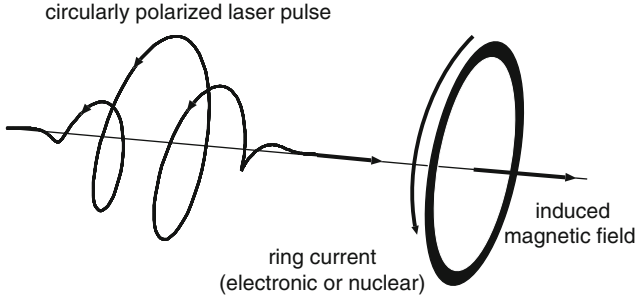


Fig. 2.1 Induction of ring currents and magnetic fields by circularly polarized laser pulses (schematic)

D_{2h} has only one-dimensional irreducible representations). Below we shall focus on quantum switching of magnetic fields which are supported by ring currents in systems with suitable symmetries. The term “quantum” implies quantum dynamics simulations of the processes which are induced by means of well-designed laser pulses. “Switching” is understood in the general sense, i.e., switching-on and -off, or switching the direction of the magnetic fields. These effects will be achieved simply by switching-on and -off the underlying ring currents, or switching their directions, e.g., from “left” to “right” ring currents (for a discussion of the definitions of left versus right circularly polarized fields and corresponding ring currents, see [4] and the literature cited therein).

The net effect from circularly polarized laser pulses via ring currents to induced magnetic fields in model systems with proper symmetry is sketched schematically in Fig. 2.1. It is related to the Inverse Faraday Effect [35–37]. The photons of the left and right circularly polarized laser pulses carry angular momenta $1\hbar$ with opposite helicities, which are transferred to the system causing corresponding opposite changes of the angular momenta of the ring currents, e.g., from the non-degenerate ground state to degenerate excited states with opposite magnetic quantum numbers $-\hbar$ or $+\hbar$, respectively. Since the circularly polarized driving fields $\mathbf{E}(t)$ may be decomposed into two perpendicular components (say $E_X(t)$ and $E_Y(t)$) perpendicular to the direction of propagation (say Z , in the laboratory frame), similar effects may also be achieved by more general laser pulses which possess two perpendicular components with proper phase relationships, [12, 17, 33, 34], e.g., optimal control fields [20]. Experimental preparations of these types of circularly polarized or more general laser pulses have been demonstrated, e.g., in [38–42], see also [43].

The ring currents and magnetic fields induced by laser pulses turn out to be much stronger (typically by two orders of magnitude) than those induced by the traditional approach which is based on applying static external magnetic fields, compare, e.g., [4] and [44, 45] (see also the reviews [46–48]), respectively. The reason is that laser pulses can induce currents which correspond to excitations of full charges (e.g., $-1e$ for single electron excitation), or even more. In contrast, present technology restricts the strength of permanent external magnetic fields to less than 100 T [49], and these

magnetic fields may induce only rather weak ring currents corresponding to stationary fluxes of $-1/100 e$ or less. Indeed, one would need external permanent magnetic fields of the order of 10,000 T in order to induce similarly strong effects as laser pulses – a scenario which exists in cosmic domains, see e.g., [50–52], but which is far out of reach of present technology in the laboratory. This comparison indicates the enormous advantage of the suggested new approach to ring currents and induced magnetic fields, generated by circularly polarized laser pulses.

Another fundamental advantage is that laser pulses allow active control of the strengths and shapes of the ring currents and, therefore, also the magnetic fields, simply by exciting different degenerate eigenstates, by means of well-designed control laser pulses [28]. In contrast, from a theoretical perspective, permanent external magnetic fields even as strong as 100 T are still in the weak-field that is linear response regime, i.e., they do not allow any control of the induced ring currents. The second advantage, i.e., controllability, puts the present topic into the general realm of quantum control by means of laser pulses, see e.g., [53–55].

The purpose of this article is twofold: In Sect. 2.2, we present a survey of the development of the field, focusing on our approach which is based on circularly polarized re-optimized π laser pulses applied to model systems from the hydrogen atom or one-electron atomic ions and to pre-oriented/aligned molecules, in the non-relativistic regime [2, 4, 7–9, 11, 28]; for relativistic extensions including ring currents caused by electron spins, see e.g., [56], see also [57]. Quantum control by π laser pulses, or series of π laser pulses, is based on some experience of our group which goes back to state-selective bond breaking [58], and subsequent extensions including control of isomerization reactions by pump-dump IR π pulses [59, 60], photo-association [61], as well as separation of enantiomers [62–64]; see also [65–68] and the reviews [69–71]. Section 2.2 will also present the nomenclature and discuss the necessary conditions for observing the effects. Most of these applications deal with switching-on the ring currents and corresponding magnetic fields starting from the systems in the non-degenerate ground state. Reversibility of time and helicity implies that subsequent application of the dump laser pulse would induce the opposite effect, i.e., switching-off; in practice, deviations from perfect reversibility might cause competition of other processes, e.g., climbing to higher levels. In Sect. 2.3, we shall present an extension, i.e., we shall assume that the system has already been switched on to a complex eigenstate, which represents a ring current with corresponding magnetic field, and then we shall show how one can employ a sequential series of re-optimized π laser pulses with opposite circular polarizations in order to switch the original direction of the ring currents to the opposite one, together with the associated switch of the direction of the magnetic fields. The concept is motivated by pioneering work by E.K.U. Gross and coworkers who could demonstrate the switch of the directionality of the ring currents in nanorings, by means of optimal laser pulses with a change of the helicity [20]. The conclusions are in Sect. 2.4, including an outlook to applications to favorable systems, and to analysis and control of nuclear vibrations and chemical reactions induced by ultrafast interactions with neutrons, due to pulsed deflections by switched magnetic fields.

2.2 Survey on Quantum Switching-on the Ring Currents and Magnetic Fields

Our previous work on quantum switching-on the ring currents and magnetic fields by means of circularly polarized re-optimized π laser pulses has been developed as documented in full detail in [2, 4, 7–9, 11, 28]. The present survey aims at a presentation of the essentials. For this purpose, let us start with setting the exemplary scenario, i.e., we assume that the system is excited by means of a right (+) or left (–) circularly polarized re-optimized π laser pulse which propagates along the Z -axis in the laboratory frame, with electric field centered at the time $t = 0$

$$\mathbf{E}_{\pm}(t) = \mathcal{E}_0 s(t) (\cos(\omega t + \eta) \mathbf{e}_X \pm \sin(\omega t + \eta) \mathbf{e}_Y), \quad (2.1)$$

where \mathcal{E}_0 is the amplitude, ω the carrier frequency, η the phase, and \mathbf{e}_X and \mathbf{e}_Y the unit vectors point along the X - and Y -directions. The electric field may also be defined in terms of the vector field,

$$\mathbf{E}_{\pm}(t) = -\frac{d}{dt} \mathbf{A}_{\pm}(t), \quad (2.2)$$

see e.g., [6–11, 28]. This option is recommended in particular for ultrashort, few-cycle laser pulses because the resulting electric fields satisfy automatically the condition [72],

$$\int_{-\infty}^{\infty} \mathbf{E}_{\pm}(t) dt = \mathbf{0}. \quad (2.3)$$

The phase η turns out to be irrelevant for the present applications to excitations of stationary ring currents and will be set to zero; in contrast, the phase may be significant in the case of excitations of time-dependent charge circulations, see e.g., [73] and Sect. 2.1, and for switching, see Sect. 2.3. The shape functions $s(t)$ of transform-limited experimental laser pulses are Gaussian envelopes, which are well approximated by \cos^n laser envelopes, in the limit $n \rightarrow \infty$ [74]; see also [6]. The application for Mg-porphyrin shown below employ a \cos^{20} laser pulse, the others use, however, the traditional \cos^2 shape function, as suggested in [65],

$$s(t) = \begin{cases} \cos^2(\pi t / t_p) & \text{for } |t| \leq t_p/2 \\ 0 & \text{for } |t| > t_p/2 \end{cases}, \quad (2.4)$$

where t_p denotes the total pulse duration. The full width at half-maximum for the corresponding time-dependent intensity [75]

$$I(t) = c \varepsilon_0 |\mathbf{E}_{\pm}(t)|^2 \quad (2.5)$$

is [4, 74]

$$\tau \approx 0.364 t_p \approx 3.295 \hbar / \Gamma. \quad (2.6)$$

where Γ is the spectral width of the laser pulse. The corresponding maximum intensity is

$$I_{\max} = c \varepsilon_0 \mathcal{E}_0^2. \quad (2.7)$$

Furthermore, we assume that the system (with system-adapted coordinates x, y, z) has been suitably pre-oriented or -aligned along the Z -axis, i.e., $z = Z$. For atoms or atomic ions, the pre-orientation or -alignment is, of course, unnecessary. Else one may employ any of the techniques which have been developed for orientations or alignments of molecules, see e.g., [76–78]. An explicit example of quantum dynamics simulations for pre-orientation of polar molecules based on the method of [79, 80], followed by the excitation of ring currents and magnetic fields, is given in [8, 9, 28]. In this scenario, initial pre-orientation or -alignment is restricted to a finite period τ_{ori} or τ_{ali} , respectively; subsequently, periodic events of similar pre-orientation or -alignment may occur due to rotational revivals. It is mandatory that the ring currents and induced magnetic fields are switched on or off during these periods of pre-orientation or -alignment, i.e., the duration τ of the exciting or de-exciting laser pulses must be shorter than τ_{ori} or τ_{ali} ,

$$\tau < \tau_{\text{ori}} \quad \text{or} \quad \tau < \tau_{\text{ali}}. \quad (2.8)$$

Next let H_{sys} be the Hamiltonian of the pre-oriented or -aligned system, with corresponding discrete (bound state) eigenfunctions $|\Psi_i\rangle$ (short-hand notation: $|i\rangle = |\Psi_i\rangle$) and eigenenergies E_i which are obtained as solutions of the time-independent Schrödinger equation

$$H_{\text{sys}}|i\rangle = E_i|i\rangle. \quad (2.9)$$

In case of the H atom or one-electron atomic ions, the $|i\rangle$ are simply the corresponding atomic orbitals (AOs); else one has to employ quantum chemical or other numerical methods in order to determine the eigenstates of the system, see e.g., [7–11]. In semi-classical dipole approximation, the laser driven dynamics is described in terms of the wave packet $|\Psi(t)\rangle$ which is obtained as solution of the time-dependent Schrödinger equation

$$i\hbar \frac{\partial}{\partial t} |\Psi(t)\rangle = (H_{\text{sys}} - \mathbf{M} \cdot \mathbf{E}_{\pm}(t)) |\Psi(t)\rangle \quad (2.10)$$

with dipole operator \mathbf{M} . Below, we assume that the laser pulses are not all too strong so that we may neglect competing transitions into the continuum such as bond breaking or ionization. The wave packet $|\Psi(t)\rangle$ may then be expanded in terms of the

eigenstates,

$$|\Psi(t)\rangle = \sum_i C_i(t) |i\rangle \exp(-iE_i t / \hbar) \quad (2.11)$$

with populations

$$P_i(t) = |C_i(t)|^2. \quad (2.12)$$

Inserting this ansatz into the time-dependent Schrödinger equation (2.10) yields the equivalent set of differential equations for the time-dependent coefficients

$$i\hbar \frac{d}{dt} C_j(t) = - \sum_i C_i(t) \langle j | \mathbf{M} | i \rangle \cdot \mathbf{E}_{\pm}(t) \exp(-i\omega_{ij} t) \quad (2.13)$$

with transition frequencies

$$\omega_{ij} = \frac{E_i - E_j}{\hbar}. \quad (2.14)$$

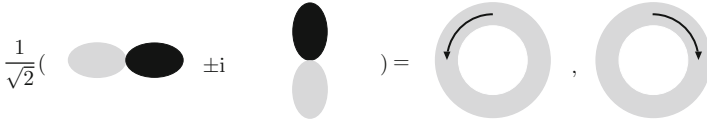
In the applications of [2–11, 28], the system is initially in the non-degenerate ground state $|g\rangle = |0\rangle$, that is, $C_i(t = t_0 = -t_p/2) = \delta_{0i}$, and the laser frequency ω is tuned resonant or near-resonant to a particular transition frequency, specifically for excitation from the ground $|g\rangle$ to a pair of degenerate excited states, $|i\rangle = |e_+\rangle$ and $|i + 1\rangle = |e_-\rangle$, denoted for simplicity as

$$\tilde{\omega} = \omega_{e+,g} = \omega_{e-,g} = \frac{E_{e\pm} - E_g}{\hbar}. \quad (2.15)$$

Here, the complex eigenstates, $|e_+\rangle$ and $|e_-\rangle$, may be expressed in terms of two real ones

$$|e_{\pm}\rangle = \frac{1}{\sqrt{2}}(|e_x\rangle \pm i|e_y\rangle), \quad (2.16)$$

similar to the relations of complex atomic orbitals $|2p_+\rangle$ and $|2p_-\rangle$ and real ones $|2p_x\rangle$ and $|2p_y\rangle$. Other examples of pairs of degenerate complex eigenstates expressed in terms of two real ones are listed schematically in Fig. 2.2. These examples include such different systems as toroidal electronic states $|\Pi_+\rangle$ and $|\Pi_-\rangle$ of linear molecules [81], or excited electronic states $|E_+\rangle$ and $|E_-\rangle$, with irreducible representation E , of Mg-porphyrin [4], or pseudorotational states with short-hand notation $|v_b^l\rangle = |1^1\rangle \equiv |v_{b,+}\rangle$ and $|1^{-1}\rangle \equiv |v_{b,-}\rangle$ representing complex linear combinations of the first excited x - and y -polarized bending vibrational states $|v_{b,x}\rangle$ and $|v_{b,y}\rangle$ of linear triatomic molecules or ions, such as CdH_2 [10] and FHF^- [11]. In general, laser pulses may generate superpositions (2.11) of these states plus other ones. Then, we are interested, e.g., in the generation of mean angular momentum or



a $\frac{1}{\sqrt{2}} \left(\begin{array}{c} \text{grey} \\ |p_x\rangle \end{array} \pm i \begin{array}{c} \text{black} \\ |p_y\rangle \end{array} \right) = \begin{array}{c} \text{clockwise arrow} \\ |p_+\rangle \end{array}, \begin{array}{c} \text{counter-clockwise arrow} \\ |p_-\rangle \end{array}$

b $\frac{1}{\sqrt{2}} \left(\begin{array}{c} \text{grey} \\ |\Pi_x\rangle \end{array} \pm i \begin{array}{c} \text{black} \\ |\Pi_y\rangle \end{array} \right) = \begin{array}{c} \text{clockwise arrow} \\ |\Pi_+\rangle \end{array}, \begin{array}{c} \text{counter-clockwise arrow} \\ |\Pi_-\rangle \end{array}$

c $\frac{1}{\sqrt{2}} \left(\begin{array}{c} \text{grey} \\ |E_x\rangle \end{array} \pm i \begin{array}{c} \text{black} \\ |E_y\rangle \end{array} \right) = \begin{array}{c} \text{clockwise arrow} \\ |E_+\rangle \end{array}, \begin{array}{c} \text{counter-clockwise arrow} \\ |E_-\rangle \end{array}$

d $\frac{1}{\sqrt{2}} \left(\begin{array}{c} \text{grey} \\ |v_{b,x}\rangle \end{array} \pm i \begin{array}{c} \text{black} \\ |v_{b,y}\rangle \end{array} \right) = \begin{array}{c} \text{clockwise arrow} \\ |v_{b,+}\rangle \end{array}, \begin{array}{c} \text{counter-clockwise arrow} \\ |v_{b,-}\rangle \end{array}$

Fig. 2.2 Complex degenerate eigenstates constructed from degenerate real ones (schematic), see also [28]: **(a)** atomic orbitals $|p\rangle$ [2]; **(b)** excited electronic states $|\Pi\rangle$ of linear molecules [7–9]; **(c)** excited electronic states $|E\rangle$ of Mg-porphyrin with irreducible representations E [3–6]; **(d)** first excited pseudorotational states of symmetric ($D_{\infty,h}$) triatomic linear molecules, represented in terms of orthogonal degenerate bending states [10, 11]

magnetic quantum numbers

$$\langle l(t) \rangle = \sum_{n,l,m} l P_{nlm}(t) \quad (2.17)$$

$$\langle m(t) \rangle = \sum_{n,l,m} m P_{nlm}(t) \quad (2.18)$$

of superpositions of atomic orbitals, or in the time evolution of the mean values of the bending (v_b) or pseudorotational (l) quantum numbers

$$\langle v_b(t) \rangle = \sum_{v_b,l} v_b P_{v_b^l}(t) \quad (2.19)$$

$$\langle l(t) \rangle = \sum_{v_b,l} l P_{v_b^l}(t) \quad (2.20)$$

of superpositions of states $|v_b^l\rangle$.

The pulse duration τ is chosen such that on one hand, the corresponding spectral width Γ is smaller than the energy gap ΔE between the target and neighboring states with the same irreducible representation,

$$\tau \geq 3.295 \hbar / \Delta E, \quad (2.21)$$

cf. (2.6). On the other hand, τ should be shorter than the time of pre-orientation or -alignment τ_{ori} or τ_{ali} (if this is required), cf. (2.8), as well as the lifetime τ_e of the excited states, which may be limited by spontaneous emission [2] and/or dissipative or other competing processes,

$$\tau \leq \tau_e. \quad (2.22)$$

The antagonistic conditions (2.21) and (2.8), (2.22) may restrict the possible choices of τ to rather narrow domains of suitable pulse duration, see the discussion in [2]. The general solution (2.11) then reduces to approximately three dominant contributions including the ground and two degenerate excited states of the target level

$$|\Psi(t)\rangle = C_g(t)|g\rangle \exp(-iE_g t/\hbar) + C_{e+}(t)|e_+\rangle \exp(-iE_{e+} t/\hbar) + C_{e-}(t)|e_-\rangle \exp(-iE_{e-} t/\hbar). \quad (2.23)$$

In rotating wave approximation (RWA, cf. [82–85]), the solutions for a right circularly polarized resonant laser pulse are

$$C_g(t) = \cos\left(\frac{M\mathcal{E}_0}{\hbar} \int_{t_0}^t s(t') dt'\right) \quad (2.24)$$

$$C_{e+}(t) = i \sin\left(\frac{M\mathcal{E}_0}{\hbar} \int_{t_0}^t s(t') dt'\right) \exp(-i\omega t_0) \quad (2.25)$$

$$C_{e-}(t) = 0, \quad (2.26)$$

where M denotes the transition dipole matrix element (assuming $x = X$)

$$M = \frac{\langle g|M_x|e_x\rangle}{\sqrt{2}}, \quad (2.27)$$

that is, the right circularly polarized laser pulse transfers population selectively from the ground state $|g\rangle$, which is assumed to be totally symmetric, to the excited state $|e_+\rangle$ excluding the decoupled state $|e_-\rangle$. Inserting the shape function (2.4) then yields complete population transfer, $C_g(t = t_f = t_p/2) = 0$ at the final time $t = t_f$, if

$$|M\mathcal{E}_0 t_p| = \pi\hbar. \quad (2.28)$$

For the chosen target transition $|g\rangle \rightarrow |e_+\rangle$ and pulse duration τ (cf. (2.8), (2.21), (2.22)), expressions (2.1) and (2.4) together with the condition (2.28) may be considered as definition of a right circularly polarized π laser pulse. The resulting field strength \mathcal{E}_0 should be sufficiently low such that the maximum intensity I_{max} (2.7) does not exceed certain thresholds I_{thr} for competing processes, e.g., ionization; typical values for one-electron atomic ions and molecules are $I_{\text{thr}} \approx 10^{15} \text{ W cm}^{-2}$ and $I_{\text{thr}} \approx 10^{12} \text{ W cm}^{-2}$, respectively. It implies the condition

$$\tau \geq \frac{0.364 \pi \hbar}{|M| \sqrt{I_{\text{thr}}/(c\epsilon_0)}}, \quad (2.29)$$

in addition to the inequalities (2.8), (2.21), (2.22). Equivalent expressions are obtained for the corresponding left circularly polarized π laser pulse yielding selective population transfer from the ground $|g\rangle$ to excited $|e_{\pm}\rangle$ states.

The laser parameters for the π pulse (2.8), (2.15), (2.21), (2.22), (2.27), (2.28), and (2.29) serve as reference. Subsequently, these parameters are varied systematically (analogous to [69, 70]) such that the time-dependent Schrödinger equation (2.10) yields optimal populations of the target state $|e_{+}\rangle$ (or $|e_{-}\rangle$) when it is solved numerically, using Runge–Kutta propagation with a large, converged ($\gg 3$) set of basis functions in the expansion (2.11). In practice, “optimal populations” of the target state are hardly ever perfectly equal to 1, but usually they are sufficiently close to 1. Accordingly, the corresponding ring currents and magnetic fields which are associated with the target states $|e_{+}\rangle$ or $|e_{-}\rangle$ are switched on more or less perfectly. The resulting laser pulses are called re-optimized π laser pulses. The subsequent dump laser pulses with same circular polarizations achieve the corresponding more or less perfect switching-off.

After the preparation of the target electronic eigenstates $|e_{+}\rangle$ or $|e_{-}\rangle$, for example, the corresponding three-dimensional (3D) one-electron ring current densities are calculated using

$$\mathbf{j}_{\pm}(\mathbf{R} = \mathbf{r}_1) = \frac{i\hbar}{2m_e} N \int \cdots \int (\Psi_{e_{\pm}} \nabla \Psi_{e_{\pm}}^* - \Psi_{e_{\pm}}^* \nabla \Psi_{e_{\pm}}) d\sigma_1 d\mathbf{q}_2 \cdots d\mathbf{q}_N \quad (2.30)$$

with electronic coordinates $\mathbf{q} = (\mathbf{r}, \sigma)$ for positions and spins of N electrons. Various approximations which facilitate the calculations have been developed in [4, 7–9, 28] for electronic ring currents. For example, if the underlying electronic eigenstate $|e_{\pm}\rangle$ is expressed as multi-configurational wave function which has a single dominant Slater determinant corresponding to single electron excitation, then the multidimensional integral for the current density (2.30) can be reduced to the corresponding 3D current density for the molecular orbital (MO) which carries the electron before or after excitation. If this MO is well approximated as linear combination of atomic orbitals (LCAO-MO), then the current density (2.30) may be decomposed into contributions of the AOs. For analysis of the current densities of the AOs, one may employ analytical expressions which have been derived in [2, 28]; for applications, see [7–9, 28]. Analogous definitions apply to nuclear ring currents [28], with approximation by analytical expressions which have been developed using simple models based on two-dimensional harmonic oscillator wave functions [10, 11, 28].

Integration of the current density $\mathbf{j}_{\pm}(\mathbf{R})$ over a half plane \mathbf{S} yields the electric ring current

$$I_{\pm} = q \int \int \mathbf{j}_{\pm}(\mathbf{R}) \cdot d\mathbf{S}, \quad (2.31)$$

which has units of charge per time, where q is the charge of the ring current, e.g., $q = -e$ in the case of ring currents which are stimulated by means of single electron excitation. The corresponding period τ_I or frequency ω_I of the current can be calculated using

$$|I_{\pm}| = \frac{|q|}{\tau_I} = \frac{|q|\omega_I}{2\pi}. \quad (2.32)$$

Moreover, $\mathbf{j}_{\pm}(\mathbf{R})$ defines the mean reciprocal radius with respect to the axis of the ring current,

$$\langle R^{-1} \rangle_j = \frac{q \int \int R^{-1} \mathbf{j}_{\pm}(\mathbf{R}) \cdot d\mathbf{S}}{I_{\pm}}, \quad (2.33)$$

or the corresponding mean ring current radius of the (unidirectional) ring current [2, 28],

$$R_{-1} = \frac{1}{\langle R^{-1} \rangle_j}. \quad (2.34)$$

The definition (2.34) in terms of the reciprocal value of R (indicated by the subscript -1) weighted by the current density is more appropriate than the mean value of R , i.e., R weighted by the density, for two reasons: First, the latter would yield paradoxical finite values of a hypothetical “mean ring current radius” even if the mean ring currents are zero. Second, we are interested in the reciprocal mean value of R , weighted by the current because we aim at calculations of the induced magnetic field $\mathbf{B}_{\pm}(\mathbf{R})$. For a classical ring loop model of a ring current I_{\pm} about the Z -axis with radius R , the Biot–Savart law yields the value

$$\mathbf{B}_{\pm} = \pm \frac{\mu_0 I}{2R} \mathbf{e}_Z \quad (2.35)$$

at the center of the ring loop, i.e., what matters is the reciprocal value of R . Accordingly, estimates of \mathbf{B}_{\pm} should employ (2.35) with mean value $R = R_{-1}$ (2.34). More rigorously and also more generally, we use the corresponding quantum mechanical expression

$$\mathbf{B}_{\pm}(\mathbf{R}) = -\frac{\mu_0}{4\pi} \int \int \int \frac{\mathbf{j}_{\pm}(\mathbf{R}') \times (\mathbf{R} - \mathbf{R}')}{|\mathbf{R} - \mathbf{R}'|^3} dV', \quad (2.36)$$

in accord with the Biot–Savart law. In the case of nuclear ring currents of pseudorotating molecules, the total ring current can be decomposed into partial ring currents of the individual nuclei, with corresponding charges, radii, and induced magnetic fields [28]. Simple analytical expressions have been derived for locations with special symmetry, e.g., at the center or along the symmetry axis (e.g., Z -axis) of the ring current [2, 7–9, 28].

The classical approximation (2.35) to the Biot–Savart law (2.36) suggests that the induced magnetic field should increase with increasing electric ring currents I , i.e., with increasing charge and frequency of the flux (2.32), and also with decreasing mean ring current radius (2.34). It allows to predict several trends which may be used as working hypotheses for the selection of systems and scenarios with large magnetic fields induced by ring currents. For this purpose, let us consider a simple picture of electronic states with corresponding dominant Slater determinants for electrons in occupied orbitals. In the case of one-electron atomic ions, it suffices to consider directly the corresponding atomic orbitals. Two degenerate complex orbitals (see Fig. 2.2) contribute to ring currents and induced magnetic fields if they are occupied by different numbers of electrons $n_{e\pm}$, i.e., $(n_{e-}, n_{e+}) = (0, 1), (1, 0), (0, 2), (2, 0), (1, 2),$ or $(2, 1)$. For a given irreducible representation, the sizes of the orbitals increase with orbital energy, implying, in general, increasing radii of the ring currents. As a consequence, single electron transitions from occupied non-degenerate orbitals to the lowest unoccupied degenerate orbitals or neighboring ones should induce stronger magnetic fields than transitions to higher degenerate unoccupied orbitals. Likewise, single electron transitions from the lowest quadruply occupied degenerate orbitals to non-degenerate unoccupied orbitals should induce stronger magnetic fields than transitions starting from higher degenerate orbitals with the same irreducible representations. As a special case of these rules, in atomic one-electron ions, the strongest magnetic fields are induced by transitions from $|1s\rangle$ to $|2p_{\pm}\rangle$ orbitals [2]. For comparison, the induced magnetic fields in Rydberg states are negligible [22–27].

Another general trend suggested by (2.36), (2.35) is that the induced magnetic fields should increase with decreasing size of the system. This rule is confirmed by the present examples, i.e., the values of \mathbf{B}_{\pm} induced by electronic ring currents increase from rather large polyatomic molecules such as Mg-porphyrin [4, 28] via diatomic molecules [7–9, 28] to one-electron atomic ions [2, 28]. Note, however, that actually R or R_{-1} in (2.35), (2.34) refer to the mean radius of the ring current, not to the size of the system, hence one may observe rather large induced magnetic fields even in large molecules, provided they support ring currents with small radii. As an example, the present linear molecule or molecular ion CdH_2 and FHF^- may be excited in degenerate states $|v_{b,+}\rangle$ or $|v_{b,-}\rangle$, cf. Fig. 2.2. These states represent pseudorotations of the nuclei about the molecular axis, corresponding, e.g., to toroidal hydrogen bond in FHF^- [11] and to ring currents with much smaller radii than the system sizes, e.g., $R_{-1} = 0.0030 a_0$ for the Cd nucleus in pseudorotating CdH_2 – it gives rise to the huge induced magnetic field of 318 T at the center of the Cd nuclear ring current. This value is also supported by the rather large current I_{\pm} (cf. (2.31), (2.32), (2.35)), which can be estimated by the charge of the nucleus, $Z_{\text{Cd}} = 48$, which is hardly shielded by electrons, within the radius of the ring current, and the current frequency which corresponds to the bending frequency, $\omega_I/(2\pi c) = \omega_b/(2\pi c) = 629.2 \text{ cm}^{-1}$ or $\tau_I = 53.0 \text{ fs}$, thus $I = 0.91 e \text{ fs}^{-1}$.

The general results are demonstrated in Figs. 2.3–2.5 for four examples, i.e., electronic or nuclear current densities and induced magnetic fields in excited degenerate states $|2p_{+}\rangle$ of He^+ [2, 28], $|5^1E_{u+}\rangle$ of Mg-porphyrin [28] as well as the

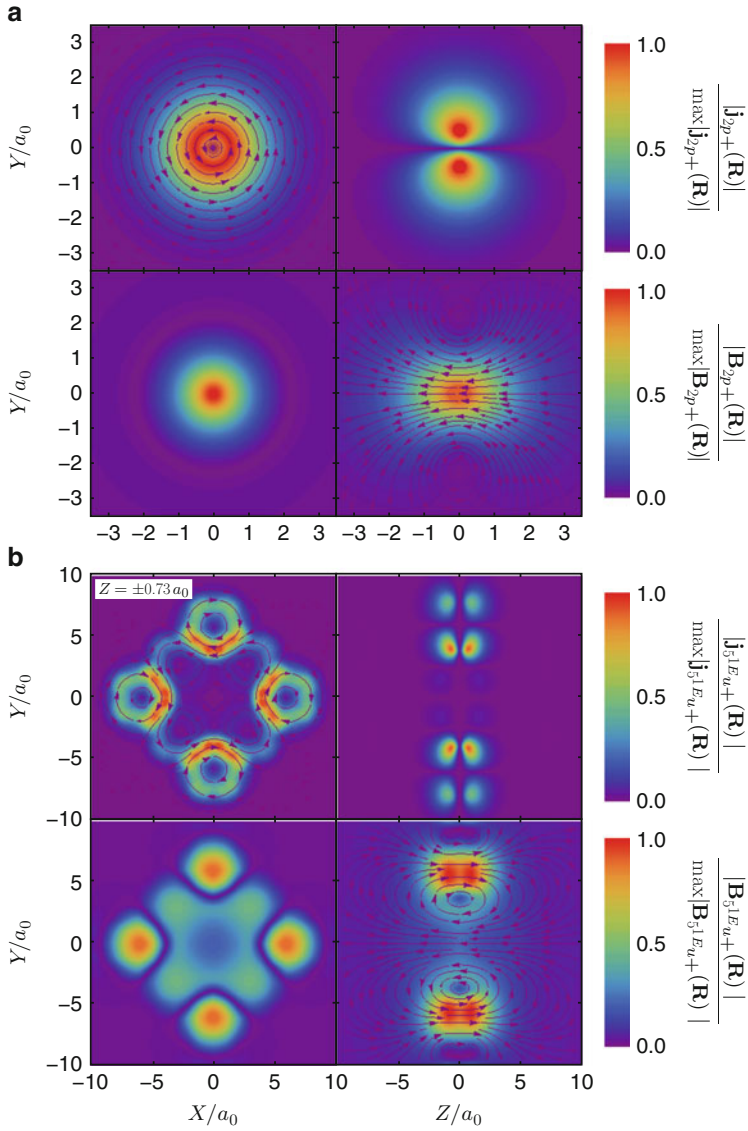


Fig. 2.3 Electronic ring current densities and induced magnetic fields for excited states (a) $|2p_+\rangle$ of the He^+ ion and (b) $|5^1E_{u+}\rangle$ of Mg-porphyrin, illustrated by color-coded cuts for the X/Y plane (left panels) and for the Y/Z plane (right panels). The maximum absolute values of the magnetic fields are $\max |\mathbf{B}_{2p_+}(\mathbf{R})| = 4.17 \text{ T}$ and $\max |\mathbf{B}_{5^1E_{u+}}(\mathbf{R})| = 0.11 \text{ T}$. The arrows indicate the directions (adapted from [28])

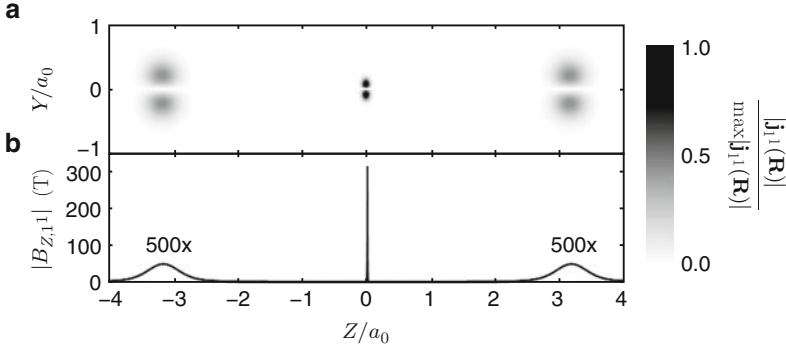


Fig. 2.4 (a) Nuclear ring current density (illustrated by a gray-scaled cut for the Y/Z plane) and (b) Z -component of the induced magnetic field along the molecular Z -axis, for the excited pseudorotational state $|1^1\rangle$ of CdH_2 . The current density close to the central Cd nucleus is zoomed in by a factor 20. The current densities and the magnetic fields close to the polar protons have been amplified by factors 2,000 and 500, respectively (adapted from [28])

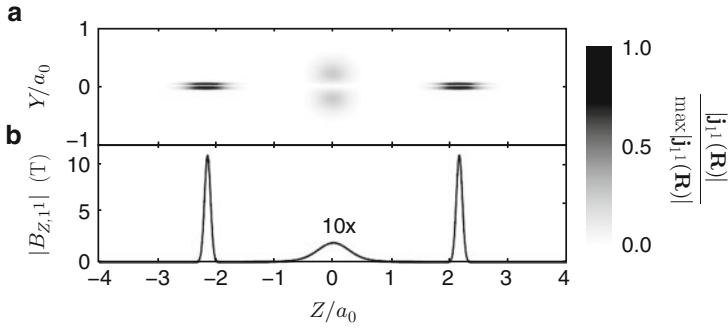


Fig. 2.5 (a) Nuclear ring current density (illustrated by a gray-scaled cut for the Y/Z plane) and (b) Z -component of the induced magnetic field along the molecular Z -axis, for the excited pseudorotational state $|1^1\rangle$ of FHF^- . The current densities close to the polar F nuclei are zoomed in by a factor 5. The current density and the magnetic fields close to the central proton have been amplified by factors 40 and 10, respectively (adapted from [28])

pseudorotational states $|v_{b,+}\rangle = |1^1\rangle$ of CdH_2 [10, 28] and FHF^- [11, 28], respectively. Most of the time, the ring currents turn out to be toroidal and so are also the induced magnetic fields. As an exception, the case of state $|5^1E_{u+}\rangle$ of Mg-porphyrin shows rich structures of ring currents and the induced magnetic field, suggesting forward and backward currents in different domains, according to the molecular topology which connects four sub-rings to one global ring.

Moreover, Figs. 2.6 and 2.7 show the components of the electric fields $E_X(t)$ and $E_Y(t)$, and intensities $I(t)$ of the circularly polarized laser pulses which excite these electronic ring currents, exemplarily for He^+ and Mg-porphyrin (panels a), together with the population dynamics (panels b). The results for He^+ employ the

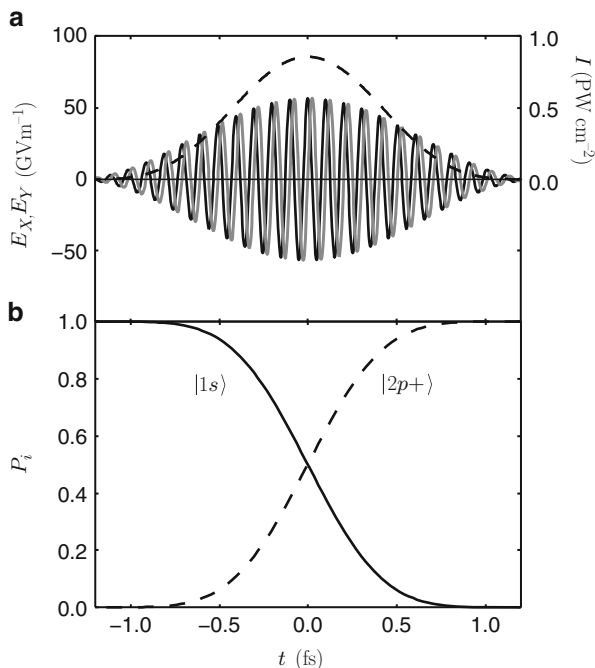


Fig. 2.6 (a) X - (black solid) and Y - (gray solid) components and intensity (dashed) of the circularly polarized π laser pulse and (b) the resulting population dynamics of the ground $|1s\rangle$ and excited $|2p_+\rangle$ states of the He^+ ion, indicating perfect population transfer from $|1s\rangle$ to $|2p_+\rangle$

RWA approximation (2.24)–(2.26), whereas the results for Mg-porphyrin have been obtained by numerical solution of the time-dependent Schrödinger equation, using (2.2) with \cos^{20} envelope [28]. Note the huge difference of the laser parameters, from ultrashort, intense laser pulses which are applicable for He^+ compared to much longer and less intense laser pulses for Mg-porphyrin. The different durations of the pulses are in accord with conditions (2.8), (2.21), (2.22), (2.29), calling for the different intensities due to (2.5), (2.28) [2, 28]. In contrast, these antagonistic conditions do not allow us to design circularly polarized re-optimized π pulse for excitations of the nuclear ring currents in CdH_2 . Nevertheless, excitations of nuclear circulations have been documented in [10, 28]. Also note the huge differences of the maximum values of the induced magnetic fields, from 0.1 to 0.2 T in Mg-porphyrin to 318 T at the center of the nuclear ring current of the Cd nucleus in CdH_2 – the latter exceeds even the largest permanent magnetic fields in present laboratories [49]. It is in accord with the Biot–Savart law (2.35), i.e., the strongest magnetic fields are induced for large charges q , small radii R_{-1} , and short periods τ_I .

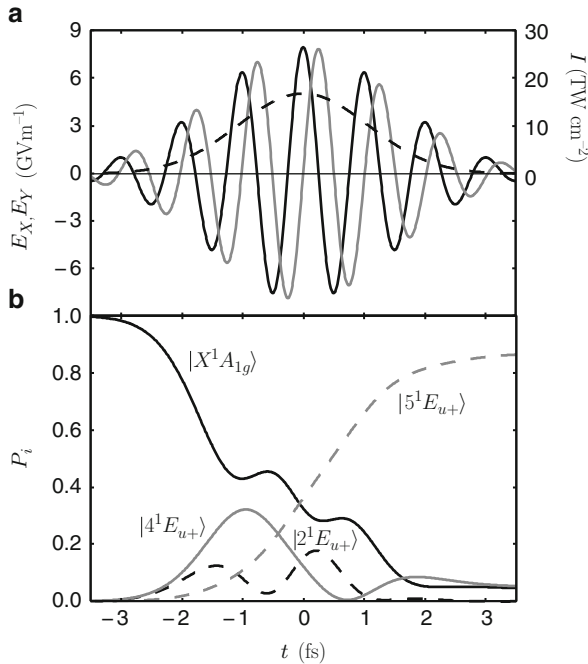


Fig. 2.7 (a) X - (black solid) and Y - (gray solid) components and intensity (dashed) of the circularly polarized re-optimized π laser pulse and (b) the resulting population dynamics of the ground $|X^1A_{1g}\rangle$ and various excited $|n^1E_{u+}\rangle$ ($n = 2, 4, 5$) states of Mg-porphyrin indicating optimal but not perfect population transfer from $|X^1A_{1g}\rangle$ to $|5^1E_{u+}\rangle$ (adapted from [28])

2.3 Quantum Switching the Directions of Ring Currents and Magnetic Fields

Our previous experience (Sect. 2.2) offers a natural basis for extensions from quantum switching-on and -off to switching the direction of a ring current and the induced magnetic field in a model system, by means of the circularly polarized re-optimized π laser pulses. For reference, we call the pulse, which has been used for switch-on the ring current and corresponding induced magnetic field, the “second” pump pulse, which follows the “first” pulse for pre-orientation or -alignment of the system (if required, see the discussion in Sect. 2.2). Then, we employ two sequential laser pulses, called the “third” dump and “fourth” pump laser pulses: The (third) dump pulse has the same parameters as the (second) pump pulse but the phase of the dump pulse is re-optimized, whereas the (fourth) pump pulse has the same parameters as the (second) pump pulse but with opposite circular polarization. The system should again be pre-oriented or -aligned along the laboratory Z -axis (if required), during these second, third, and fourth laser pulses, e.g., during orientation or alignment periods at rotational revivals after the “first” pulse. If the pulse durations τ

are several times shorter than the durations τ_{ori} or τ_{ali} for orientation or alignment, then they can be fired with time delays $\Delta t = t_p$ and $2t_p$ for (third) dump and (fourth) pump laser pulses, respectively, during the same periods τ_{ori} or τ_{ali} ; else one has to wait at least for the next rotational revivals, which will provide again the scenario of pre-oriented or -aligned systems (if required). In the subsequent quantum simulations, we shall present the results using the time delays $\Delta t = t_p$ and $2t_p$ for (third) dump and (fourth) pump laser pulses, respectively, with the understanding that larger time delays will be applied, if necessary, in order to satisfy the requirements of suitable pre-orientations or -alignments. By reversibility of time and helicity, the effect of the (third) dump pulse (with re-optimized phase) is simply to switch-off the pre-excited ring current and induced magnetic field. Subsequently, the (fourth) pump pulse will switch it on again, but with opposite directionality, due to the reversed helicity of the dump and pump pulses. Obviously, the net effect of the (third) dump and (fourth) pump pulses is to change the directionality of the ring currents and induced magnetic fields. Applications of the concept to the model systems He^+ and FHF^- are demonstrated in Figs. 2.8 and 2.9, respectively, see also the figure legends.

The primary effects of the left circularly polarized re-optimized π pulse (second pulse) is the population transfer from the ground state to the left polarized state $|2p_- \rangle$ or $|1^- \rangle$ of He^+ or FHF^- , respectively. Subsequently, the left and right circularly polarized dump and pump pulses (third and fourth pulses) transfer populations predominantly from the excited state back to the ground state, and then to the excited state with opposite magnetic or pseudorotational quantum numbers, i.e., $|2p_+ \rangle$ or $|1^+ \rangle$ of He^+ or FHF^- , respectively. The corresponding switches of the ring currents are obvious from the time evolutions of the mean values of the angular momentum or bending quantum numbers $\langle l(t) \rangle$ or $\langle v_b(t) \rangle$, and from the magnetic or pseudorotational quantum numbers $\langle m(t) \rangle$ or $\langle l(t) \rangle$, respectively. Finally, the switch-on and subsequent switch-off the directions of the magnetic fields $B_{Z,\text{He}}(t)$ and $B_{Z,\text{F}}(t)$ at the nuclei of the He^+ ion and at centers of F nuclear ring currents follow closely the time evolutions of the ring currents as monitored by the mean values of the quantum numbers $-\langle m(t) \rangle$ (due to negative electron charge) and $\langle l(t) \rangle$, respectively. The equivalent net effect has been achieved by E.K.U. Gross and coworkers using optimal laser pulses, with application to quantum switches of ring current in a nano-ring model [20]. For an alternative approach to magnetic field switching in parallel quantum dots, see [86].

2.4 Conclusions

The progresses which are documented in Sects. 2.2 and 2.3 are stimulating. First, they provide useful criteria for systematic searches for systems which should allow to switch-on or -off, or to switch the directions of magnetic fields induced by ring currents, by means of well designed left or right circularly polarized re-optimized π laser pulses. One important condition is that the chosen system should have proper

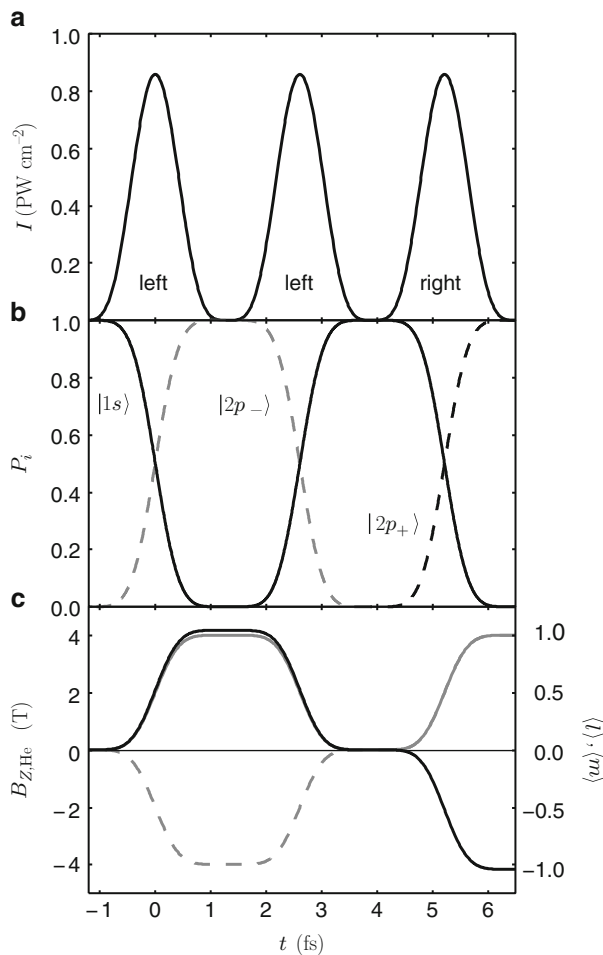


Fig. 2.8 Quantum switching of electronic ring currents and induced magnetic fields of the He^+ ion, by means of a series of pump, dump, and pump π laser pulses with left, left, and right circular polarizations, respectively (see text). **(a)** Laser intensities; **(b)** populations of ground and excited states; **(c)** mean values of angular momentum $\langle l(t) \rangle$ (gray solid) and magnetic quantum numbers $\langle m(t) \rangle$ (gray dashed) as well as Z -component of the induced magnetic field $B_{Z,\text{He}}(t)$ at the nucleus α of He^+ (black solid)

symmetry supporting degenerate states. In this respect, triply or more degenerate vibrational states, e.g., T -states of tetrahedral molecules, should be more advantageous than doubly degenerate states, e.g., E -states of planar molecules with C_{nv} rotational axes ($n \geq 3$) because in first order (harmonic) approximation, it is not necessary to pre-orient or pre-align the system in order to generate nuclear ring currents. Second, according to the Biot–Savart law (2.35), one should look for a system with strong ring current I , i.e., with large charge q , with short period τ_I

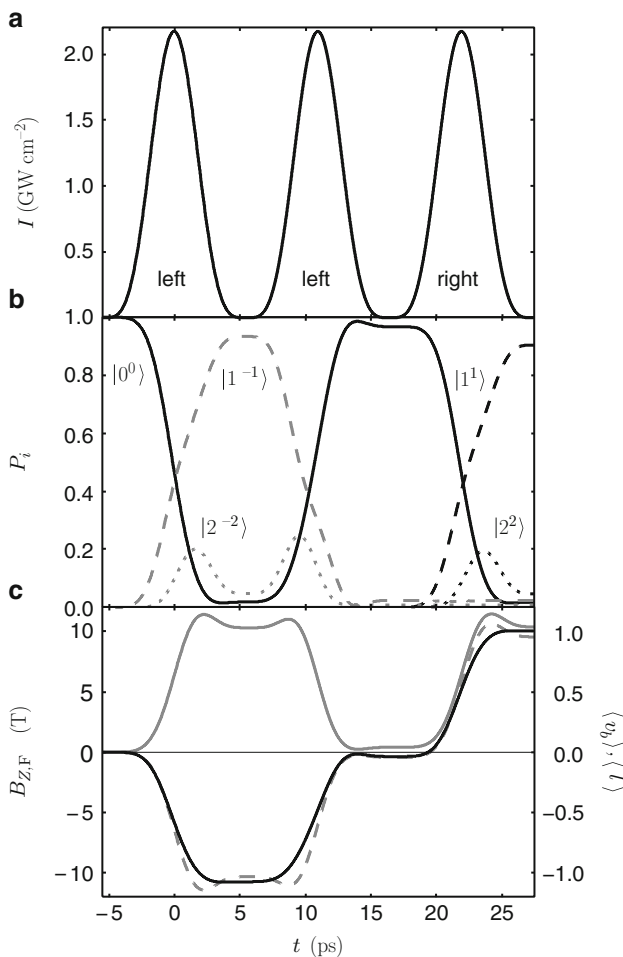


Fig. 2.9 Quantum switching of pseudorotational nuclear ring currents and induced magnetic fields of the aligned FHF^- anion, by means of a series of pump, dump, and pump re-optimized π laser pulses with left, left, and right circular polarizations, respectively (see text). (a) Laser intensities; (b) populations of ground and excited states $|v_b^l\rangle$; (c) mean values of bending $\langle v_b(t) \rangle$ (gray solid) and pseudorotational quantum numbers $\langle l(t) \rangle$ (gray dashed) as well as Z-components of induced magnetic fields $B_{Z,F}$ at centers of F nuclear ring currents (black solid)

(2.32), and with small radius of the ring current R_{-1} (2.34). The criteria for large charges and small radii point to pseudorotating heavy nuclei, and the criterion for short periods τ_I suggests corresponding high vibrational frequencies of the triply degenerate vibrational modes. Putting all criteria together, the tetrahedral molecule UH_4 , for example, should be an ideal candidate because it possesses triply degenerate vibrational T_2 states (antisymmetric modes) with high vibrational (experimental) frequency, $\omega_d/(2\pi c) = 1484 \text{ cm}^{-1}$ [87, 88] corresponding to $\tau_I = 22.5 \text{ fs}$, and

the nucleus of the U atom carries a very high charge as well as very heavy mass such that it will carry out pseudorotations with very small radius. By approximate extrapolation of the present result for CdH_2 ($B_{\text{Z,Cd}} = 318 \text{ T}$) at the center of the Cd nuclear ring current, the corresponding induced magnetic fields in UH_4 may approach 1,000 T! One may ask whether such huge fields could have feedbacks on the geometric or electronic structures of the molecule; we anticipate that this will not be the case because the very strong induced magnetic fields are typically localized in very small areas inside the mean ring current radii, without any major effect on the rest of the molecule.

Another challenge is to monitor the predicted laser driven quantum switches of ring currents and induced magnetic fields experimentally. The recent three-dimensional imaging of the corresponding toroidal structures of atoms carrying ring currents, carried out by the group of T. Baumert [29], is indeed encouraging for this purpose. In addition, one may consider and possibly extend the techniques which have already been applied successfully to analogous but much weaker effects which are induced by external magnetic fields [44–48]. Effects of magnetic fields induced by ring currents on nuclear magnetic resonance (NMR) spectra, such as chemical shifts, have already been predicted by L. Pauling [89], e.g., for aromatic molecules, and confirmed experimentally [90,91]. Extensions to the present quantum switching of these effects by means of laser pulses will be quite demanding because traditional NMR techniques would call for sufficiently long switching durations and life times of the ring currents, as well as sufficiently high densities of the samples (S. Glaser, private communication, 2009). As an alternative, we suggest to apply the option of ultrafast switch-on and -off, or switching the directionality of the rather huge magnetic fields, in particular within the rather small ring current radii of pseudorotating nuclei, to control the deflection of neutrons. This possibility is supported by recent work by Lauchli et al. [92], with references in particular to the extension from neutron scattering of orbital currents with translational symmetry [93,94] to broken [95] symmetry, see also, on one hand, the recent neutron experiments [96] indicating the presence of magnetic moments, compatible with the translation-invariant pattern of currents predicted by Varma [94], and on the other hand to Kerr effect measurements [97] showing evidence of time-reversal symmetry breaking (quoted from [92]). It would open entirely new possibilities for ultrafast analysis and control of chemical processes, by means of well-defined, pulsed interactions of molecules with neutrons. For example, the present approach would allow to design a series of circularly polarized re-optimized π laser pulses which switch on and off the ring currents and induced magnetic fields during very short periods, from attoseconds to picoseconds (depending on the model system). As a consequence, the induced magnetic fields could deflect a neutron beam such that it sweeps over a sample during these short periods. The deflected neutrons could then transfer momentum directly to the nuclei of the molecules in the sample, thus starting selected coherent vibrations or reactions, e.g., in the electronic ground state, see e.g., [98,99], during well-defined periods which are controlled by laser pulses.

Acknowledgements We should like to express our gratitude to all co-authors, partners, and friends, Dr. Nadia Elghobashi-Meinhardt (Heidelberg), Prof. Leticia González (Jena), Dr. Markus Kitzler (Wien), Prof. Caroline Lasser (München), Mr. Guillermo Pérez-Hernández (Jena), Dr. Peter Sebald (Insheim), Prof. Tamar Seideman (Evanston), Dr. Luis Serrano-Andrés (Valencia), Prof. Yasuteru Shigeta (Osaka), and Prof. Kiyoshi Yagi (Tokyo) for fruitful cooperation on this topic. Stimulating discussions with Prof. Ilya Averbukh (Rehovot/Santa Barbara), Prof. André D. Bandrauk (Sherbrooke/Santa Barbara), Prof. Thomas Baumert (Kassel), Prof. Jamal Berakdar (Halle), Mr. Timm Bredtmann (Berlin), Prof. Gerd Buntkowsky (Darmstadt), Dr. Stephan Chelkowski (Sherbrooke/Santa Barbara), Prof. Paul B. Corkum (Ottawa), PD Dr. José R. Crespo López-Urrutia (Heidelberg), Dr. Chantal Daniel (Strasbourg), Prof. Dennis J. Diestler (Lincoln), Prof. Fahrhad H.M. Faisal (Bielefeld), Prof. Yuichi Fujimura (Sendai), Prof. Steffen Glaser (München/Santa Barbara), Mr. Thomas Grohmann (Berlin), Prof. Eberhard K.U. Gross (Halle/Santa Barbara), Dr. Zoltán Harman (Heidelberg), Prof. Hirohiko Kono (Sendai), Prof. Shiro Koseki (Osaka), Dr. Andreas Läuchli (Lausanne), Monika Leibscher PhD (Berlin), PD Dr. Albrecht Lindinger (Berlin), Prof. Beate Paulus (Berlin), Dr. Serguei Patchovskii (Ottawa/Santa Barbara), Prof. Trond Saue (Strasbourg), Dr. Torsten Siebert (Berlin), Dr. Olga Smirnova (Berlin/Santa Barbara), Prof. Anthony F. Starace (Lincoln/Santa Barbara), Prof. Alain Strich (Strasbourg), Mr. David Sulzer (Strasbourg), Prof. Kazuo Takatsuka (Tokyo), Prof. Joachim Ullrich (Heidelberg), Prof. Christoph van Wüllen (Kaiserslautern), PD Dr. Matthias Wollenhaupt (Kassel), Prof. Ludger Wöste (Berlin), and Prof. Klaas A. Zachariasse (Göttingen) are also gratefully acknowledged. We also thank Prof. Misha Yu. Ivanov (London/Santa Barbara) and Prof. David Tannor (Rehovot/Santa Barbara) for organizing the workshop on “Quantum Control of Light and Matter” at the Kavli Institute for Theoretical Physics (KITP) of the University of California at Santa Barbara (UCSB), providing wonderful scientific environment, Prof. David Gross (Santa Barbara) and his staff for all hospitality, and Mr. Dominik Sattler (Berlin) and Mr. Axel Schild (Berlin) for preparing movies and snapshots for quantum switching of nuclear ring currents. On this occasion, we should also like to thank the interpreters Oya Ataman, Kathleen Bieling, Silke Brendel-Evan, Sabine Goßner, Christjane Kreuter, Carola Otto, and Ralf Wiebel who helped to translate and communicate the topic from German sign language to English and vice versa during the workshop and other meetings over several years. Above all, we thank our wives Tanja and Etsuko for understanding and supporting our passion for science. Generous financial support by Deutsche Forschungsgemeinschaft DFG (project Sfb 450 TPC1, previously also GK788 and Ma 515/23-1), Agentur für Arbeit Berlin-Nord, and by Fonds der Chemischen Industrie is also gratefully acknowledged. This research was supported in part by the National Science Foundation under Grant No. PHY05-51164.

References

1. P. Bronner, Das Elektroniummodell des Wasserstoffatoms. Diploma thesis, Universität Karlsruhe (2004), <http://www.hydrogenlab.de>
2. I. Barth, J. Manz, Phys. Rev. A **75**, 012510 (2007)
3. I. Barth, J. Manz, Angew. Chem. Int. Ed. **45**, 2962 (2006); Angew. Chem. **118**, 3028 (2006)
4. I. Barth, J. Manz, Y. Shigeta, K. Yagi, J. Am. Chem. Soc. **128**, 7043 (2006)
5. I. Barth, J. Manz, Design of Circularly Polarized Laser Pulses for Periodic Electron Circulation in Mg-Porphyrin. in *Femtochemistry VII: Fundamental Ultrafast Processes in Chemistry, Physics, and Biology*, eds. by A.W. Castleman Jr., M.L. Kimble (Elsevier, Amsterdam, 2006), pp. 441–454
6. I. Barth, L. González, C. Lasser, J. Manz, T. Rozgonyi, Laser control of nuclear and electron dynamics: bond selective photodissociation and electron circulation. in *Coherent Control of Molecules*, eds. by B. Lasorne, G.A. Worth (CCP6, Daresbury, 2006) pp. 18–27
7. I. Barth, J. Manz, L. Serrano-Andrés, Chem. Phys. **347**, 263 (2008)

8. I. Barth, L. Serrano-Andrés, T. Seideman, *J. Chem. Phys.* **129**, 164303 (2008)
9. I. Barth, L. Serrano-Andrés, T. Seideman, *J. Chem. Phys.* **130**, 109901(E) (2009)
10. I. Barth, J. Manz, P. Sebal, *Chem. Phys.* **346**, 89 (2008)
11. I. Barth, J. Manz, G. Pérez-Hernández, P. Sebal, *Z. Phys. Chem.* **222**, 1311 (2008)
12. M. Nest, F. Remacle, R.D. Levine, *New J. Phys.* **10**, 025019 (2008)
13. T. Minami, H. Fukui, H. Nagai, K. Yoneda, R. Kishi, H. Takahashi, M. Nakano, *J. Phys. Chem. C* **113**, 3332 (2009)
14. K. Nobusada, K. Yabana, *Phys. Rev. A* **75**, 032518 (2007)
15. K. Nobusada, K. Yabana, *Comp. Phys. Comm.* **177**, 54 (2007)
16. J. Sun, J. Liu, W.Z. Liang, Y. Zhao, *J. Phys. Chem. A* **112**, 10442 (2008)
17. A. Matos-Abiague, J. Beradkar, *Phys. Rev. Lett.* **94**, 166801 (2005)
18. Y.V. Pershin, C. Piermarocchi, *Phys. Rev. B* **72**, 125348 (2005)
19. Y.V. Pershin, C. Piermarocchi, *Phys. Rev. B* **72**, 245331 (2005)
20. E. Räsänen, A. Castro, J. Werschnik, A. Rubio, E.K.U. Gross, *Phys. Rev. Lett.* **98**, 157404 (2007)
21. J. Sun, W.-Z. Liang, Y. Liu, *J. Theor. Comp. Chem.* **7**, 579 (2008)
22. J.A. Yeazell, C.R. Stroud Jr., *Phys. Rev. A* **35**, 2806 (1987)
23. J.A. Yeazell, C.R. Stroud Jr., *Phys. Rev. Lett.* **60**, 1494 (1988)
24. J.J. Mestayer, B. Wyker, J.C. Lancaster, F.B. Dunning, C.O. Reinhold, S. Yoshida, J. Burgdörfer, *Phys. Rev. Lett.* **100**, 243004 (2008)
25. J.J. Mestayer, B. Wyker, F.B. Dunning, C.O. Reinhold, S. Yoshida, J. Burgdörfer, *Phys. Rev. A* **78**, 045401 (2008)
26. J.J. Mestayer, B. Wyker, F.B. Dunning, S. Yoshida, C.O. Reinhold, J. Burgdörfer, *Phys. Rev. A* **79**, 033417 (2009)
27. H. Maeda, J.H. Gurian, T.F. Gallagher, *Phys. Rev. Lett.* **102**, 103001 (2009)
28. I. Barth, Quantum control of electron and nuclear circulations, ring currents, and induced magnetic fields in atoms, ions, and molecules by circularly polarized laser pulses. PhD thesis, Freie Universität Berlin (2009)
29. M. Wollenhaupt, M. Krug, J. Köhler, T. Bayer, C. Sarpe-Tudoran, T. Baumert, *Appl. Phys. B* **95**, 245 (2009)
30. L.I. Schiff, *Quantum Mechanics* (McGraw-Hill, New York, 1968)
31. M. Okuyama, K. Takatsuka, *Chem. Phys. Lett.* **476**, 109 (2009)
32. I. Barth, H.-C. Hege, H. Ikeda, A. Kenfack, M. Koppitz, J. Manz, F. Marquardt, G.K. Paramonov, *Chem. Phys. Lett.* **481**, 118 (2009)
33. M. Kanno, H. Kono, Y. Fujimura, *Angew. Chem. Int. Ed.* **45**, 7995 (2006)
34. M. Kanno, K. Hoki, H. Kono, Y. Fujimura, *J. Chem. Phys.* **127**, 204314 (2007)
35. J.P. van der Ziel, P.S. Pershan, L.D. Malmstrom, *Phys. Rev. Lett.* **15**, 190 (1965)
36. P.S. Pershan, J.P. van der Ziel, L.D. Malmstrom, *Phys. Rev.* **143**, 574 (1966)
37. R. Hertel, *J. Magn. Magn. Mater.* **303**, L1 (2006)
38. T. Brixner, G. Gerber, *Opt. Lett.* **26**, 557 (2001)
39. L. Polachek, D. Oron, Y. Silberberg, *Opt. Lett.* **31**, 631 (2006)
40. M. Plewicz, S.M. Weber, F. Weise, A. Lindinger, *Appl. Phys. B* **86**, 259 (2007)
41. U. Graf, M. Fieß, M. Schultze, R. Kienberger, F. Krausz, E. Goulielmakis, *Opt. Express* **16**, 18956 (2008)
42. A. Staudte, S. Patchovskii, D. Pavičić, H. Akagi, O. Smirnova, D. Zeidler, M. Meckel, D.M. Villeneuve, R. Dörner, M.Yu. Ivanov, P.B. Corkum, *Phys. Rev. Lett.* **102**, 033004 (2009)
43. X. Xie, A. Scrinzi, M. Wickenhauser, A. Baltuška, I. Barth, M. Kitzler, *Phys. Rev. Lett.* **101**, 033901 (2008)
44. J. Jusélius, D. Sundholm, *J. Org. Chem.* **65**, 5233 (2000)
45. E. Steiner, A. Soncini, P.W. Fowler, *Org. Biomol. Chem.* **3**, 4053 (2005)
46. P. Lazzarotti, *Prog. Nucl. Magn. Res. Spec.* **36**, 1 (2000)
47. J.A.N.F. Gomes, R.B. Mallion, *Chem. Rev.* **101**, 1349 (2001)
48. T. Heine, C. Corminboeuf, G. Seifert, *Chem. Rev.* **105**, 3889 (2005)
49. F. Pobell, A.D. Bianchi, T. Herrmannsdörfer, H. Krug, S. Zherlitsyn, S. Zvyagin, J. Wosnitza, *AIP Conf. Proc.* **850**, 1649 (2006)

50. W. Becken, P. Schmelcher, F.K. Diakonov, J. Phys. B **32**, 1557 (1999)
51. M.V. Ivanov, P. Schmelcher, Phys. Rev. A **60**, 3558 (1999)
52. P. Schmelcher, T. Detmer, L.S. Cederbaum, Phys. Rev. A **61**, 043411 (2000)
53. S.A. Rice, M. Zhao, *Optical Control of Molecular Dynamics* (Wiley, New York, 2000)
54. M. Shapiro, P. Brumer, *Principles of the Quantum Control of Molecular Processes* (Wiley, Hoboken, 2003)
55. I. Thanopoulos, P. Král, M. Shapiro, E. Paspalakis, J. Mod. Opt. **56**, 686 (2009)
56. R. Bast, J. Jusélius, T. Saue, Chem. Phys. **356**, 187 (2009)
57. F.H.M. Faisal, S. Bhattacharyya, Phys. Rev. Lett. **93**, 053002 (2004)
58. T. Joseph, J. Manz, Mol. Phys. **58**, 1149 (1986)
59. J.E. Combariza, B. Just, J. Manz, G.K. Paramonov, J. Phys. Chem. **95**, 10351 (1991)
60. M. Dohle, J. Manz, G.K. Paramonov, H. Quast, Chem. Phys. **197**, 91 (1995)
61. M.V. Korolkov, J. Manz, G.K. Paramonov, B. Schmidt, Chem. Phys. Lett. **260**, 604 (1996)
62. Y. Fujimura, L. González, K. Hoki, J. Manz, Y. Ohtsuki, Chem. Phys. Lett. **306**, 1 (1999); Chem. Phys. Lett. **310**, 578(E) (1999)
63. Y. Fujimura, L. González, K. Hoki, D. Kröner, J. Manz, Y. Ohtsuki, Angew. Chem. Int. Ed. **39**, 4586 (2000); Angew. Chem. **112**, 4785 (2000)
64. K. Hoki, D. Kröner, J. Manz, Chem. Phys. **267**, 59 (2001)
65. G.K. Paramonov, V.A. Savva, Phys. Lett. **97A**, 340 (1983)
66. M. Holthaus, B. Just, Phys. Rev. A **49**, 1950 (1994)
67. P. Krause, T. Klamroth, P. Saalfrank, J. Chem. Phys. **123**, 074105 (2005)
68. J.C. Tremblay, T. Klamroth, P. Saalfrank, J. Chem. Phys. **129**, 084302 (2008)
69. G.K. Paramonov, Laser control of state-selective ultrafast excitation of molecular vibrations. in *Femtosecond Chemistry*, vol. 2, eds. by J. Manz, L. Wöste (VCH, Weinheim, 1995) Ch 23, pp. 671–711
70. M.V. Korolkov, J. Manz, G.K. Paramonov, Adv. Chem. Phys. **101**, 327 (1997)
71. M.V. Korolkov, J. Manz, G.K. Paramonov, Chem. Phys. **217**, 341 (1997)
72. J. Rauch, G. Mourou, Proc. Am. Math. Soc. **134**, 851 (2005)
73. C.P.J. Martiny, L.B. Madsen, Phys. Rev. Lett. **97**, 093001 (2006)
74. I. Barth, C. Lasser, J. Phys. B **42**, 235101 (2009)
75. W.H. Flygare, *Molecular Structure and Dynamics* (Prentice-Hall, Englewood Cliffs, 1978)
76. B. Friedrich, D. Herschbach, J. Phys. Chem. A **103**, 10280 (1999)
77. H. Stapelfeldt, T. Seideman, Rev. Mod. Phys. **75**, 543 (2003)
78. M. Leibscher, I.Sh. Averbukh, H. Rabitz, Phys. Rev. A **69**, 013402 (2004)
79. M. Machholm, N.E. Henriksen, Phys. Rev. Lett. **87**, 193001 (2001)
80. N. Elghobashi-Meinhardt, L. González, I. Barth, T. Seideman, J. Chem. Phys. **130**, 024310 (2009)
81. I.N. Levine, *Quantum Chemistry* (Prentice-Hall, New Jersey, 2000)
82. M. Sargent III, M.O. Scully, W.E. Lamb Jr., *Laser Physics* (Addison-Wesley, London, 1974)
83. L. Allen, J.H. Eberly, *Optical Resonance and Two-Level Atoms* (Wiley, New York, 1975)
84. G.F. Thomas, Phys. Rev. A **27**, 2744 (1983)
85. A. Salam, W.J. Meath, J. Chem. Phys. **228**, 115 (1998)
86. F. Li, X.-Q. Li, W.-M. Zhang, S.A. Gurvitz, Europhys. Lett. **88**, 37001 (2009)
87. P.F. Souter, G.P. Kushto, L. Andrews, Chem. Commun. 2401 (1996)
88. P.F. Souter, G.P. Kushto, L. Andrews, M. Neurock, J. Am. Chem. Soc. **119**, 1682 (1997)
89. L. Pauling, J. Chem. Phys. **4**, 673 (1936)
90. H.A. Staab, *Einführung in die Theoretische Organische Chemie*. (Verlag Chemie, Weinheim, 1964)
91. P. Reynders, W. Kühnle, K.A. Zachariasse, J. Am. Chem. Soc. **112**, 3929 (1990)
92. C. Weber, A. Läuchli, F. Mila, T. Giamarchi, Phys. Rev. Lett. **102**, 017005 (2009)
93. C.M. Varma, Phys. Rev. Lett. **83**, 3538 (1999)
94. M.E. Simon, C.M. Varma, Phys. Rev. Lett. **89**, 247003 (2002)
95. S. Chakravarty, R.B. Laughlin, D.K. Morr, C. Nayak, Phys. Rev. B **63**, 094503 (2001)
96. B. Fauqué, Y. Sidis, V. Hinkov, S. Pailhès, C.T. Lin, X. Chaud, P. Bourges, Phys. Rev. Lett. **96**, 197001 (2006)

97. J. Xia, E. Schemm, G. Deutscher, S.A. Kivelson, D.A. Bonn, W.N. Hardy, R. Liang, W. Siemons, G. Koster, M.M. Fejer, A. Kapitulnik, *Phys. Rev. Lett.* **100**, 127002 (2008)
98. S.W. Lovesey, *Theory of Neutron Scattering from Condensed Matter* (Clarendon, Oxford, 1984)
99. D. Ambrosek, C.A. Chatzidimitriou-Dreismann, P. Krause, J. Manz, H. Naumann, C. van Wüllen, *Chem. Phys.* **302**, 229 (2004)

Chapter 3

Alignment and Orientation of Hexapole State-Selected Molecules

Arnaud Rouzée, Arjan Gijsbertsen, and Marc J.J. Vrakking

Abstract The ability to control the orientation of small polar molecules is an important step toward experiments such as X-ray diffraction and high-harmonic generation, where structural information or ultrafast molecular dynamics can be reconstructed in the molecular frame. We present experiments where we have combined hexapole state-selection and the application of a strong DC electric field with the use of short, intense shaped laser pulses in order to demonstrate and optimize impulsive alignment and orientation of NO molecules under field-free conditions. Good agreement of the experimental results with theoretical predictions is found. In addition, impulsive alignment and orientation was investigated theoretically for a set of molecules that can be used state-selected by means of hexapole focusing.

3.1 Introduction

Much of our knowledge about molecular structure and reactivity is based on interpreting how molecules interact with light. Consequently, the invention of lasers in the infrared, visible, and ultra-violet parts of the wavelength spectrum has had an enormous impact on our understanding of chemical and physical processes. Using lasers, ultra-high resolution, frequency-domain experiments and time-resolved pump-probe studies have become possible. In the latter type of experiment, a first “pump” laser pulse initiates a dynamical event, and a second “probe” laser

M.J.J. Vrakking and A. Rouzée (✉)

FOM Instituut voor Atoom- en Molecuulfysica (AMOLF), Science Park 104, 1098 XG Amsterdam, The Netherlands

e-mail: A.rouzee@amolf.nl, vrakking@amolf.nl

and

Max Born Institute, Max Born Strasse 2A, 12489 Berlin, Germany

A. Gijsbertsen

FOM Instituut voor Atoom- en Molecuulfysica (AMOLF), Science Park 104, 1098 XG Amsterdam, The Netherlands

e-mail: gijsbertsen@amolf.nl

pulse interrogates the system after it has evolved for some time. State-of-the-art lasers can produce pulses down to a few femtoseconds, with special techniques even allowing for the generation of sub-femtosecond or “attosecond” pulses [1,2]. These short pulse durations are important, since chemical processes typically occur on time-scales of 10–1,000 fs.

In femtochemistry experiments, information about an evolving molecular structure is usually inferred by relying on available knowledge about the way that molecular absorption spectra depend on the instantaneous molecular structure. In small molecules, this is possible, but it soon becomes problematic when the size of a molecule increases. In larger molecules, it becomes more attractive to rely on diffraction [3]. Structural information is then encoded in interference patterns that result from the way that an electron or light wave scatters. In the case of light diffraction, the required wavelength is in the X-ray regime. Indeed, one of the most exciting scientific prospects at X-ray free electron lasers such as the FLASH and XFEL sources in Hamburg [4], or the LCLS at Stanford that became recently operational [5], is that it will enable X-ray diffraction experiments with femtosecond time-resolution. Diffractive information can also be obtained making use of diffraction that electrons undergo in X-ray photo-ionization, thereby “illuminating the molecule from within” [6].

When time-resolved molecular structures are studied by means of X-ray of electron diffraction, it is crucial that the direction of the scattered X-ray photons or electrons can be related to the spatial orientation of the molecule under consideration. In the last 2 decades, sophisticated coincidence techniques, in particular measurements of electron-ion coincidences, have yielded tremendous insight into atomic and molecular ionization and dissociation processes [7]. Nevertheless, there are many instances where the application of coincidence techniques may be too challenging. With this in mind, we have started working toward the development of an alternative method that establishes the angular correlation between scattered electrons or X-ray photons and the molecular structure. These methods are based on the application of samples of laser-aligned and oriented molecules, where every measurement that is performed in the laboratory frame automatically contains information about dynamics that occurs in the molecular frame [8]. Unlike the coincidence schemes, use of laser-aligned and oriented molecules allows for the collection of much larger signals (several thousand events/shot, as opposed to one or a few) and does not require fragmentation of the molecule in the course of the experiment. In addition, many applications are being developed by teams around the world where field-free laser-induced alignment is already being put to use, including experiments where high harmonic generation [9] or electron tunneling and diffraction [10] are used to determine the nuclear [11,12] and electronic [13] structure of molecules. Recently, molecular alignment was also used to investigate the fast photodissociation of CS₂ molecules [14].

In the present chapter, we present an overview of our recent activities in this area. As departure point, we take the common knowledge, developed by many research groups within the last decade, that intense laser fields can be used to align molecules [15,16]. Using intense non-resonant lasers, molecules can be exposed to oscillatory

electric fields of approximately 50 MV cm^{-1} without substantial ionization or fragmentation. Fields of this magnitude induce substantial dipoles, which in turn leads to a torque on the molecule that pulls the most polarizable axis of the molecule along the laser polarization axis [17]. Laser-induced alignment can be performed both adiabatically (using laser pulses with a duration that is long compared to the rotational period of the molecule) [18–20] or impulsively, using a short laser pulse that imparts a kick on a timescale that is short compared to the rotational period [21, 22]. An advantage of the latter technique is that it allows the preparation of samples of molecules where high degrees of molecular alignment occur at times when there is no laser present.

Alignment is typically characterized by the expectation value $\langle \cos^2 \theta \rangle$, and is to be distinguished from orientation, which relates to the definition of a preferred direction of the most polarizable axis in non-symmetric molecules. Orientation of molecules is characterized by the expectation value $\langle \cos \theta \rangle$. Unlike molecular alignment, the progress that has been achieved on laser field-free orientation has been modest. This is mainly due to the fact that a symmetric oscillating electric field cannot drive molecular orientation. Currently, many schemes have been proposed to achieve laser-field-free orientation including two-color phase-locked laser excitation [23, 24], THz half-cycle pulses (HCPs) [25, 26] or a combination of electrostatic and pulsed non-resonant laser fields [27]. So far, only the last method has experimentally been demonstrated on OCS [28, 29] and on HXeI molecules [30, 31]. These experiments have generally been affected by the fact that the degree of orientation that can be achieved is limited by the sample temperature. In this chapter, we discuss our recent progress in the preparation of samples of oriented molecules. Specifically, we discuss experiments where NO molecules are impulsively oriented, making use of the combination of (1) hexapole state-selection, (2) the application of a strong DC field, (3) the application of impulsive laser excitation, and (4) the application of laser pulse shaping to maximize the degree of orientation. We experimentally demonstrate the formation of NO samples with $\langle \cos \theta \rangle = -0.74$ [32], and argue that improvement of the orientation to $|\langle \cos \theta \rangle| > 0.95$ should be readily feasible [33], thereby creating conditions where – as desired – every measurement of scattered electrons or photons that is made in the laboratory frame has immediate implications in the molecular frame.

The organization of the chapter is as follows. After discussing relevant spectroscopic properties of the molecules that will be considered in Sect. 3.2, two elements that will be exploited in order to orient the molecules are discussed, namely the interaction of the molecules with a DC field (both in the hexapole state selection and in the establishment of an initial DC orientation, in Sect. 3.3) and the interaction with the intense laser field in Sect. 3.4, paving the way to a comparison of our expected ability to orient different molecules (see Sect. 3.5). The experimental setup that was used in our studies on NO is described in Sect. 3.6, and is followed by the description of an experiment where the sign of the dipole moment of NO was verified in Sect. 3.7, as well as a detailed discussion of the creation of macroscopic samples of strongly-oriented NO molecules by a combination of the techniques described before (Sect. 3.8). Closing remarks are given in Sect. 3.9.

3.2 Molecules

Our recent experiments and simulations with hexapole state selected molecules in intense laser fields have all been performed on nitric oxide (NO). However, hexapole state selection can in principle be applied to the rather large group of polar (pseudo-) symmetric top molecules in $|\nu, J, K, M\rangle$ low-field seeking vibronic states with $KM < 0$. Here, ν is the vibrational quantum number, J is the rotational quantum number, K is the projection of J on the molecular symmetry axis and M is the projection of J on a laboratory-fixed axis (usually the electric field vector). This group includes linear molecules excited in a bending vibration and molecules with nonzero electronic angular momentum such as NO. In the first case, the vibrational angular momentum has a non-zero projection l on the molecular axis, while in the latter case the projection of the angular momentum of the unpaired electron on the molecular axis Ω is non-zero. As K includes l and Ω and is more general, we will use quantum number K throughout this work, except when discussing specific molecules. In principle, it is also possible to focus low-field seeking linear molecules such as OCS($v = 0|JM = 10$) [34] via their second-order Stark effect, but a quadrupole is better suited for that purpose. A hexapole is an ideal focuser for the first-order Stark effect while a quadrupole is ideal for the second-order Stark effect.

The NO molecule has an unpaired anti-bonding electron, consequently it is an open shell molecule which leads to half-integer total angular momentum quantum numbers. The projection of the electronic spin angular momentum \mathbf{S} onto the internuclear axis (z) is $\Sigma = \pm\frac{1}{2}$. In its electronic ground state, the projection of the electronic orbital angular momentum \mathbf{L} is $\Lambda = \pm 1$. This leads to a $^2\Pi$ electronic state classification [35–37]. The total angular momentum \mathbf{J} , with magnitude $\sqrt{J(J+1)}\hbar$, is given as the sum of \mathbf{L} , \mathbf{S} , and \mathbf{O} , the angular momentum associated with the rotation of the molecular framework.

For low rotational states, NO can be described in a Hund’s case (a) [35] coupling scheme, where the orbital angular momentum \mathbf{L} is strongly coupled to the internuclear axis. The rotation of the nuclear framework \mathbf{O} then points perpendicular to the nuclear axis. This leaves for the projection of \mathbf{J} onto the internuclear axis $\Omega = \Sigma + \Lambda$, giving rise to two spin-orbit states: $\overline{\Omega} = \frac{1}{2}$ and $\overline{\Omega} = \frac{3}{2}$, $\overline{\Omega}$ being the absolute value of the projection Ω . Neglecting Λ -type doubling, the Hamiltonian consists of two components: one due to nuclear rotation $\mathbf{O} = \mathbf{J} - \mathbf{S} - \mathbf{L}$ and one due to spin orbit coupling $\mathbf{L} \cdot \mathbf{S}$ [36]

$$\mathcal{H}_0 = \mathcal{H}_{\text{rot}} + \mathcal{H}_{\text{SO}} = B_0(\mathbf{J} - \mathbf{S} - \mathbf{L})^2 + A_0(\mathbf{L} \cdot \mathbf{S}). \quad (3.1)$$

The spin-orbit constant A_0 and the rotational constant B_0 necessary to calculate the rotational energy of a NO molecule in the ground vibrational level, $X^2\Pi$ state are $A_0 = 123.13 \text{ cm}^{-1}$ and $B_0 = 1.6961 \text{ cm}^{-1}$ [38]. The rotational part of the wave function of an NO molecule is given by:

$$|J, \overline{\Omega}, M, \epsilon\rangle = \frac{1}{\sqrt{2}} \left[|J, \overline{\Omega}, M\rangle + \epsilon |J, -\overline{\Omega}, M\rangle \right]. \quad (3.2)$$

Here, $\epsilon = \pm 1$ is a symmetry index that relates to the total parity p of an NO rotational state via:

$$p = (-1)^{J-\epsilon/2}. \quad (3.3)$$

Equation (3.2) is strictly speaking only correct for $J = \frac{1}{2}$. For higher rotational states intermediate Hund's case coupling schemes may be applied. However, this effect remains rather small for NO in rotational states up to $J = 16.5$ [39] and we will assume Hund's case (a) for NO in the remainder of this work.

The rotational energy of a diatomic molecule in a $v = 0, {}^2\Pi$ state follows from (3.1) and (3.2). It is given by [36]:

$$E_{\text{rot}} = (J - \frac{1}{2})(J + \frac{3}{2}) \pm \frac{1}{2} \sqrt{4(J + \frac{1}{2})^2 + Y(Y - 4)} \mp (Y - 2) - \frac{1}{2B} \epsilon W_{\Lambda}(J) \quad (3.4)$$

with $Y = \frac{4}{B}$. The \pm in (3.4) distinguishes between the upper F_2 (dominated by $\overline{\Omega} = \frac{3}{2}$ if $A_0 > 0$) and the lower F_1 (dominated by $\overline{\Omega} = \frac{1}{2}$ if $A_0 > 0$) spin-orbit state. For NO, the two spin-orbit states – often indicated by ${}^2\Pi_{\frac{1}{2}}$ and ${}^2\Pi_{\frac{3}{2}}$ – differ about 121 cm^{-1} in energy, the latter having the highest energy. The Λ -type splitting for the ${}^2\Pi_{\frac{1}{2}}$ states that are well approximated by case (a) coupling varies linearly with J [36]. It is expressed as [40]:

$$W_{\Lambda} = q_{\Lambda} \left(J + \frac{1}{2} \right). \quad (3.5)$$

Burrus and Gordy [40] obtained $q_{\Lambda} = 0.0118 \text{ cm}^{-1}$ for the energy splitting of the $J = \frac{1}{2}$ Λ -doublet. The Λ -splitting for the ${}^2\Pi_{\frac{3}{2}}$ component is much smaller in its lowest $J = 3/2$ state ($4 \times 10^{-5} \text{ cm}^{-1}$) [41] but increases with the third power of J [36].

A similar expression for the energy can be obtained for molecules with l -doublet splitting, like OCS or N_2O excited in a bending vibration. The splitting between the l -doublet energy levels in the case of $\bar{l} = 1$ is:

$$W_l = \frac{1}{2} q_l (v_2 + 1) (J(J + 1)), \quad (3.6)$$

with q_l the l doubling constant. For OCS in the $(v_1 v_2^l v_3) = (01^1 0)$ state and at low values of J , the l -doubling constant is $q_l = 6.3614 \text{ MHz}$ [42] whereas for NO_2 , $q_l = 23.7437 \text{ MHz}$ [43].

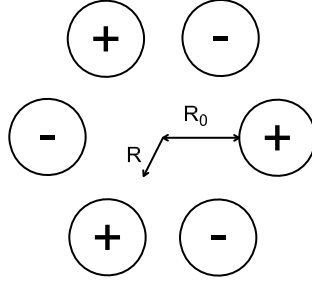


Fig. 3.1 Schematic representation of a hexapole state selector. A positive voltage ($+V_0$) is applied on three of the rods, while a negative voltage ($-V_0$) is applied to the other rods. Molecules that reside in the *upper* (low-field seeking) component of the Λ -doublet are pushed toward the center of the hexapole while those in the *lower* (high-field seeking) component are pulled toward the rods. The hexapole that was used in this work is designed to the “Dutch convention”: the rod diameter equals the hexapole inner radius R_0 [45]

3.3 Hexapole State Selection

The technique of focussing polar molecules in static electric fields was developed in the 1950s [44] and has been used in this study to avoid the inherent problem of thermal averaging in alignment/orientation experiments, where the averaging over the initially populated states has a drastic effect on the maximum degree of orientation that can be achieved. As hexapole state selection has not been used previously in the field of intense-laser physics, we will give a rather extensive introduction here. A hexapole consists of six parallel rods where three are in negative voltage while three others are in positive voltage (see Fig. 3.1) and creates an inhomogeneous field that works as a positive lens for low-field seeking molecules. The focal length of the lens is determined by the molecules’ dipole moment and rotational state. Hexapole state selection exploits the first-order Stark effect that arises as a shift of the energy levels of an atom or a molecule in an electric field \mathbf{E} . By defining the Z -axis along \mathbf{E} , the Hamiltonian in an electrostatic (hexapole) field is given by:

$$\mathcal{H} = \mathcal{H}_0 - \mu_{el} \mathbf{E} \cos \theta, \quad (3.7)$$

where μ_{el} is the electric dipole moment vector of the molecule and θ is the polar angle between the dipole and the electric field. The first-order Stark correction to the energy induced by the field depends of the sign of $\langle \cos \theta \rangle$. Molecules are labeled as low-field seeking or high-field seeking, depending on whether their potential energy increases or decreases for increasing field strengths. For molecules that have l or Λ -doublet splitting, the electric field mixes the $|J, \bar{K}, M, \epsilon' = -1\rangle$ and $|J, \bar{K}, M, \epsilon' = 1\rangle$ components of the l or Λ -doublet and the wave function in an electric field can be expressed as

$$|J, \bar{K}, M, \epsilon, E\rangle = \alpha(E) |J, \bar{K}, M, \epsilon' = -1\rangle + \epsilon \beta(E) |J, \bar{K}, M, \epsilon' = 1\rangle, \quad (3.8)$$

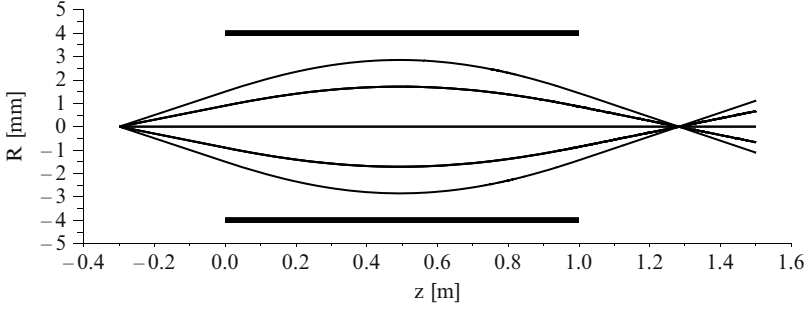


Fig. 3.2 Hexapole focusing curves for NO, the hexapole considered in this figure is the one that is used in the experiment described in the experimental section. The rod diameter and inner radius of the hexapole both equal 4 mm, the length of the hexapole is 1 m

with $\alpha(E)^2 + \beta(E)^2 = 1$. Note that K is the projection of the total angular momentum (J) on the molecular axis and thus contains either l or Ω . For relatively strong fields, where the Stark splitting is much bigger than the l or Λ -doublet splitting, the first-order correction to the energy $W_\epsilon^{(1)}$ is linear and reads:

$$W_\epsilon^{(1)} = -\epsilon\mu_{el}E \frac{\overline{MK}}{J(J+1)}, \quad \text{where: } \langle \cos \theta \rangle = \epsilon \frac{\overline{MK}}{J(J+1)}. \quad (3.9)$$

Molecules in an “ $\epsilon = -1$ ” state are low-field seeking. For molecules in states that carry a first-order Stark effect and are exposed to relatively weak electric fields ($\mu_{el}E \ll B$), higher order energy terms can be neglected [34, 46].

Here, we provide some basic equations for hexapole focusing. A schematic representation of hexapole focusing is provided in Fig. 3.2. The potential of the hexapole field is [44]:

$$V = V_0 \left(\frac{R}{R_0} \right)^3 \cos 3\phi, \quad (3.10)$$

where R_0 is the inner radius of the hexapole, and R and ϕ are cylindrical coordinates. An ideal hexapole field is given by $E = 3V_0R^2/R_0^3$. Molecules in the hexapole feel a force $F = -dW/dR$, which for the first-order Stark effect becomes:

$$F_{\text{hex}} = -\frac{dW^{(1)}}{dR} = \frac{\mu_{el}6V_0R}{R_0^3} \frac{\epsilon\overline{MK}}{J(J+1)} \quad (3.11)$$

In order to evaluate the focusing properties of the hexapole, the distance from the pulsed nozzle to the entrance of the hexapole is assumed to be L_1 , the length of the hexapole by L_2 , and the distance from the exit of the hexapole to the focal point is given by L_3 . A very convenient equation that gives the focusing distance of a

hexapole is provided by Stolte et al. [47]:

$$L_3 = \frac{L_1 + \frac{1}{\kappa} \tan \kappa L_2}{\kappa L_1 \tan \kappa L_2 - 1}, \quad (3.12)$$

with

$$\kappa = \sqrt{\frac{3V_{\text{hex}}\mu_{el}}{m_M R_0^3 v_z^2} \frac{-\epsilon \overline{MK}}{J(J+1)}}$$

In these equations, V_{hex} is the voltage difference between the rods: $V_{\text{hex}} = 2V_0$. The standard focusing equation for a hexapole [46]:

$$V_0 = \frac{(n\pi)^2 R_0^3}{6L_2^2} \frac{m_M v_z^2}{\mu_{el}} \frac{J(J+1)}{\epsilon \overline{MK}} \quad (3.13)$$

is a convenient approximation for the hexapole voltage, but neglects the effect of the straight path before entering and after exiting the hexapole. It should only be used if the hexapole (nearly) covers the whole path of the molecules. It should be noted that these equations slightly underestimate the hexapole voltage needed for the focusing of NO or OCS, if the I and Λ splitting cannot be neglected. This leads to a nonlinear dependence of $W^{(1)}$ on the electric field near the hexapole axis. For a more rigorous treatment, we refer to the work of Anderson [45], who provides a treatment to calculate the tracks that symmetric top molecules follow within a hexapole and calculates the Stark energy up to a high order.

One of the advantages of hexapole state selection is that the achievable gas density is relatively high, if a substantial amount of the focused state is present in the beam that enters the hexapole. The hexapole works as a lens, which means that one essentially makes an image of the nozzle. In the case of NO cooled in a jet, essentially all molecules in the beam are in the lowest rotational state and half of the molecules that enter the hexapole (the low-field seekers) are focussed into the interaction volume. One can estimate the density of the NO sample after hexapole state selection in our lab. Our hexapole has an inner radius of 4 mm and starts 300 mm from the pulsed nozzle. Its acceptance angle is approximately 0.57° . In case of a mixture of 10% NO in Argon, one may assume a pure argon beam with $\gamma = 5/3$ and “peaking factor” $\kappa = 2$. Assuming a temperature of 300 K, a 1 mm nozzle diameter and a stagnation pressure of 1 bar, leads to an estimated intensity of $6.6 \cdot 10^{21}$ Argon atoms per steradian per second. Five percent of this is actually NO in the low-field seeking component of the Λ -doublet. We feed $2.6 \cdot 10^{16}$ NO molecules per second into our hexapole. The hexapole therefore makes an image of the nozzle in its focus; the diameter of the nozzle was 1 mm. In combination with the velocity of the molecular beam (550 m s^{-1} , but neglecting the velocity spread), this leads to a density of $6.5 \cdot 10^{19}$ NO molecules per m^3 . We already demonstrated that this is enough for experiments with XUV beams from HHG [48]. In addition, these numbers suggest that, with moderate changes in the design and experimental conditions, it may be feasible to detect harmonics created in hexapole state-selected samples.

3.4 Interactions with an Intense Laser Field

After the hexapole, the state-selected molecules are oriented in a moderate electrostatic field (see (3.9)). Stronger impulsive orientation is obtained by application of a short intense laser pulse, polarized along the DC electric field axis to the molecules. The laser pulse is shorter than the rotational period of the molecule and creates a rotational wave-packet. The degree of orientation and alignment evolve after the laser pulse has ended. In this section, we provide a theoretical treatment of the interaction of a state selected molecular sample with the combination of a DC electric field and a short laser pulse.

Ignoring the centrifugal distortion, the interaction potential between a molecule and a non-resonant linearly polarized laser field can be written as [17, 27, 49]:

$$\begin{aligned} V_{\text{eff}} &= -\omega \cos \theta - \Delta\omega \cos^2 \theta + \omega_{\perp} \\ &= -\omega P_1(\cos \theta) - \frac{2}{3} \Delta\omega P_2(\cos \theta) + \frac{1}{3} \Delta\omega + \omega_{\perp}. \end{aligned} \quad (3.14)$$

In this expression, the $P_n(\cos \theta)$ are Legendre moments and the dimensionless electrostatic (ω) and laser field ($\Delta\omega$) are given as:

$$\omega = \frac{\mu E}{B} \quad (3.15)$$

$$\omega_{\parallel, \perp} = \frac{\alpha_{\parallel, \perp} I_l}{2B} \quad (3.16)$$

$$\text{and} \quad \Delta\omega = \omega_{\parallel} - \omega_{\perp} = \frac{\Delta\alpha I_l}{2B}. \quad (3.17)$$

Here, α_{\parallel} and α_{\perp} are the polarizability of the molecule parallel and perpendicular to the internuclear axis and θ is the angle between the permanent dipole moment μ and both the electrostatic and the laser field similar to its earlier use in the context of the hexapole focusing field. The last part of the effective potential ($\frac{1}{3} \Delta\omega + \omega_{\perp}$) is independent of θ and J and has no effect on the rotational dynamics. It will thus be omitted from here on.

In a Raman process, parity is conserved, which often (though not always) means that only $\Delta J = 2$ transitions are observed. However, an oriented wave function has no parity, it is a mix of even and odd parity functions. In the case of NO, the selection rules for excitation with a non-resonant laser pulse are $\Delta J = 0, \pm 1, \pm 2$, while the two quantum numbers \bar{Q} and M are conserved during the process. For molecules selected in a single $|J, K, M\rangle$ state, the final Hamiltonian is described by (note $M = M'$ and $K = K'$)

$$\begin{aligned} H_{J, J'}^{K, M} &= \langle J', K, M | H_0 - \omega P_1(\cos \theta) - \frac{2}{3} \Delta\omega P_2(\cos \theta) | J, K, M \rangle \\ &= \delta_{J, J'} E_{\text{rot}} - \omega Q_1(J', J, K, M) + \frac{2}{3} \Delta\omega Q_2(J', J, K, M) \end{aligned} \quad (3.18)$$

with ($n = 1, 2$):

$$Q_n(J', J, K, M) = \sqrt{(2J+1)(2J'+1)}(-1)^{M-K} \begin{pmatrix} J & n & J' \\ -M & 0 & M \end{pmatrix} \begin{pmatrix} J & n & J' \\ -M & 0 & M \end{pmatrix}. \quad (3.19)$$

In the case of l or Λ -doubling, we use (again using $M = M'$ and $K = K'$):

$$\begin{aligned} H_{J,J',\epsilon,\epsilon'}^{\bar{K},M} &= \langle J', \bar{K}, M, \epsilon' | H_0 - \omega P_1(\cos \theta) - \frac{2}{3} \Delta \omega P_2(\cos \theta) | J, \bar{K}, M, \epsilon \rangle \\ &= \delta_{J,J'} \delta_{\epsilon,\epsilon'} E_0 - \omega Q_1(J', J, M, \bar{K}, \epsilon', \epsilon) \\ &\quad + \frac{2}{3} \Delta \omega Q_2(J', J, M, \bar{K}, \epsilon', \epsilon) \end{aligned} \quad (3.20)$$

with for $n = 1, 2$:

$$\begin{aligned} Q_n(J', J, \bar{K}, M, \epsilon', \epsilon) &= \frac{1}{2} \sqrt{(2J+1)(2J'+1)} \begin{pmatrix} J' & n & J \\ M & 0 & -M \end{pmatrix} \\ &\quad \times \left[(-1)^{M-\bar{K}} \begin{pmatrix} J' & n & J \\ \bar{K} & 0 & -\bar{K} \end{pmatrix} + (-1)^{M+\bar{K}} \epsilon \epsilon' \begin{pmatrix} J' & n & J \\ -\bar{K} & 0 & \bar{K} \end{pmatrix} \right]. \end{aligned} \quad (3.21)$$

Equation (3.20) is general and can also be used for molecules that have no Λ or l splitting, as setting $E_0 = BJ(J+1)$ leads to perfect mixing of the ϵ' levels.

The wave function during and after interaction with the laser pulse is written as a sum of free rotor wave functions:

$$|\Psi(t)\rangle = \sum_{J,\epsilon} C_{J,\epsilon}^{M,\bar{K}}(t) |J, \bar{\Omega}, M, \epsilon\rangle. \quad (3.22)$$

Diagonalization of the total Hamiltonian – with the terms related to the action of the laser $\Delta \omega$ set to zero – provides the mixing of the two doublet states, before interaction with the laser. All our experiments on NO were done at 13 kV cm^{-1} . At this field strength ($\omega = 0.021$), the mixing coefficients are $\alpha = C_{1/2,-1}^{1/2,1/2}(t_0) = 0.85$ and $\beta = C_{1/2,1}^{1/2,1/2}(t_0) = 0.52$ and the degree of orientation is $\langle \cos \theta \rangle = -0.30$, close to the optimum of $\langle \cos \theta \rangle = -1/3$ for perfect mixing.

The rotational dynamics of the molecule during the laser pulse is evaluated by solving the time-dependent Schrödinger equation numerically. The initial oriented wave-function – obtained by diagonalization – is propagated using

$$i\hbar \frac{d|\Psi(t)\rangle}{dt} = (H_0 + V_{\text{eff}})|\Psi(t)\rangle. \quad (3.23)$$

After the laser pulse is over at time t_f , the rotational wave packet evolves freely and it can at every time ($t > t_f$) be calculated via:

$$|\Psi(t)\rangle = \sum_{J,\epsilon} C_{J,\epsilon}^{M,\bar{K}}(t_f) e^{iE_{\text{rot}}(t-t_f)/\hbar} |J, \bar{K}, M, \epsilon\rangle. \quad (3.24)$$

The symmetry index ϵ may be omitted for molecules selected in a single $|JKM\rangle$ state.

Orientation and alignment are often expressed as $\langle \cos \theta \rangle$ and $\langle \cos^2 \theta \rangle$ that relate to the first and second order Legendre moments as:

$$\cos \theta = P_1(\cos \theta) \quad \text{and} \quad \cos^2 \theta = \frac{2}{3} P_2(\cos \theta) + \frac{1}{3}. \quad (3.25)$$

Hence, the degree of orientation ($n = 1$) and alignment ($n = 2$) at any time after the laser pulse can be obtained from:

$$\begin{aligned} \langle P_n(\cos \theta) \rangle &= \langle \Psi(t) | P_n(\cos \theta) | \Psi(t) \rangle \\ &= \sum_{J',\epsilon'} C_{J',\epsilon'}^{M,\bar{K}*} C_{J,\epsilon}^{M,\bar{K}} e^{-i(E_{\text{rot}}(J') - E_{\text{rot}}(J))(t-t_f)/\hbar} \\ &\quad \times Q_n(J', J, M, \bar{K}, \epsilon', \epsilon). \end{aligned} \quad (3.26)$$

In the next section, we will apply the theory described above on a few suitable molecules.

3.5 Numerical Example in Several Polar Molecules

In this section, we provide and discuss selected theoretical results concerning the laser field-free orientation of state-selected molecules. An incomplete list of molecules for hexapole state selection and orientation and their properties is provided in Table 3.1. For the methyl-halides, essentially perfect state selection is possible in the $|J, K, M\rangle = |1, \pm 1, \mp 1\rangle$, $|2, \pm 1, \mp 2\rangle$ and $|2, \pm 2, \mp 2\rangle$ states [50].

In Figs. 3.3 and 3.4, the time-dependent degree of orientation and alignment is plotted for CH_3I after interaction with a 100 fs, Fourier-transform limited (FTL), $\Delta\omega = 1,920 (8 \cdot 10^{12} \text{ W cm}^{-2})$ laser pulse and considering three different initially selected states: $|J, K, M\rangle = |1, \pm 1, \mp 1\rangle$, $|2, \pm 1, \mp 2\rangle$, and $|2, \pm 2, \mp 2\rangle$. Note that

Table 3.1 Some examples of suitable molecules for hexapole impulsive orientation. Parameters were taken from [27, 38, 40, 42, 43, 51]

Molecule	μ [D]	B [cm^{-1}]	$\Delta\alpha$ [\AA]	l or Λ doubling [MHz]
CH_3Cl	1.869	0.440	3.6	0
CH_3I	1.647	0.250	6.0	0
OCS	0.709	0.204	4.1	6.36
N_2O	0.166	0.419	2.8	23.74
NO	0.16	1.703	0.84	353.7

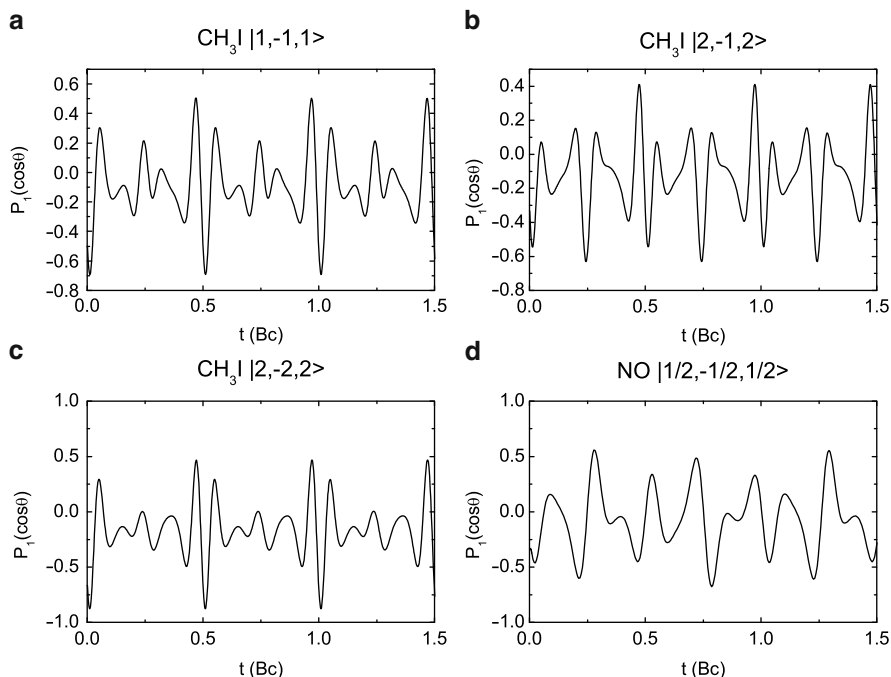


Fig. 3.3 Orientation of CH_3I selected into different states after illumination with an 100 fs laser pulse with intensity $\Delta\Omega = 1,920 (8 \cdot 10^{12} \text{ W cm}^{-2})$: (a) when starting from the $|1, -1, 1\rangle$ state, (b) from the $|2, -1, 2\rangle$ state, and (c) when starting from the $|2, -2, 2\rangle$ state. To get some insight in how the induced impulsive orientation of NO starting from $|1/2, -1/2, 1/2\rangle$ is shown as well (d). All other parameters are the same

the time axis in these figures is dimensionless and given in units of t/Bc , which in the case of CH_3I corresponds to 133 ps. A calculation for a molecule with half-integer angular momentum (NO) is also shown. In this case, we use a laser pulse that has the same duration in dimensionless time (T/Bc), but a much shorter duration in fs (15 fs) and we neglected Λ -doubling.

As we do our calculations using a dimensionless electrostatic and laser field, these calculations (as plotted in Figs. 3.3 and 3.4) are in principle also valid for the other molecules in Table 3.1 with appropriate molecule-dependent changes in the pulse duration and laser intensity.

Strong revivals of alignment and orientation are observed in Figs. 3.3 and 3.4 where the degree of orientation and alignment alternate in time. Moreover, in the case of CH_3I , one can see a strong dependence on the initial state.

In a recent paper [33], we showed that re-phasing of the wave function for states with half-integer angular momentum occurs at multiples of $1/Bc$. For states with integer angular momentum quantum numbers, this occurs at $1/2Bc$. This can be recognized when comparing the bottom right panel of Fig. 3.3 to the rest. In this figure, the time-dependent orientation repeats itself when time is advance by

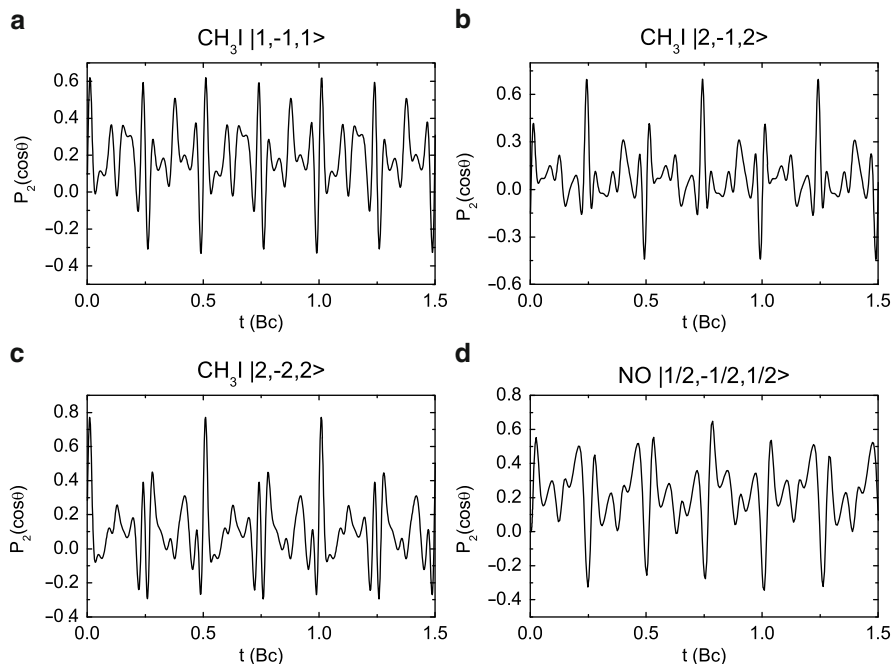


Fig. 3.4 Same as previous figure but concerning the induced laser field-free molecular alignment

1 dimensionless unit of time, while in the other figures this occurs for $\Delta t = 1/2$. The reason for this is that $\Delta J = J' - J = 1$ transitions dominate in the orientation, having energy differences of $J'(J' + 1) - J(J + 1) = 2J + 2$. For $J = 1/2, 3/2, 5/2, \dots$, this becomes 3, 5, 7, \dots , leading to the re-phasing period of $\Delta t^* = 1$. For $J = 1, 2, 3, \dots$, the energy is 4, 6, 8, \dots (i.e., multiples of 2) leading to a re-phasing period of 1/2. Furthermore, we observe in Fig. 3.3 that the optimal degree of orientation for radicals in an $|1/2, \pm 1/2, \mp 1/2\rangle$ and for molecules in an $|2, \pm 1, \mp 2\rangle$ state after interaction with a short intense laser pulse occurs at $t = 1/4, 3/4, 5/4, \dots$, while for molecules in an $|1, \pm 1, \mp 1\rangle$ and a $|2, \pm 2, \mp 2\rangle$ state this is at $t = 1/2, 1, 3/2, \dots$. In all cases, the optimal degree of orientation is enhanced compared to that obtained in the electrostatic field (at t_0) alone.

For the alignment in Fig. 3.4, we observe a different behavior. For all molecules in integer angular momentum states, the time dependent alignment repeats itself every $t = 1/2$, similar as for the orientation. In states with half-integer angular momentum, it, however, repeats itself every $t = 1/4$. In alignment of NO, both $\Delta J = 1$ and $\Delta J = 2$ transitions contribute, but $\Delta J = 2$ transitions dominate for high values of J and thus at high intensity. In this case, the energy differences are $J'(J' + 1) - J(J + 1) = 4J + 6$. For $J = 1/2, 3/2, 5/2, \dots$ this becomes 8, 12, 16, \dots ; i.e., all multiples of 4. For $J = 1, 2, 3, \dots$ this becomes 10, 14, 18, \dots

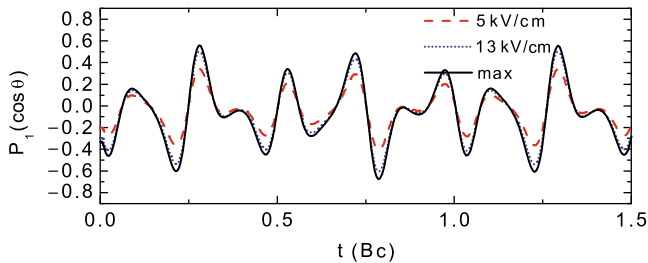


Fig. 3.5 Orientation of NO after illumination with a 100 fs laser pulse with $\Delta\Omega = 150$ ($3 \cdot 10^{13} \text{ W cm}^{-2}$) at two different electric field strengths, and the theoretical maximum for ideal mixing. In the latter case, the oriented wave before the laser can be described as a single $|JKM\rangle = |1/2 \pm 1/2 \mp 1/2\rangle$ state

(i.e., all multiples of 2, but not of 4). The slight differences between the revivals at $t = 1/4, 1/2$ and $3/4$ are caused by $\Delta J = 1$ transitions.

For both OCS and N_2O , the combination of l doubling and their dipole moments essentially completes the mixing of the two components at very moderate electric field strengths ($< 1 \text{ kV cm}^{-1}$) and the results for the methyl-halides can also be used for OCS and N_2O . For NO, this is less so: Λ -splitting cannot be neglected for field strengths that are easily achievable experimentally. We will focus on the $|J = 1/2, \bar{\Omega} = 1/2, M = 1/2, \epsilon = -1\rangle$ state for NO, that is easily focused using a hexapole.

The effect of Λ -doubling on the degree of orientation in our experiments at 13 kV cm^{-1} is, however, rather small. This is illustrated in Fig. 3.5, where the time-dependent orientation of NO is plotted for different electrostatic fields. The calculations are performed for 100 fs laser pulses at the experimentally easily achievable peak intensity of $I_l = 3 \cdot 10^{13} \text{ W cm}^{-2}$. The electrostatic field does not influence the alignment, but does influence the degree of orientation as it produces a (coherent) superposition of two states with opposite parity. If mixing becomes worse, the maximum degree of orientation decreases as is clearly illustrated in Fig. 3.5.

In a Raman process, parity is conserved. The laser only introduces higher rotational states (with higher frequency components) into the wave-function. The coherent sum can – depending on phase and amplitude of these components – give essentially any symmetric (aligned) orientation distribution when starting from a state with a certain parity. When starting from a coherent superposition of even and odd states, as happens in our experiments, one has access to the full basis of rotational states. If one has full control over the laser pulse, one has full control over the phase and amplitude of the expansion coefficients ($C_{J,\epsilon}^{M,\bar{K}}(t_f)$) in (3.26) and thus over the orientation distribution of the sample. In a recent paper [33], we showed that essentially perfect orientation $\langle \cos \theta \rangle = 0.962$ is experimentally achievable for NO, when using a pulse shaper to control the laser pulses. In the remainder of this chapter, we discuss experiments on the optimization of orientation.

3.6 Experimental Setup

Many experiments aiming to probe laser induced alignment and/or the orientation of a molecular sample have been carried out during the last 20 years. A very common technique consists of using a velocity map imaging spectrometer [52]. After the interaction with an intense laser field, the induced molecular alignment is probed using a second, short laser pulse that is intense enough to dissociatively ionize the molecules. Using a pair of electrodes that are commonly called the repeller and the extractor, the momentum of the different charged fragments is projected onto a detector consisting of a set of MCP's (micro channel plates) followed by a phosphor screen. If an ion hits the detector, its position can directly be related to the velocity of the molecule or fragment before ionization. A camera placed after the phosphor screen allows one to obtain an image of the 2D velocity distribution of the detected molecule. In the recoil approximation, i.e., if the molecule is fixed during the ionization/dissociation step, the angular distribution of the measured 2D projection is related to the angular distribution of the molecule before dissociation and can therefore be used to quantify the degree of alignment.

A schematic drawing of the experimental setup is shown in Fig. 3.6. The experiment is done in two steps. In the first step, the molecular sample is prepared in a single rotational quantum state using a hexapole. A mixture of 10% NO in Ar (room temperature at a stagnation pressure of 1.6 bar) was expanded into a vacuum chamber using a pulsed nozzle at a repetition rate of 12.5 Hz. After passing through a $\varnothing = 1$ mm skimmer positioned at 5 cm from the nozzle, the beam entered a 1 m hexapole state selector, positioned 30 cm from the nozzle. The hexapole consists of six rods raised to 9 kV voltage that alternate in sign. In our experiment, the hexapole focuses NO molecules that reside in the low-field seeking $\epsilon = -1$ component of the $J = 1/2$ Λ -doublet into the VMI spectrometer placed 30 cm downstream. NO molecules in the lower $\epsilon = +1$ component of $J = 1/2$ are rejected. Due to the adiabatic expansion of the molecules after the pulsed nozzle, higher excited rotational levels of NO are only weakly populated and pass essentially undeflected along the axis of the hexapole due to their much smaller Stark effect. The state-selected molecular sample experiences in the detection region a DC field of 13 kV cm^{-1} . This field serves both for the orientation of the molecules (to a value $\langle \cos \theta \rangle = 0.30$, where θ is defined as the angle between the electrostatic field and the molecular NO axis) and for the extraction of the ions.

To impulsively align/orient the molecules, the experiment used a pump-probe setup. The output of a linearly polarized femtosecond Ti:sapphire laser system (30 mJ, 70 fs at a repetition rate of 25 Hz) is split with a 70/30 beamsplitter to provide a moderate energy pump beam and a high energy probe beam. Alignment and orientation may be probed either with an intense 800 nm beam directly or after frequency doubling in a (3 mm KDP) crystal, using 400 nm radiation. Frequency doubling reduces eventual problems with pre-pulses in the probe process. After doubling, the pulse energy is approximately equal to 1 mJ. The pump beam (2.5 mJ) is sent into a 4-f dispersion line pulse shaper consisting of a 640 pixel spatial light modulator (SLM) placed at the Fourier plane of two cylindrical mirrors [53]. The

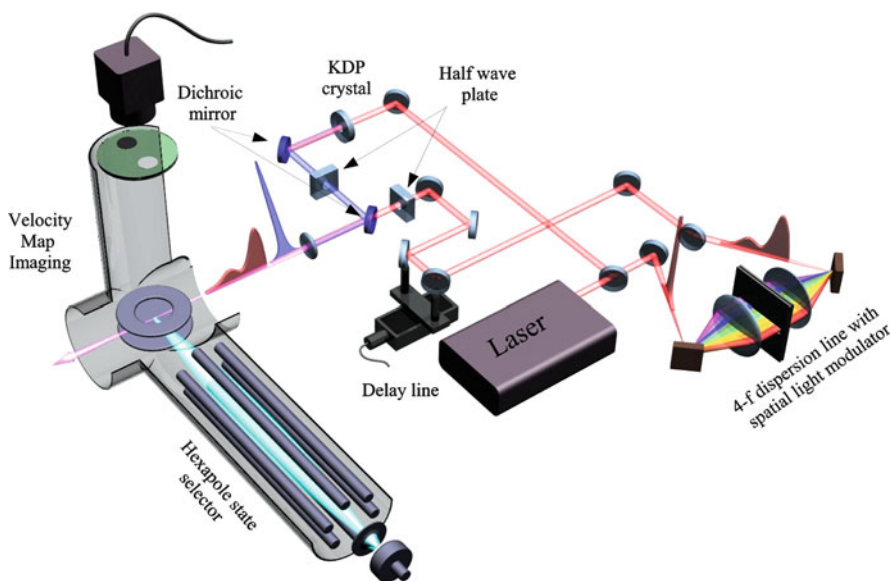


Fig. 3.6 Schematic representation of the experimental setup where a state-selected NO beam is crossed with two pulses at the center of a VMI spectrometer. State-selected NO molecules are prepared using a hexapole in front of a pulsed nozzle valve. The first 800 nm pulse is used to impulsively align and orient the molecules and the second (400 nm) pulse to probe the induced rotational dynamics by Coulomb explosion of the molecule. The fragments produced by the 400 nm pulse are detected by a velocity map imaging spectrometer and recorded with a CCD camera. Both pulses are linearly polarized and the direction of their polarization axis is controlled by rotating a half-wave plate in their respective arms. A pulse shaper controlled by a computer allows us to modify the pulse profile that is used to enhance the molecular orientation. Reprint from [32]

SLM device allows us to modify the spectral phase of the pump electric field which alters the temporal profile of the pulse. A delay stage composed of two mirrors mounted on a motorized translation stage is placed in the pump arm allowing to control the relative delay between the pump and probe beams. Both beams are then recombined collinearly using a dichroic mirror and focused into the VMIS chamber by an $f = 20$ cm achromatic lens. The laser beams intersect the molecular sample at the center of the VMIS where N^{q+} and O^{q+} fragments originating from the Coulomb explosion by the probe pulse are projected onto a position-sensitive detector consisting of a dual micro channel plate followed by a phosphor screen. A 20 ns, 1.6 kV gating pulse is applied on the MCP in order to selectively detect fragments of a certain mass/charge ratio arriving on the detector. The 2D velocity distribution on the phosphor screen is recorded by a CCD camera and then transferred to an acquisition computer. To remove the effect of background contamination, a subtraction routine was employed and the fragments were measured with and without the presence of the NO gas during every other laser shot.

3.7 Sign of the NO Dipole Moment

Before performing experiments on laser field-free alignment/orientation, the sign of the permanent dipole moment of NO was first determined. As reported by Townes and Schawlow [54], the sign of a permanent dipole moment can in principle be obtained experimentally from the isotopic dependence of magnetic susceptibility factors. However, even the highest precision measurements have been unable to determine the sign of the NO dipole moment experimentally [55]. This dipole moment has been the subject of a recent controversy [56] due to an unresolved sign discrepancy between measurements and calculations of the steric asymmetry for He-NO, Ar-NO, and D₂-NO rotationally inelastic collisions [56,57].

Experiments were performed where the fragments coming from the Coulomb explosion of the DC oriented state-selected NO molecules were recorded. Only a single laser pulse was used in this case. Representative images with detection of N²⁺ ions and O²⁺ ions originating from the interaction with a strong 800 nm laser pulse are shown in Fig. 3.7. The laser polarization was set to +20°. To allow for a quantitative interpretation of the data, the integral of the images along the vertical axis is plotted below the two-dimensional velocity distributions. In both panels, the left image shows the fragment velocity distribution without applying any voltage to the hexapole. In this case, the molecular sample contains equal distributions from both the high-field and low-field seeking component of the $J = 1/2$ Λ -doublet

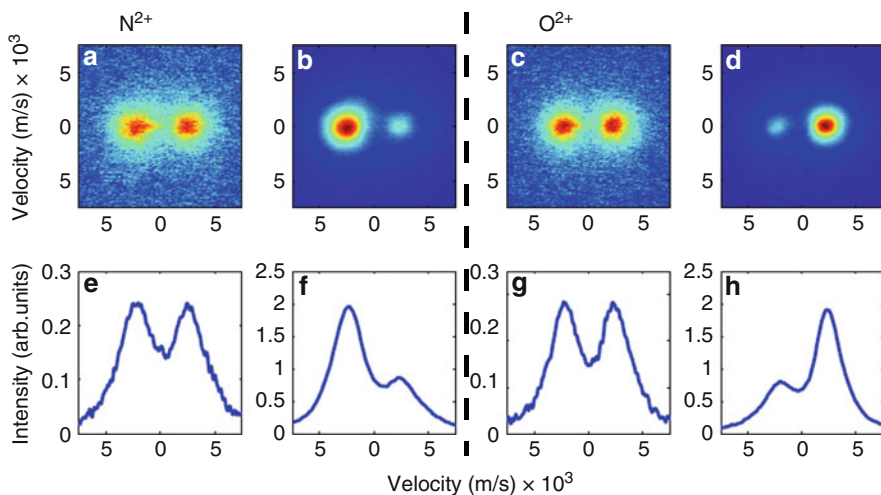


Fig. 3.7 Ion images for Coulomb explosion of oriented NO. The *left panel* (a–b) shows images if the gate is set to detect N²⁺ ions, images in the *right panel* (c–d) are from O²⁺ ions. With the hexapole off (b,d) no net orientation is present. Applying a voltage to the hexapole rods increases the ion yield and a strong orientation is visible for (b) N²⁺ and (d) O²⁺. The laser polarization is $\alpha = 20^\circ$ and the *left spot* shows the ions from atoms that originally pointed upward. (e–h) Integrated intensity along the y -axis of the images displayed above

state, and the image is symmetric. In the right images, a voltage is applied to the hexapole that focuses the low-field seeking state into the spectrometer, while defocusing the high-field seeking state. An increase in the ion yield is observed that results from the focusing of the molecules and that is accompanied by the observation of a substantial asymmetry in the images. From the figure, it can be concluded that the N^{2+} fragments preferentially recoil in the direction of the detector (i.e., along the DC electric field) while the O^{2+} ions preferentially recoil away from the detector. Accordingly, the N-end of the state selected NO molecules preferentially points upward (toward the extractor, being the negative electrode), while the O-end preferentially orients downward (toward the repeller, being the positive electrode). As the NO is in a low-field seeking state, the dipole moment (for $v = 0$) is such that N is negative and O is positive (N^-O^+).

The experiment described above is extremely sensitive to the initial orientation of the molecules. As we will show after and as demonstrated by Friedrich and co-workers [58,59], the combination of a DC field and a short laser pulse can lead to an impulsive orientation of the molecules with an orientation that periodically reverses in time. Therefore, if the probe laser field contains pre-pulses, the orientation can be altered or can change. In order to gain confidence that the NO dipole moment obtained by Coulomb imaging of N^{2+} and O^{2+} using an 800 nm laser pulse was right, other experiments were also conducted at 400 nm and using XUV generated by means of high-harmonic generation in Ar [48]. Both experimental results (see [48]) confirmed the same sign of the NO dipole moment, N being negative and O positive (N^-O^+).

3.8 Impulsive Alignment and Orientation

3.8.1 Laser Field-Free Alignment

In this section, we discuss experiments where hexapole state-selected NO molecules were used in a pump-probe arrangement coupled to a VMIS to observe and detect field-free molecular alignment of NO. As explained before, the role of the short pump laser pulse is to impart a kick to the molecule that leads to the creation of a rotational wave packet by successive two-photon Raman processes. The periodic re-phasing of this coherent superposition of states after the pulse has ended is responsible for an alignment of the molecules along the laser polarization that can be probed by Coulomb explosion of the molecules using a second laser pulse. As the molecules are initially prepared in a selected state, no effect of thermal averaging occurs and a strong degree of alignment is expected.

For this experiment, a lower DC field was used since we were interested only in measuring the induced alignment. The polarization of the pump pulse was kept parallel to the molecular beam (in the plane of the MCP detector) and the polarization of the probe beam was chosen parallel to the detector axis. In this configuration,

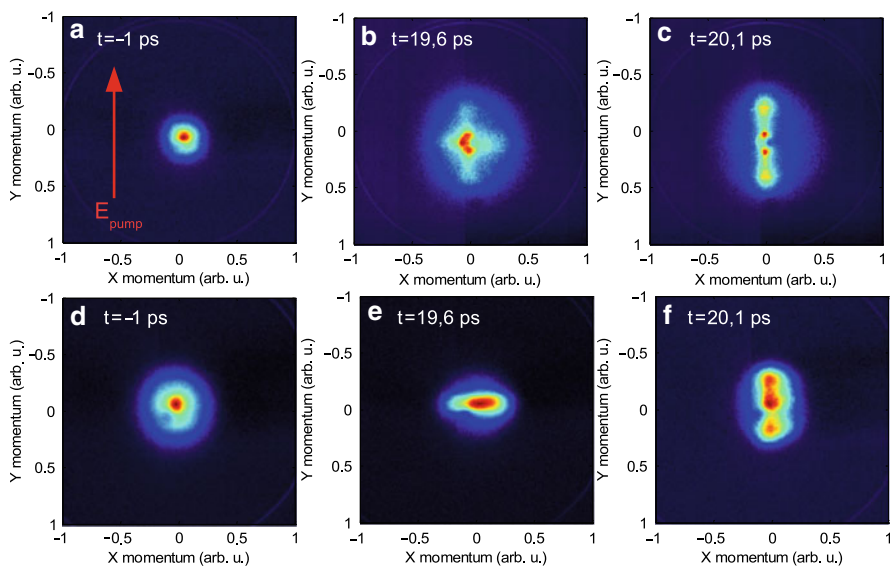


Fig. 3.8 Typical 2D velocity distributions of N^+ (top) and N_2^+ (bottom) fragments recorded for three pump-probe delays; (a) and (d) when the probe pulse is sent 1 ps before the pump pulse, (b) and (e) around 19.4 ps on a planar delocalization peak, (c) and (f) around 20.1 ps on an alignment peak

the signal is free from the contribution of the geometrical alignment that comes from the probe process which is due to the angular selectivity of the ionization process. Figure 3.8 shows the 2D velocity distributions of the N^+ and N_2^+ fragments recorded at different pump-probe time delays. When the probe pulse is sent before the pump pulse, the angular distribution of the fragments is isotropic, meaning that no alignment occurs. Rapid changes of the angular distribution are observed at later time delays, in particular at time $t = 19.4$ ps and $t = 20.1$ ps, where the angular distribution peaks perpendicular and parallel to the pump laser polarization, respectively. The former corresponds to a planar delocalization of the molecule where most molecules are aligned perpendicular to the laser polarization axis, whereas the latter corresponds to preferential alignment of the internuclear axis along the laser polarization axis.

A series of measurements was performed where images were recorded as a function of the pump-probe time delay. Results of these measurements are summarized in Fig. 3.9, which shows the expectation value $\langle \cos^2 \theta_{2D} \rangle$ obtained after integration of the images, where θ_{2D} is the angle of the measured velocity with respect to the vertical axis of the images (laser polarization, see Fig. 3.8). Strong revivals of the alignment are observed where $\langle \cos^2 \theta_{2D} \rangle$ decreases and increases on a picosecond time scale. The presence of these revivals clearly indicates that the pump laser pulse has produced a rotational wave packet that freely evolves after the pump laser excitation has ended. At high intensity, our measurements reveal that the frequency of the oscillations increases, and the revivals become regularly spaced with a separation

of approximately 5 ps. Quantum mechanically, this can be explained by the evolution of the wave function for the several rotational states that are populated by the laser (see Sect. 3.5). The revival time $1/4Bc$ that was rationalized in Sect. 3.5 corresponds to the 5 ps revival period that is observed here.

Molecular alignment is generally quantified using the expectation value $\langle \cos^2 \theta \rangle$, where θ represents the angle between the molecular axis and the polarization of the pump laser pulse. $\langle \cos^2 \theta \rangle$ can be obtained from an Abel inversion of the 2D velocity projection if the experiment contains a symmetry axis in the plane of the 2D detector. Under the conditions of the experiment, where the probe laser was polarized parallel to the detector axis, this condition is not fulfilled. In order to extract $\langle \cos^2 \theta \rangle$ from our measurements, the time dependence of $\langle \cos^2 \theta_{2D} \rangle$ was therefore compared with that of $\langle \cos^2 \theta \rangle$ calculated by solving the time-dependent Schrödinger equation. The method we have used to extract the expectation value $\langle \cos^2 \theta \rangle$ is similar to the shape base analysis performed in [60] that consists of fitting the theoretical result to the shape of the measured alignment signal. For a particular molecule, the degree and shape of the revival of the alignment depends mainly on three parameters, namely the pulse duration, the peak intensity, and the temperature of the molecular sample. As we start from a single rotational state (i.e., $T = 0$ K), we can infer the actual degree of molecular alignment by adjusting only the strength of the laser field and using the measured pulse duration in our simulation to match the measured structure. A scale factor is also needed to adjust the amplitude of the theoretical curve to that of the experimental signal. The result of this procedure is shown in Fig. 3.9 on top of the experimental signal. For the two intensities investigated here, a very good agreement was found allowing us to conclude that $\langle \cos^2 \theta \rangle$ reaches a maximum of 0.76 for the higher intensity.

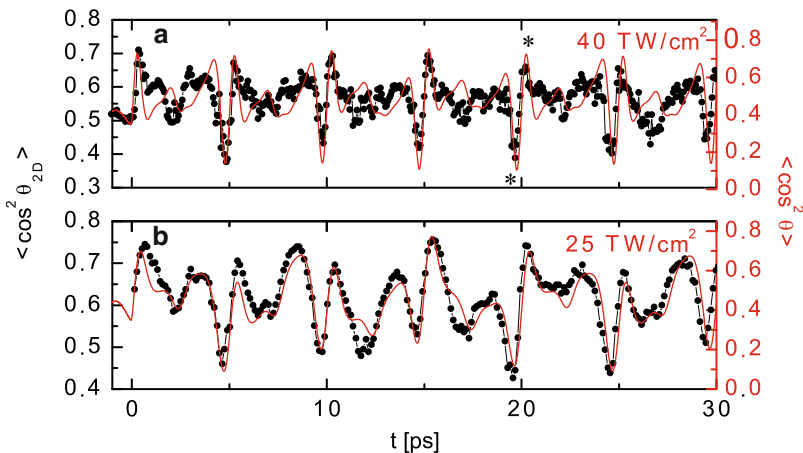


Fig. 3.9 Time evolution of $\langle \cos^2 \theta_{2D} \rangle$ (dotted line) obtained by angular integration of the images for a pump intensity of 25 TW cm⁻² (b) and 40 TW cm⁻². (a) The value of $\langle \cos^2 \theta \rangle$ (gray line) resulting from a shape-based fitting analysis is shown as well

The maximum degree of alignment for the two intensities investigated here is almost identical, meaning that the alignment is already saturated. Moreover, further experiments where the pulse energy was increased even more did not show an enhancement of the degree of molecular alignment. This is the first observation of this effect which had been predicted theoretically in the literature [49]. In other experiments performed at room temperature or in a rotationally cold molecular sample, the saturation of alignment is expected at an intensity where large ionization occurs, making the observation of the saturation more difficult. The use of a hexapole allows to observe saturation of alignment at an intensity where ionization of the molecules remains small.

The use of a sample of quantum state-selected molecules brings out new features (see Fig. 3.10) in the time-dependent alignment that have not been observed before. Given that the laser excitation starts from a single rotational state, a unique quantum mechanical wave packet is formed in the experiment, as opposed to experiments that involve thermal averaging, where different quantum mechanical wave packets are present simultaneously. Consequently, our experiments show the first hints of complicated structure in the angular distribution away from revival times, especially between revivals of the alignment at $t = 17.5$ ps. This suggests that, using an alignment detection scheme that allows full retrieval of the 3D angular distribution (such as fs XUV pulses that dissociatively ionize the aligned molecules [48]), it may be possible to fully reconstruct the amplitudes and phases of the rotational wave packet produced.

3.8.2 *Laser Field-Free Orientation*

The main goal of the experiment was to produce a high degree of laser field-free molecular orientation. A weak degree of impulsive orientation was previously demonstrated in the OCS molecule by Sakai and co-workers [29]. In this pioneering experiment, impulsive orientation was induced by the combination of a DC field with a rapid turn-off of a long laser pulse. Similar to a short laser pulse, the rapid turn-off of the field leads to the formation of a rotational wave packet that displays revivals of the alignment and orientation if an electrostatic field is added. The measured degree of orientation in this experiment was modest due to the incoherent de-phasing induced by the presence of many different rotational states in the initial sample. The use of a hexapole or an electrical device such as a deflector recently shown by Holmegaard et al. [61] allows to state-select molecules and therefore to overcome the effect of thermal averaging.

Experiments on laser field-free orientation were performed as follows: the small DC electric field used in the previous alignment experiment was increased to 13 kV cm^{-1} . This electrostatic field strength assures a good DC orientation of the state-selected NO molecule. As shown in the theoretical section, this relatively high DC field strength is only needed for molecules with a small dipole moment such as

NO. For OCS, with a dipole moment five times bigger than that of NO, a DC field strength of only 1 kV cm^{-1} is required. Impulsive orientation was then induced with a 90 fs laser pulse polarized along the detector axis (in the direction of the DC field) and probed by Coulomb explosion using a strong 400 nm laser pulse polarized at 30° with respect to the pump polarization [32, 48]. This allows to distinguish fragments with a recoil velocity away from or toward the 2D detector. The measured 2D velocity distribution consists of two spots, with a relative intensity that serves as a measure of the molecular orientation. We note that the temporal resolution of our spectrometer did not allow the determination of the molecular orientation from flight time differences (around 1 ns) for fragments initially moving toward or away from the detector as used in [29].

Figure 3.11 shows raw N^{2+} images obtained at different pump-probe time delays as well as the time evolution of the momentum distribution obtained from integrating the images along the vertical axis. For negative time delays, the asymmetry in the ion images reveals the orientation induced by the DC field strength only. At overlap, the asymmetry switches sign and is followed by a periodic inversion of the brightest spot between the upper and the lower part of the detector every 5 ps. In particular, around times $t = 8 \text{ ps}$ and $t = 19 \text{ ps}$, the N^{2+} detection occurs predominantly in the upper part of the images, while at times $t = 9 \text{ ps}$ and $t = 20 \text{ ps}$ the N^{2+} detection occurs predominantly in the lower part of the images. These periodic oscillations indicate that the 800 nm laser pump pulse has impulsively excited the molecule producing a rotational wavepacket with an orientation that periodically alternates.

Similar to the previous discussion on impulsive alignment, we can extract an expectation value $\langle \cos \theta_{2D} \rangle$ (see Fig. 3.12, left), and a corresponding $\langle \cos \theta \rangle$ (see Fig. 3.12, right) that is obtained from a TDSE simulation by fitting to the shape of the measured $\langle \cos \theta_{2D} \rangle$. $\langle \cos \theta_{2D} \rangle$ shows rapid modulations with a periodic inversion of the sign of the orientation, which is very well reproduced by our theoretical model for all intensities investigated here. At low intensity, $\langle \cos \theta_{2D} \rangle$ is mainly composed of a single oscillation period. At this low energy, the first transition $\Delta J = 1$ is predominant and leads to a rephasing period $T_1 = 1/(3Bc) = 6.5 \text{ ps}$ as observed in our experiment. Other frequencies contribute at higher intensities. For instance, at 20 TW cm^{-2} , revivals spaced by 4 ps are observed corresponding to a period $T_1 = 1/(5Bc)$. At the higher intensity investigated here, revivals appear every 5 ps. However, since only quantum beats between adjacent levels $\Delta J = \pm 1$ contribute to the impulsive orientation, the full revival period (where the wave function returns to its initial form) is given by $T = 1/(Bc) = 20 \text{ ps}$. Revivals at 5, 10, and 15 ps represent therefore the 1/4, 1/2, and 3/4 revival time.

We note that the quantitative relation between $\langle \cos \theta_{2D} \rangle$ and $\langle \cos \theta \rangle$ is a complex function of the initial orientation in the DC field, the dynamic alignment and orientation created by the probe laser, the dependence of the fragmentation probability on the angle between the probe laser polarization and the molecular axis, and the angle between the pump and probe lasers. It is therefore not straightforward to really quantify the degree of orientation using directly the expectation value

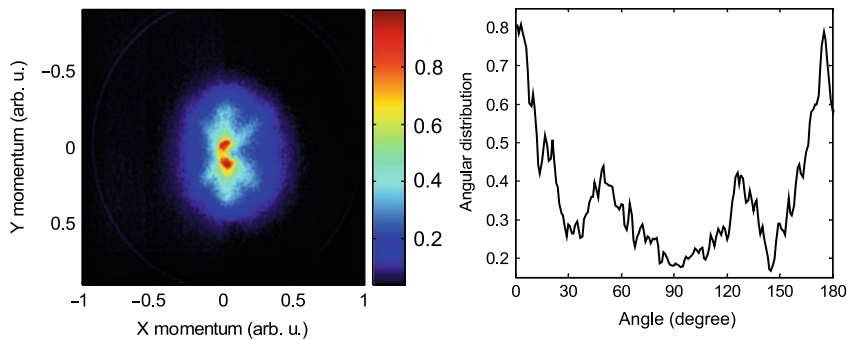


Fig. 3.10 2D velocity distribution of N^+ fragments recorded at $t = 17.5$ ps between the pump and probe laser pulse (*right*) and corresponding angular distribution (*left*). The angular distribution exhibits new peaks at 50° and 130°

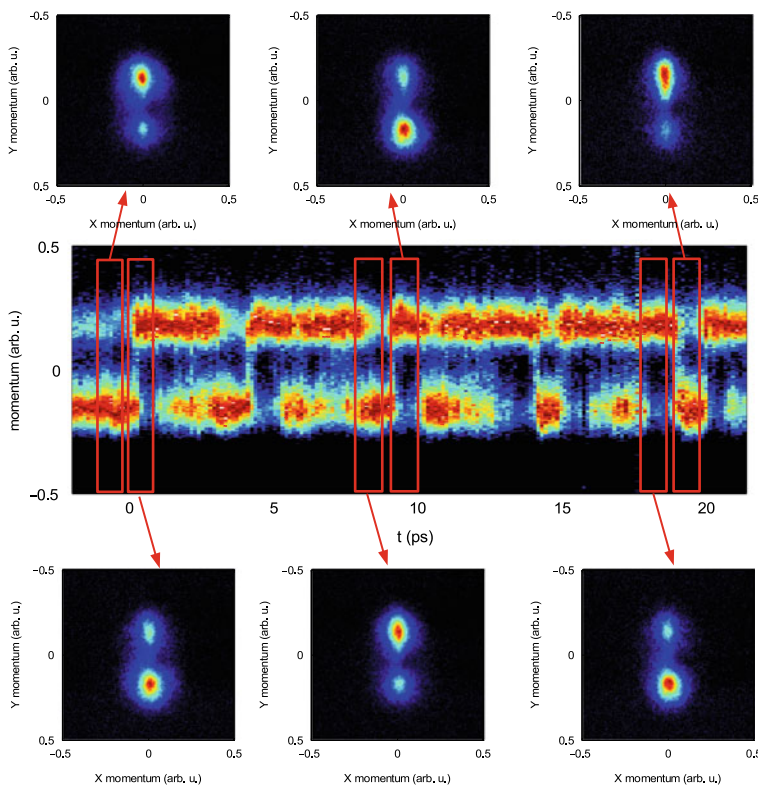


Fig. 3.11 Time evolution of the momentum distribution of N_2^+ fragments along the vertical axis of the detector. The N_2^+ 2D velocity distributions recorded at delays indicated by the *red rectangle* are shown. After the pump-probe overlap, a periodic switch of the most brighter spot between the *top* and *bottom* part of the images is observed

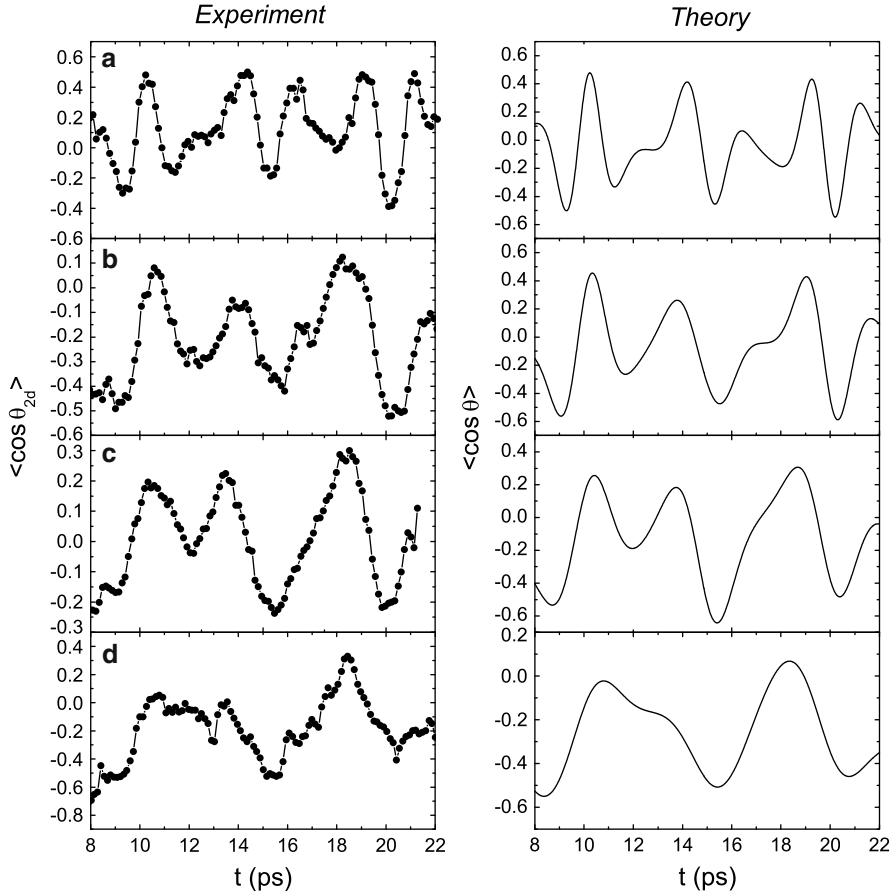


Fig. 3.12 Time-dependent degree of orientation $\langle \cos \theta_{2D} \rangle$ obtained by an integration of the recorded N^{2+} 2D momentum distributions (*left panel*) and corresponding $\langle \cos \theta \rangle$ obtained by integrating the time-dependent Schrödinger equation at different intensities: (a) 10 TW cm⁻², (b) 20 TW cm⁻², (c) 27 TW cm⁻², and (d) 40 TW cm⁻²

$\langle \cos \theta_{2D} \rangle$ obtained from integrating the images. However, the good agreement between experiment and theory allows to extract a good approximation of the degree of orientation reached experimentally. At 40 TW cm⁻², $\langle \cos \theta_{2D} \rangle$ reaches a maximum value of -0.4 , which according to the TDSE simulations corresponds to a degree of orientation $\langle \cos \theta \rangle$ equal to -0.6 . We note that, as for the alignment, the maximum degree of orientation is constant for intensities above 30 TW cm⁻², meaning that the orientation is already saturated.

3.8.3 *Orientation and Alignment with Shaped Intense Laser Pulse*

In this section, we report optimal control of the laser field-free orientation using the degree of orientation evaluated through the 2D velocity distribution of the recorded N^{2+} fragments for feedback. Since we reported in Sect. 3.8.2 that increasing the intensity does not lead to an enhancement of orientation, we may ask if the degree of orientation that was observed there corresponds to the maximum attainable orientation. Since the experiment already starts from the ideal case of having just a single initially populated state, the only parameter left is the temporal profile of the pump laser electric field. The optimization of laser field-free alignment by shape laser fields has been the subject of intense research during the last decade. Two methods have shown to be quite efficient. The first one consists to use a sequence of pulses with suitable chosen delays between the pulses. When pulses are synchronized with the revival of alignment, each pulse interacts with a pre-aligned sample, leading to a better efficiency of the alignment process [62, 63]. The second method consist of tailoring the temporal profile by a pulse shaping device such as a spatial light modulator (SLM) [64]. The role of an SLM device is to modify the temporal profile by acting on the phase, polarization, and/or amplitude of each spectral component of the electric field. Optimization of the process is then carried out by optimizing for instance the spectral phase (the n pixels of the SLM) of the electric field using, for instance, an evolutionary algorithm in an adaptative loop control [65–67].

The large averaging needed to observe a good 2D velocity distribution combined with the large number of iterations required for this kind of algorithm before converging to a solution makes a full optimization procedure very challenging. However, one can decrease the number of iterations by parameterizing the phase using a particular function. Only few parameters need then to be optimized. Recently, Hertz and co-workers [68, 69] theoretically demonstrated that the field-free alignment of diatomic molecules such as N_2 and O_2 can be increased when a sigmoidal phase mask is applied to the pulse. A sigmoidal phase function introduces a phase jump that is described by three parameters, namely an amplitude A , a central laser frequency ν_0 where the jump occurs and a slope s describing the slope of the phase-function around ν_0

$$\phi(\nu) = A \frac{1}{1 + e^{(\nu - \nu_0)/s}}. \quad (3.27)$$

The corresponding temporal profile consists of a long leading edge prior to a main kick pulse. The long leading edge pre-aligns the molecule, while the main pulse subsequently induces a strong revival that is substantially stronger than that created by a Fourier Transform Limited (FTL) pulse.

To explore the utility of sigmoidal phase patterns for achieving molecular orientation, a feedback loop-controlled experiment was performed using a simplex optimization algorithm. The three parameters of the sigmoidal phase were optimized

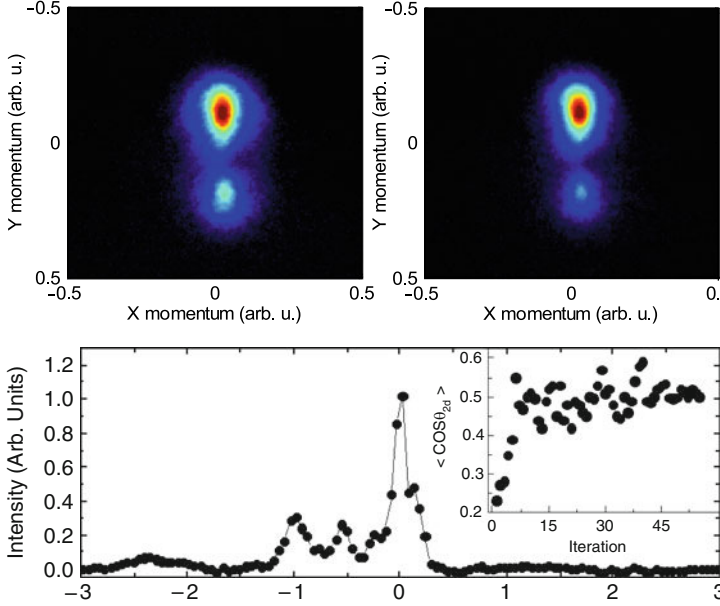


Fig. 3.13 2D velocity distribution of N^+ fragments recorded at $t = 20.1$ ps between the pump and probe laser pulse with the FTL pulse (*left*) and with the optimized pulse (*right*). The *bottom panel* shows the optimized pulse profile as well as the evolution of $\langle \cos \theta_{2D} \rangle$ during the optimization procedure in inset

in order to minimize the value $[1 - |\langle \cos \theta_{2D} \rangle|]$ at $\tau = 20.1$ ps, where the FTL pulse created a minimum in $[1 - |\langle \cos \theta_{2D} \rangle|]$.

Figure 3.13 shows N^{2+} images recorded with the FTL pulse (left) and with the best sigmoidal phase function found by the simplex method (right), respectively. The degree of orientation obtained with the shaped laser pulse clearly exceeds the one obtained with the FTL pulse. The optimized pulse shape is shown in Fig. 3.13 as well as the evolution of $\langle \cos \theta_{2D} \rangle$ with the number of iteration (phase tested) used by the simplex optimization algorithm before reaching convergence. Only few iterations are needed (less than 15) making the optimization fast enough for the experimental conditions (laser intensity, pressure, etc.) to remain constant. From this figure, we can conclude that $\langle \cos \theta_{2D} \rangle$ reached -0.5 .

To obtain $\langle \cos \theta \rangle$, N^{2+} fragment images were again recorded as a function of the pump-probe time delay, and the $\langle \cos \theta_{2D} \rangle$ from these images was compared with TDSE simulations using the laser pulse energy and the parameters of the sigmoidal phase function obtained experimentally ($A = 6\pi$, $\nu_0 = 0.375$ THz, and $s = -0.0012$ THz). The result is shown in Fig. 3.14a along with a comparison with the FTL pulse. An increase from -0.4 to -0.5 is observed experimentally, which according to the TDSE corresponds to an increase of $\langle \cos \theta \rangle$ from -0.6 to -0.74 . The sigmoidal pulse shape brings therefore the degree of orientation within 0.26 of maximum value 1. The optimized laser field consists of two weak pulses

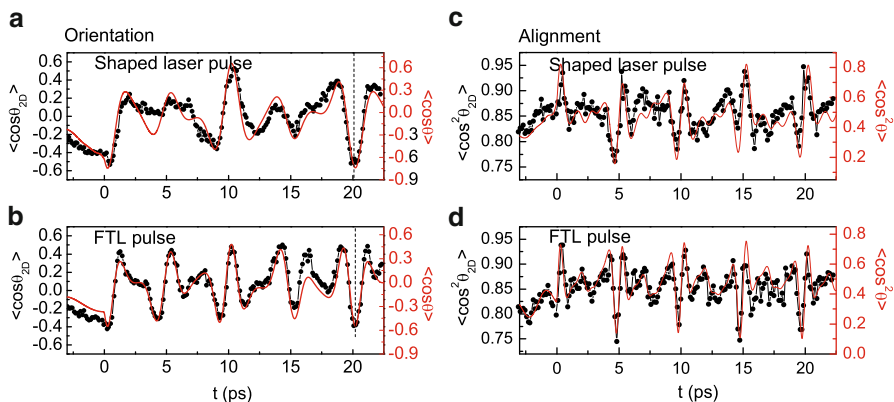


Fig. 3.14 Left panels: (a) Time-dependent degree of orientation $\langle \cos \theta_{2D} \rangle$ (dotted line) obtained by an integration of the recorded N^{2+} 2D momentum distributions and corresponding $\langle \cos \theta \rangle$ (gray line) obtained by integrating the time-dependent Schrödinger equation using the optimized pulse shape. Comparison with the FTL pulse is shown as well (b). Right panels: Corresponding degree of laser field-free alignment obtained using the same procedure for both the optimized laser pulse and the FTL pulse

(see Fig. 3.13c) with a separation of approximately 1 ps, which together act as a long adiabatic edge preceding the main kick that creates the rotational wavepacket. In this way, the pulses lead to an optimal rephasing of the rotational wave packets at the full revival period.

The alignment can also be reconstructed in this particular pump-probe polarization geometry, but it is more influenced by the probe laser pulse. This leads to an enhancement of the baseline of the measured $\langle \cos^2 \theta_{2D} \rangle$ and to a larger difference with the computed $\langle \cos^2 \theta \rangle$. Figure 3.14c, d shows $\langle \cos \theta_{2D} \rangle$ obtained experimentally using an FTL and the shape laser pulse that lead to the optimization of orientation. An optimization of the induced molecular alignment is also observed with an increase of $\langle \cos^2 \theta \rangle$ to a value 0.82.

3.9 Conclusions and Remarks

In this chapter, we have reported on experiments where we have combined hexapole state selection with short intense laser pulses and, by doing so, (1) measured the sign of the NO dipole moment, (2) demonstrated and controlled impulsive laser alignment and orientation of a fully state-selected NO molecular sample. In addition to these experiments, impulsive alignment and orientation for a set of molecules applicable for hexapole state-selection was investigated theoretically.

The ability to fully orient polar molecules allows one to observe physical and chemical processes in the molecular frame. For example, the photoelectron spectra under XUV excitation or high-harmonic generation in an oriented molecular sample

may be studied. The dependence of these two processes on the angle of the molecular axis with the laser polarization allows one to explore both molecular structure as well as to investigate fast molecular or electron dynamics.

Acknowledgements The authors gratefully acknowledge O. Ghafur, W. Siu, and S. Stolte, who have been involved in all the experiments presented in this chapter. The authors thank P. Johnsson for fruitful discussions. This work is part of the research program of the “Stichting voor Fundamenteel Onderzoek der Materie (FOM),” which is financially supported by the “Nederlandse organisatie voor Wetenschappelijk Onderzoek (NWO).”

References

1. M.F. Kling, M.J.J. Vrakking, *An. Rev. Phys. Chem.* **59**, 463 (2008)
2. F. Krausz, M. Ivanov, *Rev. Mod. Phys.* **81**, 163 (2009)
3. F. Schotte et al., *Science* **300**, 1944 (2003)
4. W. Ackermann et al., *Nat. Phot.* **1**, 336 (2007)
5. P. Emma, For the LCLS Commissioning Team. First Lasing of the LCLS X-ray FEL at 1.5 Angstrom (2009)
6. A. Landers et al., *Phys. Rev. Lett.* **87**, 013002 (2001)
7. J. Ullrich et al., *Rep. Prog. Phys.* **66**, 1463 (2003)
8. P. Johnsson, A. Rouzée et al., *J. Phys. B* **42**, 134017 (2009)
9. R. Velotta, N. Hay et al., *Phys. Rev. Lett.* **87**, 183901 (2001)
10. M. Meckel, Comtois et al., *Science*, **320**, 1478 (2008)
11. J. Itatani, J. Levesque et al., *Nature* **432**, 867 (2004)
12. R. Torres, N. Kajumba et al., *Phys. Rev. Lett.* **98**, 203007 (2007)
13. T. Kanai, S. Minemoto, H. Sakai., *Nature* **435**, 470 (2005)
14. C.Z. Bisgaard, O.J. Clarkin et al., *Science* **323**, 5920 (2009)
15. H. Stapelfeldt, T. Seideman, *Rev. Mod. Phys.* **75**, 543 (2003)
16. T. Seideman, E. Hamilton., *Adv. At. Mol. Phys.* **52**, 289 (2006)
17. B. Friedrich, D. Herschbach., *J. Phys. Chem.* **99**, 15686 (1995)
18. J.J. Larsen, H. Sakai et al., *J. Chem. Phys.* **111**, 7774 (1999)
19. H. Sakai, C.P. Safvan et al., *J. Chem. Phys.* **110**, 10235 (1999)
20. J.J. Larsen, K. Hald et al., *Phys. Rev. Lett.* **85**, 2470 (2000)
21. F. Rosca-Pruna, M.J.J. Vrakking, *Phys. Rev. Lett.* **87**, 153902 (2001)
22. E. Péronne, M.D. Poulsen et al., *Phys. Rev. Lett.* **91**, 043003 (2003)
23. M.J.J. Vrakking, S. Stolte, *Chem. Phys. Lett.* **271**, 209 (1997)
24. C. M. Dion, A. D. Bandrauk et al., *Chem. Phys. Lett.* **302**, 215 (1999)
25. M. Machholm, N.E. Henriksen., *Phys. Rev. Lett.* **87**, 193001 (2001)
26. C.M. Dion, A. Keller, O. Atabek., *Eur. Phys. J. D* **14**, 239 (2001)
27. B. Friedrich, D. Herschbach., *J. Chem. Phys.* **111**, 6157 (1999)
28. H. Sakai, S. Minemoto et al., *Phys. Rev. Lett.* **90**, 83001 (2003)
29. A. Goban, S. Minemoto, H. Sakai, *Phys. Rev. Lett.* **101**, 013001 (2008)
30. R. Baumfalk, N.H. Nahler, U. Buck, *J. Chem. Phys.* **114**, 4755 (2001)
31. B. Friedrich, N.H. Nahler, U. Buck, *J. Mod. Optic.* **50**, 2677 (2003)
32. O. Ghafur, A. Rouzée et al., *Nat. Phys.* **5**, 1225 (2009)
33. A. Rouzee, A. Gijsbertsen et al., *N. J. P.*, **11**, 105040 (2009)
34. S.R. Gandhi, R.B. Bernstein et al., *J. Chem. Phys.* **87**, 6457 (1987)
35. G. Herzberg, in *Spectra of Diatomic Molecules*. Molecular Spectra and Molecular Structure, vol 1 (Van Nostrand and Reinhold Company, New York, 1960)
36. R.N. Zare, *Angular Momentum: Understanding Spatial Aspects in Chemistry and Physics* (Wiley, New York, 1988)

37. J.M. Holas, *Modern Spectroscopy*, 3rd edn. (Krieger, Malabar, 1996)
38. C. Amiot, J. Molec. Spectrosc. **84**, 150 (1982)
39. M.J.L. de Lange, *Steric and State-to-State Dependence of Rotationally Inelastic Scattering of NO*, Thesis (Vrije Universiteit, Amsterdam, 2003)
40. C.A. Burrus, W. Gordy, Phys. Rev. **92**, 1437 (1953)
41. W.L. Meerts, A. Dymanus, J. Molec. Spectrosc. **44**, 320 (1972)
42. J.M.L.J. Reinartz, W.L. Meertz, A. Dymanus, Chem. Phys. Lett. **16**, 576 (1972)
43. B.J. Drouin, F.W. Maiwald, J. Molec. Spectrosc. **236**, 260 (2006)
44. H.G. Bennewitz, W. Paul, Ch. Schlier, Z. Phys. **141**, 6 (1955)
45. R.W. Anderson, J. Phys. Chem. **101**, 1664 (1997)
46. K.H. Kramer, R.B. Bernstein, J. Chem. Phys. **42**, 767 (1965)
47. S. Stolte, J. Reuss, H.L. Schwartz, Physica **57**, 254 (1972)
48. A. Gijsbertsen, W. Siu et al., Phys. Rev. Lett. **99**, 213003 (2007)
49. T. Seideman, Phys. Rev. Lett. **83**, 4971 (1999)
50. S.R. Gandhi, T.J. Curtiss et al., J. Chem. Phys. **132**, 6 (1986)
51. P.Th. van Duijnen, M. Swart, J. Phys. Chem. A **102**, 2399 (1998)
52. A.T.J.B. Eppink, D.H. Parker, Rev. Sci. Instrum. **68**, 3477 (1997)
53. A.M. Wiener, Rev. Sci. Instrum. **71**, 1929 (2000)
54. C.H. Townes, A.L. Schawlow, *Microwave Spectroscopy* (McGraw-Hill, New York, 1955)
55. M. Drabbels, A.M. Wodtke, Chem. Phys. Lett. **256**, 8 (1996)
56. A. Gijsbertsen, H. Linnartz et al., Phys. Scr. **72**, C1 (2005)
57. A. Gijsbertsen, M.J.L. de Lange et al., Chem. Phys. **301**, 293 (2004)
58. B. Friedrich, D.R. Herschbach, J. Phys. Chem. A **103**, 10280 (1999)
59. L. Cai, J. Marango, B. Friedrich, Phys. Rev. Lett. **86**, 775 (2001)
60. V. Renard, M. Renard et al., Phys. Rev. A **70**, 033420 (2004)
61. L. Holmegaard, J.H. Nielsen et al., Phys. Rev. Lett. **102**, 023001 (2009)
62. M. Leibscher, I.Sh. Averbukh, H. Rabitz, Phys. Rev. Lett. **90**, 213001 (2003)
63. C.Z. Bisgaard, S.S. Viftrup et al., Phys. Rev. Lett. **92**, 173004 (2004)
64. T. Suzuki, Y. Sugawara et al., Phys. Rev. Lett. **100**, 033603 (2008)
65. R.S. Judson, H. Rabitz, Phys. Rev. Lett. **68**, 1500 (1992)
66. A. Assion, T. Baumert et al., Science **282**, 919 (1998)
67. R.J. Levis, G.M. Menkir et al., Science **292**, 709 (2001)
68. E. Hertz, A. Rouzée et al., Phys. Rev. A **75**, 031403(R) (2007)
69. A. Rouzée, E. Hertz et al., J. Phys. B **41**, 074002 (2008)

Chapter 4

Quantum Interference in Ionization of Excited Molecules: X-Ray Emission Control and Dynamic Imaging

Mikhail Yu. Emelin, Mikhail Yu. Ryabikin, and Alexander M. Sergeev

We present the detailed theoretical study of high-order harmonic generation from excited molecules driven by ultraintense laser pulse. We concentrate on the quantum interference of the electron wave packets emanating from different nuclei of a stretched aligned molecule in the process of ionization. We demonstrate that, due to the quantum interference of the de Broglie waves, high harmonic spectra are extremely sensitive to the molecular configuration, which offers opportunities for coherent X-ray emission control and ultrafast dynamic imaging of molecules.

4.1 Introduction

High-order harmonic generation (HHG) in intense laser-gas interactions provides a very useful tool for the attosecond pulse production [19, 31]. The generation of isolated pulses shorter than 100 as in the HHG process with extremely short laser pulses has been reported recently [17]. First proof-of-principle experiments have demonstrated the feasibility of precise time-resolved measurements and control of atomic and molecular processes using attosecond pulses (see, e.g., reviews [24, 29]).

Future applications of HHG to ultrafast X-ray spectroscopy and quantum control will greatly benefit from the ability to spectrally shape the harmonic field [33]. Of great importance for time-resolved X-ray absorption spectroscopy [37] is the availability of the radiation with the photon energies reaching or even exceeding 1 keV, whose feasibility using the HHG source has been shown recently [36]. The key point on the way of putting such extremely short-pulse HHG-based soft X-ray sources into practice is to enhance the brilliance of HHG.

Molecular systems have attracted considerable recent interest as the media for HHG due to the fact that, because of their higher complexity as compared with the atomic ones, they provide additional means for the control of the HHG process

M.Y. Emelin (✉), M.Y. Ryabikin, and A.M. Sergeev

Institute of Applied Physics of RAS, 46 Ulyanov Street, 603950 Nizhny Novgorod, Russia
e-mail: emelin@ufp.appl.sci-nnov.ru, mike@ufp.appl.sci-nnov.ru, ams@ufp.appl.sci-nnov.ru

[2, 6, 16, 25, 39, 41], which are beyond the possibilities of their simple atomic counterparts. A variety of new opportunities are provided by using excited molecular transients to enhance the efficiency of high-harmonic and attosecond pulse generation and to control their spectral and temporal characteristics. These enhancement and control features, which are often based on various interference phenomena, can be implemented by producing molecular rotational [20, 21], vibrational [11, 32], and dissociative [30] wave packets.

In what follows, we present the results of our theoretical study of single attosecond pulse generation during ionization of molecules by an intense few-optical-cycle laser pulse. We discuss the possibilities for highly efficient production of light pulses as short as about 100 as in the process of Coulomb-barrier suppression ionization (BSI) of excited molecules. We demonstrate the possibility for continuously tunable X-ray production due to the quantum interference of the electron wave packets emanating from different nuclei of a stretched aligned molecule in the process of ionization. The possibilities for using high sensitivity of HHG spectra to molecular alignment and internuclear separation for molecular ultrafast dynamic imaging are also discussed.

4.2 Attosecond Pulse Production from Electronically Excited Atoms and Molecules

If a rapidly increasing electric field in a few-cycle driving pulse or at the leading edge of a high-power laser pulse exceeds the critical value, atoms are ionized during a short time within one optical cycle (see, e.g., [34]). The free-electron wave packet is then strongly localized. It has an oval shape that is retained in the course of laser-induced acceleration and quantum-mechanical diffusion [8]. Upon returning to a parent ion, this compact wave packet gives rise to a short burst of radiation due to the classical bremsstrahlung mechanism. Unlike in the commonly treated high-harmonic regime, in which only a part of the electron wave packet is set free each half-cycle of the driving field, in the case of quick bound-state depletion, high-energy photons are not produced via continuum-bound transitions (leading to the well-known cut-off law [5, 23]) but rather via continuum–continuum transitions. An efficiency of HHG in this regime appears to increase dramatically if the excited electronic states of atoms [8] or molecules [7] are used. To explain the nature of this enhancement, we note that the efficiency of HHG in the BSI regime is basically limited by the spreading of the free-electron wave packet. As the wave-packet spreading rate is governed by the extent of its initial delocalization, the efficiency of attosecond pulse generation can be enhanced by choosing an appropriate initial state [6, 8].

4.2.1 Roles of Different Types of Transitions in HHG

Polarization of volume element of the medium consisting of identical atoms or molecules is defined as a product $\mathbf{P}(t) = N\boldsymbol{\mu}(t)$, where N is the concentration of particles and $\boldsymbol{\mu}$ is the mean value of the dipole moment, which is defined quantum-mechanically as

$$\boldsymbol{\mu}(t) = \langle \psi(\mathbf{r}, t) | -\mathbf{r} | \psi(\mathbf{r}, t) \rangle, \quad (4.1)$$

where $\psi(\mathbf{r}, t)$ is the electron wave function.

Hereafter for simplicity we will consider one-electron systems (H atom and H_2^+ molecular ion). For the electron-field interaction, we will exploit the electric dipole approximation. The electron wave function satisfies the time-dependent Schrödinger equation (TDSE)

$$i \frac{\partial}{\partial t} \psi(\mathbf{r}, t) = \left(-\frac{1}{2} \nabla^2 + V(\mathbf{r}) + \mathbf{r} \mathbf{E} \cos(\omega_0 t) \right) \psi(\mathbf{r}, t), \quad (4.2)$$

where $V(\mathbf{r})$ is the nuclear attraction potential in the one-electron approximation and \mathbf{E} is the electric field vector. Atomic units are used throughout the chapter.

The wave function in (4.2) can be represented as the sum of parts corresponding to the bound (ψ_b) and free (ψ_f) electron: $\psi = c_b \psi_b + c_f \psi_f$. The squared modulus of the wave function in (4.1) is then written as

$$|\psi|^2 = |c_b|^2 |\psi_b|^2 + c_b^* c_f \psi_b^* \psi_f + c_b c_f^* \psi_b \psi_f^* + |c_f|^2 |\psi_f|^2. \quad (4.3)$$

The first term in the right-hand member of (4.3) corresponds to the bound-bound transitions, the second and third terms correspond to the transitions between bound and continuum states, and the last term describes the continuum-continuum transitions. The first term, which describes intraatomic transitions, is responsible for the fast-falling low-frequency part of the harmonic spectrum and is unimportant for attosecond pulse production. In the commonly treated case of weak ionization, the contribution of the continuum-continuum term to the dipole moment is relatively small and is not usually taken into account. Therefore, the theory of HHG [15, 27, 35] concentrates usually on the continuum-bound transitions. In this case, the high-energy photon emission is predominantly due to the electron recombination with the parent ion.

Until recently, much less studied from the viewpoint of attosecond pulse production was the regime of fast ionization at the leading edge of a high-power laser pulse [38]. As mentioned above, the high-energy photon emission in this case is due to the continuum-continuum transitions (the term $|c_f|^2 |\psi_f|^2$ in (4.3)).

4.2.2 *Highly Efficient HHG from Excited Atoms and Molecules Using Continuum–Continuum Transitions*

The mechanism of HHG described above is of potential use for a single attosecond pulse production [22]. However, in the usual case of atomic ionization from the ground state, HHG in the BSI regime is inefficient [13] because of the spreading of the free-electron wave packet. Nevertheless, as we have shown recently [8, 10], an efficiency of the frequency conversion in this regime can be enhanced dramatically if the properly prepared initial states are used. For example, for the case of a hydrogen atom prepared in an excited s -state, an efficiency of the visible to XUV frequency conversion can be enhanced by orders of magnitude for an optimally chosen value of the principal quantum number n of the initial state. Moreover, in this case, the generation of the radiation bursts of the duration of the order of ten has becomes possible [9]. This is due to the slowed spreading of the laser-driven electron wave packet because of higher degree of delocalization of the initial state wave function (we recall that, according to the uncertainty principle, a particle with poorly defined coordinate can be highly localized in the momentum space). In what follows, we will demonstrate that this mechanism can lead to a more efficient attosecond pulse production as compared with the recombination mechanism. Further, in Sect. 4.3 we will show that manipulations of vibrational and rotational degrees of freedom of a molecule can also lead to a greatly enhanced efficiency of attosecond pulse production using continuum–continuum transitions with the added bonus of a wide-range frequency tuning of the generated radiation.

4.2.3 *Single Attosecond Pulse Production: Bremsstrahlung vs. Recombination Radiation*

Below we present the results of numerical simulations aimed at the comparison, by the example of H atom, of two above-mentioned mechanisms of HHG – based on (a) continuum–bound and (b) continuum–continuum transitions – from the viewpoint of producing most short and intense single attosecond pulses.

Our study was based on the 3D numerical solution of TDSE for H atom driven by laser pulse. To numerically integrate the TDSE, we employed the split-operator fast Fourier transform technique [14]. The atomic nonlinear radiative response was calculated via the time-dependent dipole acceleration expectation value [4]

$$R(t) = \iiint |\Psi(x, y, z, t)|^2 \frac{\partial V}{\partial z} dx dy dz \quad (4.4)$$

using Ehrenfest's theorem. From this quantity, the harmonic emission spectra were obtained by Fourier transformation into the frequency domain.

For the first of the above-mentioned mechanisms, it is important that by the instant of electron-ion recollision a significant part of the electron wave packet remains in a bound state. That is why it is preferable that the state with the maximum binding energy, i.e., the ground state, is used as the initial one. For this mechanism, we will consider the case when the attosecond pulse is produced using a few-cycle laser pulse with spectral filtering of harmonics near the cutoff of the HHG spectrum [19]. The cosine-like few-cycle waveform is optimal for producing isolated attosecond pulse using this approach [1]. Reasoning from that, in the numerical simulations for this generation mechanism we considered the hydrogen atom in 1 s-state driven by the 5 fs laser pulse

$$E(t) = E_0 \exp \left[-\ln(4) \frac{(t - 8\pi/\omega_0)^2}{\tau^2} \right] \cos(\omega_0 t) \quad (4.5)$$

with $\omega_0 = 0.057$ corresponding to $\lambda = 800$ nm. The electric field peak amplitude E_0 was used as an objective parameter in the optimization procedure. The optimal intensity was found to lie in the range $(3-5) \times 10^{14} \text{ W cm}^{-2}$. In this intensity regime, the atomic ground-state population remains significant; therefore, the second and third terms of (4.3) are dominant for the response $R(t)$.

In the simulations for the second mechanism of HHG, we considered the hydrogen atom in the first (2 s) excited state. The driving pulse was taken as

$$E(t) = \exp \left[-5(\omega_0 t / 2\pi - 1)^4 \right] \sin \omega_0 t \quad (4.6)$$

with $\omega_0 = 0.114$ corresponding to $\lambda = 400$ nm. No optimization was made in this case. In the field given by (4.6), all bound states become depopulated almost entirely; therefore, the response $R(t)$ is dominated by the free-free part, i.e., the last term of (4.3).

The results of numerical simulations are illustrated in Fig. 4.1.

For the first (recombination) mechanism, we found that the peak intensity of the laser pulse $I_0 \approx 3.5 \times 10^{14} \text{ W cm}^{-2}$ is optimal for producing most intense attosecond pulse, while the laser pulse with the peak intensity $I_0 \approx 4.25 \times 10^{14} \text{ W cm}^{-2}$ produces the shortest (115 as) pulse (in this section; by attosecond pulse, we mean the part of the atomic polarization response corresponding to the excitation of an attosecond burst during the electron recollision with the parent ion). Figure 4.1a, b plot the time profile of the signal obtained for these intensities I_0 by filtering out all harmonics except for those belonging to the near-cutoff spectral range. The spectral window was chosen so that the net signal was a single pulse.

For the second (bremsstrahlung) mechanism, the typical attosecond burst has the characteristic shape similar to that shown in Fig. 4.1c. This figure plots the attosecond pulse produced in the field (4.6).

Note that in this case, because of full ionization during one half-cycle of the laser field and the quantum-mechanical spreading of the electron wave packet, the high-energy photon emission due to the electron-ion recollisions during the subsequent

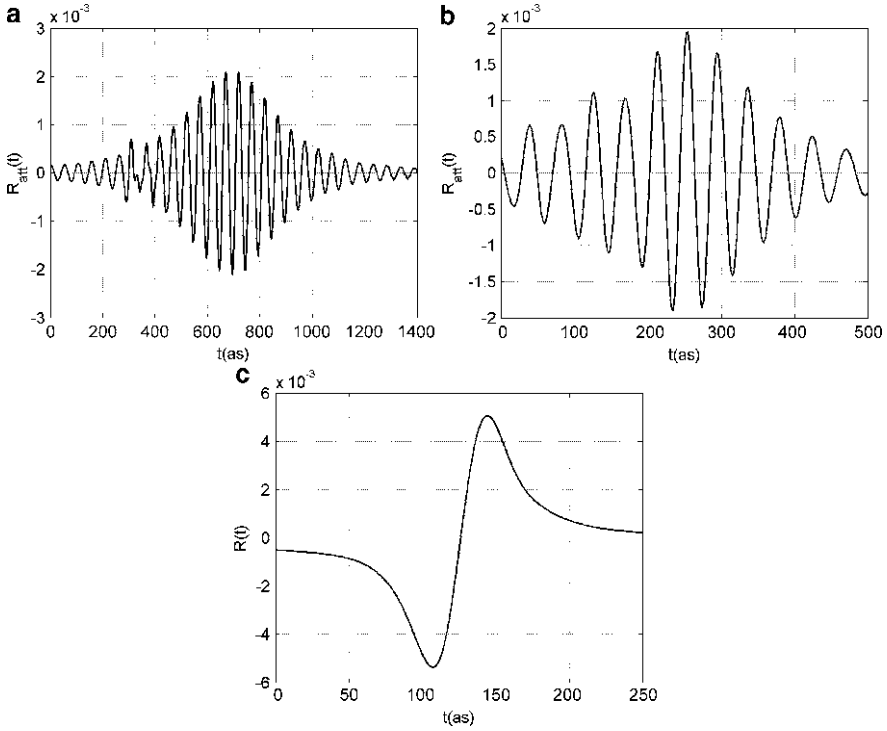


Fig. 4.1 Time profile of the attosecond burst in the polarization response of H atom for HHG using (a, b) continuum-bound and (c) continuum-continuum transitions. (a) and (b) correspond to the optimization of the intensity of laser pulse (4.5) for producing (a) most intense and (b) shortest attosecond burst

cycles of the field is negligible. The spectrum of the polarization response exhibits two pronounced parts related to two different stages of the electron wave-packet evolution. The atomic response corresponding to the electron detachment and quasi-free motion to the turning point constitutes the low-frequency part of the spectrum, while the recollision gives rise to the high-frequency continuum (see Fig. 1 in [8]). Therefore, in this case the spectral filtering does not affect the parameters of the generated attosecond burst. From the comparison of the bursts shown in Fig. 4.1 we conclude that in the case of the generation using continuum–continuum transitions, the generated burst is significantly shorter (for the case shown in Fig. 4.1c its duration is 63 as) and its peak intensity is about 6.5 times higher than for the pulse produced via the recombination mechanism. Note that while, as mentioned above, for the continuum–continuum mechanism we did not make any optimization of the laser parameters, it is clear that for higher laser intensity the attosecond burst will be shorter because of higher velocity of the recolliding electron. With laser intensity entering the subrelativistic regime, the efficiency of attosecond pulse production will be limited by the magnetic field effect (see [10]; see, in particular, the discussion on

the compensation of the magnetic field effect in aligned stretched molecules). We note also that, by optimization of the initial electronic state, the duration of the generated pulse can be significantly shortened [9].

4.3 Quantum Interference in Ionization of Stretched Molecules: Application to the X-Ray Emission Control

In molecules, because of the presence of several nuclei, there are several sources of the free-electron de Broglie waves arising from ionization. These waves interfere in the course of further propagation. For a diatomic molecule, this two-center interference, in a sense, is analogous to the Young's two-slit interference of the light beams. In the case of ionization of stretched aligned molecules in a rapidly increasing laser field, the resulting wave packet gains a regular structure with the characteristic spatial scale dependent on the geometry of the system. This interference modulation induces characteristic patterns in the emission spectra.

4.3.1 Numerical Results

In this section, we present the 3D numerical study of the time evolution of the electron wave packet released by an intense few-cycle pulse from an H_2^+ molecular ion. For H_2^+ ion, we considered the two-center potential $V(x, y, z)$ with Coulomb singularities. Calculations were made for different fixed values of the internuclear distance D and the molecular orientation angle θ with respect to the laser electric field, which was considered linearly polarized along the z axis.

The numerical results presented below were obtained for the H_2^+ ion driven by an optical pulse with electric field given as

$$E(t) = 2 \exp \left[-5 (\omega_0 t / 2\pi - 1)^4 \right] \sin \omega_0 t \quad (4.7)$$

with $\omega_0 = 0.114$; laser peak intensity is $I_0 \approx 1.4 \times 10^{17} \text{ W cm}^{-2}$. It should be mentioned that the particular waveform we chose is only an example and all the physics discussed here is not closely tied to this particular choice. The requirements we impose on the waveform are rather general: the pulse has to be intense enough to provide rapid ionization (during one half-cycle of the field) and, in addition, steeper rising edge of the pulse is desirable to more strongly accelerate the wave packet. State-of-the-art laser tools for attosecond technology are already capable of meeting these requirements [3, 18].

Figures 4.2 and 4.3 show the electron probability distribution at the beginning of the recollision with the parent molecular core after the detachment from the H_2^+ ion by laser pulse (4.7). The electron probability distribution within the box of (512×128) grid points ($dx = dz = 0.4$ atomic units) in the $y = 0$ plane is shown.

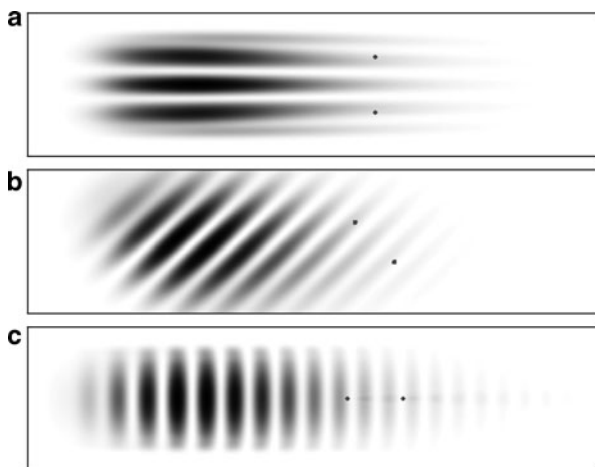


Fig. 4.2 Snapshots of the electron wave packet recolliding with the molecular core after the detachment from the H_2^+ ion by laser pulse (4.7) for different orientations of the molecular axis: (a) $\theta = 90^\circ$, (b) $\theta = 45^\circ$, and (c) $\theta = 0^\circ$. Internuclear distance is $D = 20$

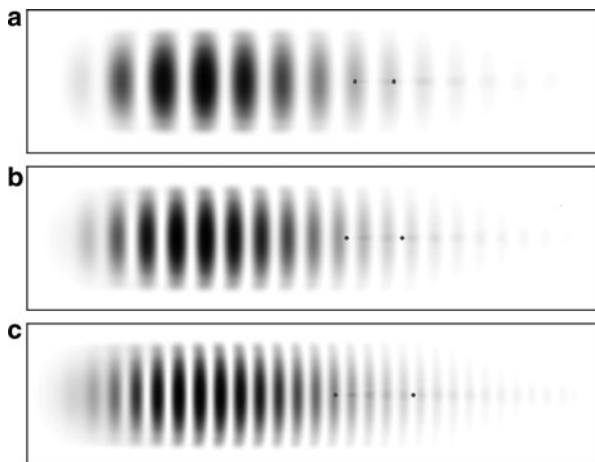


Fig. 4.3 Snapshots of the electron wave packet recolliding with the molecular core after the detachment from the H_2^+ ion by laser pulse (4.7) for different internuclear distances: (a) $D = 14$, (b) $D = 20$, and (c) $D = 28$. Molecular axis is parallel to the laser field ($\theta = 0^\circ$)

Figure 4.2 presents the results for three different orientations of the molecular axis: (a) $\theta = 90^\circ$, (b) $\theta = 45^\circ$, and (c) $\theta = 0^\circ$. The molecule is stretched to the internuclear distance $D = 20$.

Snapshots shown in Fig. 4.3 correspond to three different internuclear distances in H_2^+ aligned parallel to the electric field: (a) $D = 14$, (b) $D = 20$, and (c) $D = 28$.

The electron wave-packet evolution begins from the detachment of two separate wave packets emanating from the vicinity of two different nuclei. Later on, when these sub-packets start to overlap, the quantum interference fringes arise which are tilted at angle $90^\circ - \theta$ with respect to z axis. The fringe separation depends on the internuclear distance – see Fig. 4.3. More specifically, it is inversely proportional to D (see below).

In each case shown here, a spatial envelope of the whole wave packet is roughly the same, replicating in general terms the shape of the wave packet for the case of BSI of an atom (cf. Fig. 2 of [32]). However, the distinctive feature of the wave packet for the case of a stretched molecule is that the electron probability distribution is sliced, because of the two-center interference, and both the arrangement of slices and fineness of slicing are of great consequences to both the dipole response and the harmonic emission spectrum.

In accordance with (4.4), space modulation of a free-electron wave packet (Figs. 4.2 and 4.3) is mapped onto the temporal modulation of the induced dipole acceleration (Fig. 4.4). Figure 4.4 plots the time profile of the molecular dipole response within the time interval corresponding to the excitation of an attosecond burst during the electron recollision with the parent ion.

For perpendicular orientation of the molecular axis, the longitudinal profile of the wave packet is as smooth as in the atomic case. Hence, the dipole response is smooth as well (Fig. 4.4, black line), being also atomic-like (cf. Fig. 4a of [10]). As a result of this smoothness, the emission spectrum steadily decreases with the harmonic order (Fig. 4.5a, black solid line), in good agreement with the calculation for the hydrogen atom (cf. Fig. 5 of [13]).

For parallel orientation of the axis, the longitudinal spatial structure of the electron wave packet is quasi-periodical that is reflected in a regular temporal modulation of the dipole response (Fig. 4.4, dashed line). For a more strongly stretched molecule (Fig. 4.4b), this modulation is faster, because of a finer slicing of the

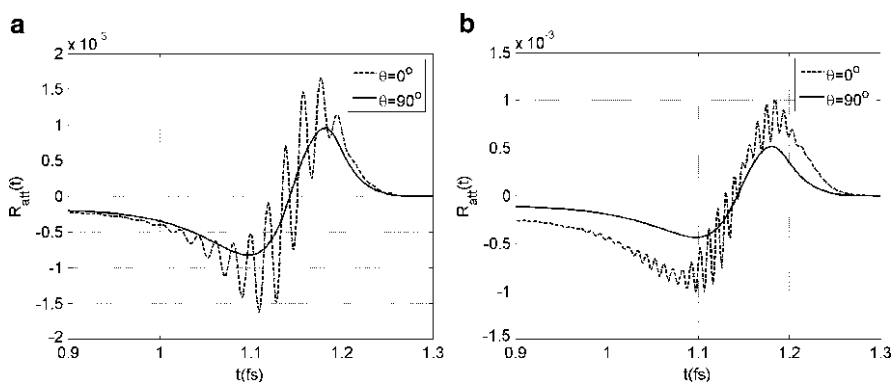


Fig. 4.4 Time profile of the attosecond burst in the polarization response of H_2^+ ion for the cases of parallel (*dashed line*) and perpendicular (*solid line*) orientation of the molecular axis. Internuclear distance is (a) $D = 14$ and (b) $D = 29$

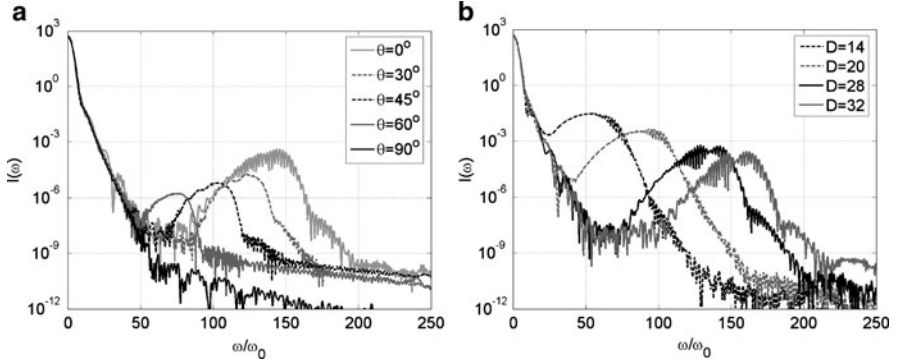


Fig. 4.5 Harmonic spectra of H_2^+ ion driven by laser pulse (4.7) for (a) various orientations of the molecular axis (internuclear distance $D = 29$) and (b) various internuclear distances (orientation angle $\theta = 0^\circ$)

wave packet. As a result of this quasi-periodical temporal modulation of the dipole response, a pronounced maximum appears in the emission spectrum. This maximum shifts toward shorter wavelengths with decreasing molecular orientation angle (Fig. 4.5a). A similar shift is observed with increasing nuclear separation (Fig. 4.5b).

It should be mentioned that the blue shifting of the maximum of the emission spectrum with decreasing angle θ (Fig. 4.5a) is accompanied by a significant increase of the harmonic yield. This can be explained by the fact that, for orientation angle closer to $\theta = 0^\circ$, the parts of the wave packet aimed directly at the nuclei are of higher density, see Fig. 4.2.

It is important to emphasize that, according to the data presented in Fig. 4.5, the mechanism discussed here provides an enhancement of the harmonic yield in the range around 3 nm (i.e., in the “water window”) by at least eight orders of magnitude as compared to the atomic case. It follows from Fig. 4.4 that this short-wavelength radiation is temporally confined to about 100 as.

4.3.2 Theory

The positions of the interference maxima in the harmonic spectra discussed above can be found analytically as follows.

If the internuclear distance is large enough as compared with the Bohr radius, the molecular ground state Ψ_0^M can be represented as a linear combination of atomic orbitals in its simplest form:

$$\Psi_0^M(\mathbf{r}, \mathbf{D}) = \frac{1}{\sqrt{2}} [\Psi_0^a(\mathbf{r} + \mathbf{D}/2) + \Psi_0^a(\mathbf{r} - \mathbf{D}/2)], \quad (4.8)$$

where $\Psi_0^a(\mathbf{r})$ is the hydrogen ground state and the overlap integral between the two atomic orbitals is neglected; $\mathbf{D} = \mathbf{R}_1 - \mathbf{R}_2$ (\mathbf{R}_i is the radius-vector of the i th nucleus). Further, we adopt the simplifying assumption that the electron wave packet remains undistorted until the instant of barrier-suppression ionization, after which time the electron becomes completely free from the atomic potential [8, 10, 13]. Under this assumption, the time evolution of the atomic electron wave packet can be described as a free evolution of a radially symmetric function (in the center-of-mass system of the wave packet) as follows [10, 40]:

$$\Psi^a(r, t) = -\frac{2i}{r\sqrt{2\pi it}} \exp\left(\frac{ir^2}{2t}\right) \int_0^\infty x \Psi^a(x, 0) \exp\left(\frac{ix^2}{2t}\right) \sin\left(\frac{rx}{t}\right) dx. \quad (4.9)$$

Taking into account strong localization of the atomic ground state, for large t (much larger than atomic unit) one can use the stationary phase approximation by setting $\exp(ix^2/2t) \approx 1$ in the integrand of (4.9). Equation (4.9) can be then represented as

$$\Psi^a(r, t) = i^{5/2} \exp\left(\frac{ir^2}{2t}\right) |\Psi^a(r, t)| \quad (4.10)$$

By analogy with (4.8), the molecular free-electron wave function can be written as

$$\Psi^M(\mathbf{r}, t) = \frac{i^{5/2}}{\sqrt{2}} [\exp(ir_1^2/2t) |\Psi^a(r_1, t)| + \exp(ir_2^2/2t) |\Psi^a(r_2, t)|], \quad (4.11)$$

where \mathbf{r}_i and \mathbf{r} are the radius-vectors of the electron relative to the center of mass of i th sub-packet and of the whole wave packet, respectively. Since at large t the two sub-packets get overlapped, we have

$$|\Psi^a(r_1, t)| \approx |\Psi^a(r_2, t)| \approx |\Psi^a(r, t)|. \quad (4.12)$$

From (4.11) and (4.12), we obtain

$$\begin{aligned} \left| \Psi^M(\mathbf{r}, t) \right|^2 &= \frac{|\Psi^a(r, t)|^2}{2} \left| \exp(ir_1^2/2t) + \exp(ir_2^2/2t) \right|^2 \\ &= \frac{|\Psi^a(\mathbf{r}, t)|^2}{2} [1 + \cos(\mathbf{D}\mathbf{r}/t)]. \end{aligned} \quad (4.13)$$

The molecular free-electron wave packet is thus spatially modulated with the modulation period

$$\Lambda = 2\pi \tau/D, \quad (4.14)$$

where τ is the electron excursion time. This spatial modulation results in the temporal modulation of the attosecond burst (see Fig. 4.4) at a frequency

$$\Omega = 2\pi V \cos \theta / \Lambda = VD \cos \theta / \tau, \quad (4.15)$$

where V is the electron velocity upon recollision. As a result, the interference maximum in the harmonic spectrum appears whose position is determined by (4.15). Therefore, changing θ or D values by producing, for example, molecular rotational, vibrational, or dissociative wave packet enables one to control the spectral content of the attosecond pulse. Since V and τ values are field-dependent, the emission spectrum can also be controlled by changing the laser pulse shape.

The examples given above show high-efficiency production of photons with the energy up to 0.5 keV. Moreover, (4.15) gives an idea of how to extend the harmonic emission well into the keV regime. For $\lambda = 400$ nm, taking into account that $\tau < T \approx 55 (= 1.333$ fs, see Fig. 4.4) and $V < c = 137$ we obtain that for a molecule stretched to $D = 30$ the photons with the energy of about 3 keV can be generated.

Figure 4.6 demonstrates wide-range tunability of attosecond radiation via manipulations of rotational and vibrational degrees of freedom of a molecule. This figure plots the harmonic intensities at the (ω, θ) and (ω, D) planes for the case of ionization of H_2^+ by laser pulse (4.7).

From the comparison of (4.15) with Fig. 4.6, we conclude that the cosine dependence on θ and the linear dependence on D of the central frequency of the interference maximum in the harmonic spectrum, which follow from our analytical approach, agree perfectly with the numerical results shown in Fig. 4.6a, b, respectively.

All means mentioned above can be used not only for the tuning of the carrier frequency of the attosecond pulse but also for a more general spectral shaping of the harmonic field [12].

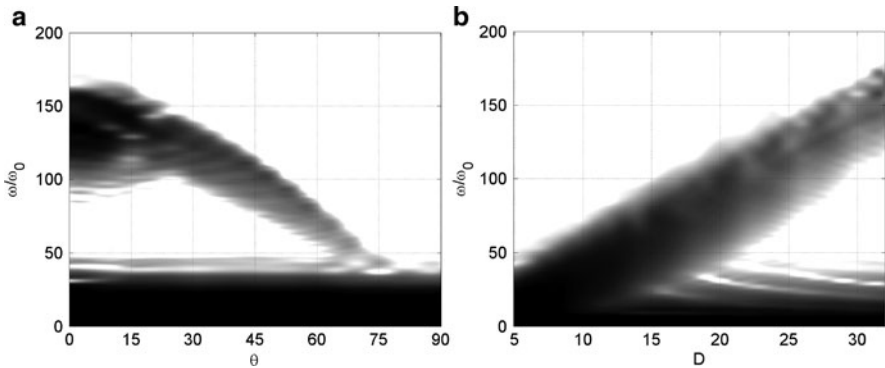


Fig. 4.6 Harmonic intensities for a stretched H_2^+ ion plotted (a) at the (ω, θ) plane (internuclear distance $D = 29$) and (b) at the (ω, D) plane (orientation angle $\theta = 0^\circ$)

4.4 Quantum Interference in Ionization of Stretched Molecules: Application to the Molecular Dynamic Imaging

It should be emphasized that strong bond-length and orientation dependence of the emission spectrum of a stretched molecule due to the quantum interference effect discussed above can be used in reverse, i.e. for probing molecular vibration-rotational dynamics. Particularly, Fig. 4.5b suggests that using an intense ultrashort laser pulse as a probe, one can monitor the early (“particle-like” – see, e.g., [32]) stage of the molecular wave-packet evolution during vibration or dissociation by analyzing the pump-probe time-delay dependence of the high harmonic spectra. This possibility can provide a new item for the toolbox of the molecular dynamic imaging [26, 28]. Because of the 100 as duration of the underlying electron recollision process, the changes of the molecular configuration during the probing are negligible. Therefore, the resulting harmonic signal, in fact, bears the imprint of the instantaneous molecular structure.

4.5 Conclusions

Our study shows that quantum interference in ionization of excited molecules by ultraintense laser field can be exploited efficiently for both the X-ray spectra control and molecular dynamic imaging. In the regime discussed, the shape of the recolliding electron wave packet is extremely sensitive to molecular alignment and internuclear separation. It results in increasing by several orders of magnitude the efficiency of laser pulse energy conversion to high-order harmonics with the photon energies reaching 1 keV and tuning their spectra over a wide range within the soft X-ray band. High sensitivity of HHG spectra to the molecular configuration offers the opportunities for ultrafast dynamic imaging of molecules.

Acknowledgements We acknowledge financial support from the Presidium of RAS, RFBR (grant № 09–02–97078-r-povolzh’ye-a) and the Russian President’s grant No. 1931.2008.2. M.Y.E. also acknowledges support from the Dynasty Foundation.

References

1. A. Baltuška, Th. Udem, M. Uiberacker, M. Hentschel, E. Goulielmakis, Ch. Gohle, R. Holzwarth, V.S. Yakovlev, A. Scrinzi, T.W. Hänsch, F. Krausz, *Nature* **421**, 611–615 (2003)
2. A.D. Bandrauk, S. Chelkowski, H. Lu, *J. Phys. B At. Mol. Opt. Phys.* **42**, 075602 (2009)
3. S. Bohman, A. Suda, M. Kaku, M. Nurhuda, T. Kanai, S. Yamaguchi, K. Midorikawa, *Opt. Express* **16**, 10684–10689 (2008)
4. K. Burnett, V.C. Reed, J. Cooper, P.L. Knight, *Phys. Rev. A* **45**, 3347–3345 (1992)
5. P.B. Corkum, *Phys. Rev. Lett.* **71**, 1994–1997 (1993)
6. M.Y. Emelin, M.Y. Ryabikin, A.M. Sergeev, M.D. Chernobrovtsseva, T. Pfeifer, D. Walter, G. Gerber, *JETP Lett.* **77**, 212–216 (2003)

7. M.Y. Emelin, M.Y. Ryabikin, A.M. Sergeev, *Radiophys. Quant. Electron.* **47**, 818–831 (2004)
8. M.Y. Emelin, M.Y. Ryabikin, A.M. Sergeev, M.D. Chernobrovtsseva, T. Pfeifer, D. Walter, G. Gerber, *Europhys. Lett.* **69**, 913–919 (2005)
9. M.Y. Emelin, M.Y. Ryabikin, A.M. Sergeev, *Laser Phys.* **15**, 903–908 (2005)
10. M.Y. Emelin, M.Y. Ryabikin, A.M. Sergeev, *JETP* **106**, 203–217 (2008)
11. M.Y. Emelin, M.Y. Ryabikin, A.M. Sergeev, *New J. Phys.* **10**, 025026 (2008)
12. M.Y. Emelin, M.Y. Ryabikin, A.M. Sergeev, *Opt. Express* **18**, 2269–2278 (2010)
13. M.V. Fedorov, J. Peatross, *Phys. Rev. A* **52**, 504–513 (1995)
14. M.D. Feit, J.A. Fleck Jr., A. Steiger, *J. Comp. Phys.* **47**, 412–433 (1982)
15. M.V. Frolov, N.L. Manakov, T.S. Sarantseva, A.F. Starace, *J. Phys. B: At. Mol. Opt. Phys.* **42**, 035601 (2009)
16. I.A. Gonoskov, M.Y. Ryabikin, A.M. Sergeev, *J. Phys. B: At. Mol. Opt. Phys.* **39**, S445–S455 (2006)
17. E. Goulielmakis, M. Schultze, M. Hofstetter, V.S. Yakovlev, J. Gagnon, M. Uiberacker, A.L. Aquila, E.M. Gullikson, D.T. Attwood, R. Kienberger, F. Krausz, U. Kleineberg, *Science* **320**, 1614–1617 (2008)
18. M.V. Guandalini, P. Eckle, M. Anscombe, P. Schlup, J. Biegert, U. Keller, *J. Phys. B At. Mol. Opt. Phys.* **39**, S257–S264 (2006)
19. M. Hentschel, R. Kienberger, Ch. Spielmann, G.A. Reider, N. Milosevic, T. Brabec, P. Corkum, U. Heinzmann, M. Drescher, F. Krausz, *Nature* **414**, 509–513 (2001)
20. J. Itatani, D. Zeidler, J. Levesque, M. Spanner, D.M. Villeneuve, P.B. Corkum, *Phys. Rev. Lett.* **94**, 123902 (2005)
21. M. Kaku, K. Masuda, K. Miyazaki, *Jpn. J. Appl. Phys.* **43**, L591–L593 (2004)
22. A.V. Kim, M.Y. Ryabikin, A.M. Sergeev, *Phys. Usp.* **38**, 54–61 (1999)
23. J.L. Krause, K.J. Schafer, K.C. Kulander, *Phys. Rev. Lett.* **68**, 3535–3538 (1992)
24. F. Krausz, M. Ivanov, *Rev. Mod. Phys.* **81**, 163–234 (2009)
25. M. Lein, N. Hay, R. Velotta, J.P. Marangos, P.L. Knight, *Phys. Rev. Lett.* **88**, 183903 (2002)
26. M. Lein, *J. Phys. B: At. Mol. Opt. Phys.* **40**, R135–R173 (2007)
27. M. Lewenstein, Ph. Balcou, M.Y. Ivanov, A. L’Huillier, P.B. Corkum, *Phys. Rev. A* **49**, 2117–2132 (1994)
28. J.P. Marangos, S. Baker, N. Kajumba, J.S. Robinson, J.W.G. Tisch, R. Torres, *Phys. Chem. Chem. Phys.* **10**, 35–48 (2008)
29. M. Nisoli, G. Sansone, *Prog. Quant. Electron.* **33**, 17–59 (2009)
30. R. Numico, P. Moreno, L. Plaja, L. Roso, *J. Phys. B At. Mol. Opt. Phys.* **31**, 4163–4172 (1998)
31. P.M. Paul, E.S. Toma, P. Breger, G. Mullot, F. Augé, Ph. Balcou, H.G. Muller, P. Agostini, *Science* **292**, 1689–1692 (2001)
32. T. Pfeifer, D. Walter, G. Gerber, M.Y. Emelin, M.Y. Ryabikin, M.D. Chernobrovtsseva, A.M. Sergeev, *Phys. Rev. A* **70**, 013805 (2004)
33. T. Pfeifer, C. Spielmann, G. Gerber, *Rep. Prog. Phys.* **69**, 443–505 (2006)
34. M. Protopapas, C.H. Keitel, P.L. Knight, *Rep. Prog. Phys.* **60**, 389–486 (1997)
35. V.T. Platonenko, *Quant. Electron.* **31**, 55–60 (2001)
36. E. Seres, J. Seres, F. Krausz, C. Spielmann, *Phys. Rev. Lett.* **92**, 163002 (2004)
37. E. Seres, J. Seres, C. Spielmann, *Appl. Phys. A* **96**, 43–50 (2009)
38. A.M. Sergeev, A.V. Kim, E.V. Vanin, D. Farina, M. Lontano, M.C. Downer, *Proc. SPIE* **2770**, 36–45 (1996)
39. R. Velotta, N. Hay, M.B. Mason, M. Castillejo, J.P. Marangos, *Phys. Rev. Lett.* **87**, 183901 (2001)
40. V.S. Vladimirov, *Equations of Mathematical Physics*, 2nd English edn. (MIR Publishers, Moscow 1983)
41. X. Zhou, R. Lock, N. Wagner, W. Li, H.C. Kapteyn, M.M. Murnane, *Phys. Rev. Lett.* **102**, 073902 (2009)

Chapter 5

Single Isolated Attosecond Pulses Generation with Double Optical Gating

Ximao Feng, Steve Gilbertson, Hiroki Mashiko, Sabih Khan, He Wang, Michael Chini, Yi Wu, and Zenghu Chang

Abstract Isolated attosecond pulses are powerful tools for exploring electron dynamics in matter. We proposed and demonstrated a technique called generalized double optical gating for generating isolated attosecond pulses. The double optical gating scheme, relaxing the stringent requirement on laser pulse duration from ≤ 5 fs to pulse duration close to the amplifier output, would make attophysics more accessible to many laboratories that are capable of producing such multicycle laser pulses. The isolated attosecond pulses were measured by reconstructing the streaked photoelectron spectrogram. The same setup was used to trace the spatial profile of a femtosecond Bessel beam, which serves as a demonstration of attosecond pulse applications. We also review a technique for stabilizing the carrier-envelope phase of grating-based laser amplifiers, which controls the grating separation. The phase-stabilized lasers are required for generating isolated attosecond pulses with double optical gating as well as other schemes.

5.1 Introduction

Ever since single isolated attosecond (as) pulses first became available in 2001 [1], they have been used in a variety of applications such as studying the ultrafast electron dynamics in gaseous atoms [2–4], in molecules [5], and in condensed-matter systems [6]. Direct measurement and control of electron motion using such pulses is key to furthering our understanding of matter on as-yet unprecedented time scales. However, until now there are still only a few laboratories that can produce such pulses. The stringent requirement of few-cycle near infrared (NIR) pulses on the input laser is one of the main hurdles in preventing the quick spread of the attosecond physics.

X. Feng, S. Gilbertson, H. Mashiko, S. Khan, H. Wang, M. Chini, Y. Wu, and Z. Chang (✉)
J. R. Macdonald Laboratory, Department of Physics, Kansas State University,
Manhattan KS 66506, USA
e-mail: xFeng@ksu.edu, smg@phys.ksu.edu, mashiko@phys.ksu.edu, sabih@phys.ksu.edu,
HeWang@lbl.gov, MChini@phys.ksu.edu, WuYi@phys.ksu.edu, zeChang@mail.ucf.edu

There are techniques that have been successful at attosecond pulse generation. The shortest isolated pulses of 80 as were produced with amplitude gating by <4 fs (femtosecond) laser pulses [7]. Isolated pulses were also produced with polarization gating (PG) [8, 9], having pulse durations of 130 as generated from 5 fs laser pulses [10]. Several ideas have been proposed to generate single isolated attosecond pulses with long pulse lasers because they are easier to access. For example, it has been proposed to mix a weak second harmonic wave with a linearly polarized fundamental field as in [11], so that a continuum spectrum in the cutoff can be generated with multiple-cycle two-color field [12]. It was predicted that a relatively long attosecond pulse 300–500 as duration would be generated because the discrete harmonic peaks in the plateau region of the spectrum cannot be used. In some other gating schemes, the continuum has been observed experimentally whereas the pulse duration is yet to be measured [13–16]. The requirement of carrier-envelope phase (CEP) stabilized driving lasers with pulse durations of 5 fs or less is one of the main obstacles which has prevented the rapid spreading of attosecond optical technologies. Here, we introduce our technique, called double optical gating (DOG), with which we can generate single attosecond pulses with multiple cycle laser pulses. Therefore, the threshold for accessing the single attosecond pulse world is lower. We expect our technique would allow more and more laboratories to be able to generate and use single attosecond pulse.

In this review chapter, we first present the fundamental principle of DOG in Sect. 5.2. Results about carrier-envelope phase stabilization of the beams from amplifier and hollow-core fiber are reviewed in Sect. 5.3. Then we introduce our experimental setup for generating, optimizing, characterizing, and utilizing these extreme ultraviolet (XUV) pulses generated with DOG (Sect. 5.4). In Sect. 5.5, properties of the single attosecond pulses generated with DOG and a generalized version of DOD (GDOG) are shown, which include the photon flux, the pulse duration, and pre-/post-pulse magnitude. Also, we show our results about how the input pulse duration and different gating methods affect the generated XUV pulse properties. Then we discuss our retrieval algorithm for characterizing the attosecond pulses (Sect. 5.6). In Sect. 5.7, we use the single attosecond pulses to measure the spatial profile of the Bessel beam. Finally, Sect. 5.8 summarizes this chapter.

5.2 Principle of Double Optical Gating

A train of attosecond pulses can be generated when atoms are driven by laser pulses containing multiple optical cycles [17]. The separation between adjacent pulses is half an optical cycle, which is 1.3 fs for Ti:Sapphire lasers, as shown in Fig. 5.1a. When a second harmonic (SH) field is superimposed on the fundamental laser field, the electric field symmetry is broken. As a result, the spacing between the adjacent attosecond bursts is a full fundamental cycle, as shown in Fig. 5.1b [11]. DOG combines two different gating methods: two-color gating and polarization gating.

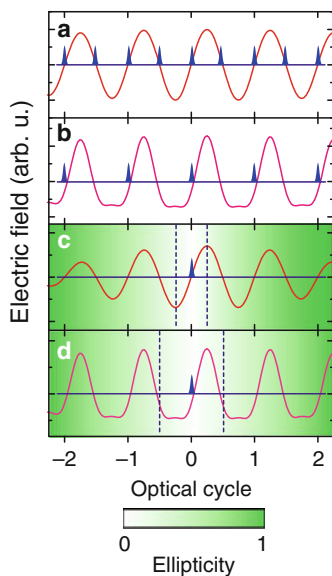


Fig. 5.1 (a) The attosecond pulse train generated with a laser field containing many cycles. The attosecond pulses are separated by one half of a laser cycle. (b) When a second harmonic field is added to the fundamental wave, the pulse spacing is a full fundamental wave cycle. (c) In the polarization gating, an optical gate (within the two vertical *dashed lines*) of one half of an optical cycle is applied to extract one attosecond pulse. (d) In the double optical gating, the gate width is twice of that for polarization gating

5.2.1 Two-Color Gating

In two-color gating, a weak second harmonic field ($\sim 20\%$ of the fundamental amplitude), with polarization direction the same as the driving field, is superimposed on the fundamental laser field to break the symmetry of the driving field. The relative phase between the two fields is chosen such that the ionization rate difference between the two adjacent field maxima differs by more than two orders of magnitude. Electrons are essentially only ionized within only one half of an optical cycle of the field. As a result, when the combined laser pulse is focused on a gas target, the spacing between the adjacent attosecond pulses is a full optical cycle, i.e., 2.6 fs for Ti:Sapphire lasers, as shown in Fig. 5.1b. The two-color gating used here is closely related to the technique demonstrated in [11, 13].

5.2.2 Polarization Gating

Polarization gating takes advantage of the feature that high-harmonic generation highly depends on the ellipticity of the electric field [18]. The laser pulse used for polarization gating is usually a combination of two counter-rotating, circularly

polarized laser pulses with a proper delay [9, 19]. When the width of the linear portion equals or is less than the spacing between adjacent attosecond pulses in the pulse train, only one attosecond pulse can be generated, as shown in Fig. 5.1c. Experimentally, the pump pulse is formed by splitting a linearly polarized laser pulse into two perpendicularly polarized fields with a birefringent plate [9, 20]. A delay between the two pulses is introduced as the difference in the group velocity along and perpendicular to the optic axis of the plate. The pulses are then converted to circularly polarized pulses with a quarter-wave plate and result in a combined pulse with a time-dependent ellipticity. The final pulse can be decomposed to two perpendicular components called the driving and gating fields, which can be expressed as [21]:

$$E_{\text{driving}}(t) = E_0[e^{-2\ln(2)(\frac{t-T_d/2}{\tau_p})^2} + e^{-2\ln(2)(\frac{t+T_d/2}{\tau_p})^2}] \cos(\omega_0 t + \phi_{\text{CE}}), \quad (5.1)$$

$$E_{\text{gating}}(t) = E_0[e^{-2\ln(2)(\frac{t-T_d/2}{\tau_p})^2} - e^{-2\ln(2)(\frac{t+T_d/2}{\tau_p})^2}] \sin(\omega_0 t + \phi_{\text{CE}}), \quad (5.2)$$

where E_0 is the peak field amplitude, T_d is the delay, ω_0 is the carrier frequency, τ_p is the laser duration, and ϕ_{CE} is the carrier-envelope phase.

These two components create a time-dependent ellipticity which can be expressed as:

$$\xi(t) = \frac{|1 - e^{-4\ln(2)(T_d/\tau_p^2)t}|}{1 + e^{-4\ln(2)(T_d/\tau_p^2)t}}. \quad (5.3)$$

The gating can be applied with ellipticity modulated pulses. The ellipticity of the pulse changes from circular to linear and finally back to circular. The center portion of the pump pulse where the ellipticity is less than a certain value (e.g., $\xi = 0.2$) is defined as the polarization gate [21, 22]. With $\xi_{th} = 0.2$, the intensity of attosecond pulses generated outside of the gate is expected to be at least ten times lower than that of the isolated main pulse, and the polarization gate width can be estimated by the expression [21]

$$\delta_t = 0.3\tau_p^2/T_d. \quad (5.4)$$

To generate single isolated attosecond pulses, the gate width should be narrower than the spacing between two adjacent attosecond pulses. As an example, in Fig. 5.1c, the two vertical dashed lines show a gate width of about half of the optical cycle.

However, if the laser pulse is too long, the ground state of the atoms will be depleted by the leading edge, leaving no atoms to emit harmonics within the polarization gate. The ionization probability of argon and neon atoms as a function of the pulse duration for PG, calculated with the Ammosov–Delone–Krainov (ADK) model [23], are shown in Fig. 5.2. In all the calculations, the laser intensity at the gate is set to be $2.8 \times 10^{14} \text{ W cm}^{-2}$. From the figure, one can see that for argon and neon gases in the PG configuration, the upper limit of the usable input pulse durations are around 8 and 10 fs, respectively.

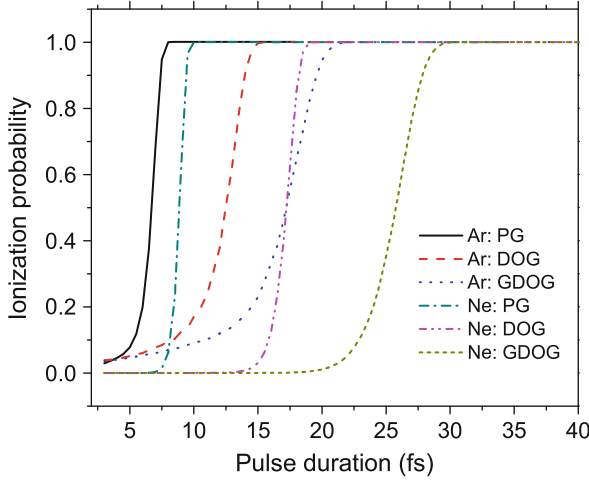


Fig. 5.2 Comparison of ionization probability of argon and neon at the center of the polarization gate as a function of pulse duration for three different gating methods: PG, DOG, GDOG

5.2.3 DOG

To generate single attosecond pulses with longer fundamental pulses, we proposed the double optical gating (DOG) scheme, combining two-color gating and polarization gating. When an SH field is added to the laser field for polarization gating, the polarization gate width can be doubled since the attosecond pulse separation becomes one optical cycle due to the effect of two-color gating, as illustrated in Fig. 5.1d. The wider gate width allows the use of longer circularly polarized lasers without decreasing the ground state population of the target by the leading edge of the laser [15].

In DOG, the gating field has the same expression as that for PG. However, due to the added second harmonic field, the driving field should be written as [24]:

$$\begin{aligned}
 E_{\text{driving}}(t) = E_0 \left\{ \left(e^{-2\ln(2)(\frac{t-T_d/2}{\tau_p})^2} + e^{-2\ln(2)(\frac{t+T_d/2}{\tau_p})^2} \right) \cos(\omega_0 t + \phi_{\text{CE}}) \right. \\
 \left. + a_{\omega,2\omega} e^{-2\ln(2)(\frac{T_d/2}{\tau_p})^2} e^{-2\ln(2)(\frac{t}{\tau_{2\omega}})^2} \cos(2\omega_0 t + 2\phi_{\text{CE}} + \phi_{\omega,2\omega}) \right\}, \quad (5.5)
 \end{aligned}$$

where $a_{\omega,2\omega}$ is the ratio between the SH and the fundamental, $\tau_{2\omega}$ stands for the pulse duration of SH, and $\phi_{\omega,2\omega}$ represents the phase difference between the SH and the fundamental.

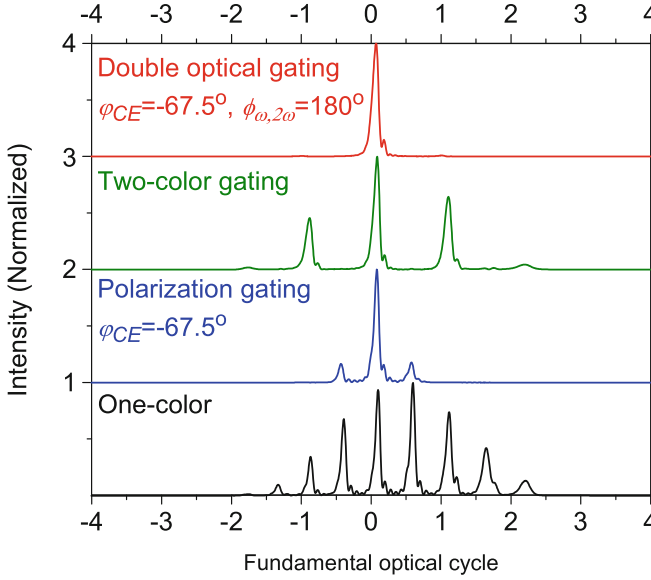


Fig. 5.3 Attosecond pulses generated by four different types of laser fields. From *bottom* panel to the *top*: one color, conventional polarization gating, two color, and double optical gating

The numerical simulations of attosecond pulses spectra generated with argon gas with different gating schemes are shown in Fig. 5.3 for comparison [24]. When high harmonics are generated from argon gas with a 10 fs linearly polarized single-color laser, a train of eight attosecond pulses are generated, as shown in the bottom panel of Fig. 5.3a. The number of pulses is reduced to three with the conventional polarization gating where the delay, T_d is assumed to be 12.5 fs. The separation between the pulses is the same as with linear polarized pump pulses, i.e., one half of the optical cycle. When a second harmonic (SH) field is added to the linearly polarized one-color electric field, the spacing between attosecond pulses in the train is a full fundamental wave cycle. In the calculation, the amplitude ratio, $a_{\omega,2\omega}$, of the SH field is set to be 15% of the fundamental wave, and the duration of the linearly polarized second harmonic field, $\tau_{2\omega}$, is set to be 25 fs. In the double optical gating case, the SH field is added to the driving field of the polarization gating pulse, which turns off the two satellite pulses left by the polarization gating. As a result, only a single attosecond pulse is generated from double optical gating, as shown in the top panel of Fig. 5.3, corresponding to a supercontinuum in the spectrum domain.

5.2.4 GDOG

To extend the duration of the input fundamental pulse close to the duration of the amplifier output, we need to reduce the ground state population depletion from the

leading edge of the laser pulse even further. A generalized version of the double optical gating can serve this purpose. Compared with DOG, the GDOG has a polarization gating field with two counter-rotating *elliptically* polarized pulses with an ellipticity, ε [14, 25] and a delay T_d , which is a generalization of double optical gating. In this case, the driving field of GDOG can be expressed as:

$$E_{\text{driving}}(t) = E_0 \left\{ \varepsilon \left(e^{-2\ln(2)(\frac{t-T_d/2}{\tau_p})^2} + e^{-2\ln(2)(\frac{t+T_d/2}{\tau_p})^2} \right) \cos(\omega_0 t + \phi_{\text{CE}}) + a_{\omega,2\omega} e^{-2\ln(2)(\frac{T_d/2}{\tau_p})^2} e^{-2\ln(2)(\frac{t}{\tau_{2\omega}})^2} \cos(2\omega_0 t + 2\phi_{\text{CE}} + \phi_{\omega,2\omega}) \right\}, \quad (5.6)$$

and the polarization gate width, δ_t , can be expressed as [21]

$$\delta_t = 0.3\varepsilon\tau_p^2/T_d. \quad (5.7)$$

By comparing (5.5) and (5.6), one can see that DOG is just a special case ($\varepsilon = 1$) of GDOG. In both DOG and GDOG cases, for the generation of single isolated pulses, the gate width, δ_t , should be equal to or less than one optical cycle, which is ~ 2.6 fs for Ti:Sapphire lasers. Therefore, to set the gate width to be one optical cycle for a given laser pulse duration, the ellipticity and the delay must have the following relation: $\frac{\varepsilon}{T_d} \approx \frac{1}{0.3} \frac{T_0}{\tau_p} = \frac{8.1}{\tau_p^2}$. As an example, for 20 fs lasers, one optical cycle can be set with two different combinations, i.e., $\varepsilon = 1$ (DOG) and $T_d \simeq 48$ fs or $\varepsilon = 0.5$ (GDOG) and $T_d \simeq 24$ fs as shown in Fig. 5.4a, b. The driving field amplitude inside the gate was kept the same for the two cases.

The ionization probability of argon and neon atoms as a function of the pulse duration for DOG and GDOG are also shown in Fig. 5.2. In the GDOG case, because the field strength before the gate is lower, 20 fs laser input can still generate

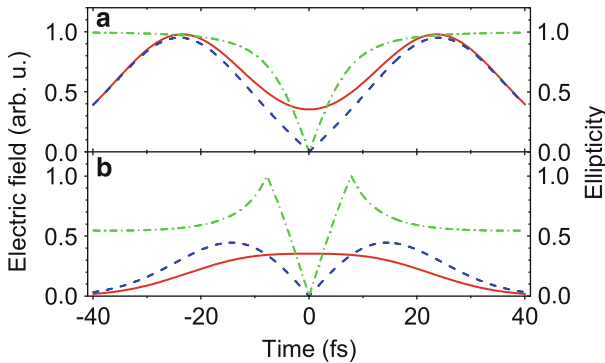


Fig. 5.4 Comparison of laser field components in DOG (a) and GDOG (b) with one optical cycle of gate width. In both (a) and (b), the driving field and gating field are plotted in the *solid line* and *dashed line*, respectively, and the ellipticity is plotted in the *dash-dot line*

attosecond pulses from argon gas, while for neon, the upper limit is 30 fs. Thus, longer lasers can be used for smaller ε . However, if the ε is too small, attosecond pulses are generated outside of the gate [25].

5.3 Carrier-Envelope Phase Stabilization of Oscillator, Amplifier and Hollow-Core Fiber Beams

The carrier-envelope phase (CEP) of a laser pulse affects a variety of high field processes such as above-threshold ionization (ATI) and high-order harmonic generation (HHG) due to the fast variation of the electric field within the pulse envelope [26,27]. The CEP can affect the high-order harmonic generation process even when the excitation laser is long [28]. Therefore, in producing and utilizing the single attosecond pulses, the CEP of the laser oscillator must be locked, and any CEP drift through the amplification process and in the hollow-core fiber and the chirped mirrors must be corrected. In this section, we introduce our results of CEP stabilization through the above-mentioned stages.

The laser setup with CEP drift measurement and stabilization is shown in Fig. 5.5 [29]. The CEP of the pulses from the laser oscillator was locked by using an f -to- $2f$ and locking electronics, which sent a correction signal to an AOM in the pump laser

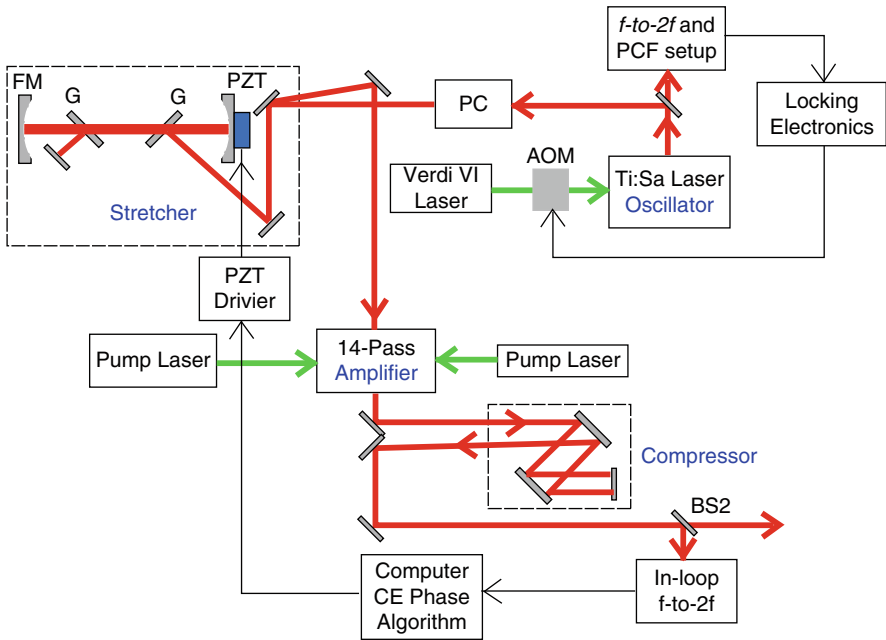


Fig. 5.5 Laser system with CEP drift measurement and stabilization

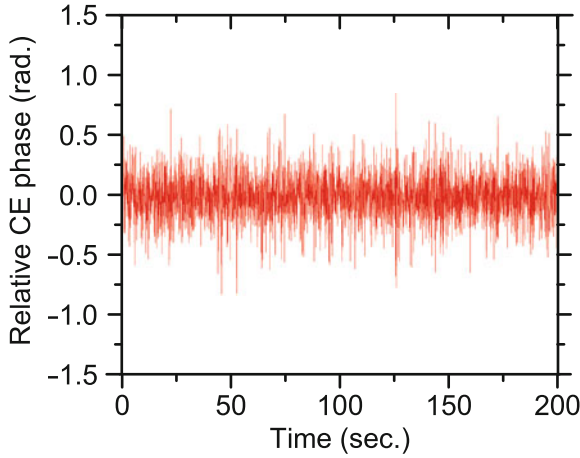


Fig. 5.6 Stabilized CEP drift of the amplifier beam [33]

path [30, 31]. By changing the pump power, the CEP of the oscillator beam was stabilized. Similarly, the 10% of the output of the amplified laser pulse train was split by a beamsplitter (BS2), and sent to the f -to- $2f$, which here is called the in-loop f -to- $2f$. The interference of the components in the frequency domain resulted in a fringe pattern, which was collected by the spectrometer and sent to a computer to obtain the pulse-to-pulse shift of the CEP using a well-known algorithm called Fourier Transform Spectral Interferometry [32]. The error signal was sent as a feedback to a PZT driver, which provided the driving voltage for the PZT in the stretcher [33–35]. By changing the stretcher-grating separation, the phase drift is corrected. Compared with the material-based stretchers and compressors, the grating-based stretchers and compressors, which is our case, can scale the CEP-stabilized amplifiers to higher energies. Furthermore, by changing the stretcher-grating separation with an attached PZT, we can easily control the relative phase without causing apparent extra vibration.

A typical amplifier beam phase drift curve was shown in Fig. 5.6 when both the oscillator and the amplifier are CEP stabilized. In the figure, the rms error of the CEP drift was 179 mrad.

For high harmonic generation, few cycle pulses are sometimes needed. Therefore, we also studied the CEP variation after the hollow-core fiber [36, 37]. In the experiment, the CEP-stabilized pulses from the laser oscillator were amplified using the KLS amplifier. 2.2 mJ of the amplifier output with CEP stabilization was focused into a ~ 1 m long hollow-core fiber filled with neon gas at a pressure of 3 bars. The output of the fiber was collimated by a focusing mirror and sent to a set of chirped mirrors for temporal compression. The output pulses from the fiber had energy of 1.2 mJ. An f -to- $2f$ interferometer was placed after the fiber to measure the CEP stability of the pulses. The power-locking system [38] gave a power stability of 0.6% before the fiber. The CEP was locked to 189 mrad rms error before the fiber. After the fiber, the measured CEP error was 370 mrad rms. The increased CEP fluctuation

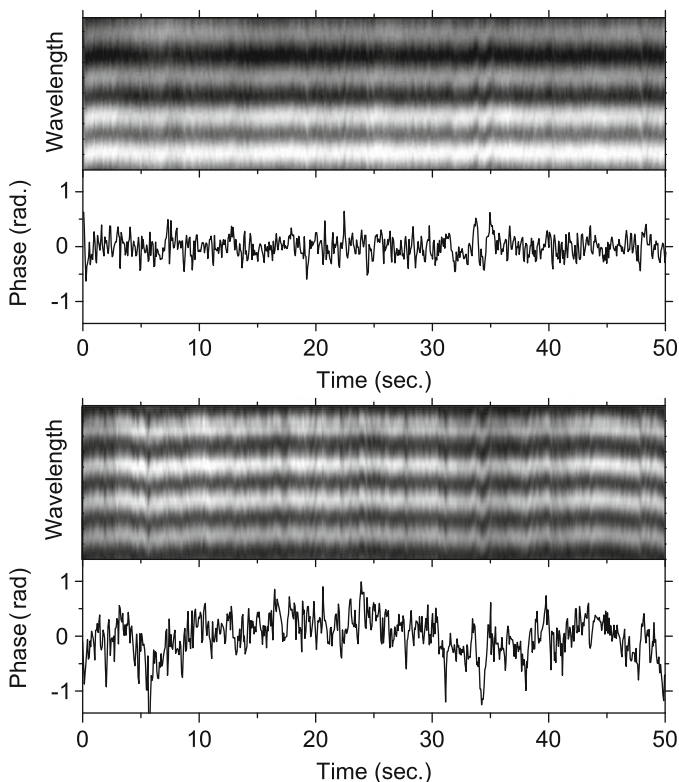


Fig. 5.7 Stabilized CEP drift before (a) and after (b) the hollow-core fiber [36]

mainly comes from the power fluctuation of the seeding laser [37]. The input CEP and output CEP for the fiber are plotted in Fig. 5.7. This CEP error was sufficiently small for use in the attosecond pulse generation.

5.4 Experimental Setup

The DOG experiments were performed with two different setups. The first one is a XUV-grating spectrometer used for collecting the spectra of the single XUV pulses. The second setup is a attosecond streak camera used for characterizing the XUV pulse with pump-probe streaking technique, and for utilizing the generated single attosecond pulses to study the electron dynamics.

The laser system used in these experiments, the Kansas Light Source, consisted of a Ti:Sapphire oscillator and a 14 pass liquid nitrogen cooled Ti:Sapphire chirped-pulse amplifier utilizing a grating-based stretcher and compressor [39]. This system produces 35 fs, 2.5 mJ pulses centered at 790 nm and with a repetition rate

of 1 or 1.5 kHz. The average power of the laser can be locked within 0.5% [38]. The CEP stabilization of the oscillator was accomplished by the self-referencing technique [30, 31]. The slow CEP drift from the amplifier was compensated by feedback control of the grating separation in the stretcher [33–35] (for details, see Sect. 5.3). The short pulses were obtained by spectrally broadening the input pulses with a gas filled hollow-core fiber and then temporally compressing them with a set of chirped mirrors. These shortened pulses could then be used with the DOG or GDOG optics.

5.4.1 DOG/GDOG Optics

The GDOG optics are constructed by two birefringent quartz plates (QP1 and QP2), one Brewster window (BW) and a barium borate (BBO) crystal as shown in Fig. 5.8 [16, 40]. The time delay between the two counter-rotating pulses is determined by the first plate thickness. The Brewster window rejects about 50% of the driving field, while leaves the gating field unchanged. The optical axis of the second quartz plate and the BBO are aligned in the same direction as the polarization of the beam from the fiber. They work together as a quarter wave plate and convert the two pulses from the first quartz plate into an ellipticity modulated pulse, similar to PG pulse. The BBO crystal generates the second harmonic (SH) field that is superimposed on the PG field for DOG. Without the Brewster window, the two quartz plates and the BBO together give the electric field of DOG.

5.4.2 XUV Grating Spectrometer

Figure 5.9 shows a schematic of the XUV-grating spectrometer. After the DOG optics, a focusing mirror (FM) with focal length of 400 mm was used to focus the laser beam on the gas cell (GC) to generate high harmonics [16, 40]. The generated harmonics passed through an aluminum filter (Al) with 200 nm thickness. The photon flux could either be measured by an XUV photodiode (IRD Inc., AXUV-100), or by a spectrometer with a toroidal grating [41]. This setup allowed only for the spectral characterization of the attosecond pulses. To temporally characterize the pulses, we used an attosecond streaking camera.

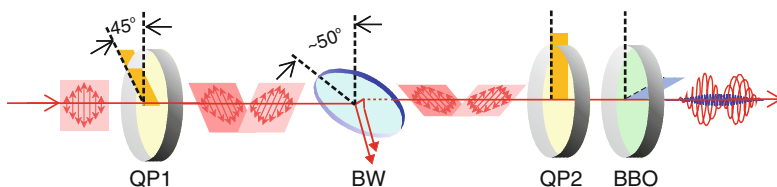


Fig. 5.8 Schematic of the optics in GDOG. In the case of DOG, the Brewster window is not used

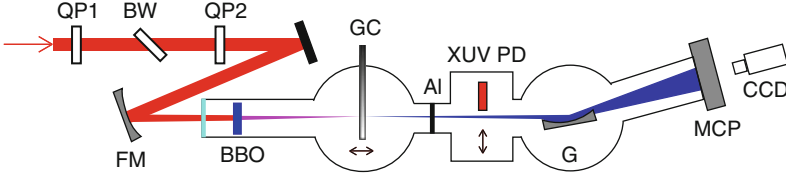


Fig. 5.9 Schematic of the grating spectrometer measuring the single attosecond pulse spectrum generated with GDOG technique. In the DOG case, the Brewster window is not used [40]

5.4.3 Attosecond Streak Camera

The experimental setup of the attosecond streak camera used for generating and measuring single attosecond pulses is shown in Fig. 5.10 [42]. The incoming Ti:Sapphire laser beam was split into two, one (17%) used for streaking and the other (83%) for high-harmonic generation. One beam propagated through the GDOG optics (see Sect. 5.4.1) and was focused by a mirror (FM) onto the argon or neon gas jet (GJ1) to generate attosecond pulses. An aluminum filter (F) was used to filter out the fundamental NIR beam and the low-energy XUV beam. The XUV beam was next focused by the Mo/Si mirror in the center of the two-component mirror onto the detection gas (GJ2). The other beam, used for streaking, traveled through a lens (L) and was focused by the annular mirror in the two-component mirror onto the detection gas. The photoelectron energy was measured by a time-of-flight spectrometer (TOF). In the DOG/GDOG experiment, the input pulse duration is 9/20 fs, and the thickness of the first quartz plate was chosen to set T_d to 4/9 laser cycles.

Since a Mach–Zehnder interferometer configuration was used to control the temporal and the spatial overlap of the attosecond XUV field and the near infrared streaking field, as shown in Fig. 5.10, the interferometer stability had to be controlled. Typically, the stability was locked to 8 as rms using a feedback control.

In order to control the time delay between the XUV pulse and the NIR streaking pulse, a closed-loop piezoelectric transducer (PZT) stage scanned the inner XUV mirror. The energies of the photoelectrons were measured by a time-of-flight spectrometer with a position sensitive delay-line detector immersed in a uniform magnetic field. This field was applied along the flight axis to increase the acceptance angle to 28° . The energy resolution of the setup was better than 0.53 eV for 17 eV electrons. The isolated XUV pulses were measured using the CRAB (Complete Reconstruction of Attosecond Bursts) method based on attosecond streaking [43,44].

5.5 Results and Discussion

In this section, we introduce our results of single attosecond pulse generation with the DOG/GDOG technique, and characterization of these pulses with the pump-probe streaking method.

5.5.1 Study of Single Attosecond Pulse Generation with XUV Grating Spectrometer

With the XUV-grating spectrometer setup, we studied the XUV pulse spectra dependence on gating schemes, input laser pulse durations, and carrier-envelope phases.

5.5.1.1 XUV Spectra with Different Gating Schemes

Figure 5.11a shows high-order harmonic spectrum images from argon gas with one-color (linearly polarized fundamental field only), two-color (a second harmonic field added to a fundamental field polarized in the same direction), conventional polarization gating, and double optical gating fields [15]. For the cases of PG and DOG, the estimated effective intensities of the fundamental and second harmonic pulses inside the gate were $2.8 \times 10^{14} \text{ W cm}^{-2}$ and $7 \times 10^{13} \text{ W cm}^{-2}$, respectively. The spectra on the long wavelength side were clipped by the detector. As projected by the numerical calculation in Fig. 5.3, only odd order harmonics are generated by the 9 fs one-color field, while both even and odd orders appeared with the two-color field. Even though the harmonic peaks are broadened in the polarization gating field, one can still see the discrete peaks with half optical cycle spacing. In contrast, the peaks form a supercontinuum in the double optical gating case.

The spectral lineouts of the DOG spectrum and the PG spectrum for delay, T_d , of 12 fs are shown in Fig. 5.11b. For comparison, the polarization gating spectrum with a delay of 15 fs is also shown. One can see that although a supercontinuum can be obtained by conventional polarization gating with larger delay, the spectrum signal is 20 times lower than that for the double optical gating.

5.5.1.2 XUV Spectra with Different Input Pulse Durations

Single attosecond spectra generated from helium, neon, and argon gases are shown in Fig. 5.12 [45]. Each gas was tested with four different input pulse durations: 8.2, 9.5, 10.6, and 11.7 fs with corresponding first quartz plate thickness (see Fig. 5.8) of 270, 350, 440, and 530 μm . In all cases, the second quartz plate thickness was chosen as 180 μm and the BBO crystal thickness was 60 μm . The peak intensities within the gate for the four different pulses were 1.7, 1.4, 1.1, and $0.9 \times 10^{15} \text{ W cm}^{-2}$.

In the argon spectra (Fig. 5.12), the estimated pulse energies from the 8.2, 9.5, 10.6, and 11.7 fs pulses were 6.5, 3.7, 2.1, and 0.42 nJ, respectively. In the neon spectra, the measured XUV pulse energies were 170, 100, 60, and 40 pJ from shortest to longest input pulse durations, respectively. In the helium spectra, the right edge is the transmission cutoff of the aluminum filter. The XUV pulse energies for this case were estimated as 45, 33, 25, and 16 pJ. The prominent peak in the helium spectra around 60 eV corresponds to the He(2s2p) resonance. The decreased signal

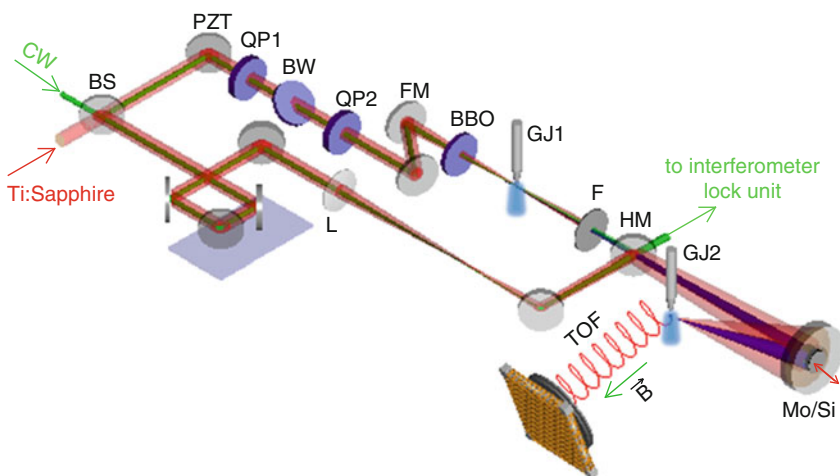


Fig. 5.10 Schematic of generating single attosecond pulses in the GDOG configuration, and characterizing these pulses with XUV-pump and NIR-probe streaking method. In the DOG setup, the Brewster window does not exist

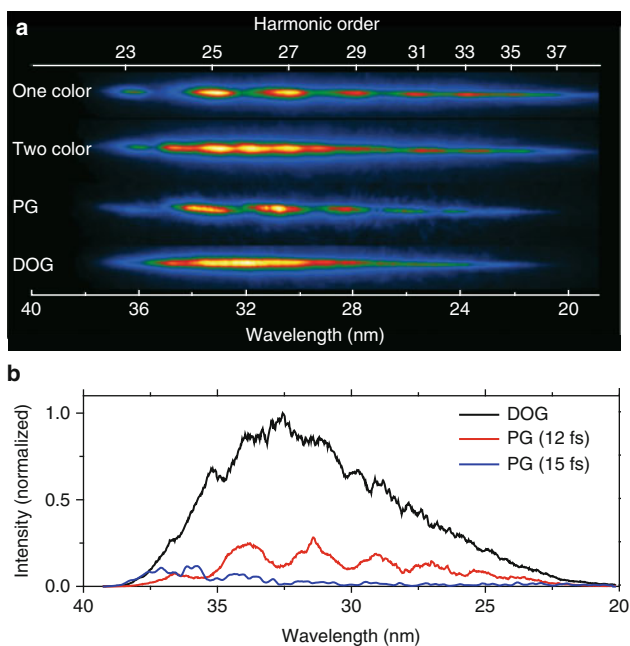


Fig. 5.11 Comparison of harmonic spectra generated from argon in different electric fields. (a) The harmonic spectrum images obtained by four different gating methods. (b) Comparison of spectra generated from DOG and from PG with two different delays [15]

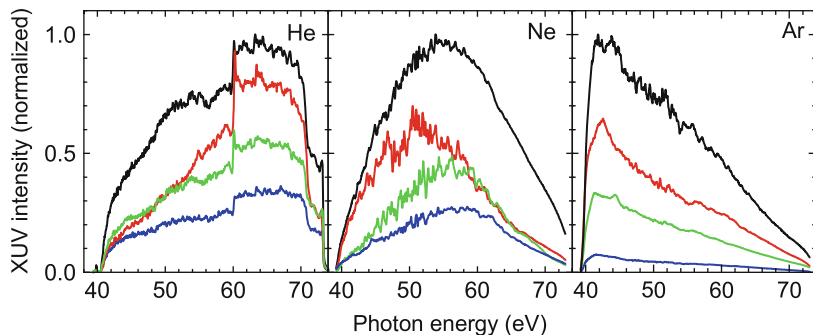


Fig. 5.12 DOG spectra of the harmonic supercontinuum generated from He, Ne, and Ar target gases with four different input pulse durations: 8.2 fs (*top-most black line*), 9.5 fs (*second-highest dark gray line*), 10.6 fs (*second-lowest light gray line*), and 11.7 fs (*lower-most dark gray line*) [45]

for the longest pulse durations as compared with the shorter durations stems from the increased target gas depletion and reduced laser intensity inside the polarization gate as described earlier. However, the XUV pulse energies from argon are substantially larger than the values reported earlier from polarization gating using 5 fs lasers [10].

5.5.1.3 XUV Spectra with Different CEPs

To verify that the supercontinuum results from the DOG field, we investigated the dependence of the high harmonic spectrum and intensity on the CEP [15]. The CEP variation was achieved by changing the effective stretcher grating separation in the laser system [35]. The harmonic spectra with different CEPs were plotted as Fig. 5.13. The unique 2π periodicity in the harmonic spectra shows the effectiveness of our gating.

5.5.2 Measurement with CRAB

Figure 5.14a shows the experimental CRAB trace of an attosecond pulse from GDOG with 20 fs laser pulses. The generation target gas is argon, and the detection gas is neon. The experimental map is composed of 32 photoelectron spectra, each of which has a delay of about 300 as between its neighbors. Figure 5.14b shows the retrieved CRAB trace. Figure 5.14c shows the temporal shape and phase of the 260 as XUV pulse. The frequency marginal comparison shows good agreement as indicated in Fig. 5.14d. A positive chirp of $7,850 \text{ as}^2$ was obtained from the phase. The XUV pulse energy spans from 29 to 51 eV with the FWHM of about 7 eV. It should be noted that the XUV spectrum shown in Fig. 5.14d is the result after being trimmed by the Al filter and Mo/Si mirror from the original XUV source.

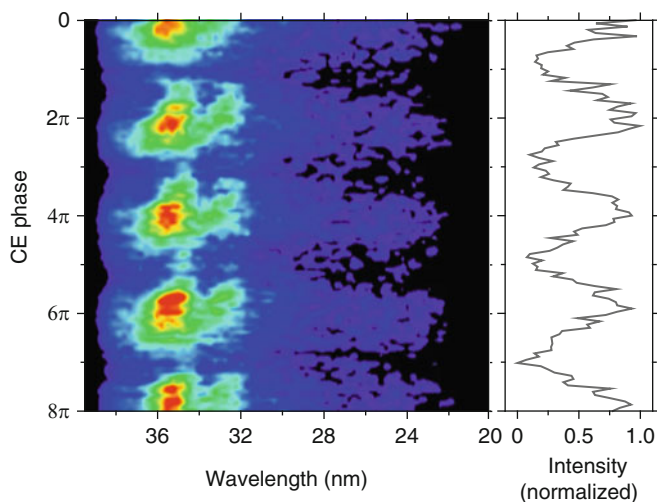


Fig. 5.13 The DOG spectra dependence on the CEP. *Left panel*: The harmonic spectrum with CEP scan. *Right panel*: The normalized integrated signal [15]

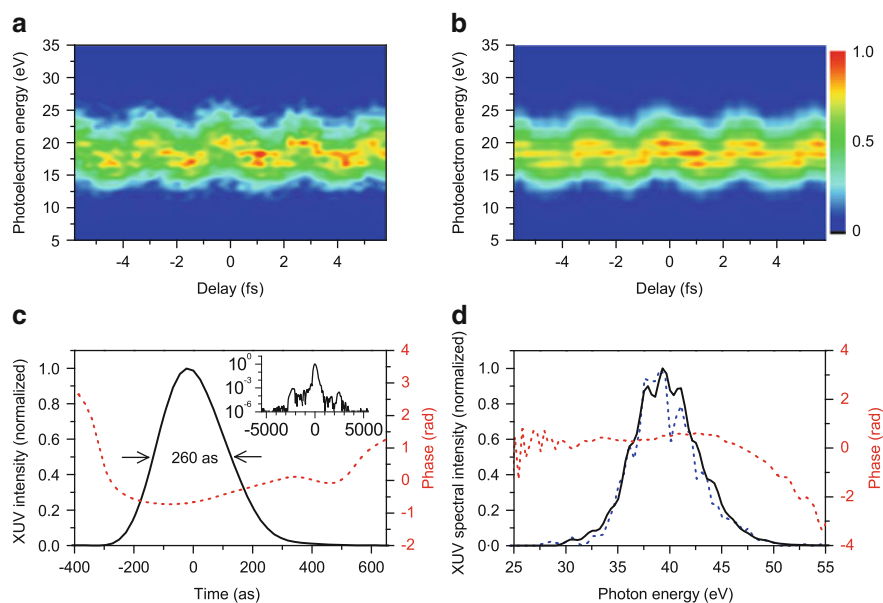


Fig. 5.14 Attosecond XUV pulse generated from argon gas with GDOG using 20 fs laser pulses. (a) Experimental CRAB trace. (b) Retrieved trace. (c) Retrieved XUV pulse (solid line) and temporal phase (dashed line). The inset shows the temporal profile over a bigger range on a log scale. (d) Comparison of the measured unstroked XUV spectrum and the retrieved XUV spectrum (solid line) accompanied by the retrieved spectral phase [42]

The minor modulation in the spectrogram was from the attosecond pre-/post-pulses. However, their intensities were three orders of magnitude lower than the main pulse, as shown in the inset of Fig. 5.14c. Here, from the reconstructed streaking field the NIR intensity was estimated to be $2.8 \times 10^{11} \text{ W cm}^{-2}$ at the second gas target. Note that it is possible to generate sub-100 as isolated pulses with GDOG from 20 or even 25 fs laser if the filter chirp compensation and Mo/Si mirror bandwidth are chosen appropriately.

As another example, Fig. 5.15 shows the experimental CRAB trace and retrieved results for single attosecond pulses generated from neon gas with 9 fs input laser pulses in the DOG method. The format of this figure is the same as that of Fig. 5.14. Since neon gas can support broad spectrum, the XUV pulse duration is shorter (136 fs) compared to that generated from argon gas with GDOG (Fig. 5.14). The two local minima in the energy spectra resulted from the reflectivity of the Mo/Si mirror. Taking into consideration the complexity of the spectrogram, the agreement between the FFT of the retrieved XUV pulse and the experimental unstreaked spectrum in Fig. 5.15d is reasonably good. It is possible to generate sub-100 as isolated pulses from neon with GDOG from 20 or even 25 fs laser if the filter chirp compensation and Mo/Si mirror bandwidth are chosen appropriately.

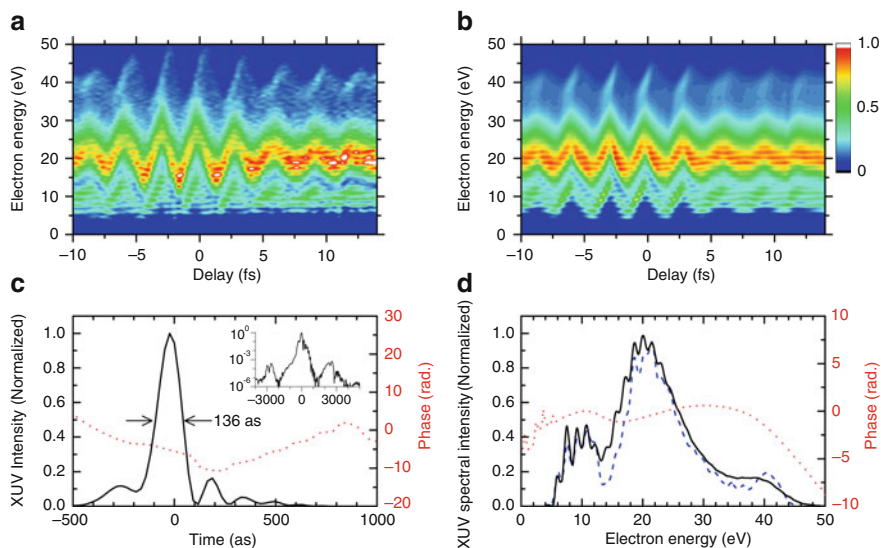


Fig. 5.15 Attosecond XUV pulse generated with DOG from neon gas using 9 fs input laser pulses. (a) Experimental CRAB trace. (b) Retrieved trace. (c) Retrieved XUV pulse (solid line) and temporal phase (dotted line). The inset shows the temporal profile over a bigger range on a log scale. (d) Comparison of the measured unstreaked XUV spectrum (dashed line) and the retrieved XUV spectrum (solid line) accompanied by the retrieved spectral phase (dotted line)

5.6 Complete Reconstruction of Attosecond Bursts

The CRAB technique has been previously demonstrated as an effective tool for the measurement of isolated attosecond pulses [43] and for attosecond pulses with satellite pulses with half-cycle [46]. In this section, we introduce our study of this technique applied on DOG/GDOG case, that is, with full-cycle periodicity.

By simulating CRAB traces similar to the experimental condition, we have studied the effects of the detector resolution, shot noise, NIR intensity variation within the XUV focus, and delay step size on the retrieved satellite pulses [47]. We also studied five major factors on the pulse retrieval using PCGPA [48]: the count rate, streaking speed, the streaking laser intensity variation, the collection angle of streaked electrons, and the time jitter between the XUV and the streaking field [49]. The main conclusions include:

1. *Detector resolution and shot noise:* With full-cycle periodicity and relative intensity of 10^{-2} and 10^{-3} , if the detector resolution is around 0.5 eV, the satellite pulse contrast is underestimated by roughly 60%. When shot noise is present, the satellite pulse contrast can be accurately retrieved when the photoelectron count of the spectrogram is 50 counts per pixel or greater, as shown in Fig. 5.16. In such condition, the retrieved pulse duration and linear chirp within 5% of the simulated pulses [49]. In contrast, our measured spectrogram is usually five times higher than this.

2. *Intensity variation:* Our simulation shows that the CRAB retrieval for single attosecond pulse generated with DOG/GDOG is not very sensitive to the NIR intensity variation within the XUV focus. Even when the XUV spot size is comparable to the NIR spot size at the focus, the XUV pulse duration and linear chirp can still be retrieved within an accuracy of 5% [49]. The satellite pulses with full-cycle separation are always retrieved within an accuracy of 2% if the XUV focus spot is equal to or smaller than the NIR spot size.

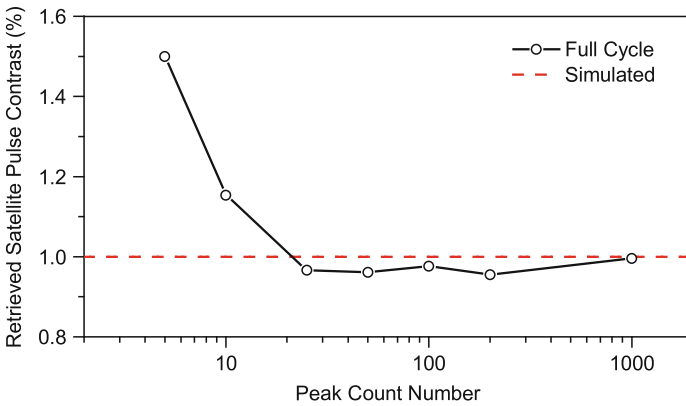


Fig. 5.16 Retrieved satellite pulse contrast as a function of the peak count number in a spectrum

3. *Minimum streaking field*: The minimum streaking field intensity needed for accurate reconstruction from a noisy CRAB trace can be nearly two orders of magnitude lower than that estimated from the classical streaking model. Such a low streaking field intensity is desirable to suppress the ATI background. However, for larger XUV bandwidth, higher streaking intensities are required, which agrees with the classical prediction qualitatively [49].

4. *Delay step*: Retrieved satellite pulse contrast for attosecond pulses with full-cycle separation is always retrieved within $\pm 4\%$ of the real one if the delay step size is no bigger than 1,000 as [47].

5. *Collection angle*: Even when the collection angle is further increased to 90° , for which the photoelectrons emitted orthogonally to the streaking laser polarization direction are also collected, the XUV pulse duration and linear chirp can still be retrieved within an error of 5%.

6. *Time delay jitter*: The reconstruction is robust against time jitter between the XUV and streaking fields. When the delay jitter is ≤ 100 as, the XUV pulse duration and chirp can be retrieved exactly. Even when the delay jitter goes to one quarter of the NIR laser cycle, the XUV pulse duration can still be retrieved within an error of 6% and the linear chirp can be retrieved within an error of 10%.

5.7 Experimenting with Single Attosecond Pulses

Owing to their unprecedented short duration, single attosecond pulses open a door for people to measure and control events that happen on the attosecond scale. The observation of periodic electric field oscillations of light pulses was first demonstrated with attosecond extreme ultraviolet (XUV) pulses in [50]. In this section, we show our measurement of the electric field variations in space and report the first direct observation of the periodic field direction reversal in the transverse plane of a Bessel–Gaussian optical beam [51].

Our measurement of the spatial profile of the Bessel beams is based on the pump-probe principle, which states that the momentum change of the electron by the electric field is proportional to the vector potential of the field. Since the vector potential is the integral of the field itself, we can derive the electric field by measuring the momentum change of the electrons. The measured momentum value of a probing electron placed at point r is

$$p(r)|_{t=\infty} \approx p_0 + \frac{e}{\omega_0} E_0 J_0(k, r) f(t_0) \sin(t_0). \quad (5.8)$$

In (5.8), e is the charge of the electron, p_0 is the momentum of the electron in the absence of the laser field, and t_0 is the time that the probe electron is placed in the field.

In the experiment, the Bessel–Gaussian spatial profile of the streaking beam was created when the beam was focused by the Ag coated annular focusing mirror. Images of the focused NIR beams were captured with a CCD camera, as shown

Fig. 5.17 CCD image of the focal spot of the streaking laser beam after reflection by the annular mirror [51]

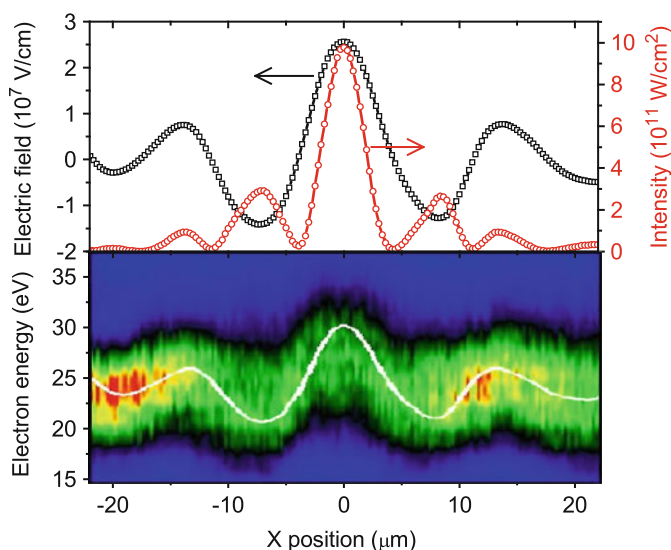
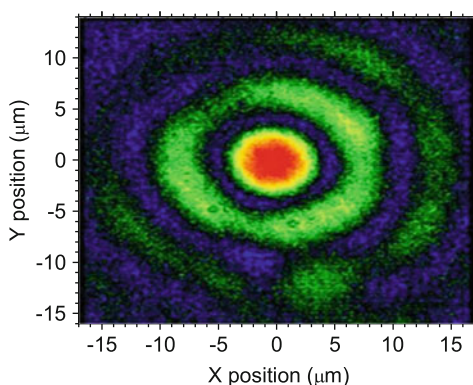


Fig. 5.18 *Low panel:* The streaked photoelectron spectrum plotted as a function of the radial position of the streaking beam. *Upper panel:* The electric field and intensity derived from the streaked spectrum [51]

in Fig. 5.17. The single attosecond XUV pulses was generated from argon gas with DOG and measured to be 276 as, which is about one tenth of the fundamental optical cycle (~ 2.6 fs), and is therefore short enough for generating the probe electrons. The same setup for characterizing the attosecond XUV pulse (Fig. 5.4) was used to measure the electric field distribution of the Bessel–Gaussian beam.

The XUV beam was scanned across the Bessel–Gaussian beam by moving the lens position in the transverse direction as shown in Fig. 5.10 while the relative delay between the NIR field and the attosecond pulse was fixed. The bottom panel in Fig. 5.18 shows the streaked electron spectrum plotted as a function of the transverse

displacement between the focused streaking beam and the focused XUV beam. As the streaking beam moves across the XUV, the momenta of the electrons either shifted above or below the field free value, p_0 , thereby accurately mapping the transverse field.

By optimizing the streaking magnitude, one can find the delay position that corresponds to $f(t_0) = 1$, and $\sin(t_0) = 1$, then the electric field value at point r was determined from $(p(r)|_{t=\infty} - p_0)\omega_0/e$. The momentum value was obtained by finding the centroid of the electron kinetic energy distribution at each spatial point in the low panel of Fig. 5.18, as shown by the white line. The resultant electric field and corresponding intensity are shown in the upper panel of Fig. 5.18. Since the XUV spot size is an important experimental parameter for attosecond pump-probe experiments, a transverse scan can be used to nonintrusively determine the spatial size of the XUV beam by de-convolving the streaked spectrogram.

5.8 Conclusion

In conclusion, we have demonstrated that the double optical gating method can be used to generate single attosecond pulses with a broad range of laser pulse durations from 8 to 20 fs. From these multicycle laser pulses, we have generated 136–260 single isolated attosecond pulses and measured the pulses unambiguously by the CRAB method. The generation of isolated attosecond pulses with such long pulse lasers offers two advantages. First, they are much easier to work with than the fragile ≤ 5 fs lasers used in previous attosecond generation experiments. Second, their energy can be much higher than the few-cycle lasers, which allows the scaling of isolated attosecond pulses to the energy level needed for studying nonlinear phenomena. Furthermore, 20 fs pulses can be delivered directly from CPAs that are commercially available [52]. With the generalized double optical gating demonstrated here, it is conceivable that high-energy single isolated attosecond pulses will be generated using high-power CPAs directly in the future. As a first application of our single attosecond pulses, we directly measured the transverse spatial profile of the electric field of a Bessel–Gauss laser beam. The electric field direction reversal from one Bessel ring to the next was clearly observed. Together with the previously demonstrated direct measurement of the electric field oscillation with time [50], attosecond streak cameras allow the noninvasive full characterization of the light field in both time and space.

Acknowledgements This material is supported by the US Army Research Office under Grant No. W911NF-07-1-0475, by the NSF under Grant No. 0457269, and by the Chemical Sciences, Geosciences, and Biosciences Division, US Department of Energy. We thank C. Lew Cocke’s group and Kevin Carnes for their help on the data acquisition system.

References

1. M. Hentschel, R. Kienberger, Ch. Spielmann, G.A. Reider, N. Milosevic, T. Brabec, P. Corkum, U. Heinzmann, M. Drescher, F. Krausz, *Nature* **414**, 509 (2001)
2. M. Drescher, M. Hentschel, R. Kienberger, M. Uiberacker, V. Yakovlev, A. Scrinzi, Th. Westerwalbesloh, U. Kleineberg, U. Heinzmann, F. Krausz, *Nature* **419**, 803 (2002)
3. R. Kienberger et al., *Nature* **427**, 817 (2004)
4. M. Uiberacker et al., *Nature* **446**, 627 (2007)
5. M.F. Kling, et al., Conference on Lasers and Electto-Optics/Quantum Electronics and Laser Science Conference and Photonic Applications Systems Technologies, OSA Technical Digest (CD) (Optical Society of America, 2008) paper JFH1
6. A.L. Cavalieri et al., *Nature* **449**, 1029 (2007)
7. E. Gouliemakis et al., *Science* **320**, 1614 (2008)
8. P.B. Corkum, N.H. Burnett, M.Y. Ivanov, *Opt. Lett.* **19**, 1870 (1994)
9. O. Tcherbakoff, E. Mevel, D. Descamps, J. Plumridge, E. Constant, *Phys. Rev. A* **68**, 043804 (2003)
10. G. Sansone et al., *Science* **314**, 443 (2006)
11. J. Mauritsson, P. Johnsson, E. Gustafsson, A. L'Huillier, K.J. Schafer, M.B. Gaarde, *Phys. Rev. Lett.* **97**, 013001 (2006)
12. T. Pfeifer, L. Gallmann, M.J. Abel, D.M. Neumark, S.R. Leone, *Opt. Lett.* **31**, 975 (2006)
13. Y. Oishi, M. Kaku, A. Suda, F. Kannari, K. Midorikawa, *Opt. Express* **14**, 7230 (2006)
14. P. Tzallas, E. Skantzakis, C. Kalpouzos, E. P. Benis, G.D. Tsakiris, D. Charalambidis, *Nat. Phys.* **3**, 846 (2007)
15. H. Mashiko, S. Gilbertson, C. Li, S.D. Khan, M.M. Shakya, E. Moon, Z. Chang, *Phys. Rev. Lett.* **100**, 103906 (2008)
16. S. Gilbertson, H. Mashiko, C. Li, S.D. Khan, M.M. Shakya, E. Moon, Z. Chang, *Appl. Phys. Lett.* **92**, 071109 (2008)
17. P.M. Paul, E.S. Toma, P. Breger, G. Mullot, F. Augé, Ph. Balcou, H.G. Muller, P. Agostini, *Science* **292**, 1689 (2001)
18. P. Antoine et al., *Phys. Rev. A* **53**, 1725 (1996)
19. V. Platonenko, V. Strelkov, *J. Opt. Soc. Am. B* **16**, 030435 (1999)
20. B. Shan, S. Ghimire, Z. Chang, *J. Mod. Opt.* **52**, 277 (2005)
21. Z. Chang, *Phys. Rev. A* **70**, 043802 (2004)
22. V. Strelkov et al., *Appl. Phys. B Laser. Optic.* **78**, 879 (2004)
23. M. Ammosov, N. Delone, V. Krainov, *Sov. Phys. JETP* **64**, 1191 (1986).
24. Z. Chang, *Phys. Rev. A* **76**, 051403(R) (2007)
25. D. Oron, Y. Silberberg, N. Dudovich, D.M. Villeneuve, *Phys. Rev. A* **72**, 063816 (2005)
26. G.G. Paulus, F. Grasbon, H. Walther, P. Villoresi, M. Nisoli, S. Stagira, E. Priori, S. De Silvestri, *Nature (London)* **414**, 182 (2001)
27. C.A. Haworth, L.E. Chipperfield, J.S. Robinson, P.L. Knight, J.P. Marangos, J.W.G. Tisch, *Nat. Phys.* **3**, 52 (2007)
28. G. Sansone, C. Vozzi, S. Stagira, M. Pascolini, L. Poletto, P. Villoresi, G. Tondello, S. De Silvestri, M. Nisoli, *Phys. Rev. Lett.* **92**, 113904 (2004)
29. E. Moon, Ph.D thesis, Kansas State University (2009)
30. D.J. Jones et al., *Science* **288**, 635 (2000)
31. E. Moon, C. Li, Z. Duan, J. Tackett, K.L. Corwin, B.R. Washburn, Z. Chang, *Opt. Exp.* **14**, 9758 (2006)
32. A.W. Albrecht, J.D. Hybl, S.M.G. Faeder, D.M. Jonas, *J. Chem. Phys.* **111**, 10934 (1999)
33. C. Li, E. Moon, Z. Chang, *Opt. Lett.* **31**, 3113 (2006)
34. Z. Chang, *Appl. Opt.* **45**, 83503 (2006)
35. C. Li, E. Moon, H. Mashiko, C.M. Nakamura, P. Ranitovic, C.M. Maharjan, C.L. Cocke, Z. Chang, G.G. Paulus, *Opt. Express* **14**, 11468 (2006)
36. H. Mashiko, C.M. Nakamura, C. Li, E. Moon, H. Wang, J. Tackett, Z. Chang, *Appl. Phys. Lett.* **90**, 161114 (2007)

37. H. Wang, M. Chini, E. Moon, H. Mashiko, C. Li, Z. Chang, *Opt. Exp.* **17**, 12082 (2009)
38. H. Wang, C. Li, J. Tackett, H. Mashiko, C.M. Nakamura, E. Moon, Z. Chang, *Appl. Phys. B Laser Optic.* **89**, 275 (2007)
39. B. Shan, C. Wang, Z. Chang, U.S. Patent 7,050,474, 23 May 2006
40. H. Mashiko, S. Gilbertson, C. Li, E. Moon, Z. Chang, *Phys. Rev. A* **77**, 063423 (2008)
41. M.M. Shakya, S. Gilbertson, H. Mashiko, C.M. Nakamura, C. Li, E. Moon, Z. Duan, J. Tackett, Z. Chang, *Proc. SPIE Int. Soc. Opt. Eng.* **6703**, 67030 (2007)
42. X. Feng, S. Gilbertson, H. Mashiko, H. Wang, S.D. Khan, M. Chini, Y. Wu, Z. Chang, *Phys. Rev. Lett.* **103**, 183901 (2009)
43. Y. Mairesse, F. Quéré, *Phys. Rev. A* **71**, 011401(R) (2005)
44. J. Itatani, F. Quéré, G.L. Yudin, M. Yu. Ivanov, F. Krausz, P.B. Corkum, *Phys. Rev. Lett.* **88**, 173903 (2002)
45. S. Gilbertson, H. Mashiko, C. Li, E. Moon, Z. Chang, *Appl. Phys. Lett.* **93**, 111105 (2008)
46. J. Gagnon, E. Goulielmakis, V.S. Yakovlev, *Appl. Phys. B Laser. Optic.* **92**, 25 (2008)
47. M. Chini, H. Wang, S.D. Khan, S. Chen, Z. Chang, *Appl. Phys. Lett.* **94**, 161112 (2009)
48. D.J. Kane, G. Rodriguez, A.J. Taylor, T.S. Clement, *J. Opt. Soc. Am. B* **14**, 935 (1997)
49. H. Wang, M. Chini, S.D. Khan, S. Chen, S. Gilbertson, X. Feng, H. Mashiko, Z. Chang, *J. Phys. B At. Mol. Opt. Phys.* **42**, 134007 (2009)
50. E. Gouliemakis et al., *Science* **305**, 1267 (2004)
51. S. Gilbertson, X. Feng, S. Khan, M. Chini, H. Wang, H. Mashiko, Z. Chang, *Opt. Lett.* **34**, 2390 (2009)
52. For manufactures of lasers with less than 20 fs pulse duration, Please see, for example, Amplitude Technologies (2-4 rue du Bois Chaland - CE 2926, 91029 EVRY - France)

Chapter 6

Toward the Generation of Isolated Attosecond Pulses in the Water Window

Ruxin Li, Zhinan Zeng, Pu Zou, Yuxing Leng, Chunmei Zhang,
and Zhizhan Xu

Abstract The coherent attosecond pulse in the water-window spectral region could be a powerful tool for studying the ultrafast electronic dynamics of biological samples in water. We propose a scheme to generate isolated attosecond pulses in water-window region, by exploring the high-order harmonic generation in helium atoms driven by a multicycle two-color optical field synthesized with an intense 2,000 nm, 20 fs pulse and its detuned frequency doubled pulse. The calculations show that isolated 67 as pulses in the water-window can be produced in this way. We also describe how to generate such a driving laser pulse with stabilized carrier-envelope phase from a two-stage optical parametric amplifier. With a pump source at 800 nm, the output pulse is tunable from 1.2 to 2.4 μm , and the output average power is 1.2 W for 1.5–1.7 μm region. Due to the differential frequency process, the output infrared pulse is self-phase-stabilized.

6.1 Introduction

Isolated extreme ultraviolet attosecond pulses are important for exploring the ultrafast electron dynamics in atoms and molecules [1–8]. The most successful way so far to generate isolated attosecond pulses is the frequency synthesis of high-order harmonic supercontinuum at the cutoff region driven with laser pulses shorter than two optical cycles [2]. The attosecond pulse width is limited by the available shortest driving laser pulse, and it has been difficult to generate attosecond pulses with duration less than 100 as until a recent breakthrough [8]. Isolated attosecond pulses have also been generated by employing a polarization gating method [3], which also requires a few-cycle driving laser pulses.

R. Li (✉), Z. Zeng, P. Zou, Y. Leng, C. Zhang, and Z. Xu
State Key Laboratory of High Field Laser Physics, Shanghai Institute of Optics
and Fine Mechanics, Chinese Academy of Sciences, Shanghai 201800, China
e-mail: ruxinli@mail.shcnc.ac.cn, zhinan_zeng@maul.siom.ac.cn, pu.zou@tuwien.ac.at,
lengyuxin@siom.ac.cn, feileiwuyu@siom.ac.cn, zzxu@mail.shcnc.ac.cn

High-order harmonic generation (HHG) driven with two-color laser field does not require a driving pulse duration of less than two cycles and has been utilized to generate attosecond pulses [4, 9]. More recently, calculations have been presented for the generation of isolated attosecond pulses in the multicycle two-color field [10, 11]. They have shown that the detuning of the second harmonic can be used to break down the symmetry of the electric field over many optical cycles and provides a coherent control for the formation of an isolated attosecond pulse. The use of multicycle driving laser pulses offers the possibility of more intense attosecond XUV pulses.

For the radiation in the water-window from 4.4 to 2.3 nm (from 280 to 550 eV), the carbon-containing biological samples absorb efficiently but water is comparatively transparent. High-contrast biological spectroscopy in this spectral window has long been one of the most important objectives of the development of coherent XUV sources [12]. High-order harmonic emission in water-window with attosecond pulse duration, is therefore, strongly desired for studying the ultrafast electronic dynamics of biological samples in water. However, the wavelengths of currently available isolated attosecond pulses are much longer than 10 nm [1–8].

The scaling law for the cutoff energy of HHG as a function of driving laser wavelength indicates that a longer wavelength infrared (IR) laser pulse will shorten the wavelength of attosecond pulses with a reduced conversion efficiency. Recently a scheme for the generation of self-phase-stabilized near-infrared (NIR) laser pulses was proposed [13].

In this chapter, we will show how the two-color scheme using NIR driving laser pulses can be used to generate intense isolated attosecond pulse in the water-window [14]. We will also describe how to generate such a driving laser pulse with stabilized carrier-envelope phase (CEP) from a two-stage optical parametric amplifier (OPA) [15].

6.2 Generation of Isolated Attosecond Pulses in the Water Window

We proposed that, a 20 fs/2,000 nm pulse and a detuned frequency-doubled 20 fs/909 nm pulse, both linearly polarized, are synchronized to form the driving field for HHG in helium atoms. The HHG calculation method, which is based on the single-active-electron approximation, has been widely used [2]. The Lewenstein model is used to calculate the dipole moment of an atom in the nonadiabatic formula [16] and the high harmonic spectrum can be obtained by Fourier transformation of the time-dependent dipole moment. The intensities of the fundamental and the frequency-doubled pulses are assumed to be $2.0 \times 10^{14} \text{ W cm}^{-2}$ and $1.0 \times 10^{14} \text{ W cm}^{-2}$, respectively. The synthesized laser field is described by:

$$E_s(t) = E_1 \exp[-2 \ln(2)t^2/\tau_1^2] \cos(\omega_1 t + \phi_1) + E_2 \exp[-2 \ln(2)t^2/\tau_2^2] \cos(\omega_2 t + \phi_2), \quad (6.1)$$

where E_1 and E_2 are the electric field amplitudes of the fundamental and the frequency-doubled pulses, respectively; ω_1 and ω_2 are the angular frequencies of the two-color pulses; and τ_1 and τ_2 are the corresponding pulse durations (FWHM). ϕ_1 and ϕ_2 are the corresponding absolute phases.

Figure 6.1a shows the electric field of the fundamental laser pulse. The temporal profile of the harmonic emission driven with only the fundamental field is showed in Fig. 6.1b. It is clear that attosecond pulses appear at almost every 0.5 optical cycle. In Fig. 6.1c, we show the synthesized electric field when an intense detuned frequency-doubled field ($\omega_2 = 2.2\omega_1$) is added to the fundamental field. The temporal profile of the harmonic emission (from 380 to 400 eV) driven with the two-color field is presented in Fig. 6.1d. The attosecond pulses with the highest intensity (labeled by I and II) are separated by about three optical cycles, with some satellite pulses appearing near the strongest emission. When such a two-color field is employed, one can overcome the general requirement of the driving laser pulse duration as two cycles for producing isolated attosecond pulses.

To better understand HHG in a detuned two-color field, we may observe the harmonic emission in the spectral domain. Significant differences from the single-color case are revealed. The calculated harmonic spectra generated with single-color (ω_1) and the detuned two-color ($\omega_1 + \omega_2$) fields are plotted in Fig. 6.2. The most pronounced difference between the two spectra is the significant extension of cutoff energies from 270 eV in the single-color field case to 400 eV in the two-color case. In addition, the harmonic intensity is increased by about one order of magnitude in the two-color case. This can be easily understood in the light of the semi-classical three-step model of HHG [5].

To clarify the role of the shaped laser field in the two-color scheme, the ionization and the classical dynamics of electrons are calculated. The results are shown in Fig. 6.3. Figure 6.3a illustrates the dependence of the kinetic energy on the recombination times in the single-color fundamental field and that in the two-color field. It is shown that there are two classes of trajectories corresponding to the same energies of the returning electrons in each half optical cycle for the fundamental field. The first trajectory, with positive chirp, is called short trajectory, and is characterized by later ionization but earlier emission time; the second trajectory, with negative chirp, is called long trajectory and displays earlier ionization but with later recombination time.

In the single-color field case, the recombination of the electron with the parent core will generate harmonic emission with slightly different maximum photon energy between the two adjacent half fundamental laser cycles. Consequently, the harmonic supercontinuum with a bandwidth of only 20 eV at the cutoff, can be spectrally selected for an isolated attosecond pulse. After the detuned frequency-doubled pulse is added to the fundamental laser pulse, there are three pairs of trajectories between $15T_0$ and $16.2T_0$ (T_0 is the optical cycle of the fundamental field) shown

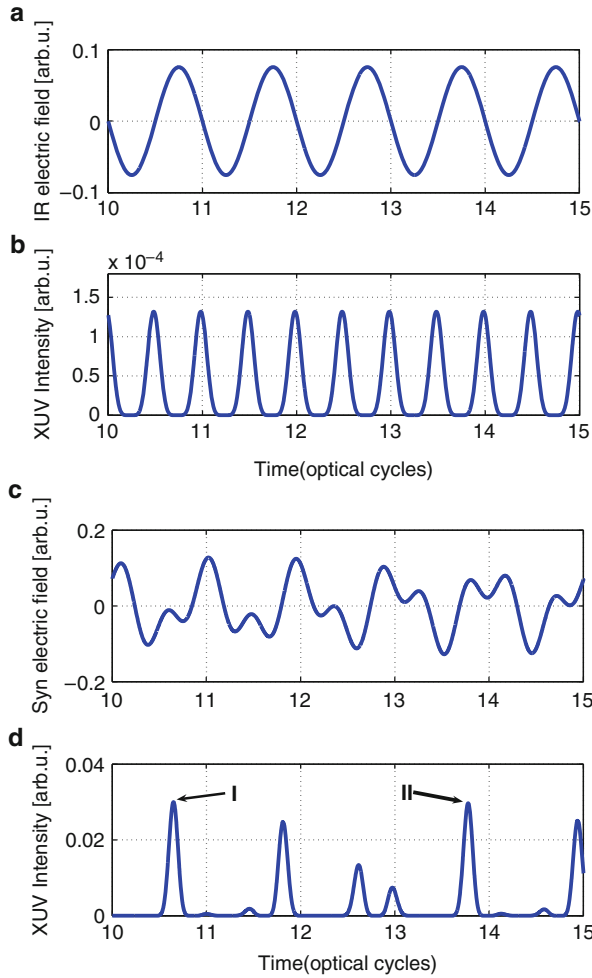


Fig. 6.1 (a) Electric field of the fundamental laser pulse (2,000 nm, ω_1), (b) Temporal profile of the harmonic emission driven with only the fundamental field, (c) Synthesized electric field for the fundamental (2,000 nm, ω_1) and its detuned frequency-doubled harmonic (909 nm, $\omega_2 = 2.2\omega_1$), (d) Temporal profile of the harmonic emission selected with a numerical spectral filter ranging from 380 to 400 eV driven with the synthesized laser field. The relative phase between the two pulses is -0.3π

by the cross curve in Fig. 6.3a. However, only the trajectories associated to the peak with highest energy contributes to the generation of supercontinuum with a bandwidth of 130 eV (from 250 to 380 eV), because the ionization ratio associated near the peak increases steeply at $15.3T_0$ shown by the dashed-dotted curve in Fig. 6.3b. Obviously, the result coincides well with the significant broadening of XUV supercontinuum (dashed curve) shown in Fig. 6.2.

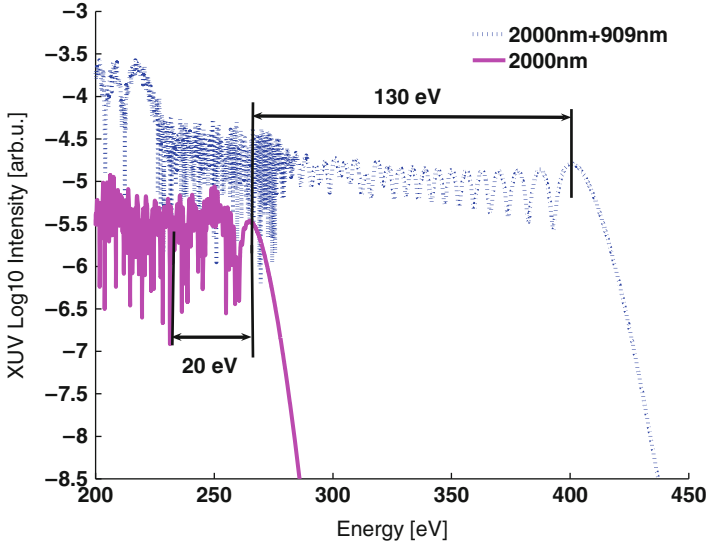


Fig. 6.2 The harmonic spectra for helium atoms. The solid curve shows the spectrum generated with only the fundamental laser field. The *dashed curve* shows the spectrum generated with the two-color field. The relative phase between the two pulses is -0.3π

It can be learned from Figs. 6.2 and 6.3 that the extension of the cutoff is consistent with the additional kinetic energy of the returning electron wave packets provided by the detuned frequency-doubled field. The XUV supercontinuum of 130 eV bandwidth is generated when the relative phase between the two pulses is -0.3π . In Fig. 6.2, we have noticed that in the dramatically extended plateau region, the harmonic spectrum shows less intensity modulation than that in the single-color case where a very large modulation inherently exists [17]. This is the region where a spectral filter can be applied to isolate an attosecond pulse.

Figure 6.3b shows the electric field of the two-color field (dotted curve), the ionization ratio [18] (dashed-dotted curve) and the high-order harmonic emission (solid curve) selected with a numerical spectral filter between 280 and 340 eV, as functions of time. One can clearly see that the ionization ratio rapidly increases near the recombination time $t = 15.3T_0$ but keeps constant after $t = 17T_0$. The ionization ratio at $t = 16.2T_0$ is relatively high, leading to the efficient broadband harmonic emission as shown in Fig. 6.2. This is consistent with the observation that the maximum energy of the returning electron appears at $t = 16.2T_0$ as shown in Fig. 6.3a.

It should be noticed in Fig. 6.3a that the kinetic energy profile consists of several regular broad peaks separated by about half of an optical period (T_0) in the single-color case. But the kinetic energy profile becomes irregular with a predominant peak at $t = 16.2T_0$ in the two-color case. This change indicates that the electron trajectory has been changed after the detuned frequency-doubled field is added. Depending upon the instantaneous phase relationship between the fundamental and

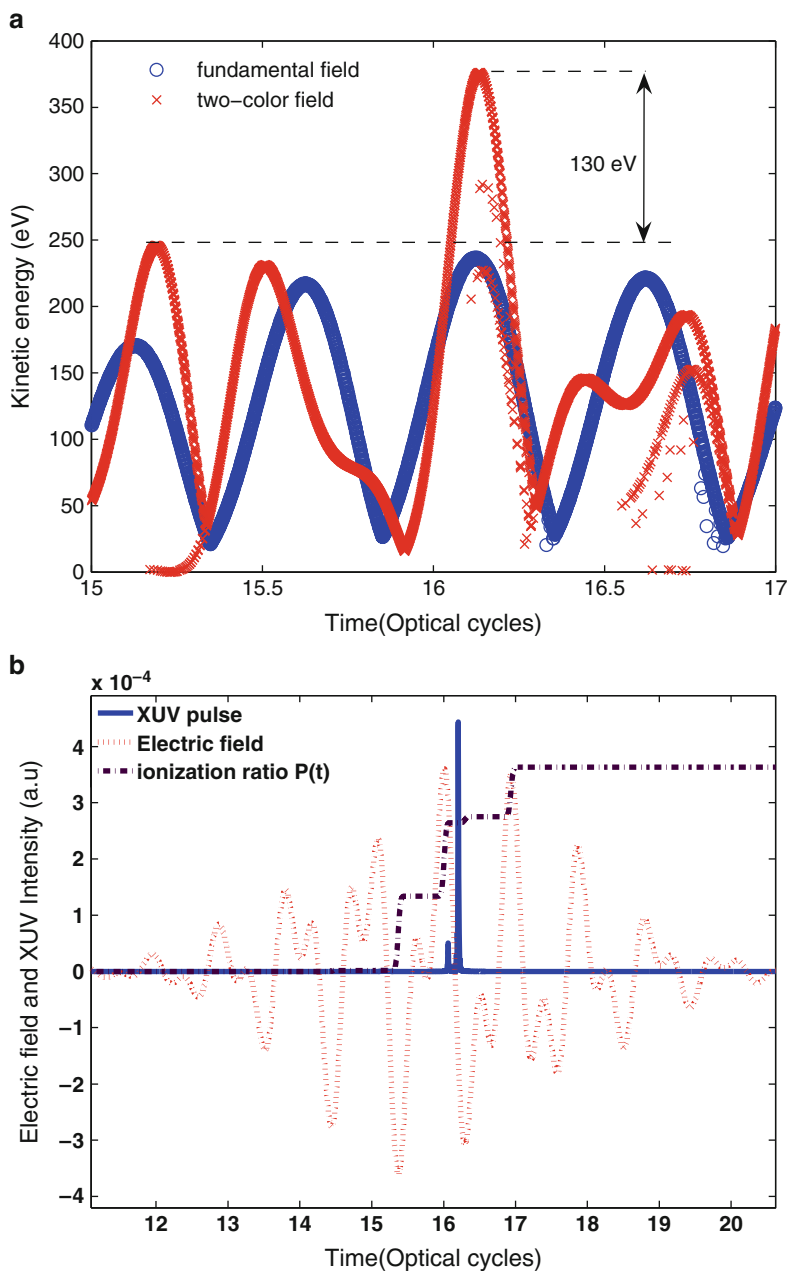


Fig. 6.3 (a) The kinetic energy of a returning electron in the fundamental field (o) and in the two-color field (x) as a function of the recombination time. (b) The electric field of the two-color field (dotted curve), the ionization ratio $P(t)$ (dashed-dotted curve) which is calculated by ADK theory, and the harmonic emission (solid curve) selected with a numerical spectral filter ranging from 280 to 340 eV, as functions of time in the two-color field

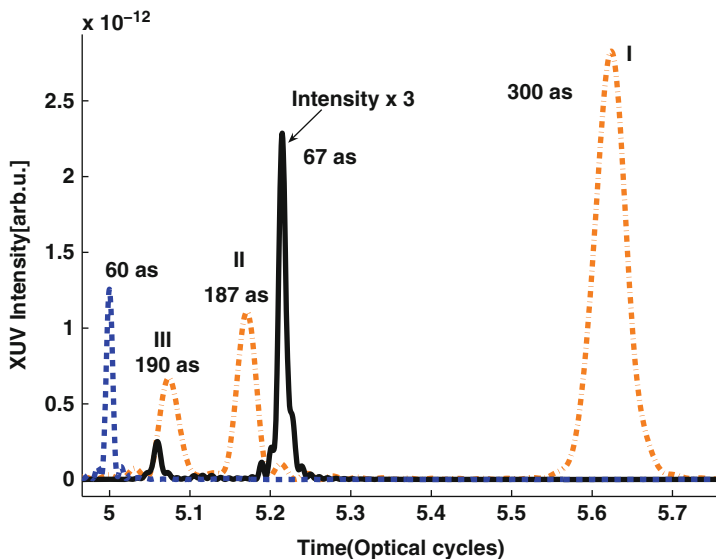


Fig. 6.4 The temporal profiles of the attosecond pulses with 60 eV bandwidth, obtained with (*dashed*) and without (*solid*) phase compensation. For comparison, the attosecond pulses generated by the single-color 20 fs pulse without phase compensation is also shown (*dashed-dotted curve*)

detuned frequency-doubled fields, the electrons may be accelerated and decelerated many times. The electron path is correspondingly stretched or shortened, which induces the returning time of electrons is earlier or later than that in the fundamental field case. Under certain conditions, only one quantum path gains the highest increase in kinetic energy while the others do not have any apparent change. In addition, the full width half maximum (FWHM) of the kinetic energy profile around $t = 16.2T_0$ is narrower in the two-color case than that of the fundamental field case, indicating that the average time interval between emissions around $t = 16.2T_0$ decreases and, thus supports a single attosecond pulse with shorter duration.

In the time domain, without employing phase compensation, an XUV supercontinuum from 280 to 340 eV (60 eV bandwidth) can lead to an isolated 67 as pulse as shown in Fig. 6.4 (the solid curve). If the dispersion is well compensated for the 60 eV spectral bandwidth, a single 60 as pulse with a clean time profile can be obtained (the dashed curve in Fig. 6.4). For comparison, we also calculated the attosecond pulses generated in the single-color fundamental laser field by performing the inverse Fourier transformation of the XUV supercontinuum with a spectral bandwidth of 20 eV in the cutoff region without employing phase compensation (the dashed-dotted curve in Fig. 6.4). Although a main attosecond pulse (peak I) is produced, two strong satellite pulses, as peak II and peak III, also appear.

To show the importance of frequency detuning for the second harmonic pulse and the relative phase shift between the two-color pulses, we performed a time-frequency analysis of the dipole response of the He atom to the four different driving

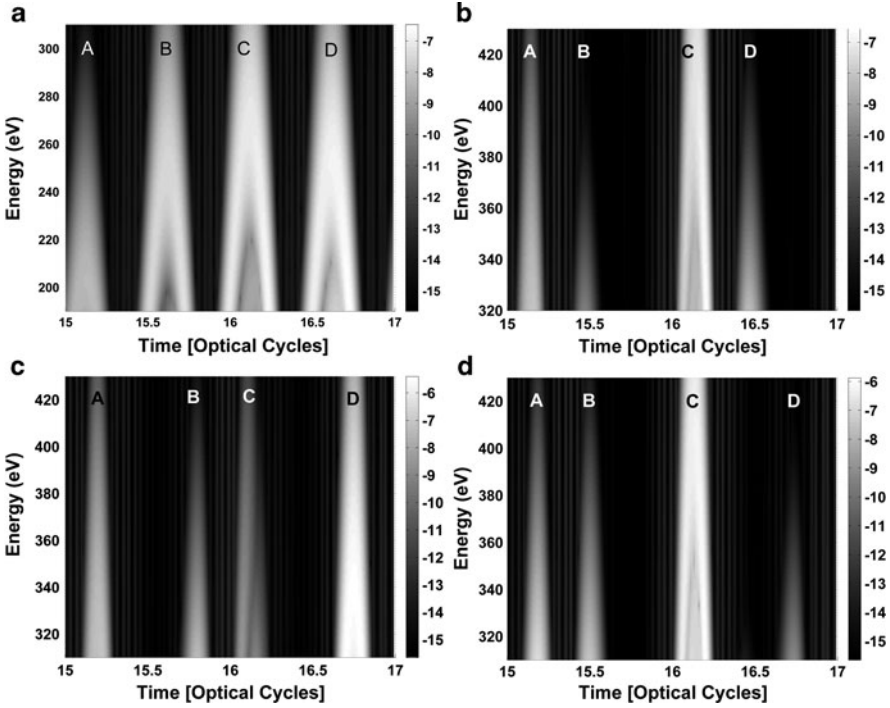


Fig. 6.5 Diagrams of the time–frequency distributions of high harmonic emission generated by (a) the single 20 fs pulse, (b) the combination of a 20 fs, 2,000 nm fundamental pulse and a frequency-doubled pulse with a relative phase of -0.3π , (c) the combination of the fundamental pulse and the detuned frequency-doubled pulse with zero phase shift, and (d) with a relative phase shift of -0.3π . Note that the color scale is in logarithmic unit

laser fields [19, 20]. If the time window around a specific moment is applied to the dipole acceleration, the spectrum can represent the strength of the dominant frequencies at that moment. By calculating the spectra with a translation of the time window, we obtain the time-frequency distribution of the XUV radiation [21]. It can be seen in Fig. 6.5a that for the HHG produced by the single 20 fs pulse, there is only a minor difference in the XUV emission peaks signed with B, C, and D. The bandwidth of the supercontinuum at the cutoff region is very narrow. When the frequency-doubled pulse is added to the fundamental pulse with relative phase $\phi = -0.3\pi$, we can see from Fig. 6.5b that the photon energy of the two peaks labeled with A and C (separated by one optical cycle in time domain) are enhanced significantly. This illustrates that the symmetry of the electric field is already broken in the two-color field. When the detuned frequency-doubled pulse is added upon the fundamental pulse with zero phase shift, only the maximum photon energy and intensity of peak D in Fig. 6.5c are greatly increased, while those of peak A, B, and C are decreased. When a relative phase shift of the detuned frequency-doubled pulse of

$\phi = -0.3\pi$ is employed, the intensities of peaks A, B, and D are greatly suppressed, while the intensity of peak C is further enhanced as shown in Fig. 6.5d, indicating the electric field symmetry has been broken down further in a larger time window. From Fig. 6.5a–d, we have shown the progress of isolating one attosecond emission by controlling the quantum path of a returning electron. It should be pointed out that this two-color scheme requires the NIR driving pulses with stabilized carrier-envelope phase.

6.3 Generation of Tunable NIR Laser Pulses with Stabilized CEP

The different frequency generation (DFG) [21] and the optical parametric amplification technique have made it possible to realize the powerful CEP stabilized ultrafast pulses in the IR regime [22, 23]. The CEP stabilized pulses can be generated from the DFG process directly and amplified in the following OPA stages. The CEP stabilized 1.5 μm pulses with the energy of up to the millijoule level have been obtained [22] based on the DFG technique. Driven by the IR CEP stabilized femtosecond source, the high-order harmonic spectrum with a shorter cutoff wavelength has been demonstrated [23].

When the pump and the signal pulses are from the same laser source with the same carrier envelop phase offset, the CEP-stabilized idler pulses can be generated from the optical parametric amplification process directly [24, 25]. Nevertheless, owing to the noncollinear phase-matching geometry, the idler beam has a strong angular dispersion with a large spatial chirp [26].

We have developed a tunable femtosecond OPA in the NIR regime, where the CEP is stabilized based on the optical parametric amplification process directly [27]. The maximum parametric conversion efficiency in the final OPA stage is above 40%, and the tunable range of the OPA output is 1.2–2.4 μm . Under the total of 6.8 W/1 kHz pump power, approximately 1 W/1 kHz tunable pulses from 1.4 to 1.9 μm have been demonstrated. For the output pulses at 1.8 μm , the CEP fluctuation is 0.103 rad (rms) in 10 min.

The experimental setup is shown in Fig. 6.6. The tunable CEP stabilized OPA system consists of three parts: (1) a white light continuum (WLC) generation stage driven by the Ti:sapphire laser pulses, generating broadband seed pulses; (2) a Ti:sapphire laser-pumped WLC-seeded IR OPA stage, generating broadband CEP-stable idler pulses; and (3) a Ti:sapphire laser-pumped IR OPA stage seeded by the reshaped idler pulses.

The pump laser source is a commercial Ti:sapphire laser system (Coherent LEGEND-HE-Cryo), providing 10 mJ laser pulses at 800 nm with 1 kHz repetition rate and approximately 40 fs pulse duration. In the experiment, 6.8 mJ energy is used to drive the infrared source. The driving pulse is split into three parts with two beam splitters. A small portion of the driven pulse is used to pump the first non-collinear OPA stage (OPA1) consisting of a 2-mm-thick $\beta\text{-BaB}_2\text{O}_4$ (BBO) crystal

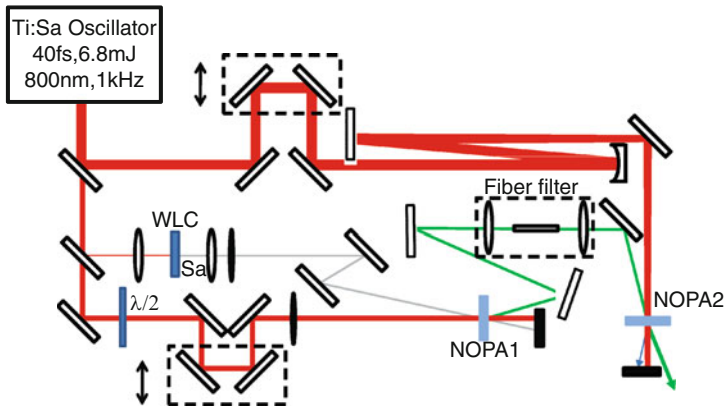


Fig. 6.6 Experimental setup for the generation of self-phase-stabilized IR laser pulses

plate, which is cut for Type I phase matching ($\theta = 21^\circ$, $\varphi = 0^\circ$). The OPA1 is seeded by the WLC generated by focusing a fraction pump laser into a 2-mm thick sapphire plate based on the self phase-modulation process, and the spectrum of the WLC covers from 0.4 to 2.4 μm . The idler pulse of the OPA1, which is used as the signal pulse in the second noncollinear OPA stage (OPA2), is self-phase stabilized due to the DFG process between the pump and the seed laser pulses with the same carrier phase offset. The OPA2 is a high-energy amplification stage with a 4-mm-thick BBO plate cut for Type II phase matching ($\theta = 28.5^\circ$, $\varphi = 30^\circ$), and pumped by the rest energy of the driven laser. Since the superfluorescent signal will reduce the laser beam quality, the pump intensities for two OPA stages are controlled to be 100 and 250 GW cm^{-2} , respectively.

In NOPA2, the tunable signal pulses can be amplified and the tunable idler pulses are generated. The idler pulses are tunable from 2.4 to 1.2 μm , as shown in Fig. 6.7a, and the signal pulses can be tuned from 1.2 to 2.4 μm , as shown in Fig. 6.7b. Due to the low sensitivity of the spectrometer in mid-infrared region, the spectrum of signal/idler pulses at 2.4 μm cannot be detected, and we can deduce the wavelength from the 1.2 μm idler/signal pulses.

The conversion efficiency of the OPA2 is up to 40% as shown in Fig. 6.8. The maximum total OPA conversion efficiency is 40.2%, when the signal pulse is tuned to 1.7 μm . With 6.6 W/1 kHz pump pulses in the OPA2, the signal pulses with the average power of 1.2 W can be obtained for 1.5–1.7 μm region. The OPA output pulse duration is determined mainly by the pump pulse width. Measured by a single-shot second-order autocorrelator, the duration of the CEP stabilized output pulses with the different central wavelengths are about 50 fs.

One of the key issues of the infrared OPA system is how to improve the performance of the idler pulses from the OPA1. First, we choose the near-collinear configuration for two OPA stages. Although, a noncollinear geometry is used for OPA stages to facilitate the separation of the beams, we keep the pump-seed angle in crystal as small as possible by using a dichromatic mirror. The small pump-seed

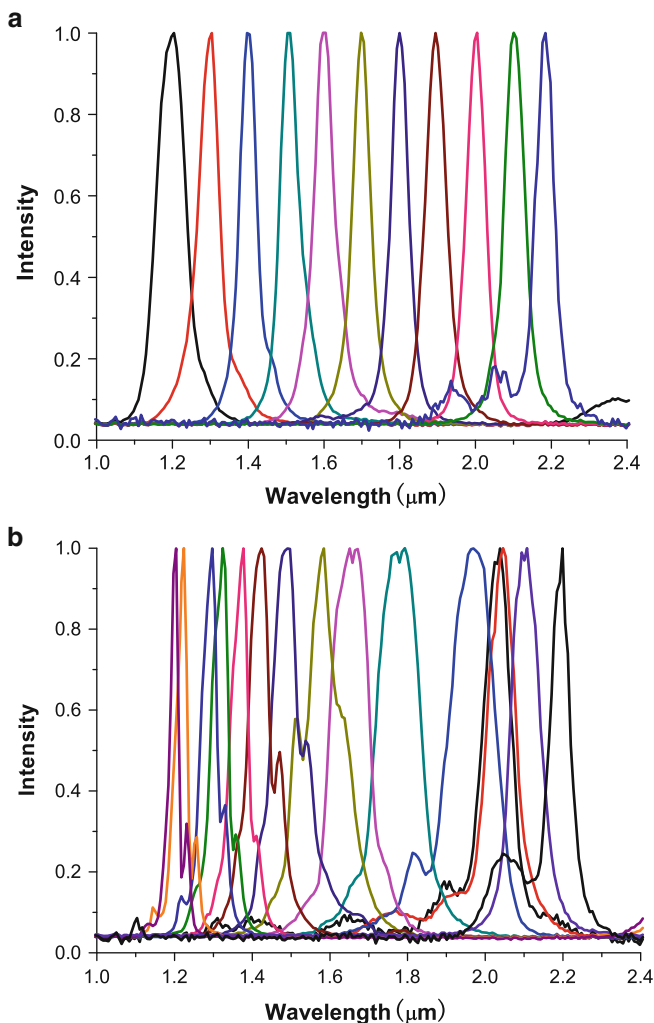


Fig. 6.7 Normalized spectra of the NOPA2 output pulses. **(a)** The idler pulses spectra with tunable central wavelength from 1.2 to 2.2 μm , **(b)** The signal pulses spectra with tunable central wavelength from 1.2 to 2.2 μm

angle leads to a small angular dispersion of the idler beam, which can be neglected in comparison to its divergence.

Then we reshape the idler pulses from the OPA1 by using a beam filter. The beam filter is based on a fused silica hollow core fiber with 200 μm inner diameter. The diameter of the incident idler pulse is about 5 mm, and there exists a large special chirp. In order to match the inner diameter of the fiber filter, the idler beam is focused into the filter with an $f = 150$ mm lens. The 8 mm-length fiber provides enough distance for the laser beam mode reshaping. After the fiber filter, the output

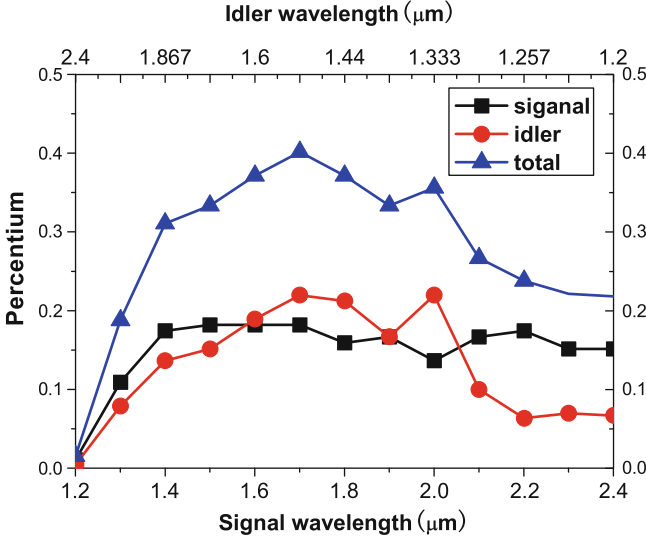


Fig. 6.8 OPA conversion efficiency curve in the final OPA stage with 6.6 mJ pump pulses, the highest total conversion efficiency up to approximately 40% is at 1.7 μm wavelength for the signal pulses

beam is recollimated by an $f = 250$ mm lens. The total energy loss of the laser beam filter is about 50%. Using the fiber filter, the spatial chirp of the idler pulses is greatly reduced and the focused beam profile is improved due to the wave-guide effect. The measured diameters of the focus for the different central wavelength pulses are about twice the diffraction limit.

Furthermore, the CEP of the tunable pulses is found to be more stable due to the improvement of the directivity of the output pulses when the fiber filter is used. We characterized the CEP stability with a homemade f-to-2f interferometer with a layout similar to [28]. Figure 6.9 shows the f-to-2f interferometric characterization of the output pulses at 1.8 μm from the OPA source. The figure shows the phase fluctuations in 10 min measurement and the CEP fluctuation is 0.103 rad (rms). Comparing to our previous work [25], the CEP fluctuation is reduced obviously with the fiber filter. The CEP stabilization of the other laser wavelengths was also demonstrated.

By using the tunable CEP stabilized laser source, we have demonstrated the HHG in argon gas target. In the experiment, the peak intensity of the 1.8 μm pulse at the focus is estimated in about $2 \times 10^{14} \text{ W cm}^{-2}$ and a 600-nm-thick Zirconium foil is placed at the entrance of the XUV spectrometer to block the residual infrared driving pulses. Figure 6.10 shows the harmonic spectrum generated in argon driven with the infrared pulses with different central wavelengths. The obtained harmonic spectrum shows a significant cutoff energy extension in comparison with the cutoff energy obtained with 0.8 μm driving laser pulses [29–31]. The cutoff is extended to the wavelength of about 9 nm, with 1.7 and 1.9 μm driving laser pulses. As we

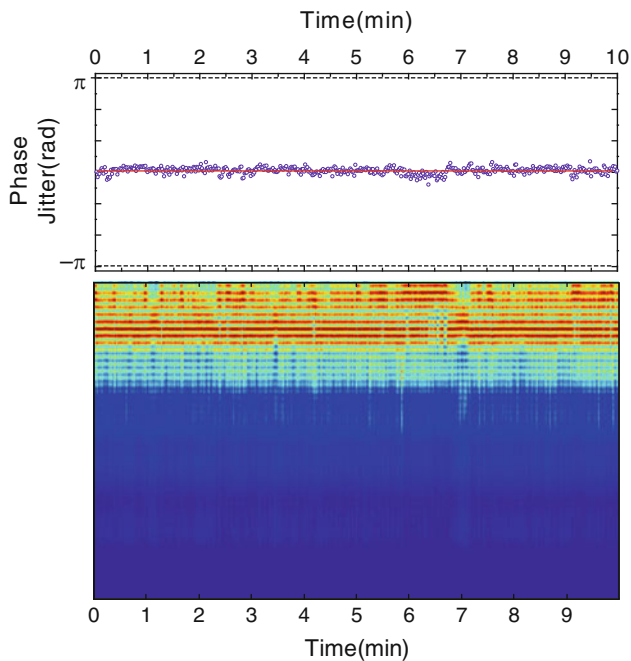


Fig. 6.9 *Lower panel*, temporal evolution of the phase-dependent interference pattern acquired in 10 min. *Upper panel*, the measured CEP fluctuation with 0.103 rad (rms) for 1.8 μm incident pulses

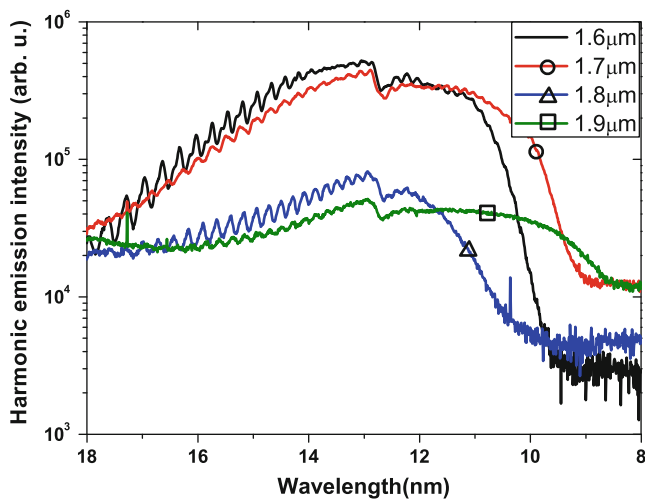


Fig. 6.10 High-order harmonic spectrum generated in argon driven by laser pulses with different central wavelengths from 1.6 to 1.9 μm

know, this is the first time that the CEP stabilized laser source based on the optical parametric amplification technique is used in HHG experiment.

One can find in Fig. 6.10 that the cut-off wavelength of HHG driven by the 1.8 μm laser pulse is longer than that driven by the 1.7 μm laser pulse. It is due to the lower conversion efficiency of the OPA at 1.8 μm than that at 1.7 μm .

6.4 Conclusions

The high order harmonic generation in helium atoms driven by two-color IR field has been investigated and the generation of isolated 67 as pulses in the water window was demonstrated when an appropriate phase shift between two driving pulses is employed. In addition, this two-color scheme can enhance the XUV emission intensity by one order of magnitude, which is important for the HHG in an IR field. For experimental implementation of the proposed scheme, we have developed an IR driving laser system with a broadband tunable range. The measured minimum CEP fluctuation of the IR laser pulses is 0.103 rad (rms) in 10 min at 1.8 μm central wavelength. The tunable range for both the signal and idler pulses is from 1.2 to 2.4 μm and the output laser power in the tunable region of 1.5–1.7 μm is about 1.2 W. HHG in argon driven with this tunable CEP-stabilized IR laser source was demonstrated. Further improvement of the OPA amplifier is in preparation and the experimental testing of the proposed scheme of water-window attosecond pulse generation is on the way.

Acknowledgements We thank the technical help offered by Pengfei Wei, Yansui Huang, Chuang Li, and Yinghui Zheng. This work was supported by National Basic Research Program of China (Grant No. 2006CB806000), National Natural Science Foundation (Grant Nos. 10734080, 60578049, 10523003), the State Key Laboratory Program of Chinese Ministry of Science and Technology, the Knowledge Innovation Program of Chinese Academy of Sciences and Shanghai Commission of Science and Technology under Grant No. 07JC14055.

References

1. M. Drescher, M. Hentschel, R. Kienberger, M. Uiberacker, V. Yakovlev, A. Scrinzi, Th. Westerwalbesloh, U. Kleineberg, U. Heinzmann, F. Krausz, *Nature* **419**, 803–807 (2002)
2. T. Brabec, *Rev. Mod. Phys.* **72**, 545–591 (2000)
3. I.J. Sola, E. Mével, L. Elouga, E. Constant, V. Strelkov, L. Poletto, P. Villoresi, E. Benedetti, J.-P. Caumes, S. Stagira, C. Vozzi, G. Sansone, M. Nisoli, *Nat. Phys.* **2**, 319–322 (2006)
4. T. Pfeifer, L. Gallmann, M.J. Abel, D.M. Neumark, S.R. *Opt. Lett.* **31**, 975 (2006)
5. P.B. Corkum, *Phys. Rev. Lett.* **71**, 1994–1997 (1993)
6. P.M. Paul, E.S. Toma, P. Breger, G. Mullot, F. Augé, Ph. Balcou, H.G. Muller, P. Agostini, *Science* **292**, 1689–1692 (2001)
7. S. Sartania, Z. Cheng, M. Lenzner, G. Tempea, Ch. Spielmann, F. Krausz, K. Ferencz, *Opt. Lett.* **22**, 1562–1564 (1997)

8. E. Goulielmakis, M. Schultze, M. Hofstetter, V.S. Yakovlev, J. Gagnon, M. Uiberacker, A.L. Aquila, E.M. Gullikson, D.T. Attwood, R. Kienberger, F. Krausz, U. Kleineberg, *Science* **320**, 1614–1617 (2008)
9. Z. Zeng, Y. Cheng, X. Song, R. Li, Z. Xu, *Phys. Rev. Lett.* **98**, 203901 (2007)
10. H. Merdji, T. Auguste, W. Boutu, J.-P. Caumes, B. Carré, T. Pfeifer, A. Jullien, D.M. Neumark, S.R. Leone, *Opt. Lett.* **32**, 3134–3136 (2007)
11. Z. Zeng, Y. Leng, R. Li, Z. Xu, *J. Phys. B* **41**, 215601 (2008)
12. Ch. Spielmann, N.H. Burnett, S. Sartania, R. Koppitsch, M. Schnürer, C. Kan, M. Lenzner, P. Wobrauschek, F. Krausz, *Science* **278**, 661–664 (1997)
13. C. Vozzi, F. Calegari, E. Benedetti, S. Gasilov, G. Sansone, G. Cerullo, M. Nisoli, S. De Silvestri, S. Stagira, *Opt. Lett.* **32**, 2957–2959 (2007)
14. P. Zou, R. Li, Z. Zeng, H. Xiong, P. Liu, Y. Leng, P. Fan, Z. Xu, *Chin. Phys. B* **19**, 019501 (2010)
15. M. Lewenstein, Ph. Balcou, M.Y. Ivanov, A. L’Huillier, P.B. Corkum, *Phys. Rev. A* **49**, 2117–2132 (1994)
16. C. Kan, C.E. Capjack, R. Rankin, N.H. Burnett, *Phys. Rev. A* **52**, R4336–R4339 (1995)
17. M.V. Ammosov, N.B. Delone, V.P. Krainov, *Sov. Phys. JETP* **64**, 1191–1194 (1986)
18. X.M. Tong, S.-I. Chu, *Phys. Rev. A* **61**, 021802 (2000)
19. J.J. Carrera, X.M. Tong, S.-I. Chu, *Phys. Rev. A* **74**, 023404 (2006)
20. L. Cohen, *Time-Frequency Analysis*, chap. 7. (Prentice Hall, Englewood Cliffs, 1995)
21. A. Baltuška, T. Fuji, T. Kobayashi, *Phys. Rev. Lett.* **88**, 133901 (2002)
22. C. Vozzi, C. Manzoni, F. Calegari, E. Benedetti, G. Sansone, G. Cerullo, M. Nisoli, S. De Silvestri, S. Stagira, *J. Opt. Soc. Am. B* **25**, 112–117 (2008)
23. C. Vozzi, F. Calegari, F. Frassetto, L. Poletto, G. Sansone, P. Villoresi, M. Nisoli, S. De Silvestri, S. Stagira, *Phys. Rev. A* **79**, 033842 (2009)
24. C.P. Hauri, R.B. Lopez-Martens, C.I. Blaga, K.D. Schultz, J. Cryan, R. Chirla, P. Colosimo, G. Doumy, A.M. March, C. Roedig, E. Sistrunk, J. Tate, J. Wheeler, L.F. DiMauro, *Opt. Lett.* **32**, 868–870 (2007)
25. C. Zhang, J. Wang, P. Wei, L. Song, C. Li, C.-J. Kim, Y. Leng, *Chin. Phys. B* **18**, 1469–1472 (2009)
26. S. Adachi, P. Kumbhakar, T. Kobayashi, *Opt. Lett.* **29**, 1150–1152 (2004)
27. C. Zhang, P. Wei, Y. Huang, Y. Leng, Y. Zheng, Z. Zeng, R. Li, Z. Xu, *Opt. Lett.* **34**, 2730–2733 (2009)
28. M. Kakehata, H. Takada, Y. Kobayashi, K. Torizuka, Y. Fujihira, T. Homma, H. Takahashi, *Opt. Lett.* **26**, 1436–1438 (2001)
29. C.G. Durfee, III, A.R. Rundquist, S. Backus, C. Herne, M.M. Murnane, H.C. Kapteyn, *Phys. Rev. Lett.* **83**, 2187–2190 (1999)
30. A. Rundquist, C.G. Durfee III, Z. Chang, C. Herne, S. Backus, M.M. Murnane, H.C. Kapteyn, *Science* **280**, 1412–1415 (1998)
31. H. Kapteyn, O. Cohen, I. Christov, M. Murnane, *Science* **317**, 775–778 (2007)

Chapter 7

High Harmonic Generation by Plasmonic Enhancement of Femtosecond Pulse Laser

Seungchul Kim, In-Yong Park, Joonhee Choi, and Seung-Woo Kim

Abstract Coherent EUV light is generated directly from a modest femtosecond laser whose pulse intensity reaches only $10^{11} \text{ W cm}^{-2}$. This value is in fact two orders of magnitude lower than the threshold pulse intensity required for high harmonic generation using noble gases. The key to this achievement is the plasmonic field enhancement by means of metallic nanostructures fabricated in bow-tie shape. This method requires no extra cavities for amplification of pulse intensity and thereby could form the basis to construct laptop-sized coherent EUV sources for many advanced applications lithographic and high-resolution imaging.

7.1 Introduction

High harmonic generation is a well-known method of generating coherent short wavelength light in the extreme ultra violet (EUV) and soft X-ray range using ultrafast laser pulses [1–3]. Focusing an intense laser pulse onto the gaseous target atom enables the generation of high harmonics by accelerating outer-bound electrons to tunnel through the atomic potential barrier with subsequent immediate recombination of the electrons toward the nucleus. This frequency up-conversion process requires strong pulse intensities typically more than $10^{13} \text{ W cm}^{-2}$, which is usually attained by adopting several sequential stages of chirped pulsed amplification (CPA) [4, 5]. Each CPA stage requires a long active cavity and a high power pumping source, thereby adding a substantial burden of hardware bulkiness and fragility in high harmonic generation. Besides, CPA is unavoidably accompanied by reduction of the pulse repetition rate because the maximum pumping energy is limited to protect the amplification crystal from thermal damage. The reduced pulse repetition rate results in a too narrowly spaced comb, implying that the generated high

S. Kim, In-Y. Park, J. Choi, and S.-W. Kim (✉)

Ultrafast Optics for Ultraprecision Group, Korea Advanced Institute of Science and Technology (KAIST), Science Town, Daejeon, 305–701, South Korea

e-mail: inter99@kaist.ac.kr, inyong@kaist.ac.kr, nguyjh@kaist.ac.kr, swk@kaist.ac.kr

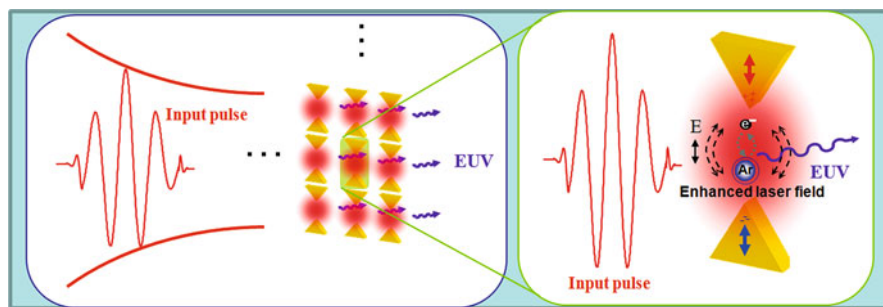


Fig. 7.1 Conceptual illustration of high harmonic generation by surface plasmon resonance. (*Left*) The nanostructure comprising bow-tie elements is illuminated by a femtosecond pulse laser. The intensity field of the incident laser is enhanced by the plasmonic resonance of the surface electrons confined within the bow-ties. (*Right*) The enhanced intensity exceeds the threshold value for high harmonic generation, so coherent EUV radiation is emitted from the gaseous Ar atom injected on the bow-ties [8]

harmonics are unable to maintain the original comb structure of the incident femtosecond pulse laser. This problem may be avoided by replacing CPA with an extra passive cavity configured to directly accumulate the output power of a femtosecond laser oscillator without reduction of the pulse repetition rate [6, 7]. However, the extra cavity demands special care in design and operation since it should well match the source oscillator cavity in dispersion and other resonance characteristics.

Here we describe another way of high harmonic generation that permits replacing CPA cavities with compact metallic nanostructures [8]. As illustrated in Fig. 7.1, the key idea is to exploit the phenomenon of surface plasmon resonance to amplify the electric field of the incident femtosecond laser pulse. Surface plasmons are the collective movement of free electrons bound in a metallic nanostructure, which oscillates or propagates along the surface of a conductor in response to the ambient electromagnetic wave [9–11]. The metallic nanostructure used here is comprises gold bow-ties fabricated on a quartz substrate. The electric field around the nanostructure is enhanced by the resonance of localized surface plasmons. The field enhancement can reach up to 100 times higher than the input intensity [12–14]. This implies that the pulse output intensity of a single femtosecond laser oscillator, which is merely in the range of $10^{11} \text{ W cm}^{-2}$, is strong enough to conduct high harmonic generation. This approach of high harmonic generation offers hardware compactness and high controllability since neither additional cavity nor pumping sources are required except a single femtosecond laser oscillator. In addition, no reduction in the pulse repetition rate is required, so the original comb of the input laser can be maintained in the generated high harmonics. Furthermore, high harmonics are emitted from point-like sources to be well suited for near-field applications of microscopy, imaging, and high resolution lithography.

A single bow-tie element in the nanostructure consists of two triangular patches that face each other tip to tip with a small separation gap in between. Single-tipped elements such as nanoparticles and nanorods suffer the problem that the enhanced

laser field rapidly decays in the vicinity of the tip [15, 16]. On the other hand, the bow-tie element is able to maintain highly enhanced field over the separation gap between two triangular patches, thereby enabling to provide a large effective area for high harmonic generation [17, 18]. This advantage can be readily verified by Finite Difference Time Domain (FDTD) analysis employed in this study to compute the near-field intensity distribution precisely around the bow-tie nanostructure. FDTD analysis enables numerical computation of the enhanced electric field with nanometer spatial resolutions while varying the dimension of the bow-tie nanostructure. In consequence, the effect of the actual tip shape that differs from the ideal shape due to imperfect fabrication can be precisely examined, which leads to establishment of the permissible dimensional tolerance on fabricated bow-ties.

7.2 Geometrical Design of Bow-Tie Nanostructure

Figure 7.2 shows the four design parameters characterizing the geometry of the bow-tie nanostructure; the height (h), thickness (t), apex angle (θ), and separation gap (d). These design parameters have to be selected to maximize the enhanced intensity field from the viewpoint of high harmonic generation. For a given set of design parameters, the corresponding enhanced field can precisely be calculated by adopting the FDTD method that permits solving the Maxwell equations numerically in consideration of the bow-tie geometry as well as the ambient conditions including the incident laser pulse. The incident laser pulse used in the FDTD simulation is assumed to be obtained from a Ti:sapphire femtosecond laser oscillator that will actually be used for the experimental validation to be explained later on. The incident pulse has an 800-nm carrier wavelength with 10 fs pulse duration. The pulse is incident normal to the planar surface of the bow-tie, and the polarization direction is positioned parallel to the line connecting the vertices as depicted in Fig. 7.2. The bow-tie material is gold (Au) and the complex dielectric constant of gold is determined by following the modified Debye model [19]. The whole bow-tie nanostructure is divided into 1 nm-sided cubic cells in for 3-D FDTD simulation. The incremental time-step in numerical computation is selected 1.9 attosecond in consideration of the predetermined size of the cubic cells. The surrounding of the bow-tie is assumed as vacuum by applying the perfectly matched layer of the free space boundary condition. For quantitative comparison of the induced field enhancement, two representative points are selected in the middle thickness layer of the bow-tie: Center point and Apex point as indicated in Fig. 7.2. The intensity enhancement factor is computed as the ratio of the enhanced field intensity to the input laser intensity.

Figure 7.3 illustrates FDTD simulation results computed repeatedly by changing the four geometrical parameters to determine the intensity enhancement factor at Center point and Apex point. In the first place, the effect of the height (h) is plotted in Fig. 7.3a. The intensity enhancement factor at Apex point reaches a maximum of 6,200 when $h = 175$ nm while it varies from 100 to 215 nm. Other three

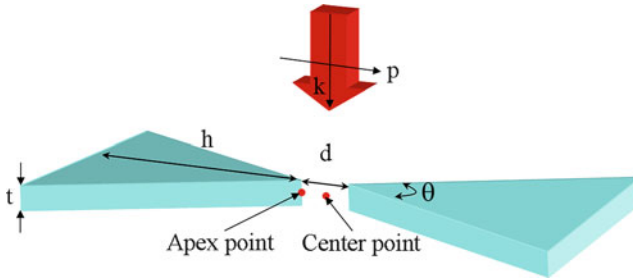


Fig. 7.2 The geometry of FDTD simulation conditions for plasmon resonance enhancement of the bow-tie nanostructure. Four geometrical parameters (height: h , thickness: t , apex angle: θ , and separation gap: d) are defined along with the incident wave vector (k) and polarization (p) of the femtosecond laser pulse. Two representative points (apex point and center point) in the middle thickness layer are selected for comparing the intensity enhancement factor for different design parameters

parameters are fixed constant; the separation gap is 20 nm, the thickness is 50 nm and the apex angle is 30° . Figure 7.3b shows a similar result in which the separation gap is changed to 40 nm with other two parameters remaining the same, while FDTD computation is performed by varying the height.

In the case of $d = 40$ nm as shown in Fig. 7.3b, the intensity enhancement significantly decreases by about 50% as compared with the previous case of $d = 20$ nm. However, its overall variation with height appears to be very similar to that of Fig. 7.3a with its maximum being at the same height of 175 nm. This implies that the vibration wavelength of free electrons within the bow-tie induced for the particular height value matches the carrier wavelength of the incident pulse well. If the carrier wavelength is taken to be smaller, the intensity enhancement finds its maximum at longer heights. For instance, FDTD simulation reveals that for a carrier wavelength of 1,060 nm, maximum enhancement occurs at a height of 220 nm.

The thickness affects field enhancement as shown in Fig. 7.3c. When the thickness is more than 40 nm, surface plasmons confined near the tips of the bow-tie structure becomes less dense, thereby decreasing field enhancement. If the thickness is too thin, not enough plasmons are concentrated on the tips. Effect of the apex angle can also be interpreted in a similar way from the simulation result of Fig. 7.3d. A too narrow or too wide apex angle fails to form a suitable tip volume for surface plasmons concentration. As shown in Fig. 7.3d, the field enhancement yields a maximum value when the apex angle is 30° . Finally, the separation gap is varied from 10 to 120 nm as shown in Fig. 7.3e. Oscillating plasmons within a triangular patch interact with other plasmons in the opposite patch. Thus a smaller gap allows for higher interaction. In practice, there is a minimum gap that can be fabricated, depending on using the fabrication process.

For high harmonic generation from a femtosecond laser with intensity less than $10^{11} \text{ W cm}^{-2}$, as attempted in this study, the enhancement factor should be more than 20 dB. A very high intensity enhancement factor may be achieved over a small area, but it cannot be a good design if the area is too small. Thus, the total volume

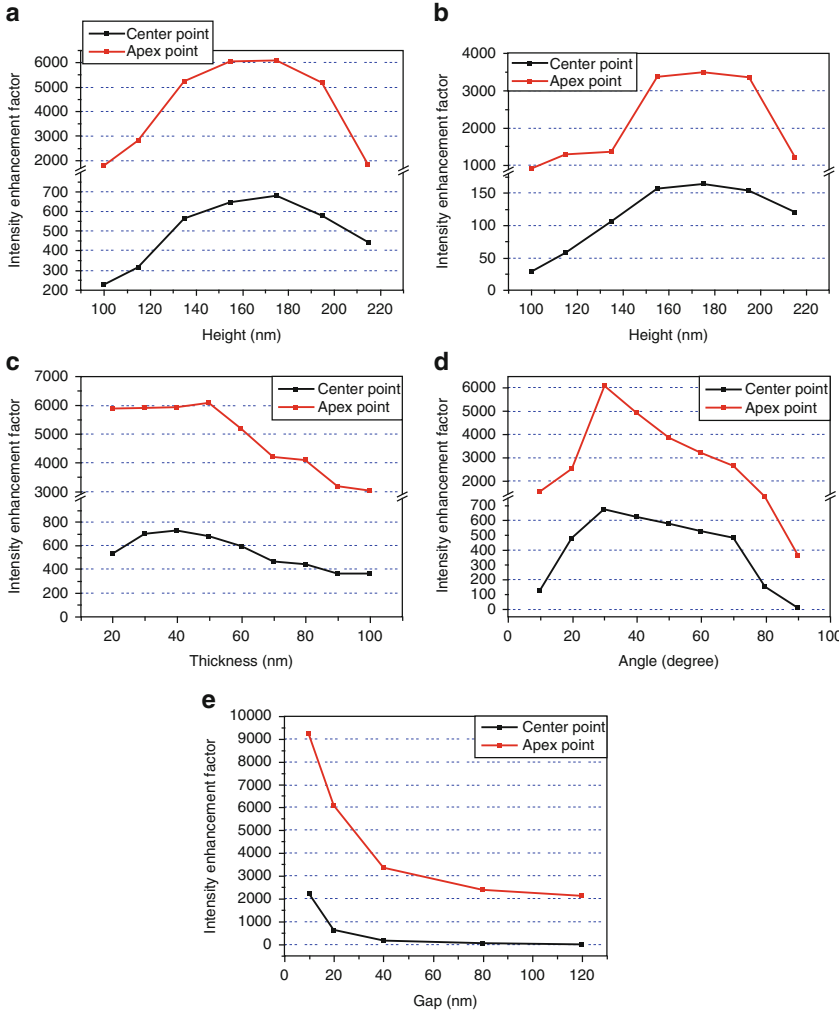


Fig. 7.3 FDTD simulation results. The intensity enhancement factor vs. design parameters at Center point (black line) and Apex point (gray line). (a) Effect of height when separation gap is fixed at 20 nm. (b) Effect of height when separation gap is 40 nm. (c) Effect of thickness. (d) Effect of apex angle. (e) Effect of separation gap. Other design parameters except each varying parameter are fixed as height at 175 nm, apex angle at 30° , thickness at 50 nm, and separation gap at 20 nm

whose intensity enhancement factor exceeding 20 dB is treated as the performance index in selecting the optimum combination of the design parameters. For example, the maximum intensity enhancement becomes higher when the separation gap is set at 10 nm than the case of 20 nm. However, the total volume of 20 dB for 20 nm gap is nearly twice that of 10 nm gap. Therefore, more high harmonic generation could be triggered with 20 nm gap. The optimum selection of the design parameters should be able to provide the largest value of the 20 dB volume.

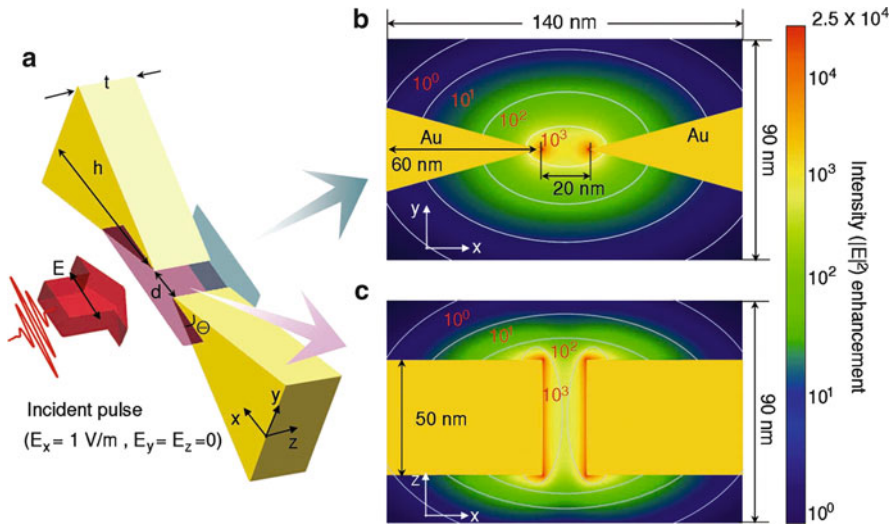


Fig. 7.4 Near field intensity distribution of the suggested bow-tie nanostructure which has a height of 175 nm, separation gap of 20 nm, apex angle of 30° , and thickness of 50 nm. The calculated near-field distribution shows highly enhanced electromagnetic field more than 20 dB within the $60 \times 50 \times 50 \text{ nm}$ volume ($x \times y \times z$) in the gap between the bow-tie vertices [8]

Among the four design parameters, the height, thickness, and apex angle share a common trend, each giving the almost identical variation to the 20 dB volume as well as the intensity enhancement factor. This is not the case for the separation gap; the largest 20 dB volume is attained when the gap is 20 nm while the maximum enhancement is when the gap is less than 10 nm. In consideration of all these effects, the optimum combination of the four design parameters is concluded as the height of 175 nm, thickness of 50 nm, angle of 30° , and gap of 20 nm. The corresponding 20 dB volume is finally computed as $60 \times 50 \times 50 \text{ nm}$ ($x \times y \times z$) in the gap between the bow-tie vertices (Fig. 7.4).

FDTD simulation also enables us to determine the temporal variation of the enhanced field in synchronization to the incident pulse. Figure 7.5 shows two representative temporal profiles computed at Center point and Apex point as defined in Fig. 7.2. Examining the two temporal profiles reveals two important facts: First, the enhanced profiles are of 90° phase delay with respect to the incident pulse. This confirms that our optimal design of the bow-tie nanostructure provides perfect resonance of surface plasmons as requested. Second, both the enhanced profiles have pulse duration longer than that of the original incident pulse, each experiencing a ringing-down oscillation at its tail. This is a general phenomenon observed in resonance, and the ringing-down oscillation is affected by the damping within the gold metal bow-tie.

In the aforementioned simulation, the bow-tie was assumed to have an ideal shape with two perfectly sharp tips, but in practice this is always not the case due to imperfection of nanofabrication. The focused ion beam process or E-beam lithography may be used as they are able to provide fine machining resolutions in

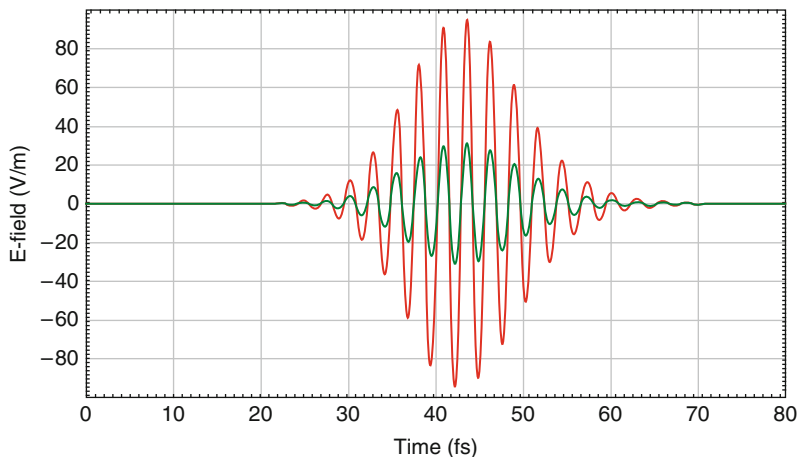


Fig. 7.5 Temporal profiles of the plasmonic enhanced near-field at Center point (*dark gray*) and apex point (*light gray*). This simulation reveals a uniform phase delay of 90° with respect to the incident pulse. Ringing-down oscillation is observed at the tails of the two profiles.

the nanometer range. Nonetheless, actually fabricated bow-ties yield blunt tips, not enabling us to achieve the field enhancement originally pursued by the ideal sharp tip. To know the degrading effect caused by imperfect machining more precisely, two commonly encountered actual tip shapes are taken into FDTD simulation; one is the rounded shape and the other is the flat tip as illustrated in Fig. 7.6. Other geometrical parameters remain identical to the ideal bow-tie nanostructure having a height of 175 nm, thickness of 50 nm, apex angle of 30° , and separation gap of 20 nm. This simulation is aimed to find how the two imperfect tips affect the intensity enhancement factor as well as the 20 dB volume. As in the simulation result plotted in Fig. 7.6a, the intensity enhancement factor at Center point experiences a slight decrease even though the curvature diameter of the rounded tip significantly increases. On the other hand, the intensity enhancement factor at Apex point is much affected following an exponential decrease. This is because the enhancement at Apex point is contributed by the dense electric flux that strongly depends on the confinement density of oscillating surface plasmons at the tip end. It is unlikely that the electric field at Center point will be more influenced by the overall plasmons interaction between the two tips facing each other within the bow-tie, thus slight spreading of surface plasmons over the rounded tips is found not very influential to the enhancement at this location in the middle of the separation gap. It is also noteworthy that when the curvature diameter of the rounded tip increases to 50 nm, the 20 dB volume reduces by 40% compared to the ideal tip. Nonetheless, high harmonic generation is still possible by the remaining 60% of the 20 dB volume. It is therefore safely concluded that the height and separation gap are more important parameters than the tip shape. The same tendency is observed in the case of the flat tip as shown in Fig. 7.6c, d, with the exception that the decaying rate of intensity enhancement with increase of the flat tip length is slightly larger than the case of the rounded tip.

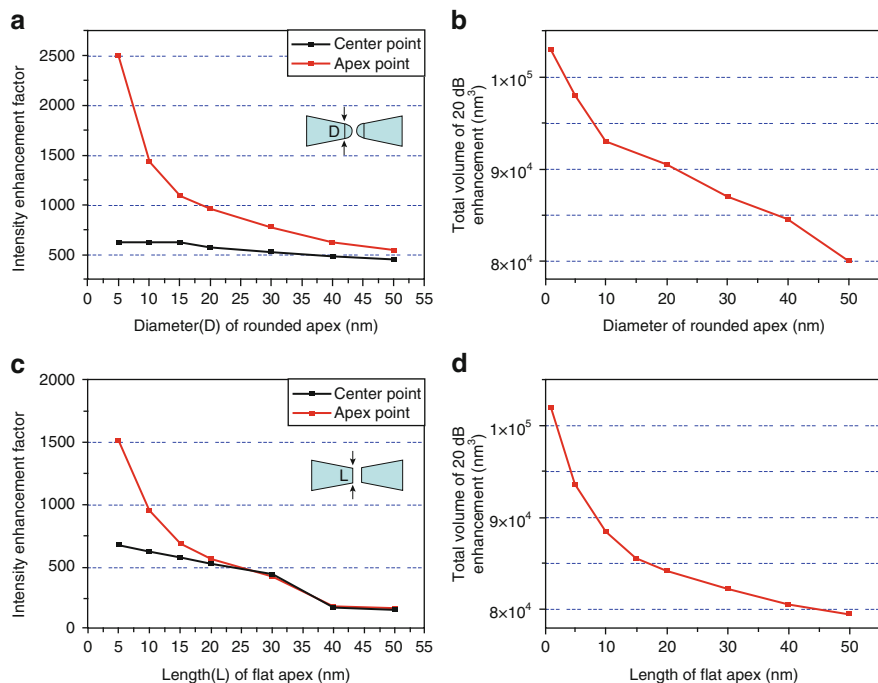


Fig. 7.6 Effects of non-ideal tip shapes on the intensity enhancement capability of the bow-tie nanostructure. **(a)** Enhancement factor vs. curvature diameter of the rounded tip. **(b)** 20 dB volume vs. curvature diameter. **(c)** Enhancement factor vs. length of flat apex. **(d)** 20 dB volume vs. flat length

7.3 Fabrication of Bow-Tie Nanostructure

Figure 7.7 shows SEM images of the bow-tie nanostructure fabricated in this study by the focused ion beam process. The nanostructure is comprises bow-tie elements arranged in a two-dimensional array. Bow-ties are made on a 400- μm thick sapphire wafer, on which a 50 nm gold layer is evaporated on the top of a 5-nm chromium adhesion layer. The sapphire wafer provides high thermal conductivity, thereby being able to dissipate heat from the nanostructure when the bow-tie array is illuminated by a consecutive train of femtosecond laser pulses for high harmonic generation. The beam acceleration voltage of the used focused ion beam machine (SMI 3050 TB) is 30 kV along with a 1 pA current and 50 μs dwell time. The current level is directly related to the focused beam size, so it needs to be set as low as possible to produce fine structural patterns. The dwell time determines the total amount of beam scanning, thus it is adjusted to minimize the broadening of the machined structure due to the beam drift during the focused beam-milling process. As shown in Fig. 7.7, a total of 30×15 bow-ties occupy an area of $10 \times 10 \mu\text{m}$

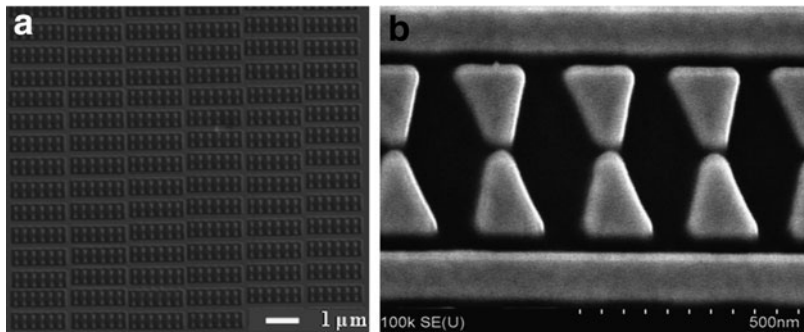


Fig. 7.7 SEM images of the fabricated bow-tie nanostructure. (a) The nanostructure occupies a planar area $10 \times 10 \mu\text{m}$ in which 30×15 bow-tie elements are accommodated in a 2-D array. (b) Magnified image of the bow-tie nanostructure. Owing to the high magnification, edge lines are seen blurred by multiple scattering of electrons in imaging

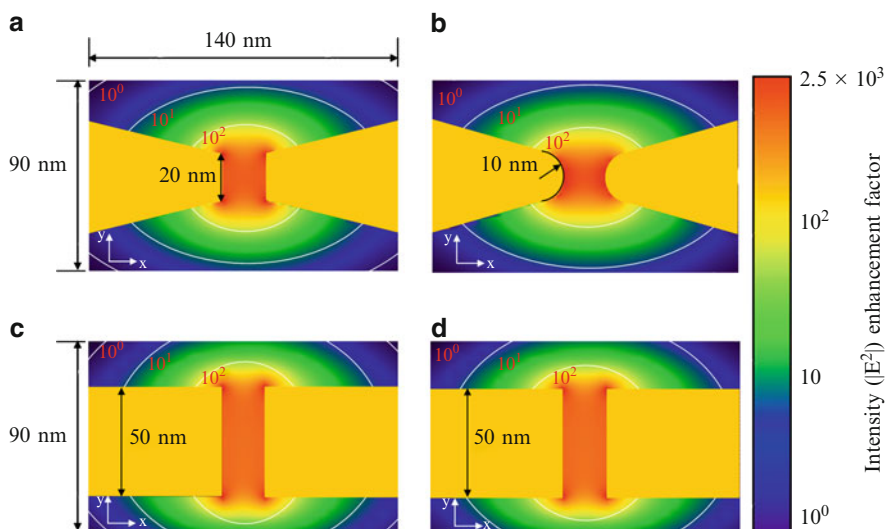


Fig. 7.8 FDTD simulation for actual blunt tips. (a) Top view of the induced enhancement for the flat tip of 20 nm cut length. (b) Top view of the intensity enhancement for the round tip of 10 nm radius. (c) Side view for the flat tip. (d) Side view for the round tip

on the sapphire substrate, which is approximately the spot diameter of the incident femtosecond laser.

In the magnified SEM image of Fig. 7.7, the tips and edge lines are seen blurred due to the multiple scattering of electrons in imaging. By examining the SEM image, it is estimated that the actual tips can be regarded as a round tip of an effective curvature radius of approximately 10 nm, or as a flat tip of 20 nm cut length. Figure 7.8 shows the result of FDTD analysis performed for these actual tip shapes. In comparison to the case of the perfect tip shown in Fig. 7.4, the simulation result confirms

that the blunt tips cause no significant reduction in the 20 dB volume. Particularly the intensity enhancement over the entire separation gap of the bow-tie exceeds the threshold of 20 dB that is minimally required for the high harmonic generation intended in this study.

7.4 Experiments of High Harmonic Generation

For high harmonics generation, the fabricated bow-tie nanostructure is located inside the vacuum chamber as illustrated in Fig. 7.9. Then it is illuminated by the focused beam of a femtosecond laser through the sapphire substrate. The group delay dispersion caused by the chamber window, the focusing lens, and the sapphire substrate is compensated using a pair of chirped mirrors and a wedge. The focused beam on the target nanostructure yields a spot diameter of $5\text{ }\mu\text{m}$ in FWHM (full width half maximum), a peak pulse intensity of $3.6 \times 10^{11}\text{ W cm}^{-2}$, and pulse duration of approximately 12 fs measured by using the optical correlation method.

In the apparatus configured for the high harmonic generation and detection, the photon multiplier is located at a distance of 469 mm from the varied line spacing grating that consequently disperses the generated EUV light over the wavelength range of 22–124 nm. The photon multiplier is mounted on a precision stage that moves along the dispersing line of the grating. No Al filters are required to block the incident femtosecond laser, since the used photon multiplier is sensitive to only high harmonics below 200 nm wavelength. The grating has a narrow acceptance angle of $\pm 1.0^\circ$, and provides a 1.0 nm wavelength sampling resolution. To reduce

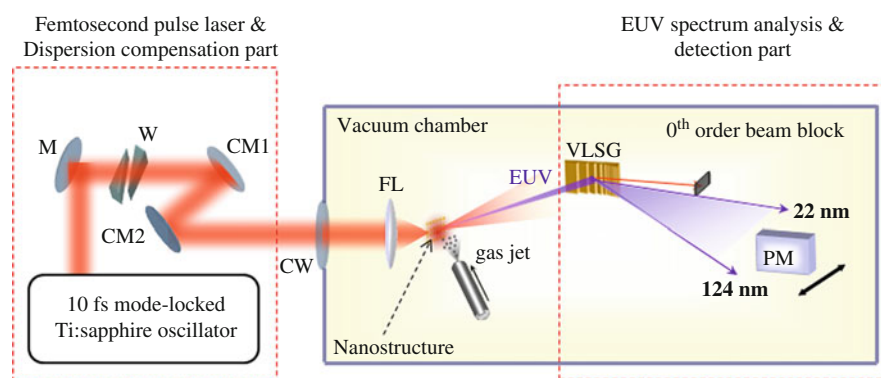


Fig. 7.9 Apparatus for high harmonic generation by means of plasmonic resonance using the bow-tie nanostructure. The whole system is divided into three major parts; A dispersion-controlled femtosecond pulse laser source, a vacuum chamber to accommodate the nanostructure and the injecting module of gas jet, and the EUV spectrum detector consisting of a dispersive grating and a photon multiplier *CM*, chirped mirror; *CW*, chamber window; *L*, focusing lens; *M*, mirror; *PM*, photon multiplier; *VLSG*, varied-line-spacing grating; *W*, wedge plate

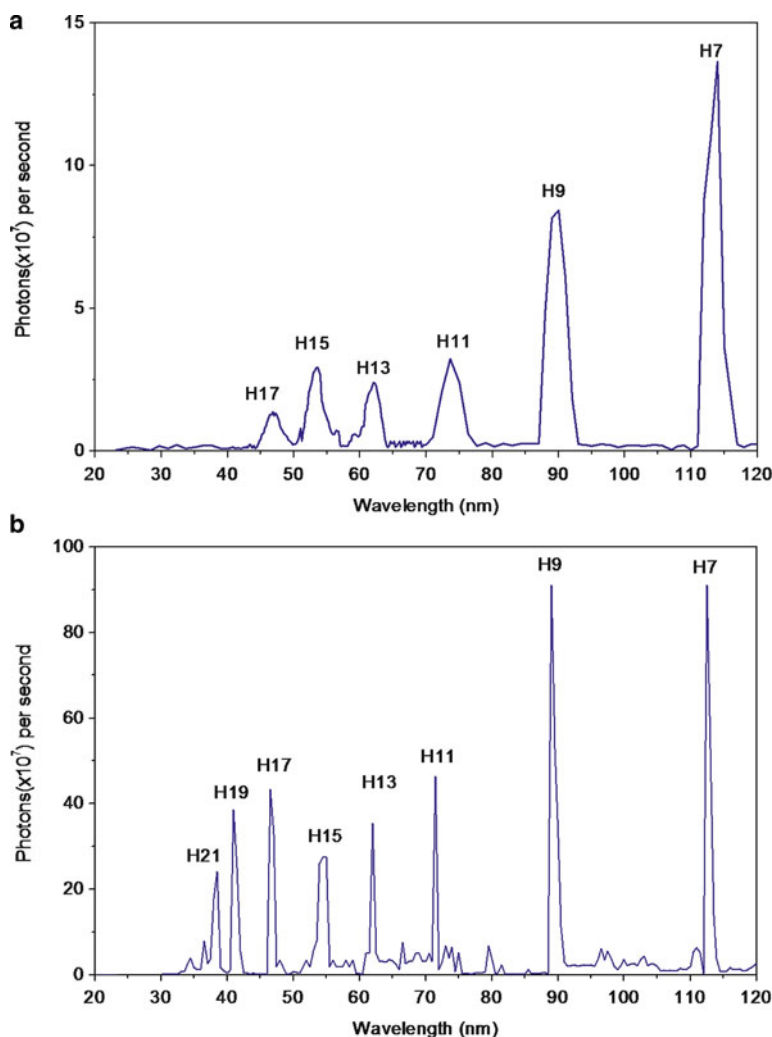


Fig. 7.10 High harmonic spectra obtained using plasmonic enhancement by injection of argon (a) and xenon (b). A varied-line-spacing grating was used to disperse the 22–124 nm wavelength band. H7, H9, and H21 were collected by moving a photon multiplier in fine steps along the disperse line. The aperture of photon multiplier was covered by a slit of 1.0 mm width to reduce the convolution of neighboring harmonic signals. Given the input pulse power of 100 mW, the efficiencies for the harmonics were different with a type of gas in use. The case of xenon injection shows more efficient photon emission than that of argon injection

the convolution effect on the measured harmonics, a slit of 1.0 mm width is attached in front of the photon multiplier.

Figure 7.10 shows the spectrums of generated high harmonics from argon and xenon gases. Each noble gas is injected on to the nanostructure continuously through a metal nozzle of a 100- μ m diameter. The back pressure of the injected gas jet is

set at 115 torr using a mass flow controller. From the xenon gas, odd harmonics up to 21st order are detected. The used spectrometer for the high harmonic detection consists of a varied line spacing grating (Hitachi, 001-0639) and a photon multiplier (Photonics, 4751G CSI). In the measured spectrums, H3 (266 nm) and H5 (160 nm) are not seen because they are out of the detection range of the used spectrometer.

The spectral characteristics typically seen in the high harmonics generated by chirped power amplification (CPA) are observed [20, 21] as evidenced by the rapid decrease of the lowest order harmonics region from H7 to H11 harmonic, a plateau from H11 to H15, and a abrupt cut-off at H17 with the argon gas. In the case of xenon gas, the cut-off appears at higher orders than the case of the argon gas. Given that the input femtosecond laser provides a small peak power of 100 kW, the observed harmonics yield relatively low power in the range of a few nW in total. However, the conversion efficiency with Ar gas was found to be in the level of 2.4×10^{-9} for H7 and all the way down to 6.9×10^{-10} for H17, which is comparable to those of CPA. As listed in Table 7.1, harmonic generation with Xenon gas shows more efficient energy conversion of 10^{-8} which is generally observed in generation of high harmonics.

It is expected that the original comb structure is maintained in each of the generated harmonics as there was no reduction in the repetition rate of the incident femtosecond pulses. When sapphire is exposed to an intensity of greater than $10^{13} \text{ W cm}^{-2}$, it could break down due to multi-photon ionization [22]. However,

Table 7.1 Photon efficiency of generated high harmonics with injection of (a) argon and (b) xenon gases

(a)			
Wavelength	Photon number, N (/s)	P(λ) [nW]	Efficiency
H7 (114 nm)	1.1×10^8	0.240	2.4×10^{-9}
H9 (89 nm)	8.0×10^7	0.223	2.2×10^{-9}
H11 (73 nm)	2.8×10^7	0.095	9.5×10^{-10}
H13 (61 nm)	2.2×10^7	0.090	9.0×10^{-10}
H15 (53 nm)	2.8×10^7	0.131	1.3×10^{-9}
H17 (47 nm)	1.3×10^7	0.069	6.9×10^{-10}
(b)			
Wavelength	Photon number, N (/s)	P(λ) [nW]	Efficiency
H7 (114 nm)	1×10^9	2.4	2.4×10^{-8}
H9 (89 nm)	1×10^9	2.78	2.78×10^{-8}
H11 (73 nm)	6×10^8	2.03	2.03×10^{-8}
H13 (61 nm)	5×10^8	2.04	2.04×10^{-8}
H15 (53 nm)	4×10^8	1.87	1.87×10^{-8}
H17 (47 nm)	5.4×10^8	2.87	2.87×10^{-8}
H19 (47 nm)	5.1×10^8	3.01	3.01×10^{-8}
H21 (47 nm)	3×10^8	1.95	1.95×10^{-8}

The first column denotes the order and wavelength of high harmonics. The second column lists the detected photon number per second. The energy conversion efficiency shown in the fourth column was calculated from the emitting power of each harmonics presented in the third column

this is not seen in our experiments since the enhanced electric field is formed in the gap of each bow-tie. This was verified by SEM images after the experiment. The gold bow-tie electrode itself is also susceptible to thermal damages due to photon-electron coupling if the pulse intensity exceeds the thermal threshold of $10^{11} \text{ W cm}^{-2}$ [23]. As the sapphire substrate functions as a good heat dissipater, no serious ablation or melting on the gold bow-ties is observed as long as the incident intensity is well controlled not to exceed the threshold intensity.

Another concern is the spatial distribution of emitted high harmonics from the bow-tie nanostructure. The intense spot of focused femtosecond pulse on the surface of the nanostructure has a $5 \mu\text{m}$ diameter, which involves approximately 150 bow-ties simultaneously in high harmonic generation. Each bow-tie could be approximated as a dipolar source that radiates high harmonics with a broad angle distribution. The consequent wave collectively observed from the bow-ties is therefore the constructive interference of the individual waves emitted from all the bow-ties maintaining high coherence in both spatial and temporal terms. These multiple interferences cause the particular spatial diffraction pattern that the nanostructure would produce as a two-dimensional diffractive grating as a whole. For instance, H17 harmonic of 47-nm wavelength has the first-order diffraction angle of 13.6° in one direction and 4.9° in the other direction, with other higher-order diffraction angles being larger than those of the first-order angles. In the experiment, only the zeroth-order diffraction of H17 harmonic was collected by the photon multiplier because all other diffraction angles lie beyond the acceptance angle of $\pm 1.0^\circ$ of the used spectrometer, and this is also the case for other detected harmonics of H7–H15. Obviously all the zeroth-order diffracted rays of the generated harmonics proceed in the same propagation direction of the incident femtosecond pulse, thereby residing within a narrow cone-shaped $\pm 7^\circ$ angle distribution being formed in response to the focusing angle of the incident pulse. An additional concern was the dispersion-induced phase mismatch due to the interaction of generated harmonics with the injected Ar gas. However, no particular attention was paid to this problem since the field enhancement for high harmonics generation is confined to a short length of less than $1 \mu\text{m}$ as the incident femtosecond pulse passes through bowties.

Monitoring the cut-off frequency of generated high harmonics allows us to estimate the enhanced intensity of the incident femtosecond laser around the bow-tie nanostructure. The photon energy of the emitted harmonics is determined as,

$$E_{\text{max}} = I_p + 3.17U_p, \quad (7.1)$$

where E_{max} is the maximum energy of emitted harmonic photons, I_p is the ionization energy of the injected gas, and U_p is the ponderomotive potential. For a linearly polarized incident field, U_p has the form of

$$U_p = 9.33 \times 10^{-14} I_L \lambda^2, \quad (7.2)$$

where I_L and λ are the intensity and wavelength of the incident field, respectively. From the generated harmonic spectrum of the xenon gas, E_{max} can be set to be

32.6 eV, because the highest harmonic is 21st order. By adopting the first ionization energy of xenon (12.1 eV), the enhanced laser intensity is worked out to be $1.1 \times 10^{14} \text{ W cm}^{-2}$. For the case of argon injection, using the same procedure, the enhanced laser intensity is obtained as $5.4 \times 10^{13} \text{ W cm}^{-2}$, which is in the same order of magnitude as the xenon. Thus the intensity enhancement induced by the bow-tie nanostructure can be expected to be more than 20 dB or 100 times. Our FDTD simulation predicts that the intensity enhancement factor could reach 1,000 within the separation gap of bow-ties, but such a high intensity enhancement is not easily detected. The reason is that high enhancement is localized to an extremely tiny area as small as a few cubic nm.

Generally argon allows for higher order harmonic than xenon due to its higher ionization energy. When the local field enhancement by argon occurs in the same way as in xenon, the highest harmonics must be 23rd order (34 nm in wavelength). However, the corresponding experimental highest harmonic is 17th (47 nm in wavelength), which is 3 orders less than the simulation prediction. The reason may be the low conversion efficiency of argon, not enabling us to detect due to too low power. The overall conversion efficiency is found to be around 10^{-8} – 10^{-9} which is lower than the traditional way of high harmonic generation using CPA. This is due to the short interaction length between the femtosecond laser and the injected gas, which is about few 10 nm along the propagation direction of the femtosecond laser [24]. With CPA, the femtosecond pulse laser could be focused loosely to extend the interaction range up to a millimeter, but this is not possible with the bow-tie nanostructure.

Selection of a longer wavelength femtosecond laser enables improvement of the field enhancement by surface plasmons. This is because the negative real part of the dielectric constant of a metal yields a larger absolute value for a longer wavelength. For example, as demonstrated by simulation in Fig. 7.11a, when the carrier wavelength of the femtosecond laser increases from 800 to 1,064 nm, the intensity enhancement factor at Apex point reaches 10^4 along with tripled 20 dB volume. Another alternative way of improving the field enhancement is to narrow the spectral bandwidth of the femtosecond laser by choosing a wider pulse duration. Narrower bandwidth leads to more effective resonant oscillation of localized surface plasmons at a given geometrical shape of the nanostructure. As an example, Fig. 7.11b shows that a femtosecond pulse laser of a pulse width of 100 fs gives higher field enhancement than a 10-fs pulse duration. Besides, the wider pulse duration lessens the instantaneous peak pulse power delivered to the gold bow-tie nanostructure, reducing possible thermal damages.

7.5 Conclusion

The bow-tie nanostructure designed and tested in this study successfully amplifies the femtosecond pulse laser strong enough to generate high harmonics up to 21st order with xenon gas. FDTD simulation can be usefully adopted to analyze the behaviors of the surface plasmons confined within the bow-tie nanostructure.

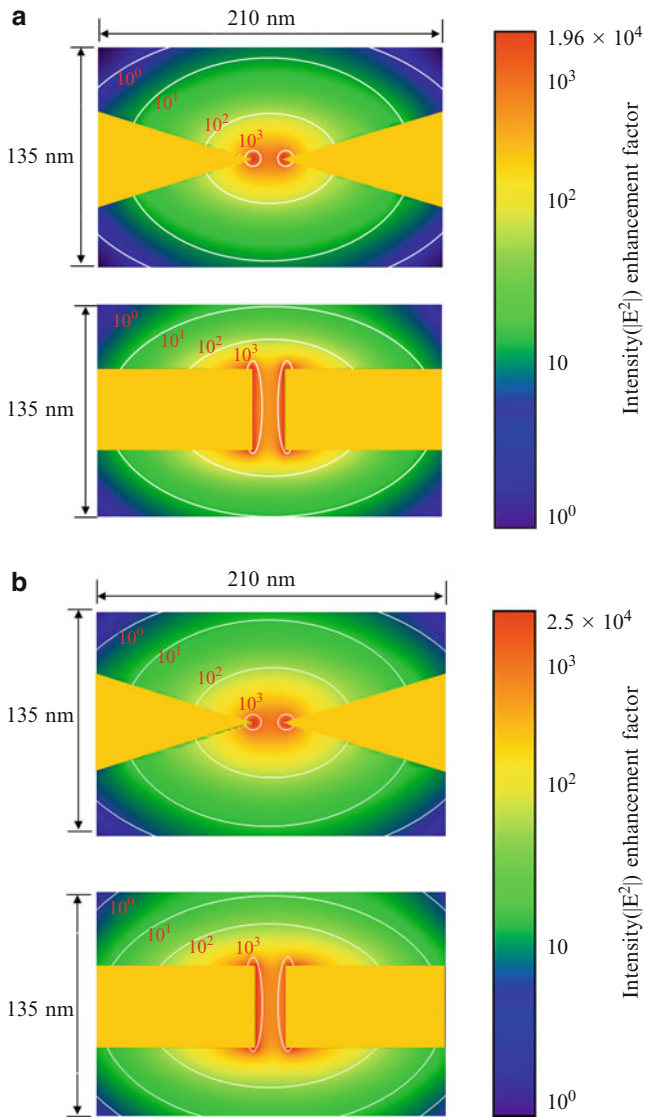


Fig. 7.11 (a) Calculated near-field distribution around the bow-tie nanostructure excited by a longer wavelength of 1,064 nm with a corresponding pulse duration of 10 fs. The bow-tie height is changed to 220 nm in accordance with the change of the incident laser wavelength to match the resonance condition. Nearly tripled 20 dB volume is observed at the gap of bow-tie. (b) Due to the narrow spectrum bandwidth of the 100 fs input laser, the enhanced area increases compared with the case of 10 fs pulse laser excitation

Experimental results obtained with the bow-tie nanostructure fabricated by the focused ion beam process validate the simulation results. The field enhancement can reach up to 100 times higher than the input intensity, allowing the output intensity of a single femtosecond oscillator of $10^{11} \text{ W cm}^{-2}$, and is strong enough to conduct high harmonic generation. This approach of high harmonic generation offers hardware compactness and high controllability since neither additional cavities nor pumping sources are required except a single femtosecond laser oscillator. In addition, no reduction in the pulse repetition rate is required, so the original comb of the input laser can be maintained in the generated high harmonics. Furthermore, high harmonics are emitted from point-like sources to be well suited for near-field applications of microscopy, imaging and high resolution lithography.

Acknowledgements This research was supported by the Creative Research Initiative program funded by the Korea Science and Engineering Foundation.

References

1. P.B. Corkum, Phys. Rev. Lett. **71**, 1994 (1993)
2. M. Lewenstein, P. Balcou, M.Y. Ivanov, A. L'Huillier, P.B. Corkum, Phys. Rev. A **49**, 2117 (1994)
3. Z. Chang, A. Rundquist, H. Wang, M.M. Murnane, H.C. Kapteyn, Phys. Rev. Lett. **79**, 2967 (1997)
4. D. Strickland, G. Mourou, Opt. Comm. **56**, 219 (1985)
5. J. Seres, E. Seres, A.J. Verhoef, G. Tempea, C. Strelci, P. Wobrauschek, V. Yakovlev, A. Scrinzi, C. Spielmann, F. Krausz, Nature **433**, 596 (2005)
6. C. Gohle, T. Udem, M. Herrmann, J. Rauschenberger, R. Holzwarth, H.A. Schuessler, F. Krausz, T.W. Hänsch, Nature **436**, 234 (2005)
7. R.J. Jones, K.D. Moll, M.J. Thorpe, J. Ye, Phys. Rev. Lett. **94**, 193201 (2005)
8. S. Kim, J. Jin, Y.-J. Kim, I.-Y. Park, Y. Kim, S.-W. Kim, Nature **453**, 757 (2008)
9. M. Nisoli, Nat. Photon. **1**, 499 (2007)
10. R.M. Roth, N.C. Panoiu, M.M. Adams, R.M. Osgood, C.C. Neacsu, M.B. Raschke, Opt. Express **14**, 2921 (2006)
11. G.C. Schatz, R.P. Van Duyne, *Handbook of Vibrational Spectroscopy: Electromagnetic Mechanism of Surface-enhanced Spectroscopy* (Wiley, Chichester, 2002)
12. M.I. Stockman, Phys. Rev. Lett. **93**, 137404 (2004)
13. T.D. Onuta, M. Waegle, C.C. DuFort, W.L. Schaich, B. Dragnea, Nano Lett. **7**, 557 (2007)
14. E.X. Jin, X. Xu, Appl. Phys. Lett. **88**, 153110 (2006)
15. W.X. Sun, Z.X. Shen, J. Opt. Soc. Am. A. **20**, 2254 (2003)
16. J.T. Krug, E.J. Sa'nchez, X.S. Xie, J. Chem. Phys. **116**, 10895 (2002)
17. P. Mühlischlegel, H.J. Eisler, O.J.F. Martin, B. Hecht, D.W. Pohl, Science **308**, 1607 (2005)
18. D.P. Fromm, A. Sundaramurthy, P.J. Schuck, G. Kino, W.E. Moerner, Nano Lett. **4**, 957 (2004)
19. H. Gai, J. Wang, Q. Tian, Appl. Opt. **46**, 2229 (2007)
20. J. Zhou, J. Peatross, M.M. Murnane, H.C. Kapteyn, I.P. Christov, Phys. Rev. Lett. **76**, 752 (1996)
21. C.G. Wahlström, J. Larsson, A. Persson, T. Starczewski, S. Svanberg, P. Salières, P. Balcou, A. L'huillier, Phys. Rev. A **48**, 4709 (1993)
22. X.C. Wang, G.C. Lim, H.Y. Zheng, F.L. Ng, W. Liu, S.J. Chua, Appl. Surf. Sci. **228**, 221 (2004)
23. J. Gädde, J. Hohlfeld, J.G. Müller, E. Matthias, Appl. Surf. Sci. **127–129**, 40 (1998)
24. G. Tempea, T. Brabec, Appl. Phys. B **70**, S197 (2000)

Chapter 8

High-Order Harmonic Generation from Nanostructured Material Using the Laser-Plasma Method

T. Ozaki, R.A. Ganeev, L.B. Elouga Bom, and J. Abdul-Hadi

Abstract We show that highly efficient harmonics in the extreme ultra-violet spectral range can be achieved by using various nanostructured materials, such as metal nanoparticles and fullerenes. Conversion efficiencies near 10^{-4} have been achieved for harmonics from C_{60} fullerene plasma. Experimental results reveal that the extension of the harmonic cutoff is negligible for such nanostructured material. Harmonics generated from plasma containing an abundance of nanomaterials were between 5 and 12 times more intense than plasma abundant with monatomic particles, depending on the harmonic order and pump laser conditions. Since the intense harmonics disappear with ionization, we attribute these harmonics to contributions from neutral atoms within the nanostructured material. Experiments and calculations reveal that for C_{60} fullerenes, there is also contribution from their surface plasmon resonance centered at 20 eV.

8.1 Introduction

High-order harmonic generation (HHG) of ultrashort laser pulses is an effective method to generate extreme ultraviolet (XUV) radiation and attosecond light pulses. Currently, various techniques are used for HHG, such as the interaction of intense laser with gases [1], with low-density laser-produced plasmas [2], and by reflecting

T. Ozaki (✉), L.B.E. Bom, and J. Abdul-Hadi
Institut National de la Recherche Scientifique, Énergie, Matériaux et Télécommunications,
1650 Lionel-Boulet, Varennes, QC, Canada J3X 1S2
e-mail: ozaki@emt.inrs.ca, elouga@emt.inrs.ca, ahadi@emt.inrs.ca

R.A. Ganeev
Institut National de la Recherche Scientifique, Énergie, Matériaux et Télécommunications,
1650 Lionel-Boulet, Varennes, QC, Canada J3X 1S2
e-mail: rashid_ganeev@mail.ru
and
Scientific Association Akademprigor, Academy of Sciences of Uzbekistan, Akademgorodok,
Tashkent 100125, Uzbekistan

relativistic intensity laser pulses from solid surfaces [3]. Such harmonics are promising sources of coherent soft X-ray radiation with various applications, such as XUV nonlinear optics and spectroscopic studies. However, the relatively low brightness of such HHG sources is an obstacle to explore new applications. Thus, many methods have been explored to increase HHG conversion efficiency. These include (a) improving phase matching conditions [4], (b) periodically modulating the atomic density in the nonlinear medium [5], (c) exploiting the resonance of an ionic transition with a specific harmonic order [6], (d) using atomic clusters that results in increased recombination probability of the recolliding electron with the parent particle and in resonant enhancement due to expanding clustered plasma [7–10], and (e) applying surface plasmon resonances (SPR) for low-order harmonics [11] and in large molecules and nanostructures [12]. However, the maximum harmonic efficiency demonstrated in the XUV range remains rather low ($10^{-6} - 10^{-5}$) for atomic and ionic media.

By using particles with larger size (such as gas clusters and metal atoms), enhancement of HHG efficiency has been observed, compared with those from media rich in single atoms or ions. For example, clusters subject to intense laser pulses produce strong low-order nonlinear optical response (such as nonlinear refraction and nonlinear absorption) and can also emit coherent radiation through harmonic generation [13, 14]. Also, fullerenes are an attractive molecule to study HHG as they have rather large sizes (approximately 0.8 nm) and display broadband SPR in the XUV ($\lambda_{\text{SPR}} = 60$ nm, 10 nm full width at half maximum (FWHM)) [15, 16]. We have recently reported the first demonstration of HHG from fullerenes and showed an enhancement of harmonics near its SPR [17].

In this paper, we review our recent studies on high-order nonlinear optical properties of various nanostructured materials, including nanoparticles and fullerenes. These studies were performed using the laser-plasma HHG method. In this method, a sub-nanosecond laser pulse produces low-density plasma from a solid target, which is used as the nonlinear medium. We studied the presence of nanoparticles in the plumes by analyzing the spatial characteristics of the ablated material deposited on nearby substrates. We have found that the nanoparticles keep their integrity in the laser plume under ideal conditions for harmonic generation. The presence of such nanostructured material led to the enhancement of the HHG yield, when compared with plasma that mainly contains monatomic particles.

8.2 Experimental Setup

We show in Fig. 8.1 the schematic diagram of the experimental setup. For harmonic generation from low-density plasma, one needs two pump lasers synchronized in time. The first beam is used to create low-temperature plasma, while the second beam generates the harmonics. In the present work, we used the multibeam laser of the Canadian advanced laser light source (ALLS) as the pump laser. Plasma plume was created by loosely focusing picosecond prepulse from the uncompressed Ti:sapphire laser (210 ps pulse duration, 800 nm central wavelength) on to

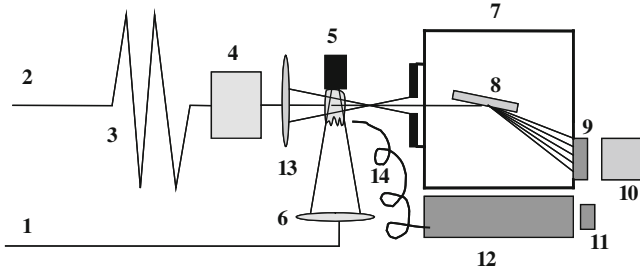


Fig. 8.1 Schematic diagram of the experimental setup for HHG from laser plasma. (1) Sub-nanosecond prepulse; (2) Femtosecond main pulse; (3) Optical delay line; (4) Pulse compressor; (5) Target; (6,13) Focusing lenses; (7) XUV spectrometer; (8) Grating; (9) MCP; (10,11) CCD; (12): UV spectrometer; (14) Fiber

a target placed in the vacuum chamber, using a plano-convex lens (focal length $f = 150$ mm). The focal spot diameter of the prepulse on the target surface was about $600 \mu\text{m}$. We varied the intensity of the prepulse on the target surface between $2 \times 10^9 \text{ W cm}^{-2}$ and $1 \times 10^{10} \text{ W cm}^{-2}$. After a delay time (between 6 and 74 ns), we focused the femtosecond main pulse (25 mJ maximum, 35 fs, 800 nm central wavelength) on to the plasma using an MgF_2 plano-convex lens ($f = 680$ mm). The maximum intensity of the femtosecond main pulse used in this work was $7 \times 10^{14} \text{ W cm}^{-2}$ at the plasma position, above which the HHG efficiency started to decrease. Since the characteristics of the freely expanding plasma can change rapidly, it is necessary to synchronize temporally the main pulse with the prepulse for efficient HHG. The ideal incidence position of the pump laser for HHG was found to be at 200–300 μm above the target surface, both for bulk targets and nanoparticle targets.

The harmonics were spectrally dispersed using a homemade spectrometer with a flat-field grating (1,200 lines/mm, Hitachi). The XUV spectrum was then detected by a micro-channel plate (MCP) and finally recorded using a charge-coupled device (CCD). We also performed time-resolved ultraviolet plasma spectroscopy of the plume using a spectrometer (SpectraPro500i, Acton Research Corp.) and a time-resolved CCD camera (DH501-18F-01, Andor Technology).

8.3 Results

8.3.1 Silver Nanoparticles

First, we performed harmonic generation experiments using silver nanoparticles glued on various substrates. We observed the nanoparticles used in this experiment with a scanning tunneling microscope, and we confirmed that their size varied between 90 and 110 nm. We initially verified that harmonics generated from the substrates themselves (glue, tape, and glass) without the nanoparticles were negligible compared with those from silver plasma. We fabricated the target so that a slab silver

target was next to the nanoparticle target, with the two target surfaces at the same height. This target was placed on to the target holder, so that they interacted with both the prepulse and main pump laser at the same intensities. First, the prepulse and main pulse were aligned using a solid silver target, to search for conditions for maximum harmonic intensity within the plateau. Next, the target was translated so that the prepulse beam now irradiates the Ag nanoparticle target.

We compared the harmonic yield for silver nanoparticle targets with those from bulk silver targets, under the same prepulse and main pulse conditions. Figure 8.2 shows the lineout of the harmonic spectra between the 21st and the 29th harmonics within the plateau. One clearly sees that the HHG intensity from the nanoparticle target was more than six times higher compared with that from bulk silver target. We can estimate the energy of these harmonics based on calibrations we have performed using longer (130 fs) pulses [18]. For 130 fs pump lasers, we have measured a conversion efficiency of 8×10^{-6} for bulk silver target. This would be a conservative estimate of the conversion efficiency for bulk silver targets in the present work, which uses shorter 35 fs pulses. We therefore estimate a minimum harmonic conversion efficiency of 4×10^{-5} from silver nanoparticles within the plateau region. For the maximum main pump laser energy of 25 mJ used, the energy of the 21st to 29th harmonics is evaluated to be more than 1 μ J.

When we compare the cutoff observed for harmonics from nanoparticle and slab silver targets, we also noted a slight extension of the harmonic cutoff for nanoparticles (Fig. 8.3). Harmonic up to the 67th order (103 eV photon energy) was observed in these studies with silver nanoparticles, while, for bulk silver target, the cutoff was at the 61st order (94 eV photon energy) under the same conditions. This slight extension of harmonic cutoff agrees with past observations, which noted similar extension in the cutoff for argon clusters, compared with isolated atoms [19]. This difference has been explained by the increase in the effective binding energy of electrons in the cluster. The higher binding energy will allow the cluster to interact with laser intensities that are much higher than for isolated atoms, resulting in the extended cutoff for the former. In past works with Ar [19], the cutoff for clusters was at the 33rd order, compared with the 29th order cutoff for monomer harmonics.

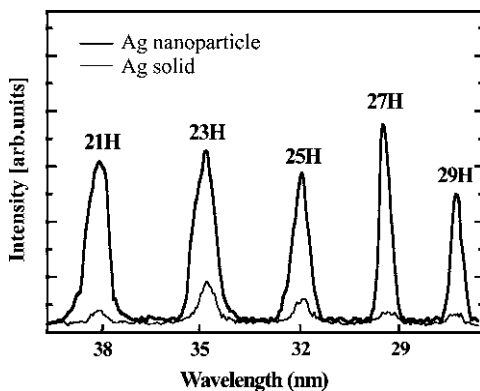


Fig. 8.2 Harmonic distribution in mid-plateau region for produced from bulk Ag target (*thin lineout*) and Ag nanoparticle plasma (*thick lineout*)

Fig. 8.3 High-order harmonic spectra generated from (1) silver nanoparticle plasma and (2) plasma produced from bulk silver target

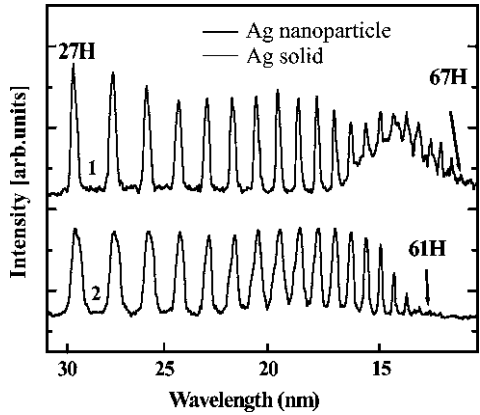
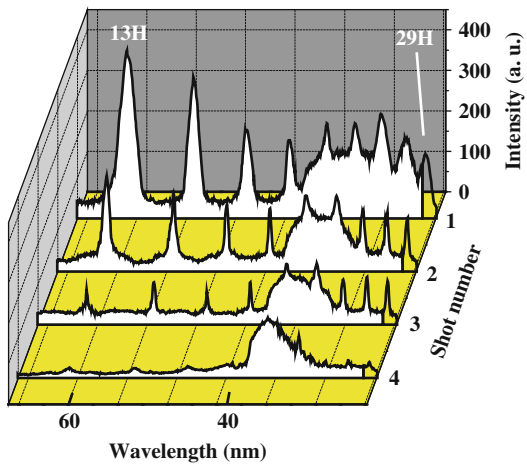


Fig. 8.4 Low-order harmonic spectra from Ag nanoparticle plasma for different shots (from first to the fourth) on the same target position



Next, we studied the dependence of the harmonic yield on the pump intensity. However, the measurement was made difficult by the rapid shot-to-shot change in the harmonic intensity from Ag nanoparticle target. For experiments with solid slab targets, stable harmonic generation can be obtained for about 10 min at 10 Hz repetition rates, without translating for a new target surface. However, for nanoparticle targets, the harmonics were strong for the first few shots, which were followed by a rapid decrease in harmonic yield when the plasma was created at the same target position. We attribute this effect to evaporation of the thin layer of nanoparticles. Figure 8.4 shows this shot-to-shot change in the harmonic spectrum, when the target was not moved. The first shot results in a strong harmonic spectrum, with the typical plateau-like structure starting from the 17th order. Then, for the second and third shots, the intensity of the harmonics decreased drastically, and for the fourth shot and after, the harmonics almost disappeared. We repeated the experiments with nanoparticles many times, revealing the same feature. We also observed that when we used different material as the substrate, there was a different behavior of the shot-to-shot decrease in harmonic yield. Another interesting feature found in the

experiments with nanoparticle targets was that the prepulse intensity necessary for HHG was lower than that used for bulk targets.

These observations give us a rough picture of the ablation for nanoparticle targets. The material directly surrounding the nanoparticles is polymer (epoxy glue), which has a lower ablation threshold than metallic materials. Therefore, the polymer starts to ablate at relatively low intensities, carrying the nanoparticle with it, resulting in the lower prepulse intensity. Polymer also has a lower melting temperature than metals. Therefore, repetitive irradiation of the target leads to melting and change in the properties of the target. This results in the change in conditions of the plasma plume, resulting in a rapid decrease in the harmonic intensity with increased shots. The different shot-to-shot harmonic intensities for different substrates can be explained by the different adhesion properties of nanoparticles to the substrate.

Due to such rapid change in the conditions for harmonic generation with nanoparticle targets, it was difficult to define precisely the dependence of harmonic yield on prepulse and main pulse intensities. Nevertheless, approximate measurements of the dependence of harmonic yield on the main pulse intensity for Ag nanoparticles have shown a saturation of this process at relatively moderate intensities ($I_{\text{fp}} \approx 8 \times 10^{14} \text{ W cm}^{-2}$).

Harmonics from plasma nanoparticles also displayed several characteristics similar to gas harmonics. First, the harmonic intensity decreased exponentially for the lower orders, followed by a plateau, and finally a cutoff. Next, the harmonic intensity was strongly influenced by the focus position of the main pump laser, along the direction parallel to the harmonic emission. The strongest harmonic yield was obtained when the main pump laser was focused 4–5 mm after the nonlinear medium. We observed the same tendency of the harmonics using bulk silver target. The typical intensity of the pump laser for maximum harmonic yield was between 5×10^{14} and $2 \times 10^{15} \text{ W cm}^{-2}$. These results agree with those of gas harmonics [20], and are due to the selective short-trajectory-generated harmonics when the pump laser is focused after the medium. Harmonics from short-trajectories have a flat and large area on-axis, with excellent phase matching conditions, resulting in the higher harmonic yield. In our case, we needed to focus the pump laser away from the medium, since the total intensity that would be produced at focus would exceed the barrier suppression intensity for multiply charged ions. This would result in over-ionization of the plasma, leading to the decrease in the harmonic yield.

To study the size effect of nanoparticles, we performed harmonic generation experiments using colloidal silver targets, which contains blocks of silver with sizes between 100 and 1,000 nm. We confirmed the size of the silver blocks by viewing with a scanning tunneling microscope. The results showed that the harmonic yield for these sub- μm -sized silver blocks was much lower than that from nanoparticles and was comparable to those from bulk silver targets. We also noted a tendency of slightly extended harmonic cutoff for smaller particle sizes. The cutoffs for the harmonics were at the 61st, 63rd, and 67th order, for bulk silver, sub- μm silver colloid, and silver nanoparticle targets, respectively.

These studies have shown that the increasing the particle size over some limit is undesirable due to the disappearance of enhancement-inducing processes. The

observed enhancement of harmonic yield for plasma plume with 90–110 nm size nanoparticles can probably be further improved by using smaller nanoparticles.

These experiments show that the size of the nanoparticles is of essential importance for harmonic generation. To gain maximum HHG conversion efficiency, it is essential to know the maximum tolerable particle size for increased harmonic yield. On one hand, increasing the size of the particles increases its polarizability, and large polarizability of a medium is critical for efficient harmonic generation [21]. On the other hand, the increase in particle size leads to phenomena that reduce harmonic yield (such as HHG only from surface atoms [22] and reabsorption of harmonics).

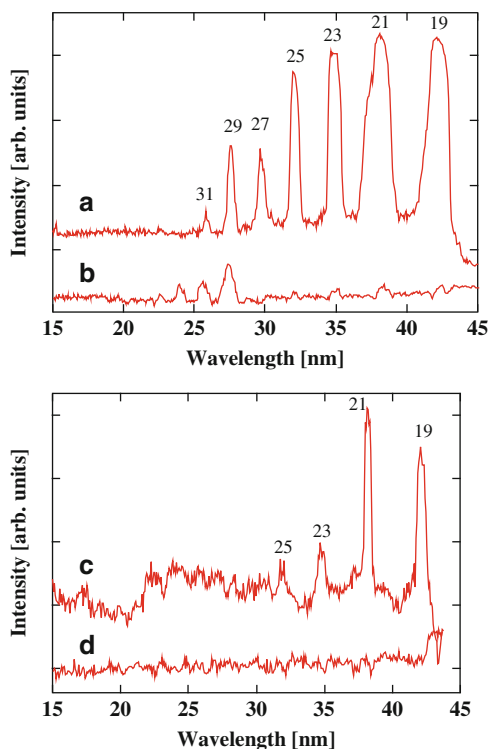
The increased HHG efficiency for silver nanoparticles might also be an important factor for explaining the high conversion efficiency of HHG from plasma produced from bulk silver targets. Silver has been known to be a highly efficient material for plasma HHG, but up to now, the reason was not clear [23]. However, it is known that nanoclusters (such as Ag_2 and Ag_8) and nanoparticles are abundantly produced by laser ablation. Since our laser plume expanded adiabatically for 100 ns before irradiation by the main pulse, one can expect that the silver plume from bulk silver target also contained many nanomaterials, which would contribute to increasing the HHG efficiency.

8.3.2 Other Nanoparticles

8.3.2.1 Cr_2O_3 and MnTiO_3 Nanoparticle Targets

To study what parameters affect the strong harmonics from nanoparticles, we next performed experiments using nanoparticles of different materials. An example of the harmonic spectrum from chromium oxide (Cr_2O_3) nanoparticle target is shown in Fig. 8.5a. The spectrum from nanoparticle targets showed a featureless plateau with a cutoff at the 31st harmonic, with harmonic yield that is much stronger than that from bulk Cr_2O_3 targets (Fig. 8.5b). Another important observation is that the relative intensities between harmonic orders differ for different targets. For nanoparticle targets, the harmonic spectrum resembles that observed from gas, with a plateau followed by a cutoff. However, harmonics from bulk Cr_2O_3 target has a characteristic enhancement of the 29th order, and a cutoff at the 35th harmonic, which has also been observed in previous studies of HHG in chromium plasma [24]. For bulk chromium oxide targets, the 29th harmonic is about ten times stronger than the lower 27th harmonic. Such enhancement was not observed with Cr_2O_3 nanoparticle targets at moderate prepulse intensities ($5 \times 10^9 \text{ W cm}^{-2}$). We should note that by further increasing the prepulse intensity to $9 \times 10^9 \text{ W cm}^{-2}$, we could generate intense 29th harmonic from Cr_2O_3 nanoparticle targets. This is a sign of ionization of the nanoparticles in the plasma, since enhanced single harmonic in chromium has previously been attributed to the proximity of the 29th harmonic with the giant 3p–3d ionic transitions of singly ionized chromium ions [25]. The delay between the prepulse and main pulse in these experiments was kept at 25 ns.

Fig. 8.5 Harmonic spectrum for (a) chromium oxide nanoparticles, (b) chromium oxide bulk, (c) manganese titanium oxide nanoparticles, and (d) manganese titanium oxide bulk targets



High-order harmonics from other nanoparticles also showed similar features, with a notable enhancement of low-order harmonics at the plateau and a decrease in the harmonic cutoff compared with harmonics using bulk targets. For example, Fig. 8.5c, d shows the harmonic spectrum for manganese titanium oxide (MnTiO_3) nanoparticles and bulk targets, respectively. The MnTiO_3 nanoparticles show relatively strong 19th and 21st harmonics, with a cutoff at the 25th order, whereas the bulk MnTiO_3 targets show only weak harmonics that are comparable to noise. Increasing the femtosecond pump intensity did not lead to extension of the harmonic cut-off for nanoparticle targets, which is a sign of saturation of the HHG in these media. Also, at relatively high femtosecond pump intensities, we noted a decrease in the harmonic conversion efficiency due to the onset of negative effects (such as increase in the free electron density, self-defocusing, and phase mismatch). Similar effects were also observed when we increased the prepulse intensity, which is attributed to the increase in the free electron density of the plasma, resulting in phase mismatch.

8.3.2.2 Discussion

In this section, we discuss the mechanism for the efficient harmonic generation from nanostructured material.

A comparison of the low-order harmonic generation using the single atoms and multiparticle aggregates has previously been reported for Ar atoms and clusters [7]. It was demonstrated that a medium of intermediate-sized clusters with a few thousand atoms of an inert gas has a higher efficiency for generating the harmonics, compared with a medium of isolated gas atoms of the same density. The reported enhancement factor for the third to ninth harmonics from gas jets was about 5. In our HHG experiments with the laser-ablated nanoparticles, these observations were extended toward the higher-order harmonics, and stronger enhancement for the harmonics up to the 25th order was achieved. These results have also shown that the dependence of the HHG efficiency on the prepulse and main pulse intensity is much more prominent for nanoparticles than for monatomic particles.

Since nanoparticles are smaller than the laser wavelength, they contain many equivalent, optically active electrons at effectively the same point in the laser field. This leads to the possibility that each of these electron oscillators may contribute coherently to a global nanoparticle dipole. However, this statement is true only for low-order harmonics. For HHG (such as those considered in this paper), the dipole approximation is inapplicable, because the harmonic radiation wavelength is shorter than the size of nanoparticles (about 100 nm).

We would like to point out that in our experiments with nanoparticles, the intense harmonics were observed (a) only for lower orders and (b) when the intensity of the picosecond prepulse (which generates the plasma plume) was moderate. When the prepulse intensity was increased, phenomena that are explained by the presence of ions appeared. For example, enhancement of the 29th harmonic in chromium is related to the giant 3p–3d ionic transitions of Cr^+ , which started to appear for Cr_2O_3 nanoparticles when the prepulse intensity was increased to $9 \times 10^9 \text{ W cm}^{-2}$. These results suggest that one major reason for the intense harmonics from nanoparticles is the contribution from neutral atoms. Since neutral atoms are larger compared with its ions, the recombination probability of the electron wave packet that was liberated by the laser electric field is also larger for neutral atoms. As a result, the neutral atoms emit stronger harmonics than ions, but with a lower cutoff due to its lower ionization potential.

8.3.3 C_{60} Fullerenes

8.3.3.1 Harmonic Generation from C_{60} Fullerenes

A problem with experiments using nanoparticles is that there is always a distribution in their size and shape. Since phenomena such as ionization and nonlinear response to intense laser fields should vary with nanoparticle dimensions, it becomes difficult

to determine how the various characteristics of the nanostructured material affect harmonic generation. To study HHG from a more uniform nanomaterial, we decided to next explore C_{60} fullerenes. In our previous experiments, we demonstrated HHG from laser-produced plasma of fullerene targets [17]. In that work, we showed that (a) the harmonics lying within the spectral range of SPR in C_{60} (20–22 eV) are enhanced, (b) the harmonic efficiency from C_{60} targets is 20–25 times larger for the 13th harmonic compared with that generated from carbon monomer rich plasma, and (c) the harmonic cutoff in C_{60} is lower (19th order) than carbon but extends beyond the value (11th order) predicted by the three-step model. Here, we present a more detailed account of HHG from C_{60} fullerenes.

Figure 8.6 shows the harmonic spectra from C_{60} for different delays between the pump pulse and the femtosecond driving pulse. HHG by ablation of bulk materials is influenced by the temporal delay between the pump pulse and driving pulse, as it results in a change in the atomic density and plasma length of the nonlinear medium. To study their effects on the harmonic intensity, we varied the delay from 18 to 100 ns. Our measurements showed no significant changes in the harmonic intensities in C_{60} (see Fig. 8.6a, b) for delays of 22 and 63 ns, with some two fold increase of harmonic efficiency for the shorter delay. By comparing with calibrated harmonics from silver plasma [2], we estimate the efficiency of the 13th harmonic from fullerene plasma to be near 10^{-4} .

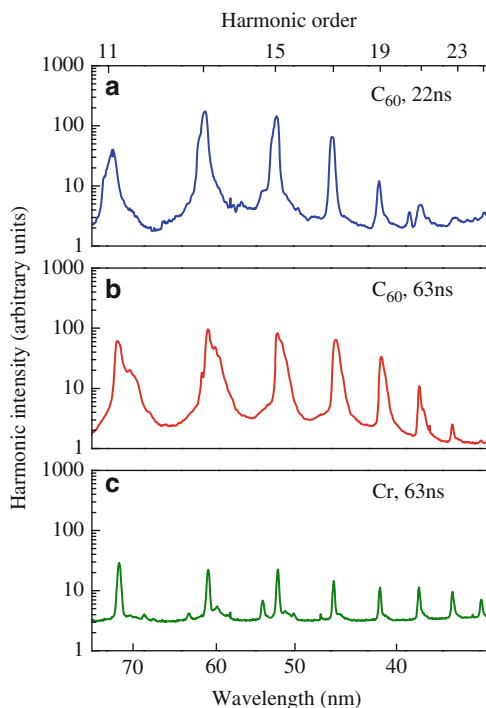


Fig. 8.6 Harmonic generation observed in C_{60} plasma at (a) 22 ns, (b) 63 ns delays between the prepulse and main pulse, and (c) in chromium plasma

However, for bulk targets such as C, Cr, and Mn, no harmonics were observed from plasmas when we used the shorter delays, which is contrary to the case of C₆₀. This can be attributed to the nonoptimal plasma conditions, since it requires time for the plasma to ablate on the bulk surface and expand into the area where the femtosecond beam interacts with the plasma. This can also be inferred from the lower pump pulse intensity ($I_{pp} \sim 2 \times 10^9 \text{ W cm}^{-2}$) needed for HHG from C₆₀-rich target, compared with that needed for bulk targets [$I_{pp} > 10^{10} \text{ W cm}^{-2}$]. We believe that short delays lead to more favorable evaporation conditions and higher particle density for the cluster-rich medium compared with the monatomic medium, thus resulting in a higher harmonic yield. Usually for heavy bulk targets, the strong harmonics were observed using longer delays (40–70 ns). The use of light targets (B, Be, Li) showed an opposite tendency, where one can obtain effective HHG for shorter delays. The optimization is related to the presence of a proper density of particles within the volume where harmonics are generated, which depends on the propagation velocity of the plasma front. For C₆₀, one can expect to optimize HHG at longer delays due to the larger weight of the fullerene particles. However, one also needs to take into account the possibility of the presence of the fragments of C₆₀ in the plume, in which case, the density of the medium within the laser-interaction region becomes sufficient even for shorter delays.

An interesting feature of the fullerene harmonic spectra is that the spectral width is about three to four times broader compared with those generated in plasma rich with monatomic particles (1.2 and 0.3 nm FWHM, respectively). For comparison, Fig. 8.6c shows the harmonic spectra for Cr bulk targets. Broader width of the harmonics can be explained by self-phase modulation and chirping of the fundamental radiation propagating through the fullerene plasma. Broadening of the main beam bandwidth causes the broadening of the harmonic's bandwidth. Increase in the harmonic bandwidth with delay can be explained by the longer length of the fullerene plasma for the longer delay, and thus stronger self-phase modulation of the femtosecond pump laser.

The intensities of the pump pulse and driving pulse are crucial for optimizing the HHG from C₆₀. Increasing the intensity of the driving pulse did not lead to an extension of the cut-off for the fullerene plasma, which is a sign of HHG saturation in the medium. Moreover, at relatively high femtosecond laser intensities, we observed a decrease in the harmonic output, which can be ascribed to phase mismatch resulting from higher free electron density. We observe a similar phenomenon when the pump pulse intensity on the surface of fullerene-rich targets is increased above the optimal value for harmonic generation. This reduction in harmonic intensity can be attributed to phenomena such as the fragmentation of fullerenes, an increase in free electron density, and self-defocusing. At relatively strong ablation intensity for fullerene film ($I_{pp} > 1 \times 10^{10} \text{ W cm}^{-2}$), we observed only the plasma spectrum, without any sign of harmonics.

The stability of C₆₀ molecules to ionization and fragmentation is of particular interest, especially for their application as a medium for HHG. The structural integrity of the fullerenes ablated off the surface should be intact until the driving pulse arrives. Therefore, the pump pulse intensity is a sensitive parameter. At

lower intensities, the density of clusters in the ablation plume would be low, while at higher intensities, one can expect fragmentation. C_{60} has demonstrated both direct and delayed ionization and fragmentation processes and is known to survive even in intense laser fields. This can be attributed to the large number of internal degrees of freedom that leads to the fast diffusion of the excitation energy [26, 27]. At 796 nm, multiphoton ionization is the dominant mechanism leading to the ionization of C_{60} in a strong laser field. The collective motion of π electrons of C_{60} can be excited by multiphoton process. Since the laser frequency is much smaller than the resonance frequency of π electrons, barrier suppression and multiphoton ionization are the dominant mechanisms leading to the ionization in a strong laser field.

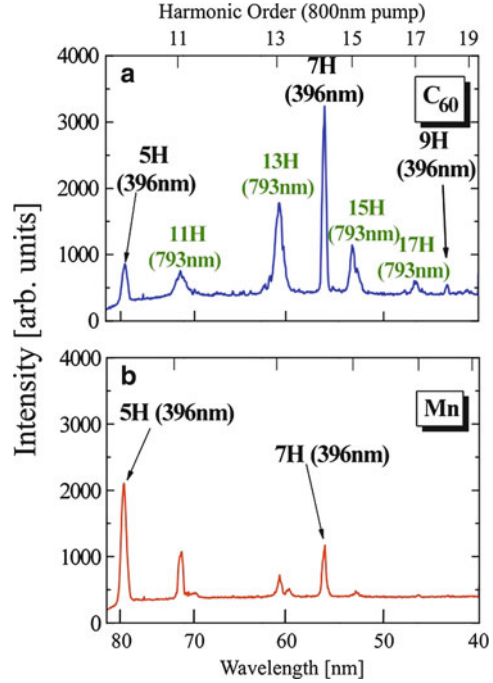
Another important parameter that affects the stability of HHG process is the thickness of the fullerene target. We obtained stable harmonic generation with low shot-to-shot variation in harmonic intensity by moving the fullerene film deposited on the glass substrate after several laser shots. This avoids decrease in the fullerene density due to ablation of the thin film. The number of laser shots at the same target position that resulted in stable harmonic emission decreased drastically with the film thickness. For example, in a 10 μm film, the harmonic emission disappeared after 70–90 shots, whereas in a 2 μm film, the harmonics disappeared after 5–7 shots.

To understand the origin of the harmonic emission in C_{60} , we studied its dependence on the polarization of the main pulse. This also allows one to distinguish the plasma emission from the HHG. HHG is highly sensitive to laser polarization, since the trajectories of the recolliding electrons are altered significantly for elliptically polarized pump lasers, thus inhibiting the recombination process. We noted that the harmonic signal drop rapidly and disappear with ellipticity of the laser polarization. For circular polarization, as expected, the harmonic emission disappears and the resulting background spectrum corresponds to the plasma emission.

Does the influence of plasmon resonance on the HHG in fullerene plasma depend on the wavelength of the driving field? To address this question, we also studied HHG using the second harmonic (396 nm, 4 mJ, 35 fs) of the main pulse (793 nm, 30 mJ). The low second harmonic conversion efficiency did not allow us to achieve the laser intensities reached with the 793 nm fundamental laser. As a result, we were able to generate harmonics up to the ninth order of the 396 nm driving pulse, while simultaneously generating harmonics using the 793 nm laser. Harmonic generation using two main pulses (793 and 396 nm) did not interfere with each other, due to different focal positions of these two beams (approximately 2 mm in the Z -axis and approximately 0.2 mm in the X -axis). Therefore, the two HHG processes occurred in different regions of the laser plasma. Here, the Z -axis is the axis of propagation of the driving beam, and the X -axis is the axis vertical to the Z -axis. This axis is defined by the walk-off direction of the second harmonic with respect to the fundamental driving pulse.

Figure 8.7a shows the HHG spectrum from C_{60} fullerene optimized for the second harmonic driving pulse. The energy of the second harmonic is approximately 1/7th of the fundamental. One can see the enhancement of the seventh harmonic (which is within the spectral range of the SPR of C_{60}) compared with the fifth harmonic. This behavior is similar to that observed for the 793 nm driving pulse.

Fig. 8.7 Harmonic spectra from (a) C_{60} and (b) Mn plasma, when both the 793 and 396 nm laser were simultaneously focused on the laser-produced plasma



For comparison, we present in Fig. 8.7b the optimized harmonics generated using the 396 nm pump and the weak harmonics from the 793 nm radiation in manganese plasma. One can see a decrease in harmonic intensity from the Mn plasma for each subsequent order, which is a common case, when one uses a nonlinear optical medium containing atomic or ionic particles. These studies confirmed that, independent of the driving pulse wavelength, the harmonics near SPR in C_{60} are enhanced.

8.3.3.2 Simulations of C_{60} Harmonic Spectra

To understand the influence of the absorptive properties of surface plasmon resonance on the harmonic emission spectrum in C_{60} , we simulated the emission spectrum using parameters that are roughly identical to those used in experiments. The HHG efficiency can be understood by three length parameters. For optimum HHG, the length of the nonlinear medium L_{med} should be (a) larger than the coherence length $L_{\text{coh}} = \pi/\Delta k$, which is defined by the phase mismatch between the fundamental and harmonic fields ($\Delta k = k_q - qk_0$, where k_q and k_0 are the harmonic and fundamental wave vectors, respectively) and depends on the density and ionization conditions, and (b) smaller than the absorption length of the medium $L_{\text{abs}} = 1/\rho\sigma$, where ρ is the atomic density and σ is the ionization cross-section.

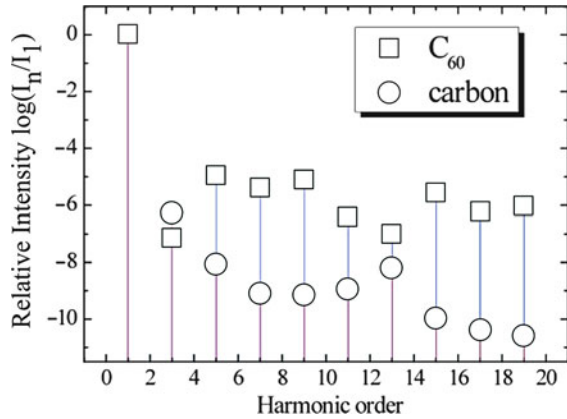
The photoionization cross-section of C_{60} is well-known, both experimentally and theoretically. It displays a giant and broad plasmon resonance at approximately 20 eV (around the 11th, 13th, and 15th harmonics, with a bandwidth of 10 eV FWHM). We calculated the absorption length using the estimated fullerene density in the interaction region ($5 \times 10^{16} \text{ cm}^{-3}$) and the known photoionization cross-sections. The absorption length varies from 0.8 mm (for the 7th and 17th harmonic) to 0.3 mm (for the 11th, 13th, and 15th harmonic), suggesting that harmonics near the plasmon resonance should be more strongly absorbed in the medium (whose length is estimated to be about 0.8–1 mm). Due to this increased absorption in C_{60} , we expect a dip in the harmonic spectrum for the 11–15th harmonics. Our calculations also point out that harmonics produced in bulk carbon target are not absorbed by the nonlinear medium. With an assumed medium length of 1 mm, theoretical spectra are obtained by using the proper wavelength-dependent index of refraction and dispersion data.

From our calculations, we find that for bulk carbon, the influence of absorption on the harmonic yield is negligible, and as a result, the overall harmonic spectrum is determined by dispersion. The harmonic yield decreases with increasing order as it becomes difficult to phase match higher orders. In C_{60} , absorption of harmonics by the nonlinear medium is dominant due to large photoabsorption cross-sections. The effect of dispersion only lowers the HHG efficiency but does not affect the overall shape of the spectrum. As a result, one expects the harmonic yield to decrease considerably near the surface plasmon resonance, if one does not consider the nonlinear optical influence of this resonance on the harmonic efficiency in this medium. On the contrary, in our experiment, we observed a notable enhancement of these harmonics in the fullerene-rich plume (Figs. 8.6 and 8.7). This is a signature of multielectron dynamics in a complex molecule such as C_{60} and has no atomic analogue.

To understand the origin of enhancement of harmonic yield near SPR, we theoretically studied the interaction of monatomic carbon and fullerene C_{60} molecule with a strong laser pulse by the time-dependent density functional theory (TDDFT) [28]. In the TDDFT approach, the many-body time-dependent wave-function is replaced by the time-dependent density $n(r, t)$, which is a simple function of the three-dimensional vector r . $n(r, t)$ is obtained with the help of a fictitious system of non-interacting electrons by solving the time-dependent Kohn-Sham equations. These are one-particle equations, so it is possible to treat large systems such as fullerenes. For all calculations, we used the OCTOPUS code [29] with norm-conserving non-local Troullier-Martins pseudopotentials [30], Slater exchange, Perdew and Zunger correlation functionals [31] and grid spacing of 0.6 Å for parallelepiped box of $8 \times 8 \times 60$ Å.

We analyzed the relative harmonic intensities calculated for C_{60} and bulk carbon (Fig. 8.8). A significant increase in HHG efficiency for C_{60} molecule can be attributed to additional oscillation of the time-dependent dipole in the C_{60} molecule. This can be a sign of an induced collective plasmon-like response of the molecule to external field. At the same time, the cutoff for the carbon atom is higher than that for a fullerene molecule. Treating relatively high-order harmonics with our simulation codes can become inaccurate, due to an exponential cutoff of the exchange and

Fig. 8.8 Calculated relative intensities of harmonics generated from neutral carbon monoatom and C_{60} fullerene molecule



correlation potential. The effects of correlation for lower harmonics are nevertheless conserved, so a collective oscillation can be responsible for the relative increase of the time-dependent dipole and, respectively, HHG conversion efficiency observed in plasma of fullerene molecules.

8.4 Conclusions

We have shown that one can achieve enhancement of the harmonic yield in the low-energy plateau range for various nanostructured material, such as metal nanoparticles and fullerenes. Experimental results reveal that there is only a slight extension of the harmonic cutoff for such nanostructured material. Harmonics generated from plasma containing an abundance of nanomaterials were between 5 to 12 times more intense than plasma abundant with monatomic particles, depending on the harmonic order and pump laser conditions. Since the intense harmonics disappear with ionization, we attribute these harmonics to contributions from neutral atoms within the nanostructured material. Experiments and calculations reveal that for C_{60} fullerenes, there is also contribution from their surface plasmon resonance centered at about 20 eV. Harmonics from nanostructured material could be a way toward generating intense coherent X-rays and attosecond pulses.

References

1. S. Kazamias, D. Douillet, F. Weihe, C. Valentin, A. Rousse, S. Sebban, G. Grillon, F. Audebert, D. Hulin, P. Balcou, Phys. Rev. Lett. **90**, 193901 (2003)
2. R.A. Ganeev, J. Phys. B At. Mol. Opt. Phys. **40**, R213 (2007)
3. P.A. Norreys, M. Zepf, S. Moustazis, A. P. Fews, J. Zhang, P. Lee, M. Bakarezos, C.N. Danson, A. Dyson, P. Gibbon, P. Loukakos, D. Neely, F.N. Walsh, J.S. Wark, A.E. Dangor, Phys. Rev. Lett. **76**, 1832 (1996)

4. E.A. Gibson, A. Paul, N. Wagner, R. Tobey, D. Gaudiosi, S. Backus, I.P. Christov, A. Aquila, E.M. Gullikson, D. T. Attwood, M.M. Murnane, H.C. Kapteyn, *Science* **302**, 95 (2003)
5. J. Seres, V.S. Yakovlev, E. Seres, Ch. Strel, P. Wobrauschek, Ch. Spielmann, F. Krause, *Nat. Phys.* **3**, 878 (2007)
6. R.A. Ganeev, H. Singhal, P.A. Naik, V. Arora, U. Chakravarty, J.A. Chakera, R.A. Khan, I.A. Kulagin, P.V. Redkin, M. Raghuramaiah, P.D. Gupta, *Phys. Rev. A* **74**, 063824 (2006)
7. T.D. Donnelly, T. Ditmire, K. Neuman, M.D. Pery, R.W. Falcone, *Phys. Rev. Lett.* **76**, 2472 (1996)
8. J.W.G. Tisch, T. Ditmire, D.J. Fraser, N. Hay, M.B. Mason, E. Springate, J.P. Marangos, M.H.R. Hutchinson, *J. Phys. B At. Mol. Opt. Phys.* **30**, L709 (1997)
9. R.A. Ganeev, M. Suzuki, M. Baba, M. Ichihara, H. Kuroda, *J. Phys. B At. Mol. Opt. Phys.* **41**, 045603 (2008)
10. R.A. Ganeev, M. Suzuki, M. Baba, M. Ichihara, H. Kuroda, *J. Appl. Phys.* **103**, 643 (2008)
11. B. Shim, G. Hays, R. Zgadzaj, T. Ditmire, M.C. Downer, *Phys. Rev. Lett.* **98**, 123902 (2007)
12. S. Kim, J. Jin, Y.-J. Kim, I.-Y. Park, Y. Kim, S.-W. Kim, *Nature* **453**, 757 (2008)
13. H.B. Liao, R.F. Xiao, J.S. Fu, G.K.L. Wong, *Appl. Phys. B* **65**, 673 (1997)
14. N.I. Shvetsov-Shilovski, S.P. Goreslavski, S.V. Popruzhenko, W. Becker, G.G. Paulus, *Laser Phys. Lett.* **4**, 726 (2007)
15. R.G. Polozkov, V.K. Ivanov, A.V. Solov'yov, *J. Phys. B At. Mol. Opt. Phys.* **38**, 4341 (2005)
16. S. Hunsche, T. Starczewski, A. l'Huillier, A. Persson, C.-G. Wahlström, B. van Linden van den Heuvel, S. Svanberg, *Phys. Rev. Lett.* **77**, 1966 (1996)
17. R.A. Ganeev, L.B. Elouga Bom, J. Abdul-Hadi, M.C.H. Wong, J.P. Brichta, V.R. Bhardwaj, T. Ozaki, *Phys. Rev. Lett.* **102**, 013903 (2009)
18. R.A. Ganeev, M. Baba, M. Suzuki, H. Kuroda, *Phys. Lett. A* **339**, 103 (2005)
19. T.D. Donnelly, T. Ditmire, K. Neuman, M.D. Perry, R.W. Falcone, *Phys. Rev. Lett.* **76**, 2472 (1996)
20. F. Lindner, W. Stremme, M.G. Schätzel, F. Grasbon, G.G. Paulus, H. Walther, R. Hartmann, L. Strüder, *Phys. Rev. A* **68**, 013814 (2003)
21. Y. Liang, S. Augst, S.L. Chin, Y. Beaudoin, M. Chaker, *J. Phys. B* **27**, 5119 (1994)
22. E.S. Toma, P. Antoine, A. de Bohan, H.G. Muller, *J. Phys. B* **32**, 5843 (1999)
23. R. Taïeb, V. Vénier, J. Wassaf, A. Maquet, *Phys. Rev. A* **68**, 033403 (2003)
24. R.A. Ganeev, M. Suzuki, M. Baba, H. Kuroda, *Appl. Phys. Lett.* **86**, 131116 (2005)
25. R.A. Ganeev, L.B. Elouga Bom, J.-C. Kieffer, T. Ozaki, *Phys. Rev. A* **75**, 063806 (2007)
26. I. Shchatsinin, T. Laarmann, N. Zhavoronkov, C.P. Schulz, I.V. Hertel, *J. Chem. Phys.* **129**, 204308 (2008)
27. V.R. Bhardwaj, D.M. Rayner, P.B. Corkum, *Phys. Rev. Lett.* **91**, 203004 (2003)
28. E. Runge, E.K.U. Gross, *Phys. Rev. Lett.* **52**, 997 (1984)
29. M.A.L. Marques, A. Castro, G.F. Bertsch, A. Rubio, *Comp. Phys. Comm.* **151**, 60 (2003)
30. N. Troullier, J.L. Martins, *Phys. Rev. B* **43**, 1993 (1991)
31. J.P. Perdew, A. Zunger, *Phys. Rev. B* **23**, 5048 (1981)

Chapter 9

Filamentation in Ultrafast Laser Material Processing

Wataru Watanabe, Takayuki Tamaki, Yasuyuki Ozeki, and Kazuyoshi Itoh

Abstract When an ultrashort laser pulse is focused inside the bulk of a transparent material, filamentation occurs as a result of the dynamic balance between the Kerr self-focusing and defocusing effects in the electron plasma, which is generated through the ionization process. The optical intensity in the filamentary volume can become high enough to induce permanent structural modifications. In this chapter, we review the applications of filamentation in the microprocessing of transparent materials and in microwelding.

9.1 Introduction

The nonlinear propagation of an ultrafast laser pulse through a material can result in dynamic changes in its temporal, spatial, and spectral properties. The self-guiding of the beam created from laser pulses, which is also called filamentation, occurs as a result of the dynamic balance between the Kerr self-focusing and defocusing effects in the electron plasma generated through the ionization process. Applications resulting from filamentary propagation include pulse self-compression, lightning control, harmonic generation, terahertz radiation, atmospheric analysis, remote sensing of molecules, and supercontinuum generation [1–6].

W. Watanabe (✉)

Photonics Research Institute, National Institute of Advanced Industrial Science and Technology,
Higashi 1-1-1, Tsukuba, Ibaraki, 305-8565, Japan
e-mail: wataru.watanabe@aist.go.jp

T. Tamaki

Department of Control Engineering, Nara National College of Technology, 22, Yatacho,
Yamatokoriyama, Nara 639-1080, Japan
e-mail: tamaki@ctrl.nara-k.ac.jp

Y. Ozeki and K. Itoh

Department of Material and Life Science, Graduate School of Engineering, Osaka University,
2-1, Yamadaoka, Suita, Osaka 565-0871, Japan
e-mail: ozeki@mls.eng.osaka-u.ac.jp, itoh@mls.eng.osaka-u.ac.jp

Ultrafast laser filamentation is observed in condensed media such as transparent solids and liquids. When an ultrafast laser pulse is focused inside the bulk of a transparent material, the intensity of the laser pulse in the filamentary region can become high enough to cause nonlinear absorption, leading to localized modification in the filamentary volume. Ultrafast laser processing using filamentation is a versatile technique for welding and for the fabrication of three-dimensional photonic devices in transparent materials, because material modification is initiated by the nonlinear absorption.

In this chapter, we highlight filament formations and modifications in transparent materials and review filamentation applications in microprocessing and microwelding. In Sect. 9.2, we cover various aspects of the filamentation of ultrafast laser pulses. In Sect. 9.3, we describe bulk modifications by filamentation. In Sect. 9.4, we review filamentation methods of fabricating photonic devices. Finally, in Sect. 9.5, we describe a welding technique in which filamentation processes are used.

9.2 Filamentation

9.2.1 Filamentation and Supercontinuum Generation

When a laser pulse is focused in a transparent material, the nonlinear propagation of the pulse leads to filamentation – a phenomenon whereby the laser beam maintains a near-constant beam radius over many Rayleigh lengths due to a temporal balance between self-focusing and plasma defocusing [7–9]. The propagation of an ultrafast laser pulse in a nonlinear medium can lead to filament formation. Above the critical power for self-focusing, $P_{\text{cr}} = \pi (0.61)^2 \lambda^2 / 8 n_0 n_2$, where λ is the wavelength, and n_0 and n_2 are the linear and nonlinear refractive indexes, respectively [10], a single filament can be formed. When the beam power sufficiently exceeds the critical power for self-focusing, the beam breaks up into multiple filaments with nearly constant diameters [11, 12]. The filamentary propagation of an ultrashort laser pulse can produce a spectrally broadened pulse ranging from ultraviolet to infrared, which is called supercontinuum. Supercontinuum generation was first observed in 1970, and it has since been demonstrated to occur in a wide variety of solids, liquids, and gasses [13–18].

9.2.2 Control of Multiple Filaments

The control of filament formation in a liquid or a solid is important for the stabilization of supercontinuum generation and micromachining. When the intensity distribution of an input laser beam was modulated, the beam exhibited self-focusing. A diffraction pattern of the beam produced a periodic self-focusing pattern [19, 20].

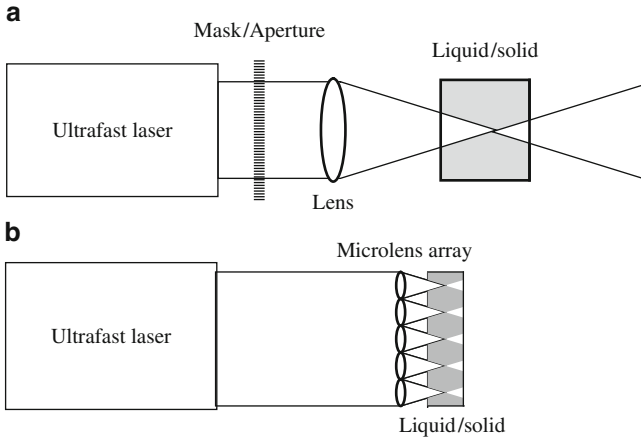


Fig. 9.1 Spatial control of filament formation by the intensity distribution of an input laser beam. (a) A spatial mask or an aperture is placed in front of a focusing lens. (b) A microlens array is used for parallel focusing

The spatial control of filament formation can be performed using a spatial amplitude-modification mask or phase mask, which is placed in front of a focusing lens (Fig. 9.1a) [21–25]. A microlens array (Fig. 9.1b) or cylindrical lens has been used to focus a beam using multiple foci [26–28]. Alternatively, the modification of the amplitude and phase of the input beam, for example, by the introduction of a beam astigmatism or ellipticity, has also been demonstrated to control filament formation processes [29, 30].

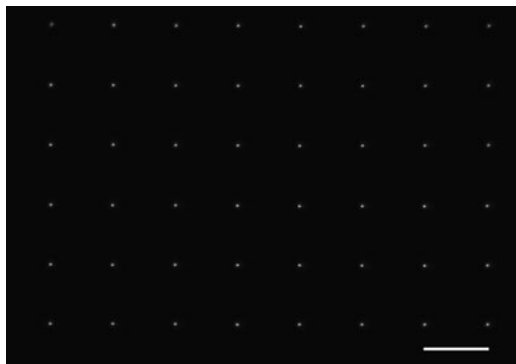
Watanabe et al. demonstrated the spatial control of filaments using a microlens array with the setup shown in Fig. 9.1b [26]. The 1-mJ, 130-fs, 1-kHz laser pulses at a wavelength of 800 nm were focused into water through a microlens array with a pitch of 10 mm and a focal length of 300 μm . Figure 9.2 shows a photograph of a 6×8 array of filaments. Each microlens produced a single filament, and a filament array was generated by the multifocusing of the femtosecond laser pulses with the microlens array.

9.3 Filamentation and Bulk Modifications

9.3.1 Filamentation and Bulk Modifications

Nanosecond laser pulses have been found to produce permanent filamentary tracks in optical glass. The long pulse duration leads to the initiation of avalanche ionization. Accordingly, scattering damage is produced by the optical breakdown process [31–35].

Fig. 9.2 Focused image of an array of supercontinuum. An array of 6×8 filaments is shown. The scalar bar shows $300 \mu\text{m}$. Reprinted with permission from [26]



When femtosecond laser pulses are focused inside the bulk of transparent materials, the intensity in the focal volume becomes high enough to cause nonlinear absorption, which leads to localized modification in the focal volume. Filamentary modifications in solid materials are mostly conducted by the external focusing of femtosecond laser pulses. Different types of filamentary tracks, such as color-centers, scattering damage, and refractive index changes, have been produced in transparent materials depending on the laser parameters (i.e., the wavelength, pulse duration, energy, and repetition rate), focusing conditions, and materials [36]. For example, filament formation has led to filamentary modifications, such as the crystallization of silver nanoparticles in silver-doped glass [37], color-center generation [38], and modification of optical fibers [39].

9.3.2 Femtosecond Filamentary Track

The filamentation of femtosecond laser pulses induces a permanent refractive index change in silica glass [40–45]. Figure 9.3a shows a microscopic image of a single filament under excitation by femtosecond laser pulses in silica glass [40]. The 85-fs, 800-nm, 1-kHz laser pulses, at an energy of $1.0 \mu\text{J}/\text{pulse}$, were focused by an objective lens with a numerical aperture (NA) of 0.1. Figure 9.3b shows an optical image of the refractive index change induced after 60 s of exposure to the focused laser pulses. Figure 9.3 shows that the region of refractive index change spatially coincides with that of the filament. By using lower NA lenses, smooth filamentary tracks, with single or multiple-filament refractive index changes, were induced in silica glass. Varying the NA of the focusing lens resulted in a region of refractive index change that was $10\text{--}500 \mu\text{m}$ long. Due to the self-focusing effect, the diameter of the region of refractive index change was approximately $2 \mu\text{m}$, which was much smaller than the diffraction-limited beam spot size, and was independent of the NAs of the focusing lenses. The magnitude of the refractive index change saturated with irradiation, and no void-like damage occurred, even under irradiation by multiple shots. The maximum refractive index change was 0.8×10^{-2} .

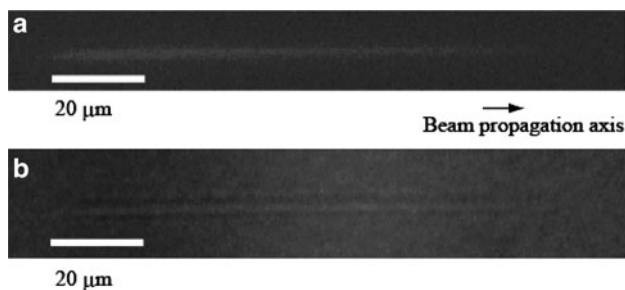


Fig. 9.3 Relationship between a filament and the region of refractive index change by focusing femtosecond laser pulses in silica glass: (a) the filament and (b) optical images of the region of refractive index change after filament irradiation (Reprinted with permission from [40])

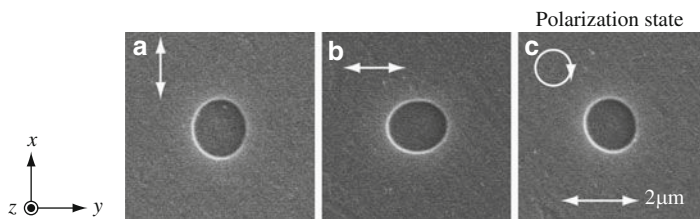
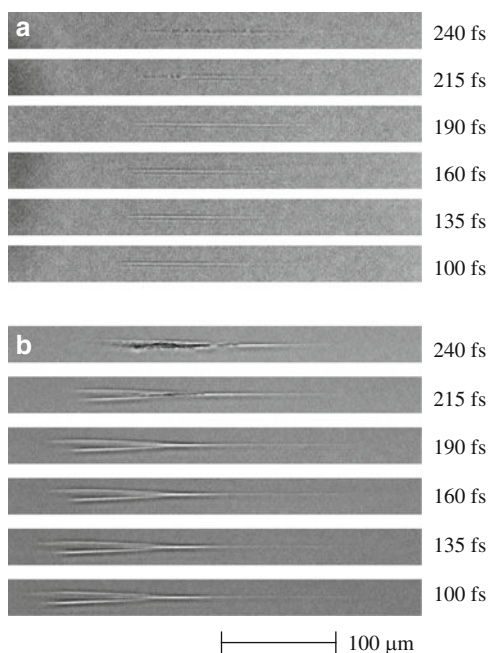


Fig. 9.4 Scanning-electron microscope images of cross-sectional regions of refractive index change. The refractive index changes were induced by (a) x -polarized pulses, (b) y -polarized pulses, and (c) circularly polarized pulses. The laser pulses propagated along the z axis (Reprinted with permission from [41])

The refractive index change induced by filamentation was dependent on the polarization of the incident ultrashort laser pulses [41]. After the induction of the filamentary refractive index, the sample was polished, and then etched by 5 mol% hydrofluoric acid solution for 150 s. Figure 9.4 shows scanning electron microscope images of the etched cross sections. The cross section of the filamentary refractive index was elliptical, with the long axis parallel to the polarization direction of the incident laser pulses. When the refractive index change was induced by circularly polarized pulses, the ellipticity was negligible.

Onda et al. investigated the filamentary tracks induced in silica glass by varying both the duration and energy of the laser pulses (800 nm, 1 kHz), using an NA of 0.1 [42]. Figure 9.5a shows an optical image of the filamentary tracks formed along the laser propagation axis. The pulse duration was varied from 100 to 240 fs by applying a positive chirp to constant-energy pulses of $2 \mu\text{J}/\text{pulse}$ for a fixed exposure time of 5 min. Below a pulse duration of 190 fs, refractive-index change was induced by a single filament. When the pulse duration was 215 fs, scattering damage occurred at the head of the track. At 240 fs, the scattering damage was found to be spread throughout the entire track. Figure 9.5b shows the filamentary tracks produced at an energy of $5 \mu\text{J}/\text{pulse}$ for a fixed exposure time of 5 min. For the positive-chirped pulses with durations below 190 fs, complex refractive-index changes were induced

Fig. 9.5 Dependence of structural changes on pulse duration when laser pulses were focused by 0.10-NA objective lens: (a) under the condition of a constant incident energy of $2.0 \mu\text{J}/\text{pulse}$ and (b) under the condition of a constant incident energy of $5.0 \mu\text{J}/\text{pulse}$. The pulses propagate from left to right in the figure (Reprinted with permission from [42])



by multiple filaments. Pulse durations longer than 190 fs induced scattering damage in the filamentary tracks.

Figure 9.6 shows a summary of the thresholds for filamentary tracks as a function of the pulse duration and energy of the laser pulses (800 nm, 1 kHz), with an NA of 0.1. In region 1, no filament or permanent tracks could be created. In region 2, a refractive-index change was induced by a single filament. Region 3 corresponds to the induction of a complex refractive-index change by the formation of multiple filaments. In region 4, optical breakdown occurred and scattering damage was produced in the filamentary tracks. Short-duration pulses induced a single filament or multiple filamentary refractive-index change that could be annealed out by heating the material at 900°C , whereas longer pulses produced birefringent scattering damage in filamentary tracks that persisted when the material was heated at 900°C . Increasing the energy of the laser pulses led to multiple filamentary tracks. A similar investigation was performed by Guo et al. Two kinds of filamentary tracks in the forms of refractive-index change and scattering damage were induced by varying the pulse duration of femtosecond laser pulses [43].

By using $\text{NA} = 0.25\text{--}0.5$, two types of filamentary tracks were observed due to two intensity thresholds [46–48]. Above the first energy threshold, an isotropic refractive-index change was induced, and only weak birefringence was displayed. Intensities in excess of the second energy threshold created stronger scattering damage and resulted in strong birefringence. Under the focusing conditions of $\text{NA} = 0.5$, Sudrie et al. found that birefringent scattering damage was followed by the formation of sub-micrometer filamentary tracks extending up to $80 \mu\text{m}$ in silica glass (Fig. 9.7a) [48]. A scanning electron microscope showed that the

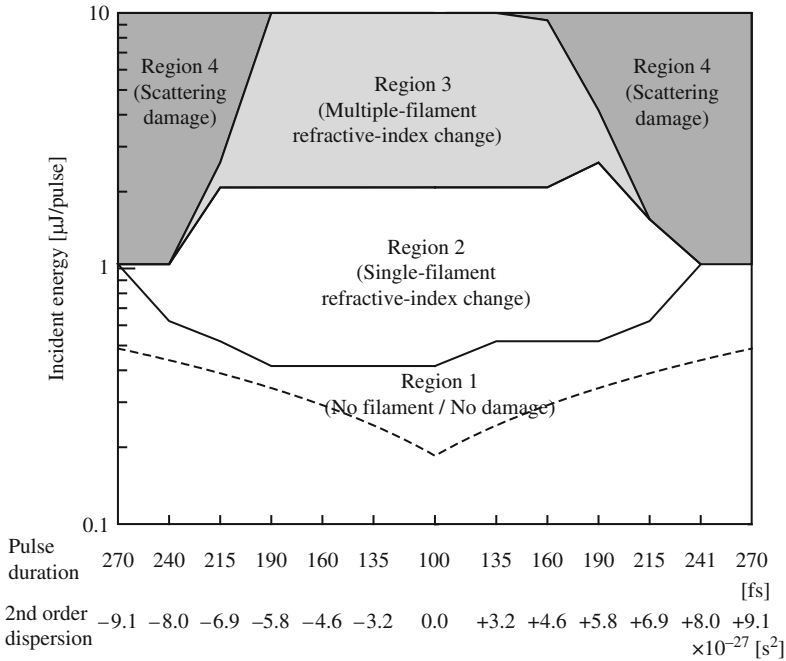


Fig. 9.6 Energy thresholds for filamentary tracks of single-filament refractive-index changes, multiple-filament refractive-index changes, and scattering damage by varying the pulse duration and incident energy. The underscore line denotes the critical energy for self-focusing (Reprinted with permission from [42])

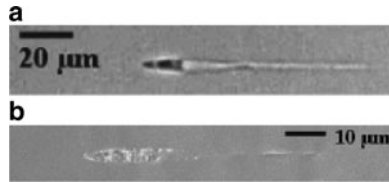


Fig. 9.7 (a) Optical image of damage tracks viewed along the propagation axis of the pulse. (b) Damage tracks in fused silica viewed under a scanning electron microscope. Damage tracks were produced by a 160-fs laser operating at 800 nm, at a repetition rate of 200 kHz. A laser pulse with an energy of 2 μ J was focused inside fused silica with an objective NA of 0.5 [48] (Reprinted with permission from [48])

birefringent zone was highly disordered and consisted of a cluster of sub-micron cavities (Fig. 9.7b).

Nguyen et al. investigated the conditions required for the formation of filamentation and optical breakdown and the competition between filamentation and optical breakdown in bulk fused silica in terms of the external focusing conditions for 45-fs, 810-nm laser pulses in fused silica [49]. The appearance of optical breakdown in a high-density plasma is usually accompanied by an isotropic broadband plasma emission due to electron recombination, which appears as a white spot around

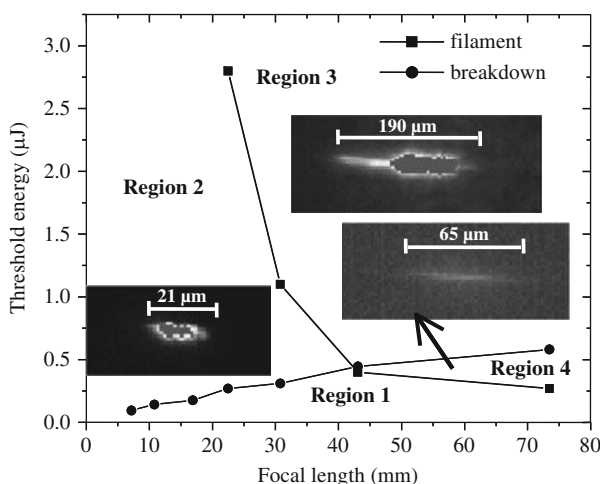


Fig. 9.8 Threshold energies for optical breakdown and filamentation as a function of focal length. The insets show typical optical breakdown and filamentation plasma images corresponding to each region (Reprinted with permission from [49])

the geometrical focus, while filamentation results in supercontinuum generation. According to the abovementioned criteria for confirming the formation of optical breakdown and filamentation, four regions were categorized as shown in Fig. 9.8. In region 1, no optical breakdown or filamentation was formed. Region 2 corresponded to the energy and focal lengths for which only optical breakdown occurred and no filamentation was formed. Filamentation occurred at a lower power compared with optical breakdown in region 4. In region 4, the required power for optical breakdown was higher than the critical power for self-focusing. The filamentation and optical breakdown coexisted for the input energies and focal lengths in region 3. Figure 9.8 shows that the energy threshold for optical breakdown in fused silica was lower than the filamentation threshold for short focal lengths, while filamentation occurred below the threshold for optical breakdown for long focal lengths.

Filamentary modifications can be produced at various wavelengths of laser pulses. Papazoglou et al. demonstrated that ultraviolet laser pulses (248 nm, 450 fs) focused in the bulk of fused silica samples produced filamentary modifications. Depending on the energy and number of pulses, three distinct types of structural changes in the material were observed, including changes in the refractive index, birefringence, and even cracks and voids [50]. Saliminia et al. inscribed optical waveguides in fused silica using 70-fs, 1.5- μ m laser pulses from an optical parametric amplifier [51, 52]. Despite the bandgap of fused silica, the refractive index modifications were of the same order as those produced at 800 nm.

Self-Organized Void Arrays

Self-organized void arrays can be induced by tightly focusing the femtosecond laser beam into fused silica glass [53–55]. A void array could be induced inside the



Fig. 9.9 A void string induced by tightly focusing femtosecond laser pulses in silica glass through an objective lens with $NA = 0.9$. The pulse energy was fixed at $50 \mu\text{J}$ and the number of pulses was 32 (Reprinted with permission from [55])

sample (Fig. 9.9) or on the rear surface of the sample [55]. The interface spherical aberration resulting from the refractive index mismatch is a possible reason for the self-formation of the void array under tightly focused conditions with high-NA objectives.

Filamentary Modifications in Polymer Materials

Focused femtosecond laser pulses produce filamentary modifications inside polymer materials [56–58]. The length of the filamentary refractive index change region was approximately $300 \mu\text{m}$ by focusing femtosecond laser pulses through an objective lens with $NA = 0.13$ [56]. Spectral broadening was observed for the filamented pulse in bulk polymers during bulk modifications [57]. At tight focusing conditions ($NA = 0.55$), a single femtosecond laser pulse created a filamentary structural change along the optical axis inside bulk poly (methyl methacrylate) (PMMA). The cavity had a diameter of $0.8 \mu\text{m}$ and a length of $125 \mu\text{m}$ [58].

9.4 Photonic Device Fabrication Using Filamentation

The femtosecond laser modification technique allows the formation of three-dimensional structures in transparent materials [36, 59–61]. In this section, we focus on the fabrication of photonic devices using filamentation. The induction of filamentary modifications is a potential method for creating photonic structures in transparent materials, such as waveguides, couplers, gratings, and lenses.

9.4.1 Fabrication of Waveguide Device

9.4.1.1 Waveguide Fabrication

In femtosecond laser micromachining, the fabrication of waveguides is accomplished in one of two ways: by moving the focus of the femtosecond laser pulses through the sample parallel either to the axis of the laser beam or perpendicular to it [62–64]. The former technique, called parallel writing, offers the advantage that

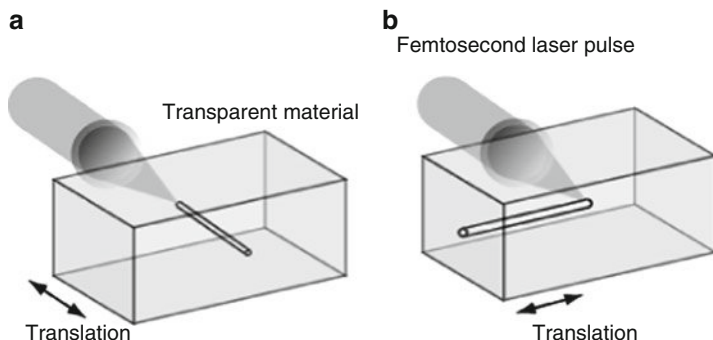


Fig. 9.10 Scheme for fabrication of waveguides embedded in glass. (a) Side-writing and (b) Parallel writing

the waveguides are circular in shape; however, the working distance of the objective lens limits the writing length of the waveguide (Fig. 9.10a). Thus, low-NA objectives with long working distance focal lengths are needed to produce waveguides. Such focusing conditions offer the potential for the generation of filamentation using laser pulses [40, 65–67]. Yamada et al. demonstrated waveguide fabrication by filamentation in silica glass [40]. By translating the sample at $1 \mu\text{m s}^{-1}$ along the optical axis, a waveguide with a core diameter of approximately $2 \mu\text{m}$ was fabricated. Cho et al. demonstrated waveguide writing in various types of glasses using filaments [65, 66].

In the transverse writing geometry, called side writing, waveguides can be fabricated within the bulk material (Fig. 9.10b). Such a waveguide has an elliptical cross section. Circular waveguides can be obtained by beam shaping using a slit in front of the focusing objective [63, 64]. In this writing regime, filamentation should be avoided.

Bending of Filament

When the filamentary region is translated alternately in the directions parallel and perpendicular to the beam axis, a curved area of modifications can be created [68] (Fig. 9.11). The curvature can be tailored by the respective sizes of the steps. The filament created in the latest step motion follows the previously induced region of refractive index change, forming a bent waveguide. Thus, a curved region of refractive index change is created from smoothly connected filaments.

Couplers and Splitters

Filamentation was used to fabricate directional couplers containing a 2-mm-long straight waveguide and a curved waveguide connected to a different straight section

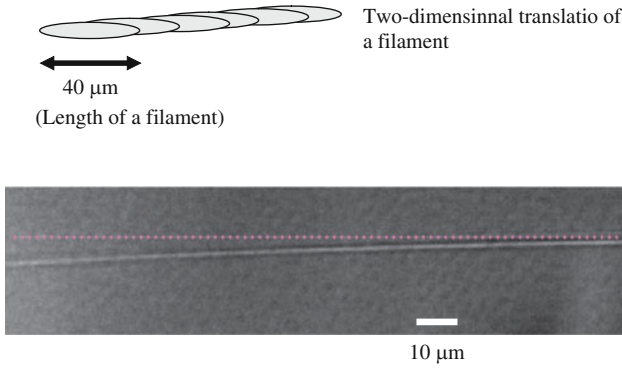


Fig. 9.11 Fabrication of a curved waveguide. Two-dimensional translation of a filament with a length of 40 μm produces a curved refractive index structure by bending the filament

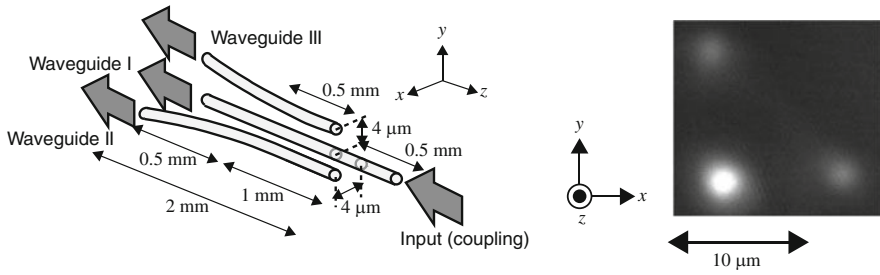


Fig. 9.12 (Left) Schematic of a three-dimensional directional coupler. (Right) Near-field patterns of coupler output when coupling to a laser beam at a wavelength of 632.8 nm (Reprinted with permission from [68])

[68]. Waveguides with a length of 2 mm were made into directional couplers with coupling ratios of 1:1 and 1:0.5 for 632.8-nm light. The realization of three-dimensional directional couplers using filamentation was demonstrated (Fig. 9.12) [68]. Figure 9.12a shows the schema of a three-dimensional directional coupler consisting of three waveguides: a 2-mm-long straight waveguide (waveguide I) and two curved waveguides that are connected to straight sections (waveguides II and III). The straight sections of waveguides II and III were parallel to the straight waveguide, with a 4 μm center-to-center separation in the x and y directions, respectively. The lengths of the straight sections of waveguides II and III were 0.5 and 1.0 mm, respectively. Figure 9.12b shows the near-field pattern of beams from the coupler at a wavelength of 632.8 nm. The beam was split among the three waveguides at different intensities. When white-light was coupled, the spectra were different at the output because the coupling properties were dependent on the wavelengths. These structures can act as wavelength-division demultiplexers or multiplexers.

A multimode interference coupler was successfully fabricated in silica glass [69]. By translating the sample parallel and perpendicular to the optical axis, multimode interference waveguides ($500 \times 30 \mu\text{m}^2$ with a 2 μm thickness) were fabricated. In

order to couple the incident beam to the fabricated multimode interference waveguides, a straight waveguide with a core diameter of $2\text{ }\mu\text{m}$ was connected to the center of the waveguide by translating the sample along the optical axis. Such fabricated multimode interference waveguides can be used as compact power splitters with large fan-outs.

9.4.2 Fabrication of Diffractive Optical Element

Volume Grating

Gratings can be fabricated in glass by a direct-writing method [46, 70]. Sudrie et al. fabricated birefringent gratings in bulk silica using birefringent refractive index changes [46]. The grating was written by the two-dimensional displacement of a silica glass sample perpendicular to the beam propagation axis. A grating with a period of $6\text{ }\mu\text{m}$ and a thickness of $20\text{ }\mu\text{m}$ had a diffraction efficiency of 20% [46]. Gratings with 10- and $2\text{-}\mu\text{m}$ periods were fabricated in fused silica and BK7, and shown to be thermally stable [70].

A volume grating can be embedded by the two-dimensional displacement of a filament perpendicular to the beam propagation axis. Yamada et al. reported the fabrication of Bragg gratings in silica glass by the two-dimensional translation of a filament with a length of $150\text{ }\mu\text{m}$ [71]. When a laser beam with a wavelength of 632.8 nm was directed into the grating embedded in the silica glass at the Bragg angle, a maximum diffraction efficiency of 74.8% was obtained when the grating had a period of $3\text{ }\mu\text{m}$ and a thickness of $150\text{ }\mu\text{m}$.

Dammann Grating

A Dammann grating is a diffractive optical element that can generate regular one- or two-dimensional beam patterns of equal intensity spots and is used as an optical splitter. By using the femtosecond laser filamentation writing technique, Dammann gratings have been embedded in glass [72–74]. Nakaya et al. reported the fabrication of Dammann gratings in silica glass [72]. They fabricated a 6×6 grating with a diffraction efficiency of only 7.7%. In order to increase the diffraction efficiency, they carried out preliminary experiments by writing multilayer 1×2 gratings with a diffraction efficiency of 70%.

Li et al. demonstrated the fabrication of single-layer Dammann gratings in silica glass [73]. The refractive index change was induced by the use of a $160\text{ }\mu\text{m}$ -long filament, and the filament was translated two-dimensionally. The diffraction efficiency of a 5×5 Dammann grating with 8×8 periods was 56%, close to the theoretical value of 77%.

Hologram and Beam Shaper

Ran et al. demonstrated the fabrication of a computer-generated hologram of the optical vortex inside glass induced from a filament with a length of 200 μm . The optical vortex beam was reconstructed, and the first-order diffraction efficiency at a wavelength of 632.8 nm was 19.6% [75]. Wang et al. fabricated several refractive index-modified beam shapers, including a grid grating, square grating, and ring gratings, by filament formation [76].

Diffraction Lens

The fabrication of two-level phase-type diffractive lenses was demonstrated by inducing a birefringent refractive index change in silica glass. The efficiency of this lens reached approximately 40% at a wavelength of 404 nm and was dependent on the polarization of the incident beam [77]. However, the efficiency was only 17% at a wavelength of 642 nm because the length of the filamentary refractive index region was only 30 μm .

Two-level diffractive lenses with multiple layers were fabricated to increase the overall thickness of the diffractive lenses due to filamentary refractive index change. The maximum efficiency of the two-level diffractive lenses was 37.6% at a wavelength of 632.8 nm [78]. Furthermore, four-level diffractive lenses were shown to provide a maximum efficiency of 56.9% (Fig. 9.13) [78].

Srisungsitthisunti et al. fabricated a volume Fresnel zone plate, which consists of a number of layers of Fresnel zone plates designed to focus light together, in fused silica. Experimental results indicated that volume Fresnel zone plates increased the

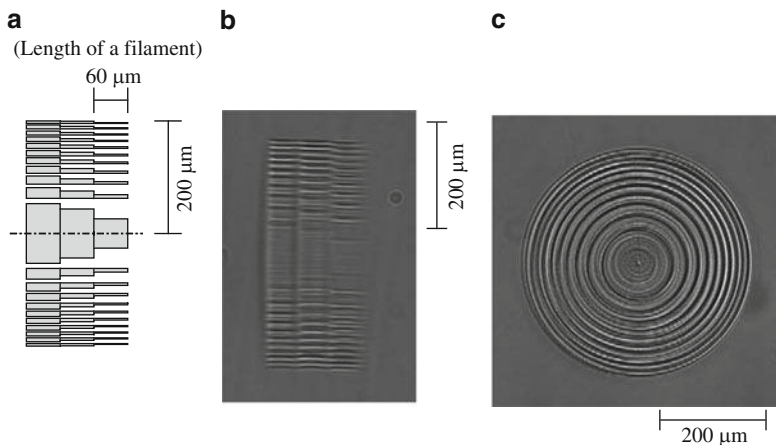


Fig. 9.13 (a) Design of four-level phase-type diffractive lens. (b) Side view and (c) top view of fabricated four-level phase-type diffractive lens (Reprinted with permission from [78])

overall diffraction efficiency [79, 80]. In order to achieve a volumetric lens in glass, collinear femtosecond laser beams with different wavefront curvatures were used to produce two filaments at different depths below the surface of the silica glass. Hence, multiple filaments along the optical axis existed in the glass simultaneously, and parallel writing on multiple layers was realized [81]. Siiman et al. successfully fabricated a cylindrical phase Fresnel lens in photosensitive glass by a two-step process that included infrared ultrashort laser pulse exposure and thermal development, resulting in the precipitation of nanocrystals in the exposed areas [82].

9.4.3 Fabrication of Diffractive Optical Elements in Polymer Materials

The fabrication of diffractive optical elements inside polymer materials has been reported [56, 83–88]. Mochizuki et al. embedded diffractive optical elements in a wide variety of polymers [56]. In polymethylpentene, which had the lowest density of the polymers examined, large volume contraction by femtosecond laser irradiation was observed by transmission electron microscopy. The larger refractive index change in polymethylpentene was attributed to its large volume contraction based on its low density. In particular, a large refractive index change in PMMA was induced by laser irradiation at a wavelength of 400 nm or less, with a pulse width of 100 fs or less [87, 88].

9.5 Microwelding Using Filamentation

9.5.1 Femtosecond Laser Welding of Transparent Materials

The development of techniques for welding/joining materials on a micrometer scale is of great importance in a number of applications, including the production of electronic, electromechanical, and medical devices. Laser microwelding/joining is a prospective technique due to the following advantages: (1) high-flexibility, (2) high-precision, (3) high-speed, (4) noncontact processing, and (5) substantially room-temperature processing. The laser welding of dissimilar materials can find applications in the assembly of sensors, microsystem components, and microfluidic devices, as well as the sealing of microelectromechanical systems (MEMS) and organic light-emitting diodes. In this section, we describe a welding/joining technique that uses ultrashort laser filamentation.

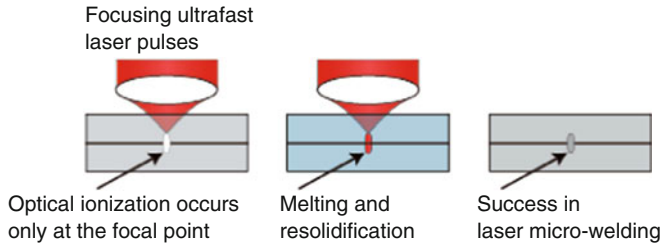


Fig. 9.14 Schematic diagram of ultrafast laser microwelding of transparent materials using ultrafast laser pulses. (a) When an ultrafast laser pulse is focused on the interface of two substrates, a filament bridges the two substrates. (b) Localized melting and quenching occur at the interface of the two substrates around the filament. (c) Resolidification of the materials can result in the samples being joined (Reprinted with permission from [90])

9.5.1.1 Principle of Femtosecond Laser Welding Using Filamentation

Figure 9.14 shows a schematic diagram of an ultrafast laser welding technique [89]. By focusing an ultrafast laser pulse at the interface between transparent materials (Fig. 9.14a), a filament bridges the two substrates, and the energy deposited by the laser pulse melts the materials in the neighborhood of this filament. The melted material fills up the original gap between the two materials (Fig. 9.14b). By the subsequent resolidification dynamics, the precise welding of transparent materials can be realized without any intermediate layers (Fig. 9.14c). Because there is minimal heating outside the focal volume, ultrashort laser joining allows space-selective joining without requiring the insertion of any intermediate layers, and it can be applied even to transparent materials with insufficient absorption at the wavelength used. Arbitrary joint volumes are produced by two-dimensionally translating the substrates with respect to the focal volume. The gap between the samples in the joined area should be below $\lambda/4$ (where λ is the wavelength), in order to avoid ablation at the surfaces of the substrates.

9.5.1.2 Welding of Similar Materials

Tamaki et al. demonstrated the welding of transparent materials using ultrashort laser pulses [89]. A femtosecond laser system producing 85-fs, 800-nm, 1-kHz pulses was used to join pieces of glass. A 30- μm -long filament bridged the glass samples, and a refractive index change was induced within the joint volume. The sample was two-dimensionally translated with respect to the focal region. Figure 9.15 shows schematic and optical images of a 4×4 array of joint volumes ($100 \times 100 \times 30 \mu\text{m}$) after welding the glass samples by irradiating them with ultrashort laser pulses with a pulse energy of $1.0 \mu\text{J}$ and a translation velocity of 0.1 mm s^{-1} [91]. The welding of both borosilicate glass substrates and fused silica substrates was demonstrated. The joint strength was approximately 15 MPa.

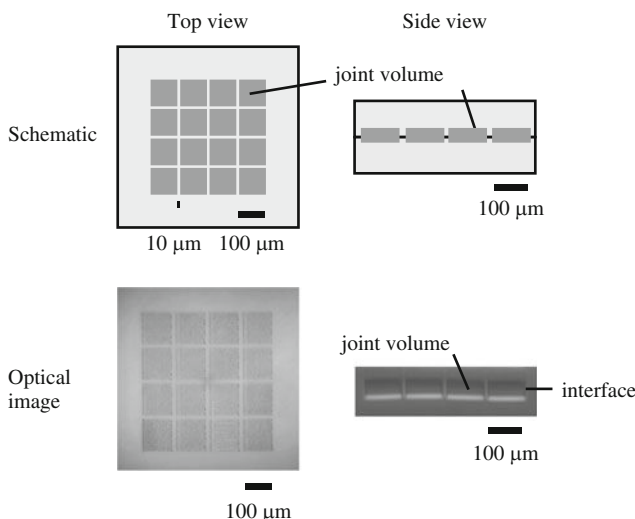


Fig. 9.15 Schematic and optical images of top and side views after ultrashort laser joining with a pulse energy of $1.0\ \mu\text{J}$ and a translation velocity of $0.1\ \text{mm s}^{-1}$ in borosilicate glass

9.5.1.3 Welding of Dissimilar Materials

The welding of dissimilar glasses has also been realized by this ultrashort laser welding technique. The joining of borosilicate and fused silica glass substrates, which have different coefficients of thermal expansion, has been demonstrated [92].

9.5.1.4 Ultrashort Laser Welding with High Repetition Rate

With high-repetition-rate lasers, the ultrashort laser welding technique can be achieved based on a localized heat accumulation effect. In this regime, the focused laser pulses collectively act as a point heat source at the focal volume within the bulk material when the time interval between successive pulses is much shorter than the time scale for the diffusion of heat out of the focal volume. The accumulated energy around the focal volume makes it possible to achieve very high temperatures and melt the material around the focal volume. The length of the joint volume is elongated due to filamentation and heat accumulation. The ultrashort laser welding of non-alkali aluminosilicate glass substrates was performed based on a localized heat accumulation effect using an amplified femtosecond Er-fiber laser (1 ps, 1,558 nm, 500 kHz) [93]. Tamaki et al. also successfully demonstrated the welding of a non-alkali glass substrate and a silicon substrate. The wavelength of the femtosecond laser pulses was 1,558 nm, where silicon and borosilicate glass are transparent. A 1-MHz ultrashort laser was used to weld borosilicate glass substrates [94,95]. High-repetition-rate laser pulses are suitable for the rapid welding of glass plates with a

low glass transition temperature, such as borosilicate glass; however, a complex pattern of refractive index change is induced within the weld region.

9.5.1.5 Welding Between Transparent Material and Absorbing Material

The ultrafast laser welding technique can be applied to welding a transparent substrate and one that is opaque at the wavelength of the laser radiation used. Absorbance on the opaque substrate induces localized melting and subsequent joining. Glass–silicon welding has been achieved by focusing high-repetition rate ultrafast laser irradiation (350 fs, 1045 nm, 700 kHz) [96]. At this laser wavelength, silicon is not transparent. Glass–silicon welding is an important step toward the welding of semiconductor materials.

9.5.1.6 Femtosecond Laser Welding Between Metal and Glass

As mentioned in the previous section, the technique of ultrashort laser welding is a powerful tool for joining transparent materials. The ability to weld together different materials, such as glass and metal, will lead to wider application areas, such as in the assembly and packaging of microdevices. Nanosecond pulses were used to weld a glass cover slip and copper ball [97].

Ozeki et al. reported laser welding between copper and glass substrates to demonstrate the effectiveness of using femtosecond laser pulses compared to nanosecond ones [98]. Figure 9.16 shows the tensile joint strengths of the welded samples as a function of the pulse energy. The joint strength was greater than 16 MPa with femtosecond pulses and greater than 13 MPa with nanosecond pulses. Considering the wide variation in the pulse energy, the dependence of the joint strength on pulse energy was less significant. Interestingly, the pulse energy required for the welding was dependent on the pulse width. With femtosecond pulses, welding was successful when the pulse energy was higher than approximately 0.4 μJ . On the other hand, with nanosecond pulses, the pulse energy needed to be higher than 50 μJ for successful welding. Thus, the use of femtosecond pulses reduces the required pulse energy by two orders of magnitude compared to nanosecond pulses. Presumably, femtosecond pulses can melt, not only the copper but also the glass, through the formation of a filament, whereas nanosecond pulses cannot melt the glass due to the lower peak power. Therefore, the formation of a molten pool with nanosecond pulses requires a sufficient amount of pulse energy, to allow the glass to be melted after the thermal conduction from the copper to the glass.

The difference in the required pulse energy results in different morphologies for the irradiated regions. Figure 9.17a, b show optical microscopic images of the samples after irradiation by femtosecond pulses and nanosecond pulses, respectively. The pulse energies of the femtosecond and nanosecond pulses were set to 4 and 100 μJ , respectively. The black regions correspond to the irradiated areas. These images show a clear difference at the boundary of the regions. With femtosecond

Fig. 9.16 Dependence of joint strength on the irradiated pulse energy. *Filled circles*: welding with femtosecond pulses. *Open circles*: welding with nanosecond pulses (Reprinted with permission from [98])

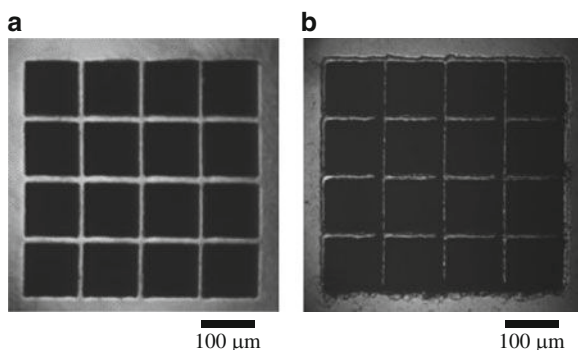
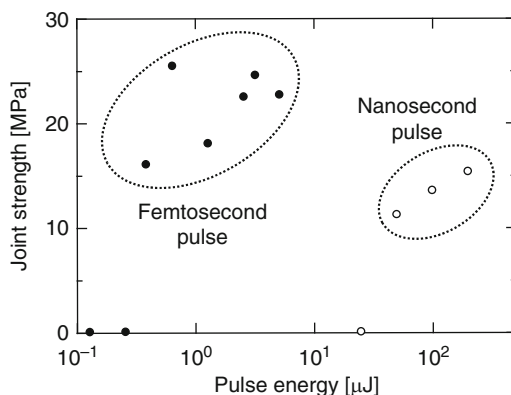


Fig. 9.17 Reflection optical microscope images of welded copper and glass substrates with (a) femtosecond pulses and (b) nanosecond pulses, observed from the top of the sample (Reprinted with permission from [98])

pulses, a separation between the welded regions was clearly present, as shown in Fig. 9.17a. In contrast, with nanosecond pulses, as seen in Fig. 9.17b, the intervals almost disappear, due to the effect of excess heat. These results prove that femtosecond pulses are able to precisely control the welded region by suppressing the excess heat.

Femtosecond laser welding is advantageous because it allows for precise microwelding between glass and metal. Because of the different expansion coefficients of various glasses and metals, mechanical stresses during the melting process are inevitable. By adopting ultrafast laser welding for glass and metal, this effect is avoided, which leads to a strong joint strength. Glass-metal welding is important for the hermetically sealed packaging of electronic components within a single container; for example, the passivation or hermetic sealing of solar collectors and electric devices. In particular, hermetic sealing (i.e., an air-tight seal) can secure electronic components from any external factors that could impact their functions and workable lifetimes.

9.6 Conclusion

In this chapter, we reviewed filament formations and modifications in materials, along with applications of filamentation in microprocessing and microwelding. Processing and welding techniques using filamentation produced by femtosecond laser pulses have the potential for precise and micromachining in bulk solids. Filamentary modifications in bulk transparent materials have a number of features that make them attractive for a broad range of applications, such as the fabrication of integrated photonic devices and welding.

References

1. S.L. Chin, F. Théberge, W. Liu, *Appl. Phys. B* **86**, 477–483 (2007)
2. A. Couairon, A. Mysyrowicz, *Phys. Rep.-Rev. Sect. Phys. Lett.* **441**, 47–189 (2007)
3. L. Berge, S. Skupin, R. Nuter, J. Kasparian, J.P. Wolf, *Rep. Prog. Phys.* **70**, 1633–1713 (2007)
4. J. Kasparian, J.P. Wolf, *Opt. Express* **16**, 466–493 (2008)
5. R.W. Boyd, Svetlana G. Lukishova, Y.R. Shen (eds.), *Self-focusing: Past and Present*, Topics in Applied Physics, vol. 114 (Springer, Heidelberg, 2009)
6. V.P. Kandidov, S.A. Shlenov, O.G. Kosareva, *Quant. Electron.* **39**, 205–228 (2009)
7. A.L. Gaeta, *Phys. Rev. Lett.* **84**, 3582–3585 (2000)
8. Z.X. Wu, H.B. Jiang, Q. Sun, H. Yang, Q.H. Gong, *Phys. Rev. A* **68**, 063820 (2003)
9. S. Tzortzakis, L. Sudrie, M. Franco, B. Prade, A. Mysyrowicz, A. Couairon, L. Berge *Phys. Rev. Lett.* **87**, 213902 (2001)
10. R.W. Boyd, *Nonlinear Optics* (Academic, San Diego, 1992)
11. R.Y. Chiao, M.A. Johnson, S. Krinsky, H.A. Smith, C.H. Townes, E. Garmire, *IEEE J. Quant. Electron.* **2**, 467–469 (1966)
12. R.G. Brewer, J.R. Lifshits, E. Garmire, R.Y. Chiao, C.H. Townes, *Phys. Rev.* 166326 (1970)
13. R.R. Alfano, S.L. Shapiro, *Phys. Rev. Lett.* **24**, 584–587 (1970)
14. R.R. Alfano, *The Supercontinuum Laser Source* (Springer, New York, 1989)
15. S.L. Chin, A. Brodeur, S. Petit, O.G. Kosareva, V.P. Kandidov, *J. Nonlinear Opt. Phys. Mater.* **8**, 121 (1999)
16. A. Brodeur, S.L. Chin, *Phys. Rev. Lett.* **80**, 4406–4440 (1998)
17. A. Brodeur, S.L. Chin, *J. Opt. Soc. Am. B Opt. Phys.* **16**, 637–650 (1999)
18. W. Watanabe, K. Itoh, *Jpn. J. Appl. Phys. Part 1 Regular Papers Short Notes Rev. Papers* **40**, 592–595 (2001)
19. A.J. Campillo, S.L. Shapiro, B.R. Suydam, *Appl. Phys. Lett.* **23**, 628–630 (1973)
20. A.J. Campillo, S.L. Shapiro, B.R. Suydam, *Appl. Phys. Lett.* **23**, 178–180 (1973)
21. V.P. Kandidov, N. Akozbek, M. Scalora, O.G. Kosareva, A.V. Nyakk, Q. Luo, S.A. Hosseini, S.L. Chin, *Appl. Phys. B Lasers Opt.* **80**, 267–275 (2005)
22. O.G. Kosareva, T. Nguyen, N.A. Panov, W. Liu, A. Saliminia, V.P. Kandidov, N. Akozbek, M. Scalora, R. Vallee, S.L. Chin, *Opt. Commun.* **267**, 511–523 (2006)
23. G. Mechain, A. Couairon, M. Franco, B. Prade, A. Mysyrowicz, *Phys. Rev. Lett.* **93**, 035003 (2004)
24. H. Schroeder, J. Liu, S.L. Chin, *Opt. Expr.* **12**, 4768–4774 (2004)
25. T. Pfeifer, L. Gallmann, M.J. Abel, D.M. Neumark, S.R. Leone, *Opt. Lett.* **31**, 2326–2328 (2006)
26. W. Watanabe, Y. Masuda, H. Arimoto, K. Itoh, *Opt. Rev.* **6**, 167–172 (1999)
27. K. Cook, R. McGeorge, A.K. Kar, M.R. Taghizadeh, R.A. Lamb, *Appl. Phys. Lett.* **86**, 021105 (2005)

28. K. Cook, R. McGeorge, A.K. Kar, M.R. Taghizadeh, *Appl. Phys. Lett.* **83**, 3861 (2003)
29. G. Fibich, S. Eisenmann, B. Ilan, A. Zigler, *Opt. Lett.* **29**, 1772–1774 (2004)
30. A.D. Dubietis, G. Tamošauskas, G. Fibich, B. Ilan, *Opt. Lett.* **29**, 1126–1128 (2004)
31. N. Bloembergen, *IEEE J. Quant. Electron.* **10**, 375–386 (1974)
32. E. Yablonovitch, *Appl. Phys. Lett.* **19**, 495–497 (1971)
33. G.N. Steinberg, *Phys. Rev. A* **4**, 1182–1194 (1971)
34. M.J. Soileau, W.E. Williams, N. Mansour, E.W. Vanstryland, *Opt. Eng.* **28**, 1133–1144 (1989)
35. D. Ashkenasi, H. Varel, A. Rosenfeld, S. Henz, J. Herrmann, E.E.B. Cambell, *Appl. Phys. Lett.* **72**, 1442–1444 (1998)
36. K. Itoh, W. Watanabe, S. Nolte, C.B. Schaffer, *MRS Bull.* **31**, 620–625 (2006)
37. Y. Kondo, T. Suzuki, H. Inouye, K. Miura, T. Mitsuyu, K. Hirao, *Jpn. J. Appl. Phys. Part 2-Lett.* **37**, L94–L96 (1998)
38. O.M. Efimov, K. Gabel, S.V. Garnov, L.B. Glebov, S. Grantham, M. Richardson, M.J. Soileau, *J. Opt. Soc. Am. B Opt. Phys.* **15**, 193–199 (1998)
39. S.H. Cho, H. Kumagai, I. Yokota, K. Midorikawa, M. Obara, *Jpn. J. Appl. Phys. Part 2-Lett. Exp. Lett.* **37**, L737–L739 (1998)
40. K. Yamada, W. Watanabe, T. Toma, K. Itoh, J. Nishii, *Opt. Lett.* **26**, 19–21 (2001)
41. K. Yamada, W. Watanabe, J. Nishii, K. Itoh, *J. Appl. Phys.* **93**, 1889–1892 (2003)
42. S. Onda, W. Watanabe, K. Yamada, K. Itoh, J. Nishii, *J. Opt. Soc. Am. B Opt. Phys.* **22**, 2437–2443 (2005)
43. H.C. Guo, H.B. Jiang, Y. Fang, C. Peng, H. Yang, Y. Li, Q.H. Gong, *J. Opt. A Pure Appl. Opt.* **6**, 787–790 (2004)
44. M. Kamata, M. Obara, *Appl. Phys. A Mater. Sci. Process.* **78**, 85–88 (2004)
45. J.B. Ashcom, R.R. Gattass, C.B. Schaffer, E. Mazur, *J. Opt. Soc. Am. B Opt. Phys.* **23**, 2317–2322 (2006)
46. L. Sudrie, M. Franco, B. Prade, A. Mysyrowicz, *Opt. Commun.* **171**, 279–284 (1999)
47. L. Sudrie, M. Franco, B. Prade, A. Mysyrowicz, *Opt. Commun.* **191**, 333–339 (2001)
48. L. Sudrie, A. Couairon, M. Franco, B. Lamouroux, B. Prade, S. Tzortzakis, A. Mysyrowicz, *Phys. Rev. Lett.* **89**, 186601 (2002)
49. N.T. Nguyen, A. Saliminia, W. Liu, S.L. Chin, R. Vallee, *Opt. Lett.* **28**, 1591–1593 (2003)
50. D.G. Papazoglou, I. Zergioti, S. Tzortzakis, G. Sgouros, G. Maravelias, S. Christopoulos, C. Fotakis, *Appl. Phys. A Mater. Sci. Process.* **81**, 241–244 (2005)
51. A. Saliminia, N.T. Nguyen, S.L. Chin, R. Vallee, *J. Appl. Phys.* **99**, 093104 (2006)
52. A. Saliminia, R. Vallee, S.L. Chin, *Opt. Commun.* **256**, 422–427 (2005)
53. E. Toratani, M. Kamata, M. Obara, *Appl. Phys. Lett.* **87**, 171103 (2005)
54. S. Kanehira, J.H. Si, J.R. Qiu, K. Fujita, K. Hirao, *Nano Lett.* **5**, 1591–1595 (2005)
55. J. Song, X.S. Wang, X. Hu, Y. Dai, J.R. Qiu, Y. Cheng, Z.Z. Xu, *Appl. Phys. Lett.* **92**, 092904 (2008)
56. H. Mochizuki, W. Watanabe, R. Ezoe, T. Tamaki, Y. Ozeki, K. Itoh, M. Kasuya, K. Matsuda, S. Hirono, *Appl. Phys. Lett.* **92**, 091120 (2008)
57. W. Watanabe, *Laser Phys.* **19**, 342–345 (2009)
58. S. Sowa, W. Watanabe, J. Nishii, K. Itoh, *Appl. Phys. A Mater. Sci. Process.* **81**, 1587–1590 (2005)
59. J.R. Qui, *Chem. Rec.* **4**, 50–58 (2004)
60. R.R. Gattass, E. Mazur, *Nat. Photon.* **2**, 219–225 (2008)
61. Y. Shimotsuma, K. Hirao, P.G. Kazansky, H.R. Qiu, *Jpn. J. Appl. Phys. Part 1-Regular Papers Brief Commun. Rev. Papers* **44**, 4735–4748 (2005)
62. K.M. Davis, K. Miura, N. Sugimoto, K. Hirao, *Opt. Lett.* **21**, 1729–1731 (1996)
63. G. Della Valle, R. Osellame, P. Laporta, *J. Opt. A Pure Appl. Opt.* **11**, 013001 (2009)
64. M. Ams, G.D. Marshall, P. Dekker, M. Dubov, V.K. Mezentsev, I. Bennion, M.J. Withford, *IEEE J. Sel. Top. Quan. Electron.* **14**, 1370–1381 (2008)
65. S.H. Cho, W.S. Chang, J.G. Kim, K.H. Whang, *Appl. Phys. Lett.* **91**, 121907 (2007)
66. S.H. Cho, H. Kumagai, K. Midorikawa, *Opt. Mater.* **26**, 57–63 (2004)
67. A. Saliminia, N.T. Nguyen, M.C. Nadeau, S. Petit, S.L. Chin, R. Vallee, *J. Appl. Phys.* **93**, 3724–3728 (2003)

68. W. Watanabe, T. Asano, K. Yamada, K. Itoh, J. Nishii, *Opt. Lett.* **28**, 2491–2493 (2003)
69. W. Watanabe, Y. Note, K. Itoh, *Opt. Lett.* **30**, 2888–2890 (2005)
70. C. Florea, K.A. Winick, *J. Lightwave Technol.* **21**, 246–253 (2003)
71. K. Yamada, W. Watanabe, K. Kintaka, J. Nishii, K. Itoh, *Jpn. J. Appl. Phys. Part 1-Regular Papers Short Notes Rev. Papers* **42**, 6916–6919 (2003)
72. T. Nakaya, J.R. Qiu, C.H. Zhou, K. Hirao, *Chin. Phys. Lett.* **21**, 1061–1063 (2004)
73. Y.D. Li, W. Watanabe, T. Tamaki, J. Nishii, K. Itoh, *Jpn. J. Appl. Phys. Part 1-Regular Papers Brief Commun. Rev. Papers* **44**, 5014–5016 (2005)
74. S. Lee, S. Nikumb, *Opt. Laser Technol.* **39**, 1328–1333 (2007)
75. L. Ran, S. Qu, *Curr. Appl. Phys.* **9**, 1210–1212 (2009)
76. X. Wang, H.C. Guo, H. Yang, H.B. Jiang, Q.H. Gong, *Appl. Opt.* **43**, 4571–4574 (2004)
77. E. Bricchi, B.G. Klappauf, P.G. Kazansky, *Opt. Lett.* **29**, 119–121 (2004)
78. K. Yamada, W. Watanabe, Y.D. Li, K. Itoh, J. Nishii, *Opt. Lett.* **29**, 1846–1848 (2004)
79. P. Srisungsitthisunti, O.K. Ersoy, X.F. Xu, *J. Opt. Soc. Am. B Opt. Phys.* **24**, 2090–2096 (2007)
80. P. Srisungsitthisunti, O.K. Ersoy, X.F. Xu, *Appl. Phys. Lett.* **90**, 011104 (2007)
81. Y.D. Li, C. Xing, Y.S. Ma, J.G. Tian, J.J. Xu, Q. Sun, *J. Opt. A Pure Appl. Opt.* **11**, 045601 (2009)
82. L.A. Siiman, J. Lumeau, L.B. Glebov, *Opt. Lett.* **34**, 40–42 (2009)
83. S. Katayama, M. Horiike, K. Hirao, N. Tsutsumi, *Jpn. J. Appl. Phys. Part 1-Regular Papers Short Notes Rev. Papers* **41**, 2155–2162 (2002)
84. S. Katayama, M. Horiike, K. Hirao, N. Tsutsumi, *J. Polym. Sci. Part B Polym. Phys.* **40**, 537–544 (2002)
85. P.J. Scully, D. Jones, D.A. Jaroszynski, *J. Opt. A Pure Appl. Opt.* **5**, S92–S96 (2003)
86. C. Wochnowski, Y. Cheng, K. Meteava, K. Sugioka, K. Midorikawa, S. Metev, *J. Opt. A Pure Appl. Opt.* **7**, 493–501 (2005)
87. A. Baum, P.J. Scully, M. Basanta, C.L.P. Thomas, P.R. Fielden, N.J. Goddard, W. Perrie, P.R. Chalker, *Opt. Lett.* **32**, 190–192 (2007)
88. A. Baum, P.J. Scully, W. Perrie, D. Jones, R. Issac, D.A. Jaroszynski, *Opt. Lett.* **33**, 651–653 (2008)
89. T. Tamaki, W. Watanabe, J. Nishii, K. Itoh, *Jpn. J. Appl. Phys. Part 2-Lett. Exp. Lett.* **44**, L687–L689 (2005)
90. T. Tamaki, W. Watanabe, K. Itoh, *Opt. Photon. News* **18**, 46 (2007)
91. W. Watanabe, S. Onda, T. Tamaki, K. Itoh, *Appl. Phys. B Lasers Opt.* **87**, 85–89 (2007)
92. W. Watanabe, S. Onda, T. Tamaki, K. Itoh, J. Nishii, *Appl. Phys. Lett.* **89**, 021106 (2006)
93. T. Tamaki, W. Watanabe, K. Itoh, *Opt. Exp.* **14**, 10460–10468 (2006)
94. J. Bovatsek, A. Arai, C.B. Schaffer, Three-dimensional micromachining inside transparent materials using femtosecond laser pulses: new applications. CLEO/QELS and PhAST 2006, California, USA, (2006)
95. A. Horn, I. Mingareev, J. Gottmann, A. Werth, U. Brenk, *Meas. Sci. Technol.* **19**, 015302 (2008)
96. A. Horn, I. Mingareev, A. Werth, M. Kachel, U. Brenk, *Appl. Phys. A Mater. Sci. Process.* **93**, 171–175 (2008)
97. A. Utsumi, T. Ooie, T. Yano, M. Katsumura, *J. Laser Micro/Nano Eng.* **2**, 133 (2007)
98. Y. Ozeki, T. Inoue, T. Tamaki, H. Yamaguchi, S. Onda, W. Watanabe, T. Sano, S. Nishiuchi, A. Hirose, K. Itoh, *Appl. Phys. Exp.* **1**, 082601 (2008)

Chapter 10

Plasma Electron Kinetics and Distribution Functions in Laser Fields

Gaetano Ferrante and Roberto Luigi Oliveri

Abstract A concise review of the properties of electron distribution functions in a fully ionized plasma in the presence of a high-frequency laser field is presented. In detail is discussed the physical origin of most of the reported results in the case of strong fields. The presence of a laser field, through the inverse bremsstrahlung absorption, alters dynamically the roles of and the interplay between electron–ion and electron–electron collisions shaping the distribution function. Special attention is paid to the role of e–e collisions in the process of laser–plasma interaction.

10.1 Introduction

When an external field produces or interacts with a plasma, as a rule, the problem arises concerning the actual shape of the electron distribution function (EDF), accounting for the electron kinetics in the system. To some extent, the situation is similar to that arising in a quantum mechanical context, when the knowledge of the wavefunction of a given system in a external field is a prerequisite to be in the position to perform calculations of properties and processes characterizing the system. Of course, in both cases, the availability of advanced numerical methods and of powerful computing means gives the possibility to by pass the problem, at least when only specific information is needed. In general, the problem remains, and the awareness that the action of an external field may alter the plasma EDF shape and that these alterations may be relevant for applications has prompted many extensive investigations over the years, both theoretical and experimental, intended to gain an adequate understanding of the problem. By the way, such an understanding is necessary if one wishes to induce and/or control specific aspects of the plasma behaviour.

G. Ferrante and R.L. Oliveri (✉)

Dipartimento di Fisica e Tecnologie Relative, Università di Palermo, Viale delle Scienze, 90128 Palermo, Italy

e-mail: luigi.oliveri@difter.unipa.it, ferrante3@unipa.it

In recent years, increasing attention has been paid to the issue of the EDFs of plasmas under the action of a strong laser field. It is intended that the present chapter gives a concise overview of the methods, ideas, results and implications typical of this subject. More specifically, we report on the kinetics of electrons in a fully ionized, two-component plasma under the action of strong high-frequency laser fields.

Among others, below we report on recent new results on the role of electron–electron collisions during the electron–plasma interaction and its effect on plasma heating efficiency and rate, and on a more accurate analysis concerning the issue, when a laser-modified EDF may be approximated by an anisotropic bi-Maxwellian. A concise overview of some of the previous work on the present issues may be found in [1]. Field intensities and plasma electron velocities are confined to the nonrelativistic domain (classical plasmas). For an overview on the effects of constant electric, radiofrequency and microwave fields on the plasma behaviour, see [2]. Information on the issues of EDF in the relativistic domain may be found in [3] and reference therein, and in [4]. A detailed report on EDF formed after tunnelling ionization may be found in [5].

The equation for the plasma EDF in the presence of a high-frequency radiation field is known since many years. Besides, for a long time, it has been adequate for the real physical conditions to consider the electron distribution to be close to a Maxwellian (or to a Maxwellian in a coordinate system oscillating with the same frequency as the external field). The situation has changed significantly with the emergence of powerful sources of laser radiation. Perhaps, the first important indication for the need of careful investigations concerning the actual shape of plasma EDF in the presence of a laser field is contained in the paper by Langdon [6] (see also [7]), where significant results were reported. In [6], the case of a relatively weak laser field was considered, when the amplitude of the electron quiver velocity v_E is smaller than the thermal velocity v_T , but larger than v_T/\sqrt{Z} , Z being the ionization multiplicity. In [6], it was shown that, as a result of electron heating due to inverse bremsstrahlung absorption made possible by electron–ion collisions, in the process of plasma–laser interaction (LPI), a distribution function is established, exhibiting a far-reaching depletion of slow electrons. Afterwards, a lot of papers were published along the same lines addressing, among other things, the influence on the EDF of the electron–electron collisions and the plasma spatial nonuniformity (see, for instance, [8–22]). It has been shown that the establishment of a field-modified EDF, like that obtained in [6], is responsible for a series of important physical consequences of direct concern to plasma physics applications. In particular, it has been shown that the field modified EDFs yield, (1) reduction of the absorption coefficient [6, 17], (2) modification in the characteristics of electron transport [8–10, 17, 20], (3) reduction in the rates of collisional ionization and ion excitation [23–25], and (4) reduction in the rate of magnetic field generation [26–28]. That, as a result of inverse bremsstrahlung absorption of high-frequency radiation, a distribution function is in fact established, which exhibits slow electron depletion has been confirmed in [29, 30].

In the theory of distribution functions of plasma electrons interacting with laser radiation, a case of particular relevance is that when $v_E \geq v_T$ and the influence of the high-frequency radiation field cannot be accounted for by using a perturbation treatment. A mostly analytical method to deal with EDFs in strong field situations has been proposed in [31], where a number of interesting cases were examined as well. In particular, it has been shown that when the inequalities $Zv_T > v_E > v_T$ are fulfilled, an anisotropic EDF is formed, which is well approximated by a bi-Maxwellian. Another way to deal with the problem under examination is to solve numerically the appropriate kinetic equation, yielding a two-dimensional EDF [32–35].

The results of the two approaches, when the problem parameters allow comparison, are found to qualitatively agree. Further, numerical calculations have shown that the field-modified EDF has an anisotropic shape close to a bi-Maxwellian over a broad parameter range, and in particular also when $v_E \approx v_T$. In [34], it has also been found that, depending on the parameters, two kinds of two-temperature anisotropic EDFs are possible namely, one elongated parallel to the laser polarization direction and, for stronger fields, another elongated perpendicular to it. Besides, the second kind of EDF, in its evolution, transforms into an EDF of the first kind before relaxing towards a slow isotropization.

More recent and detailed investigations [36, 37], to be summarized below, show that while the two-temperature picture and the EDF shape reversal as well are confirmed, the directions along which the electron velocity components are in the average larger or smaller are an intricate issue and may not coincide with the “intuitive” ones (field polarization direction or direction perpendicular to the laser). The reported “angular” EDFs are a sensitive test to it.

The fact that anisotropic EDFs may form during the LPI has prompted the generalization of the theory of high-order harmonic generation in plasmas [38] to the case when anisotropic heating takes place [39–41] and of the inverse bremsstrahlung absorption [42]. The possibility of anisotropic two-temperature EDFs has prompted new investigations into the linear theory of Weibel instability, yielding the generation of strong quasistationary magnetic fields [43–46]. Plasmas with non-equilibrium anisotropic EDFs possess unusual optical properties, which were investigated in [47–51] and reviewed in [52]. As the anisotropic EDF significantly influences the polarization properties of the plasma X-ray radiation, it is hoped that the new EDF features, evidenced by theoretical analysis and calculations, might be demonstrated in experiments like those performed or discussed in [26, 53–55]. Below we discuss in more detail the most interesting new features of EDFs in a plasma interacting with a strong, high-frequency laser field.

10.2 Theoretical Framework

The physical phenomena occurring in a fully ionized plasma interacting with a laser field form a rather large subject. Of particular interest are the processes that take place in the presence of a high-frequency field of the form

$$\mathbf{E} \cos(\omega_0 t - \mathbf{k}_0 \mathbf{r}), \quad (10.1)$$

where \mathbf{E} is the electric field strength, \mathbf{k}_0 is the wavevector and ω_0 is the frequency of the wave. In the following, we consider the case when the radiation frequency ω_0 significantly exceeds the electron plasma frequency $\omega_L = (4\pi e^2 N/m)^{1/2}$, where e and m are, respectively, the electron charge and mass and N is the electron density. In this case, the relation between the radiation frequency ω_0 and the wavenumber \mathbf{k}_0 given by the dispersion law is similar to that valid in the vacuum $\omega_0 \approx k_0 c$, where c is the speed of light. We limit ourselves to plasmas with electron thermal velocity v_T much less than the speed of light. This corresponds to the following restriction on the electron temperature

$$T(eV) \ll mc^2 \sim 5 \times 10^5 eV. \quad (10.2)$$

We also assume that the amplitude of the quiver velocity in the high-frequency field $v_E = |eE/m\omega_0|$ is much smaller than c . The last condition corresponds to the following restriction on the radiation flux density

$$I = \frac{c}{8\pi} E^2 \ll 1.5 \times 10^{18} \left[\frac{\omega_0(s^{-1})}{2 \times 10^{15}} \right] \text{W cm}^{-2}. \quad (10.3)$$

Conditions (10.2) and (10.3) are widely employed in modern laboratory experiments. When such conditions are fulfilled, the average distance covered by a thermal electron during a period of high-frequency laser field $\approx \max(v_T, v_E)2\pi/\omega_0$ is much shorter than the radiation wavelength $\lambda_0 = 2\pi/k_0 \approx 2\pi c/\omega_0$. Then, in a large number of physical phenomena not connected with radiation momentum transfer to the plasma, the dipole approximation is valid. Using such an approximation, we neglect the coordinate dependence in (10.1).

Bearing in mind the above-mentioned conditions, for the EDF $f(v, t)$ in the presence of a high-frequency field, we write the kinetic equation

$$\frac{\partial}{\partial t} f + \frac{e}{m} \mathbf{E} \cos(\omega_0 t - \mathbf{k}_0 \mathbf{r}) \frac{\partial f}{\partial \mathbf{v}} = St(f) + St(f, f), \quad (10.4)$$

where $St(f)$ and $St(f, f)$ are, respectively, the electron-ion and the electron-electron collision integrals. On considering the influence of the electron-ion collisions on the EDF, it is natural to neglect the small corrections of the order of the ratio between the electron and the ion masses. With such an approximation for the electron-ion collision integral, one has the simple expression

$$St(f) = \frac{1}{2} v(v) \frac{\partial}{\partial v_i} (v^2 \delta_{ij} - v_i v_j) \frac{\partial f}{\partial v_j}, \quad (10.5)$$

where $\nu(v)$ is the electron–ion collision frequency

$$\nu(v) = \frac{4\pi Ze^4 N \Lambda}{m^2 v^3}. \quad (10.6)$$

Λ is the Coulomb logarithm. Strictly speaking, the explicit form of the Coulomb logarithm depends on the electron velocity. Nevertheless, below we do not consider such a dependence and we assume $\Lambda = \text{const} \gg 1$. This simple approximation permits to avoid the discussion of the weak variation of the Coulomb logarithm with the electron kinetic energy. If necessary, the dependence of Λ on the radiation and the plasma parameters can be taken into account in the final results. The expression for the electron–electron collision integral has the form:

$$St(f, f) = \frac{1}{2NZ} \frac{\partial}{\partial v_i} \int d\mathbf{v}' \nu(|\mathbf{v} - \mathbf{v}'|) \left[(|\mathbf{v} - \mathbf{v}'|)^2 \delta_{ij} - (v_i - v'_i)(v_j - v'_j) \right] \cdot \left(\frac{\partial}{\partial v_j} - \frac{\partial}{\partial v'_j} \right) f(\mathbf{v}, t) f(\mathbf{v}', t). \quad (10.7)$$

Using (10.6) in (7), the additional assumption of neglecting the difference between the electron and the ion Coulomb logarithms is made.

With the expressions for the collision integrals (10.5) and (10.7), (10.4) is a non-linear integro-differential equation for the EDF in the presence of a laser field. A huge number of papers (see, for instance, [6, 7, 9–22, 31–37, 56]) have been devoted to the solution of this equation. Nevertheless, a general solution to this equation has still not been found. At the same time, in order to describe numerous physical phenomena occurring in the presence of high-frequency radiation interacting with a plasma, it is necessary to have an EDF evolving according to (10.4). For this reason, it is worthwhile briefly to summarize the established results for the EDF available at this moment.

10.3 Distribution Function in a Weak Field

In this section, we discuss the results for the EDF obtained in the limit of a weak high-frequency field. A field is considered weak if the amplitude of the electron oscillatory velocity in the high-frequency field is smaller than the electron thermal velocity

$$v_E \leq v_T. \quad (10.8)$$

Such an inequality corresponds to a limitation on the radiation flux given by

$$I < 3 \times 10^{15} T(\text{eV}) \left[\frac{\omega_0(\text{s}^{-1})}{2 \times 10^{15}} \right] \text{Wcm}^{-2}. \quad (10.9)$$

The condition (10.8) means that for the thermal and suprathermal electrons, the field may be assumed weak. In this case, the action of the field may be considered as a perturbation. For slow electrons with a velocity smaller than v_E , on the other hand, the field is strong, and its action on the electrons must be described exactly. Below we discuss the kinetics of the fast electrons with $v > v_E$. For these electrons, a solution of (10.4) is looked in the form

$$f = f_0(\mathbf{v}, t) + \text{Re} \{ f_1(\mathbf{v}, t) \exp(-i\omega_0 t) \} + \dots \quad (10.10)$$

where $f_0(\mathbf{v}, t)$ and $f_1(\mathbf{v}, t)$ are slowly varying during the high-frequency period $2\pi/\omega_0$. The small value of the ratio v_E/v permits to neglect the higher harmonics of the distribution functions $f_l(\mathbf{v}, t) \exp(-il\omega_0 t)$ with $l \geq 2$. It is also assumed that the field frequency ω_0 is much higher than the electron collision frequency (6)

$$\omega_0 \gg \nu(v). \quad (10.11)$$

Moreover, as $\omega_0 \gg \omega_L \gg v = v(v_T)$ in an ideal plasma, the inequality (10.11) is automatically fulfilled for the thermal electrons with $v \approx v_T$ and indicates, for slow electrons, the limiting value of v that can be considered in our analysis $v \gg v_T(\nu/\omega_0)^{1/3}$. Taking into account (10.11) from (10.4), one gets

$$f_1 = -\frac{e\mathbf{E}}{m\omega_0} \frac{\partial f_0}{\partial v} + \frac{e}{m\omega_0^2} St \left(\mathbf{E} \frac{\partial f_0}{\partial v} \right). \quad (10.12)$$

In (10.12), the correction due to the electron–electron collision integral is omitted. This approximation is valid for $Z > 1$. Using expression (10.12), averaging (10.4) over the field period $2\pi/\omega_0$, for the distribution function in the linear approximation for small values of the ratio v_E^2/v^2 , the equation is obtained as

$$\frac{\partial}{\partial t} f_0 + \frac{e^2}{4m^2\omega_0^2} (E_i E_j^* + E_j E_i^*) \frac{\partial}{\partial v_i} St \left(\frac{\partial f_0}{\partial v_j} \right) = St(f_0) + St(f_0, f_0). \quad (10.13)$$

In (10.13), the term containing the electric field is small compared to the electron–electron collision integral. This means that in the region of velocities under consideration, the function f_0 is close to the isotropic function

$$F(v, t) = \int \frac{d\Omega}{4\pi} f_0(\mathbf{v}, t) \quad (10.14)$$

where $d\Omega$ is the solid angle of the velocity vector \mathbf{v} . The difference between f_0 and F is given by the small anisotropy part $\delta F = f_0 - F$, $|\delta F| \ll F$. Averaging (10.13) over the velocity angles and neglecting the small correction given by the function δF , for the function F , the equation is obtained as

$$\begin{aligned}
\frac{\partial F(v, t)}{\partial t} = & \frac{v_E^2}{6v^2} \frac{\partial}{\partial v} \left[v^2 v(v) \frac{\partial F(v, t)}{\partial v} \right] + \frac{4\pi}{3NZ} v v(v) \frac{\partial}{\partial v} \\
& \times \left\{ \left[v^2 \int_v^\infty dv' v' F(v', t) + \frac{1}{v} \int_0^v dv' v'^4 F(v', t) \right] \right. \\
& \left. \times \frac{\partial F(v, t)}{\partial v} + 3F(v, t) \int_0^v dv' v'^2 F(v', t) \right\}. \quad (10.15)
\end{aligned}$$

Subtracting (10.15) from (10.13) and omitting the terms proportional to the second power of δF , a linear equation for the function δF is obtained as

$$\begin{aligned}
\frac{\partial}{\partial t} \delta F - St(\delta F) - St(\delta F, F) - St(F, \delta F) = & \frac{e^2}{2m^2 \omega_0^2} E_i E_j^* \left(v_i v_j - \frac{1}{3} v^2 \delta_{ij} \right) \\
& \frac{1}{v} \frac{\partial}{\partial v} \left[\frac{v(v)}{v} \frac{\partial F}{\partial v} \right]. \quad (10.16)
\end{aligned}$$

Assuming that at $t = 0$ the EDF is isotropic, for $Z > 1$, the approximate solution of (10.16) is obtained as

$$\begin{aligned}
\delta F(\mathbf{v}, t) = & \frac{e^2}{2m^2 \omega_0^2} \left(v_i v_j - \frac{1}{3} v^2 \delta_{ij} \right) \int_0^t dt' E_i E_j^* \times \exp[3v(v)(t' - t)] \frac{1}{v} \frac{\partial}{\partial v} \\
& \left[\frac{v(v)}{v} \frac{\partial F(v, t')}{\partial v} \right]. \quad (10.17)
\end{aligned}$$

The small correction given in (10.17) is useful for the study of physical problems where the anisotropic part of the distribution function plays an important role. In particular, (10.17) gives the basis of the Weibel instability analysis. The Weibel instability leads to the generation of a quasistationary magnetic field in a plasma heated via inverse bremsstrahlung absorption of a relatively weak electromagnetic radiation [26–28, 57]. A useful peculiarity of (10.17) is that it has been derived without specifying the form of the large isotropic part of the distribution function $F(v, t)$.

Let us consider the form of the function $F(v, t)$ for different situations of interest. To this end, it is appropriate to introduce the so-called Langdon parameter

$$\alpha = \frac{Z v_E^2}{v_T^2}. \quad (10.18)$$

This parameter is given by the ratio between the electron Maxwellization time Z/v , determined by the electron–electron collisions, and the electron heating time in the presence of the field due to the electron–ion collisions $v_T^2/\nu v_E^2$.

10.3.1 Case $\alpha \geq 1$

Let us now consider the condition

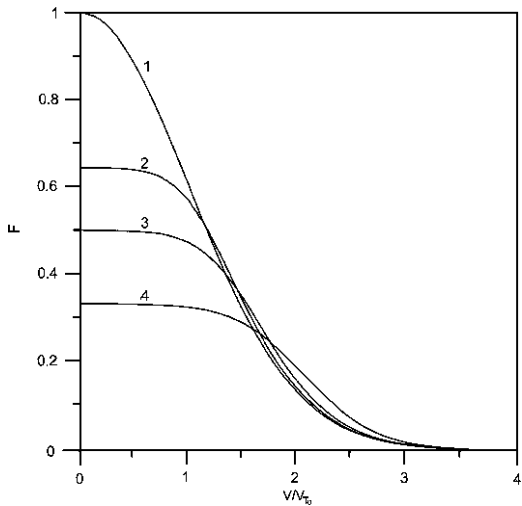
$$v_T > v_E > \frac{v_T}{\sqrt{Z}}, \quad (10.19)$$

which is realized in a plasma with multi-charged ions. Due to the right-hand side of inequality (10.19), the Langdon parameter is greater than unity, $\alpha > 1$. Then the electron–electron collisions in (10.15) can be treated as a small correction in considering the distribution function of the bulk electrons. The approximate equation describes the evolution of the initial EDF due to electron heating in the high-frequency field. Such an equation has been considered in [6] where the shape of the initial EDF has been assumed to be Maxwellian. It has been shown [6] that because of the electron heating due to the high-frequency field, the underthermal electrons move in the region of thermal velocity and the resulting EDF exhibits a significant slow electron depletion. The basic features of the EDF evolution in the velocity space are reported in Fig. 10.1. The different curves in Fig. 10.1 correspond to different time moments, which are small compared with the time for the doubling of the initial electron temperature $\sim 4.5v_T^2/\nu v_E^2$. For greater times, the EDFs assume the selfsimilar form [7]

$$F(v, t) = \frac{3N}{20\pi\sqrt{5}v_T^3(t)} \left[\Gamma\left(\frac{8}{5}\right) \right]^{-5/2} \exp \left\{ -\frac{v^5}{25\sqrt{5}v_T^5(t)} \left[\Gamma\left(\frac{8}{5}\right) \right]^{-5/2} \right\}, \quad (10.20)$$

where $\Gamma(x)$ is the gamma function. The effective thermal velocity increases with time according to the equation

Fig. 10.1 The electron distribution function (EDF) evolution due to inverse bremsstrahlung absorption in a weak field, according to Langdon [6]. Curves correspond to different time moments $\tau = (v_E^2 v_0 t) / (6v_T^2)$, $v_0 = v(v_{T0})$, v_{T0} the initial electron thermal velocity, v_E the electron quiver velocity. (1) $\tau = 0$, (2) $\tau = 0.1$, (3) $\tau = 0.3$, (4) $\tau = 1$. The EDF are normalized to $1/(2\pi)^{3/2}v_{T0}^3$



$$v_T^4(t) \frac{d}{dt} v_T(t) = \frac{1}{30\sqrt{5}} \left[\Gamma\left(\frac{8}{5}\right) \right]^{-5/2} v(v_E) v_E^5. \quad (10.21)$$

The self-similar EDF (10.20) is formed because of the very rapid inverse bremsstrahlung heating of the electrons. Figure 10.1 clearly shows that the energy is mainly absorbed by the slow electrons, and consequently, the EDF portion which suffers the most significant rearrangement is that related to the slow electrons.

With the aim of future comparisons, $F(v, t)$ (10.20) is rewritten as

$$F_L(v, t) = \Phi_L(t) \exp \left\{ -\frac{2}{5} B_0 e^{5/2} \right\}, \quad (10.22)$$

with

$$\Phi_L(t) = \frac{1}{20\pi\sqrt{5}v_T^3(t)} \left[\Gamma\left(\frac{8}{5}\right) \right]^{-5/2}, \quad (10.22a)$$

$$B_0 = \left(\frac{2}{5} \right)^{3/2} \left[\Gamma\left(\frac{8}{5}\right) \right]^{-5/2}, \quad (10.22b)$$

and

$$\varepsilon = \frac{mv^2}{2\kappa T} = \frac{1}{2} \frac{v^2}{v_T^2(t)} \quad (10.22c)$$

being κ the Boltzmann constant.

10.3.2 Case $\alpha \ll 1$

In this limit [56], the electron–electron collisions play a crucial role in determining the shape of the thermal electrons distribution, which is found to approach a Maxwellian. The conditions for the under-thermal electrons are different. To take into account the heating of the under-thermal electrons due to the absorption of the high-frequency field, in the region of small velocities,

$$v_E \ll v \ll v_T, \quad (10.23)$$

for the electron–electron collision integral $St(F, F)$, the approximate form is used

$$St(F, F) = \frac{\sqrt{2}v}{3\sqrt{\pi}Zv^2} \frac{\partial}{\partial v} \left[v^3 \left(\frac{v_T}{v} \frac{\partial}{\partial v} F(v, t) + F(v, t) \right) \right]. \quad (10.24)$$

With the help of formula (10.24), it is possible to obtain the quasistationary solution of (10.15). This solution is reached after a time interval of the order of $v_T/v(v_L)v_E^2 \sim Z/v$, and F has the form [56]

$$F(v, t) \cong \frac{1}{(2\pi)^{3/2} v_T^3} \exp \left[-\frac{1}{v_T^2} \int_0^v \frac{u^4}{u^3 + v_L^3} du \right] \quad (10.25)$$

with $v_L = v_T \left(\alpha \sqrt{\pi/8} \right)^{1/3} < v_T$. In the velocity regions where $v \sim v_T$ and when $v \gg v_T$, the distribution (10.25) becomes Maxwellian. The shape of the distribution (10.25) depends on time via the thermal velocity v_T , which increases with time because of the electron heating due to the absorption of the high-frequency field according to

$$\frac{d}{dt} v_T^2 = \frac{2}{9\sqrt{2}\pi} \nu v_E^2. \quad (10.26)$$

In the conditions under consideration, the distribution (10.25) is numerically close to a Maxwellian. Nevertheless, if the velocity v is small enough $v \leq v_L$, the derivative of function (10.25) is different as compared to that of a Maxwellian. This discrepancy is important for the theory of parametric instabilities. As shown in [56, 58], an adequate description of phenomena such as filamentation and stimulated Brillouin scattering is possible only taking into account the variation of the EDF due to inverse bremsstrahlung absorption.

10.3.3 Case of Arbitrary α

In this case [16], Z is arbitrary and e–e collisions are treated on the same footing as e–i collisions.

Following a procedure in which numerical calculations and asymptotic considerations are jointly exploited, the self-similar EDF is obtained in the form

$$F(v, t) = \Phi(t) \exp \left\{ -\frac{\varepsilon^{5/2} + 2/5 (\alpha B \varepsilon^4)}{(1 + \alpha) \varepsilon^{3/2} + 5/2 [(\alpha)/B(1 + \alpha)]} \right\}, \quad (10.27)$$

where ε is defined by (10.22c), $\Phi(t)$ is the EDF normalization depending on time through $v_T(t)$

$$B = B_0 + \left(\frac{0.016}{\alpha + 0.06} \right)^{4/5} \quad (10.27a)$$

α is the Langdon parameter (10.18) and B_0 is given by (10.22b).

In the limit $\alpha \ll 1$ (very small fields, high electron velocities and not very large Z), (10.27) goes over, as it must, to a Maxwellian:

$$F(v, t) \rightarrow F_M(v, t) = \frac{1}{(2\pi)^{3/2} v_T^3} \exp\{-\varepsilon\}, \quad (10.28)$$

In the opposite limit $\alpha \gg 1$ (high Z), the Langdon EDF (10.22) is recovered.

Concerning the results reported in this Section, a couple of comments are necessary. The self-similar EDF (10.22) predicts tail truncation, namely, a significant rearrangement of the EDF also in the high-velocity region. However, this second feature is physically ungrounded, especially in the absence of electron–electron collisions, as the energy exchanged by fast electrons and the laser field is very small, and the EDF of fast electrons remains close to the initial Maxwellian for long periods. Thus, caution must be exercised in using the EDF (10.22) in applications where fast electrons play a significant role.

The self-similar EDF (10.25) for velocities $v \ll v_L$ predicts a slow electron depletion like the Langdon EDF. Such a behaviour too is ungrounded as the physical parameters under which it has been obtained imply that the EDF must remain essentially close to a Maxwellian.

The self-similar EDF (10.27) exhibits, in general, a behaviour vs v intermediate between F_L (10.22) and F_M (10.28), with the same temperature as shown by Fig. 10.2.

Remarkable is the behaviour of the EDF (10.27) at very low and very high velocities. Further investigations on the plasma EDFs in weak fields have been reported in [19, 21, 22]. The results of [19] largely support the findings of [16], while those of [21, 22] address the issue of the EDF anisotropy and of e–e collisions role in the weak field domain. The formation of self-similar distributions leads to significant changes in the values of plasma parameters such as the absorption coefficient [6, 17], the electron transport coefficients [8–10, 17, 20], the rate of radiation recombination processes [23–25] and the growth rate of many instabilities [26–28, 56, 57].

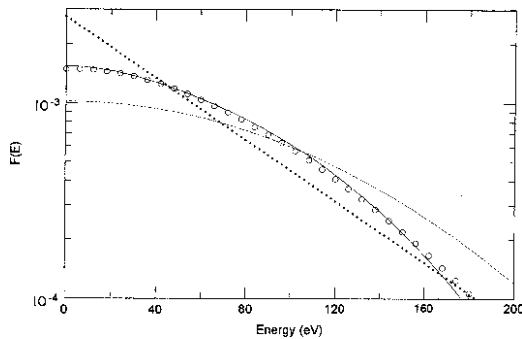


Fig. 10.2 Comparison of the EDF (10.27) of the main text (*solid line*), with the exact numerical solution of the kinetic equation (10.4) (*circles*). $A = 0.4$, $Z = 10$, $E = 1.5 \times 10^9 \text{ V/cm}$, $t = 10^{-9} \text{ s}$, $T_e = 55.2 \text{ eV}$ initial electron temperature, $B = 0.406$. For completeness, also plotted are the Langdon (10.22) (*dashed line*), and the Maxwellian (10.28) EDFs (*dots*). (After [16])

10.4 Distribution Function in a Strong Field

In this section, we consider the electron kinetics in a strong laser field, when the condition

$$v_E > v_T \quad (10.29)$$

is fulfilled. In this case, it is useful to remove the rapid oscillations from (10.4) by transformation to the new velocity variable

$$\mathbf{u} = \mathbf{v} - \mathbf{v}_E \sin \omega_0 t \quad (10.30)$$

Then, in a cylindrical coordinate system with the anisotropy axis directed along the direction of polarization of the high-frequency field, for the distribution function in the oscillating system

$$F_{\text{os}}(\mathbf{u}, t) = f(\mathbf{u} + \mathbf{v}_E \sin \omega_0 t, t), \quad (10.31)$$

the equation is obtained [31] as

$$\begin{aligned} \frac{\partial}{\partial t} F_{\text{os}} = & \frac{1}{u_{\perp}} \frac{\partial}{\partial u_{\perp}} \left[u_{\perp} D_{\perp\perp} \frac{\partial}{\partial u_{\perp}} F_{\text{os}} + u_{\perp} D_{\perp z} \frac{\partial}{\partial u_z} F_{\text{os}} \right] \\ & + \frac{\partial}{\partial u_z} \left[D_{\perp z} \frac{\partial}{\partial u_{\perp}} F_{\text{os}} + D_{zz} \frac{\partial}{\partial u_{\perp}} F_{\text{os}} \right] + St(F_{\text{os}}, F_{\text{os}}). \end{aligned} \quad (10.32)$$

The (10.32) has been obtained taking into account the axial symmetry of the electron distribution. In (10.32), the diffusion tensor in the velocity space oscillates with time as

$$\begin{pmatrix} D_{\perp\perp} \\ D_{\perp z} \\ D_{zz} \end{pmatrix} = \frac{v_E^3 \nu(v_E)}{2 |\mathbf{u} + \mathbf{v}_E \sin \omega_0 t|^3} \begin{pmatrix} (v_z + v_E \sin \omega_0 t)^2 \\ -u_{\perp} (v_z + v_E \sin \omega_0 t) \\ u_{\perp}^2 \end{pmatrix}. \quad (10.33)$$

In the oscillating coordinate system, the electron–ion collision integral takes a different form, while the electron–electron collision integral is always given by (10.7) with f replaced by F_{os} . The field has no effect on the electron–electron collisions due to the dipole approximation.

10.4.1 Analytical Investigations

In a very strong field, when the condition

$$v_E > Z v_T \quad (10.34)$$

is fulfilled, the electron–electron collisions dominate in the EDF evolution, while the decrease in importance of the electron–ion collisions implies a concomitant LPI decoupling with the ensuing reduction of the laser energy deposition in the plasma. In such conditions, the establishment in the oscillating coordinate system of the Maxwellian EDF

$$F_{\text{os}} = \frac{1}{(2\pi)^{3/2} v_T^3} \exp \left[-\frac{1}{2v_T^2} (\mathbf{v} - \mathbf{v}_E \sin \omega_0 t)^2 \right] \equiv F_M(u) \quad (10.35)$$

takes place, and the residual electron heating, with logarithmic accuracy, is described by the equation

$$\frac{d}{dt} v_T^2 = \frac{4}{3\pi} \nu(v_E) v_E^2 \ln \left(\frac{v_E}{v_T} \right). \quad (10.36)$$

Equation (10.36) is obtained by integrating (10.32) over the velocities with the weight $m u^2/2$ and averaging it over the high-frequency field period.

Of particular importance and relevance to present-day laboratory conditions is the case when

$$Z v_T > v_E > v_T, \quad (10.37)$$

which implies moderately strong fields and covers a physical situation opposite, to some extent, to that of (10.34). In fact, if conditions (10.37) are satisfied, one can omit the electron–electron collision term in (10.32). For time intervals greater than the high-frequency field period $t \gg 2\pi/\omega_0$, taking into account that $u < v_E$, one can replace in (10.32) the diffusion tensor (10.33) by its average value over the high-frequency field period

$$\begin{pmatrix} D_{\perp\perp} \\ D_{\perp z} \\ D_{zz} \end{pmatrix} = \frac{1}{\pi} v_E^3 \nu(v_E) \begin{pmatrix} \ln \left(\frac{4v_E}{v_{\perp}} \right) - 1 \\ 0 \\ 1 \end{pmatrix} \quad (10.38)$$

Equation (10.32) with the coefficients (10.38) and without the electron–electron collisional integral can be solved approximating $\ln(v_E/u_{\perp})$ by $\ln(v_E \sqrt{2\kappa T_{\perp}/m})$, where T_{\perp} is the effective electron transverse temperature. The solution of (10.32) and (10.38) with the initial condition that at $t = 0$ the distribution is an oscillating Maxwellian $F_{\text{os}}(\mathbf{u}, t = 0) = F_M(u)$ and the boundary condition $F_{\text{os}}(u \rightarrow \infty, t) = 0$ has the form [31]

$$F_{\text{os}}(\mathbf{u}, t) = \frac{m^{3/2}}{(2\pi\kappa)^{3/2} T_{\perp} \sqrt{T_z}} \exp \left[-\frac{m v_{\perp}^2}{2\kappa T_{\perp}} - \frac{m (v_z - v_E \sin \omega_0 t)^2}{2\kappa T_z} \right]. \quad (10.39)$$

(10.39) is a two-temperature anisotropic EDF, oscillating along the field direction, having the analytical form of a bi-Maxwellian.

The early evolution of the transverse and longitudinal effective temperatures T_{\perp} and T_z is described by the heating equations

$$\kappa \frac{d}{dt} T_{\perp} = \frac{1}{\pi} m v(v_E) v_E^2 \left[\ln \left(\frac{8 m v_E^2}{\kappa T_{\perp}} \right) - 3 + C \right], \quad (10.40)$$

$$\kappa \frac{d}{dt} T_z = \frac{2}{\pi} m v(v_E) v_E^2, \quad (10.41)$$

where $C \cong 0.577$ is Euler's constant. A comment on the validity of heating equations (10.40) and (10.41) is given in the following sub-section.

10.4.2 Numerical Investigations

The important, intermediate region when the external field is strong and both electron-ion and electron-electron collisions need to be taken into account in the same footing cannot be dealt with analytically, and direct numerical solution of the kinetic equation is required.

This task has been dealt with in a series of publications [32–37], and the main results of numerical calculations are summarized and discussed in the next Section. Here we anticipate with the help of Fig. 10.3 some general features concerning the EDF shape and its evolution in the space of electron velocities for *sufficiently strong* fields. Figure 10.3 shows qualitatively the evolution of the anisotropy parameter

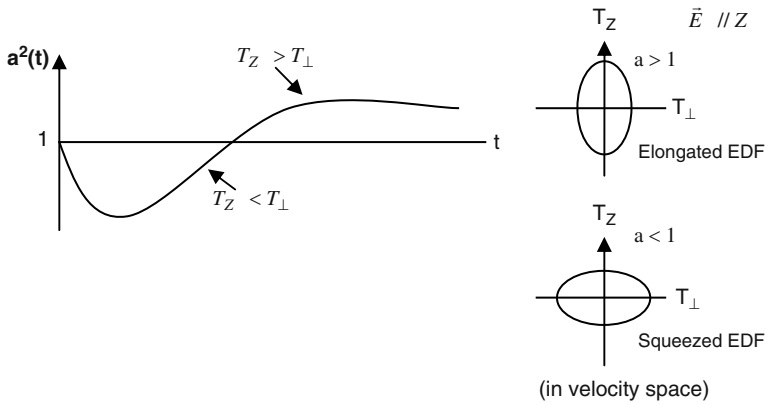


Fig. 10.3 Characteristic time-evolution of the anisotropy parameter $a(t) = \sqrt{(T_z)/(T_{\perp})}$ in strong fields, providing information on the EDF shape and its evolution. $a(0) = a_0 = 1$ – initially isotropic EDF. When $a > 1$, in the velocity space the EDF has roughly the shape of an ellipsoid obtained by rotating around the larger axis an ellipse having the two temperatures T_z and T_{\perp} along its axes, with the larger one along the field. When $a < 1$, the ellipse to be rotated has the larger axis (T_{\perp}) perpendicular to the field. For the two cases $a > 1$ and $a < 1$, sometimes, the related EDF shapes are called respectively “sigar-like” and “pancake-like”. $a = 1$ corresponds to a spherical EDF

$$a(t) = \sqrt{\frac{2\bar{u}_Z^2(t)}{\bar{u}_\perp^2(t)}} = \sqrt{\frac{T_z}{T_\perp}} \quad (10.42)$$

obtained calculating

$$\bar{u}_\alpha^2(t) = \frac{\int u_\alpha^2(t) f_C(\mathbf{u}) d^3u}{\int f_C(\mathbf{u}) d^3u}, \alpha = Z, \perp \quad (10.43)$$

with

$$T_Z = \frac{m}{k} \bar{u}_Z^2, \quad (10.44)$$

$$T_\perp = \frac{m}{k} (\bar{u}_x^2 + \bar{u}_y^2) = \frac{m}{k} \bar{u}_\perp^2, \quad (10.45)$$

and $f_C(\mathbf{u})$ the numerical EDF solution of the kinetic equation. The plasma electrons overall temperature is $T = (2T_\perp + T_Z)/3$, and when the EDF is isotropic $a = 1$ and $T_\perp = T_Z$. In Figs. 10.3–10.6, $a^2(t)$ is plotted instead of $a(t)$.

Figure 10.3 shows that for sufficiently strong fields (to be specified below), an initially isotropic EDF, $a(0) = 1$, becomes squeezed ($a < 1$) in the field polarization direction (z direction). In other words, the electron velocity components along z are on the average smaller than those perpendicular to z , $T_Z < T_\perp$. Figure 10.3 shows also that $a(t)$ in its evolution becomes greater than 1, $T_Z > T_\perp$, meaning that now the EDF is elongated along z , with a reversal of its shape. Further, the EDF appears to evolve slowly towards isotropization from the elongated form. We note that the heating equations (10.40), (10.41) give only the early evolution of $a(t)$ when it starts to become smaller than one; all the remaining evolution as schematically shown by Fig. 10.3 is not accounted for. For fields not particularly strong, $a(t)$ never becomes smaller than one taking from $t = 0$ values slightly greater than 1.

For initial values of a different from 1 (initial anisotropic EDFs, $a(0) > 1$ or $a(0) < 1$), the $a(t)$ curves differ from that of Fig. 10.3 essentially in the first, early time part, when $a(t)$ keeps still memory of the initial conditions.

10.5 Main Results of Numerical Investigations

10.5.1 Characteristic Parameters and Their Behaviour in the Course of Laser–Plasma Interaction

As repeatedly seen above, the investigations concerned with EDF shape and its evolution are based on the kinetic equation (10.4) in which plasma electrons are assumed to interact with the external field, the plasma ions and with themselves. Within such a physical framework, a key role is played by the behaviour of few

characteristic parameters. Most of the reported results are easily understood on the basis of such parameters.

a) The most important is the ratio

$$R(t) = v_E/v_T(t), \quad (10.46)$$

which during the LPI monotonically decreases, due to the electron heating and the increase of the thermal velocity $v_T(t)$. As seen above, $R < 1$ identifies a physical situation where the plasma electrons experience the external field as weak. $R \geq 1$ and $R \gg 1$ identify, respectively, moderately strong and very strong field situations. As $R(t)$ decreases with time, an intense field with initially $R(0) \gg 1$, in the course of electron heating is gradually experienced by electrons only as a moderately intense (with $R \geq 1$), and ultimately as weak ($R < 1$).

- b) *The ion charge Z .* High values of Z usually allow to neglect e–e collisions. In strong fields, $Z \gg 1$ is not sufficient to do so. It must be supplemented by the requirement $Z > R(t)$. The reason is that very strong fields ($R \gg 1$), forcing the electrons to oscillate very fastly, with $v_E \gg v_T(t)$, reduce the e–i collision cross sections and thus electron heating but leave unaffected e–e collisions (in dipole approximation), which may become dominating or not negligible even when Z is high. As $R(t)$ decreases with time, an interaction started in a physical situation when $Z < R$, with time enters into a stage in which the reverse becomes true $Z > R$ and the e–e collisions loose part of their relevance.
- c) Effective collision frequencies v_{ei} and v_{ee} .

The different behaviour of v_{ei} and v_{ee} in different physical stages is ultimately responsible for the anisotropy in EDF shape and in electron heating.

Let us briefly discuss how $R(t)$ and the other parameters influence the processes under consideration. Plasma heating is proportional to the effective e–i collision frequency v_{ei} , which depends on the electron velocity as u^{-3} (see (10.6) and (10.30)). $u_Z = v_Z - v_E \cos \omega t$, $u_{\perp} = v_{\perp}$. In the following the initially EDF is assumed isotropic.

1. When $R < 1$, the velocities of the plasma electron bulk in the different directions are on the average greater than v_E . v_{ei} is only weakly affected by the laser field \mathbf{E} and remains practically isotropic, and so do the heating and the EDF shape.
2. When $R \geq 1$, v_Z and v_{\perp} are *on the average* comparable with v_E , and the component u_Z may become very small for significant fractions of the field period. As a result, the collision frequency of electrons flying mostly along the field (let it be $v_{ei}^{//}$) is larger than that of electrons flying mostly perpendicularly to it (v_{ei}^{\perp}). As a consequence, electron heating is more effective along the field. Thus, in the regime $R \geq 1$, one has $v_{ei}^{//} > v_{ei}^{\perp}$, $T_Z > T_{\perp}$ and the EDF takes a shape elongated in the field direction.
3. When $R \gg 1$, v_E is on the average much greater than all the plasma electron velocities of interest for the process under consideration. For this regime,

$v_{ei}^{//} \sim v_E^{-3}$, while the characteristic velocities of v_{ei}^\perp are much smaller than v_E . Thus, $v_{ei}^\perp > v_{ei}^{//}$, and heating is more effective perpendicularly to the field ($T_\perp > T_Z$), and the EDF takes a shape squeezed along the field direction. An initially isotropic EDF starts to evolve towards a squeezed shape when $R(t = 0)$ values, under broad conditions, are equal or larger than $4 \div 5$. However, with time, an initially large $R(t)$, thanks to the $v_T(t)$ increase, diminishes to values only slightly larger than one ($R \geq 1$). The physical situation of the previous point 2) is thus restored: again $T_Z > T_\perp$. The result is the reversal of the EDF shape from squeezed to elongated (with respect to the field direction). We note that the EDF shape reversal implies the interesting facts that isotropization is still to come and that, eventually, it will be approached always from an elongated shape.

From the above discussion [especially points (a) and 1–3], it implicitly follows that the small anisotropy and heating taking place when $R < 1$ will be of the elongated type with $T_Z > T_\perp$, [21].

4. The considerations of the previous points 1–3 apply also to the interplay between v_{ei} (more precisely $v_{ei}^{//}$ and v_{ei}^\perp) and v_{ee} . Here the only new consideration to keep in mind is that v_{ee} is not affected by the field \mathbf{E} , as v_{ee} does not contain v_E due to the dipole approximation, and accordingly does not suffer the modifications, due to the field strength, undergone by v_{ei} .

As a final comment, it must be observed that R is a very predictive parameter insofar as the laser field has a constant amplitude. For short-pulsed fields [59] or for cases when more than one field act simultaneously [60], as v_E too changes with time, the R values require, as a rule, a more detailed physical interpretation.

In conclusion, in strong laser fields, the electron kinetics, the EDF shape and the heating characteristics are controlled by a dynamic interplay between the changing roles of e–i and e–e collisions in different moments of LPI, with the laser field depositing energy in the plasma through e–i collisions.

10.5.2 Results of Selected Calculations. EDF Shape Evolution and Role of e–e Collisions

Figures 10.4–10.7 report on calculations concerning the EDF shape evolution for the cases when the initial EDF is an isotropic Maxwellian (Fig. 10.4) and when instead is a bi-Maxwellian with both a > 1 and a < 1 (Fig. 10.5).

The results reported in Fig. 10.6 are concerned with the EDF shape evolution, comparing the two cases when the e–e collisions in the solution of the kinetic equation are included and when not. A similar comparison is carried out in Fig. 10.7 where results on electron heating are reported. Most of the reported results are easily understood on the basis of the considerations given in the previous subsection, so that we may confine to few specific remarks. Among the aims of the reported calculations, there is the wish to disentangle the contribution due to e–e collisions, in both the cases when they are expected to be important and when not. To the best

Fig. 10.4 Evolution of $a^2(t) = T_Z/T_\perp$, with T_Z and T_\perp the effective electron temperatures parallel and perpendicular to the laser electric field; (1) $Z = 10$, $R_0 = 4.15$; (2) $Z = 10$, $R_0 = 8.89$; (3) $Z = 10$, $R_0 = 11.88$; (4) $Z = 20$, $R_0 = 11.88$. For all the curves $a_0 = 1$

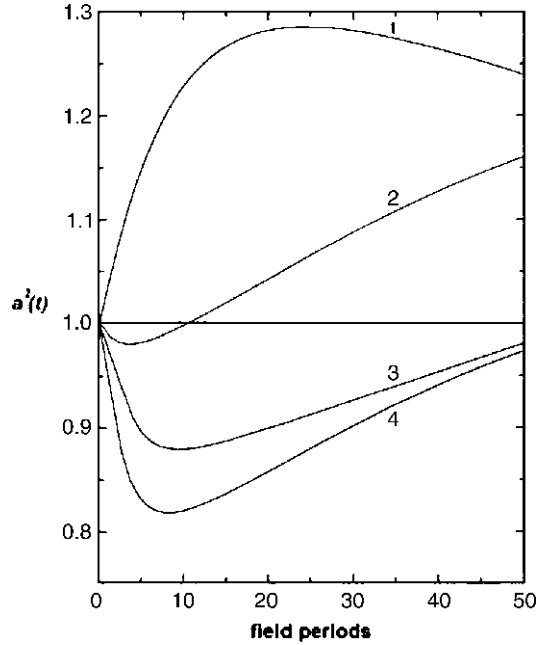
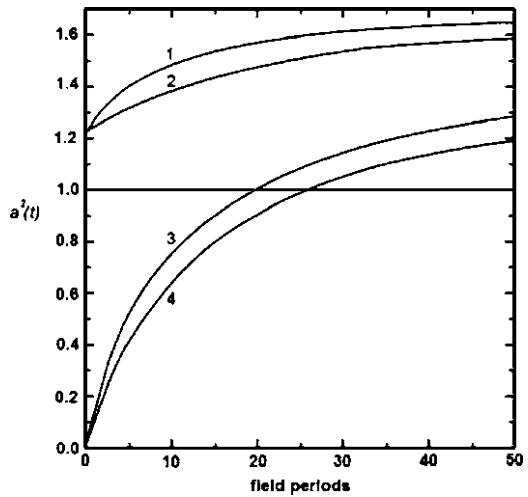


Fig. 10.5 Evolution of $a^2(t) = T_Z/T_\perp$, with T_Z and T_\perp the effective electron temperatures parallel and perpendicular to the laser electric field; (1) $a_0 = 1.1$, $R_0 = 11.88$; (2) $a_0 = 1.1$, $R_0 = 4.15$; (3) $a_0 = 0.1$, $R_0 = 11.88$; (4) $a_0 = 0.1$, $R_0 = 4.15$. For all the curves $Z = 1$



of our knowledge, the issue for strong fields until now has been not sufficiently addressed. Preliminary results are reported in [1, 36, 37, 59]; for the weak field case, see [16, 19, 21, 22, 61].

In absence of an external field able to deposit energy into the plasma, the role of e-e collisions is quite well understood. It consists in randomizing the electron velocities and in making the EDF isotropic and Maxwellian. Besides, insofar as the

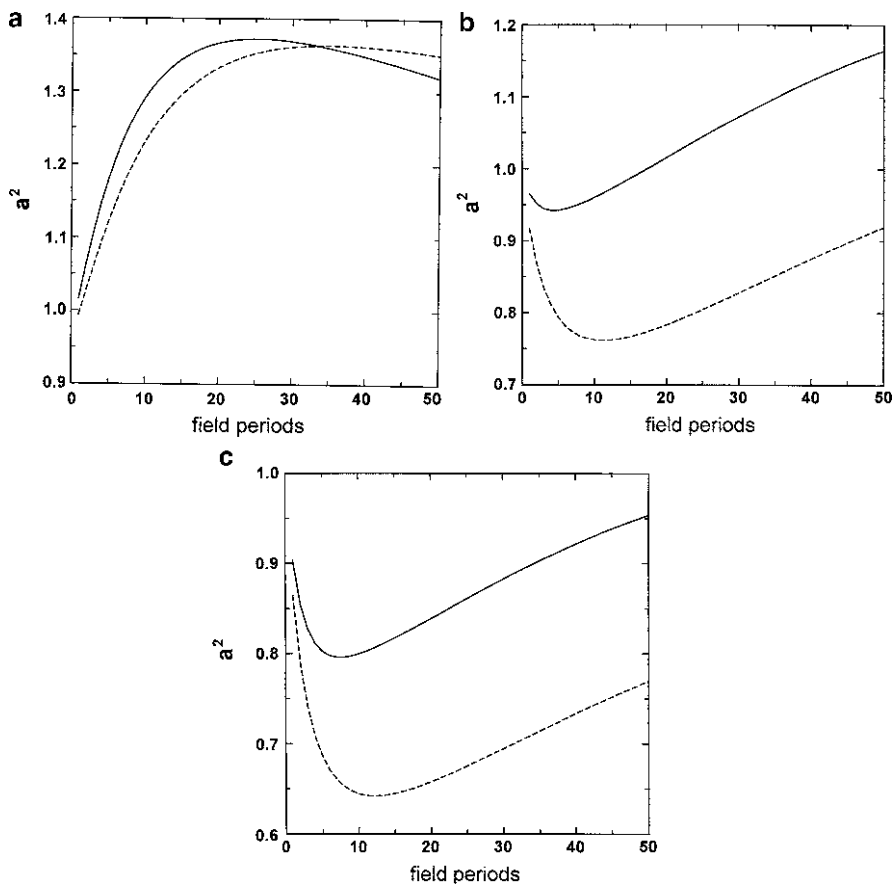


Fig. 10.6 Evolution of $a^2(t) = T_Z/T_\perp$; continuous line – both e–i and e–e collisions included when solving the kinetic equation; dashed line – e–e collisions omitted; (a) $R_0 = 4.15$, $Z = 10$; (b) $R_0 = 8.89$, $Z = 10$; (c) $R_0 = 11.88$, $Z = 20$; For all the cases $a_0 = 1$

dipole approximation is adopted, the term in the kinetic equation accounting for e–e collisions remains unchanged as compared with the field-free case.

The reported calculations, which are restricted generally to the first 50 field periods, show among other the following.

The EDF shape evolution, irrespective of the initial $a(t)$ value, takes place more rapidly, as compared with the case when e–e collisions are neglected, but there are only weak or no indications concerning randomization. Shape reversal is observed.

The initially elongated anisotropy is increased, the increase being larger for the stronger field despite the decreased role of e–i collisions. When the field is strong, even if $Z \gg 1$, e–e collisions are responsible of (1) a faster energy redistribution in favour of the electron degrees of freedom parallel to the field polarization direction and (2) a faster and larger heating (Fig. 10.7).

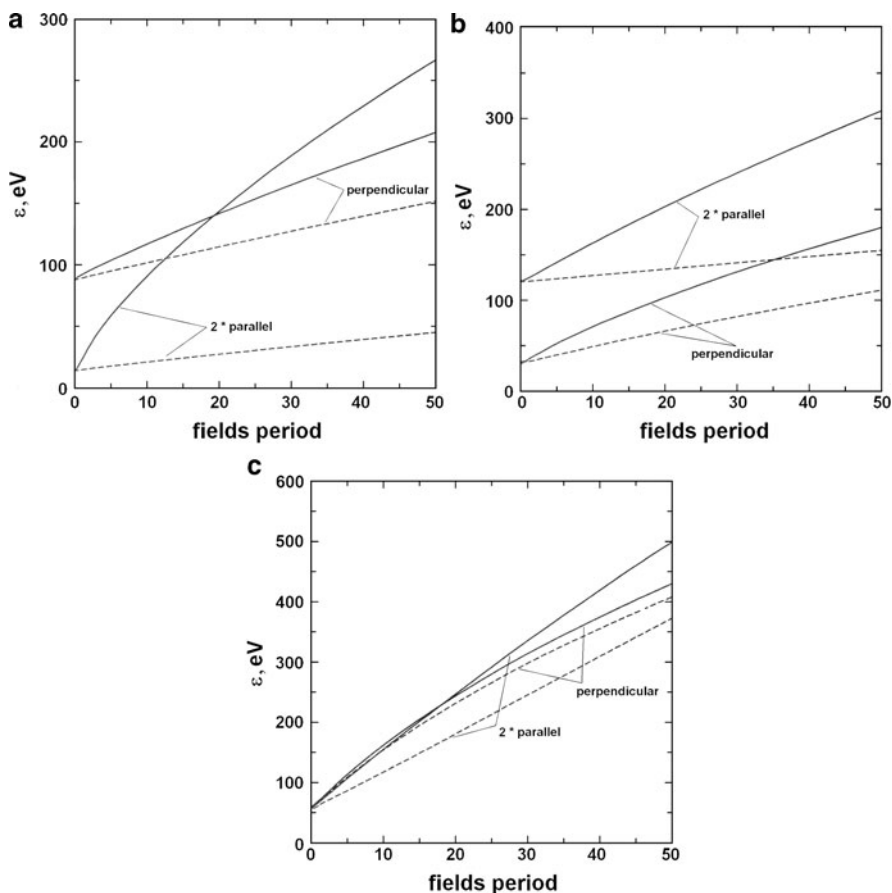


Fig. 10.7 Evolution of average kinetic energies (in eV) along and perpendicularly to the laser field direction, solving the kinetic equation with e-e collisions included (*continuous lines*) and neglected (*dashed lines*). (a) $R_0 = 11.88$, $a_0^2 = 0.05$, $Z = 1$; (b) $R_0 = 11.88$, $a_0^2 = 4$, $Z = 1$; (c) $R_0 = 8.89$, $a_0^2 = 1$, $Z = 10$; For the sake of comparison, the parallel energy is multiplied by 2 as the perpendicular energy is formed by 2 equivalent degrees of freedom

We conclude the comments on the observed role of e-e collisions in the intermediate stages of LPI reminding basic facts helping to appreciate the novelty of the reported data: (1) energy deposition in the plasma is made possible only through electron-ion collisions, (2) absorption is more effective for slow plasma electrons and (3) heating of slow electrons yields a decrease of e-i collisions role and a saturation in absorption (a sort of bottleneck in heating process). Evidently, in the evolving LPI, the e-e collisions not only redistribute the energy among the degrees of freedom but at the same time also remove the bottleneck transferring part of electrons to still higher energies, making possible the inverse bremsstrahlung absorption to keep

going. Moreover, $R(t)$ drops to values only slightly larger than unity ($R(t) \leq 4$), and heating along the field becomes more effective. It, when appropriate, yields the shape reversal with the ensuing delay of randomization to larger times. It is worth to be noted that some of the observed features are found also in the weak field case [16, 19, 21, 22, 61]

10.5.3 “Angular” Electron Distribution Function

As seen above, calculations frequently show that the EDF is anisotropic with two temperatures in the velocity space. As a rule, the observations are based on the evaluation of the electron average kinetic energies (effective temperatures) along and perpendicularly to the field polarization direction. Thus, the informations on the EDF anisotropy are based in an essential way on the calculation of two integral quantities, T_Z and T_\perp . On the other hand, as mentioned above, both analytical and numerical investigations have shown that under rather broad conditions during LPI, the establishment of a bi-Maxwellian EDF (10.39) is possible.

Below we introduce the “angular” EDF, which is a more sensitive quantity as compared to EDF depending on the absolute values of velocity; more to the point, this new quantity is particularly suited when issues such as EDF anisotropy or anisotropic heating are of interest. For the aim of a comparison, two angular EDFs are now defined starting from the numerical solution of the kinetic equation f_C and from the analytical bi-Maxwellian EDF f_{BM} , both functions taken in spherical coordinates.

The normalized bi-Maxwellian EDF (10.39) in spherical coordinates looks like

$$\begin{aligned} f_{BM}(u, \vartheta, \phi, t) &= C_Z C_\perp \exp \left\{ -\frac{m}{2kT_Z} u^2 \cos^2 \vartheta - \frac{m}{2kT_\perp} u^2 \sin^2 \vartheta \right\} \\ &= C_Z C_\perp \exp \left\{ -\frac{m}{2kT_{\text{eff}}} u^2 \right\} \end{aligned} \quad (10.47)$$

with

$$T_{\text{eff}} = \frac{T_Z T_\perp}{T_\perp \cos^2 \vartheta + T_Z \sin^2 \vartheta} \quad (10.48)$$

$$C_Z = \left(\frac{m}{2\pi k T_Z} \right)^{1/2}, \quad C_\perp = \frac{m}{2\pi k T_\perp} \quad (10.48a)$$

Integrating (10.47) over all the absolute velocities and azimuthal angles, one finds

$$f_{\text{BM}}(\vartheta, t) = \frac{1}{2} \frac{T_{\perp}^{1/2} T_Z}{(T_{\perp} \cos^2 \vartheta + T_Z \sin^2 \vartheta)^{3/2}}, \quad (10.49)$$

the “angular” EDF corresponding to the bi-Maxwellian (10.49), a part of the time dependence through the temperature, is a 1D-EDF depending on the polar angle ϑ . $dN = N f_{\text{BM}}(\vartheta, t) d\vartheta$ is the number of electrons in a unit volume and at time t in the small polar angle interval $\vartheta, \vartheta + d\vartheta$ with all the possible absolute velocities and all the azimuthal angles. If $T_{\perp} = T_Z$ (isotropic EDF) (10.49) goes over to the result expected for a Maxwellian f_{M} with the temperature $T = (2T_{\perp} + T_Z)/3$:

$$f_{\text{BM}}(\vartheta, t) \rightarrow f_{\text{M}}(\vartheta, t) = \frac{1}{2}. \quad (10.50)$$

Proceeding similarly for the calculated 2D-EDF $f_{\text{C}}(u, \vartheta, \phi, t)$, the angular 1D-EDF is defined

$$f_{\text{C}}(\vartheta, t) = \int_0^{2\pi} d\phi \int_0^{\infty} u^2 du f_{\text{C}}(u, \vartheta, \phi, t). \quad (10.51)$$

Figures (10.8–10.10) show some calculations of $f_{\text{C}}(\vartheta, t)$ and $f_{\text{BM}}(\vartheta, t)$ vs the polar angle ϑ at different times, aimed in particular at getting a more accurate representation on how close a calculated two-temperature EDF is to a bi-Maxwellian. In fact, the angular EDF is a sensitive quantity giving on the EDF shape and evolution significant supplementary information with respect to two integral quantities such as the effective temperatures and their ratio $a(t)$ at different times. We note that interesting information may be obtained in other ways as well, working either in cylindrical coordinates or in spherical ones. Another possibility, for instance, is to compare the 1D-EDF $f_{\text{C}}(u, t)$ and $f_{\text{BM}}(u, t)$ vs the absolute values of the velocity u . The comparison vs ϑ is certainly more sensitive and in some cases spectacular.

The results reported in Figs. 10.8–10.10 follow from calculations based on the following procedure:

1. The 2D kinetic equation is solved propagating from $t = 0$ a Maxwellian f_{M} , $a(t = 0) = a_0 = 1$ or a bi-Maxwellian f_{BM} of elongated ($a_0 > 1$) or squeezed ($a_0 < 1$) form.
2. At some field periods the effective temperatures T_{\perp} and T_Z are calculated (using the calculated f_{C} at those moments).
3. T_{\perp} and T_Z are then inserted into the bi-Maxwellian. It amounts to assume that during the laser–plasma interaction, the initial EDF has taken or kept the exact shape of a bi-Maxwellian (oscillating reference frames are generally understood). For $t > 0$, the trial bi-Maxwellian de-facto is forcedly assumed to undergo self-similar evolution, but admitting shape reversal.
4. According to 1–3, at a given time moment, one has two anisotropic, two-temperature EDFs, the one calculated exactly f_{C} and the bi-Maxwellian f_{BM} . Both have the same total temperature T . From now on, the two EDFs may be compared vs time in several ways.

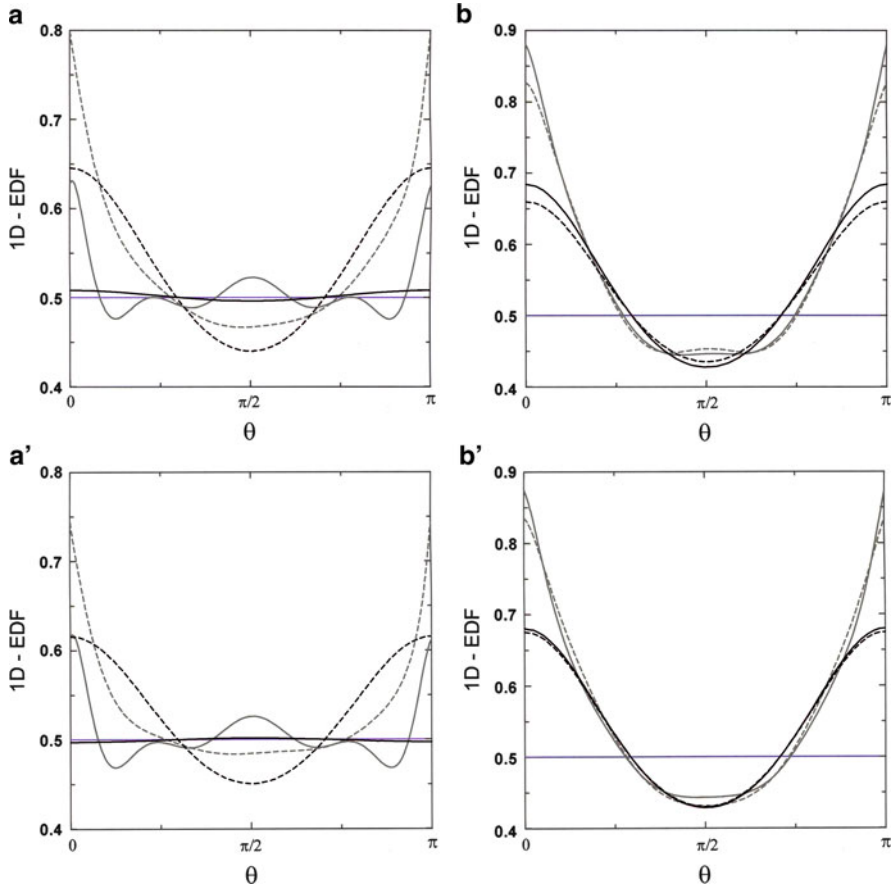


Fig. 10.8 The angular EDF $f_C(\vartheta, t)$, (10.51), and $f_{BM}(\vartheta, t)$, (10.49), vs the polar angle at different time moments of the laser–plasma interaction. Only the upper half of the polar plane is considered, the lower half being a repetition of the upper one. The curves (a') and (b') differ from (a) and (b) in that e–e collisions are neglected. In the curves (a) and (a'), Black curves – f_{BM} ; Gray curves – f_C ; Continuous curves at 1 periods; Dashed curves at 10. In the curves (b) and (b'), Black curves – f_{BM} ; Gray curves – f_C ; Continuous curves at 30 periods; Dashed curves at 50 periods; Constant line at 0.5 in the ordinate corresponds to the constant value of a Maxwellian, (10.50) of the main text. The laser field direction corresponds to $\theta = 0$ and π . For all calculations, $R_0 = 4.15$; $a_0 = 1$

The most important observation concerning the comparisons of $f_C(\vartheta, t)$ vs $f_{BM}(\vartheta, t)$ is that in the first stages of interaction (50 field periods) in several situations, due to the interplay of ν_{ei} and ν_{ee} , the calculated EDF is more structured than f_{BM} . It may acquire a four-lobe shape, rather symmetrically located in the polar plane (see Figs. 10.8 and 10.10). It is considered an indication that definitions of new effective temperatures, other than T_\perp and T_Z , could be required. As a rule, e–i collisions appear to favour the establishment of two-temperature anisotropic EDFs like a f_{BM} . As before, e–e collisions favour faster heating and energy redistribution among the

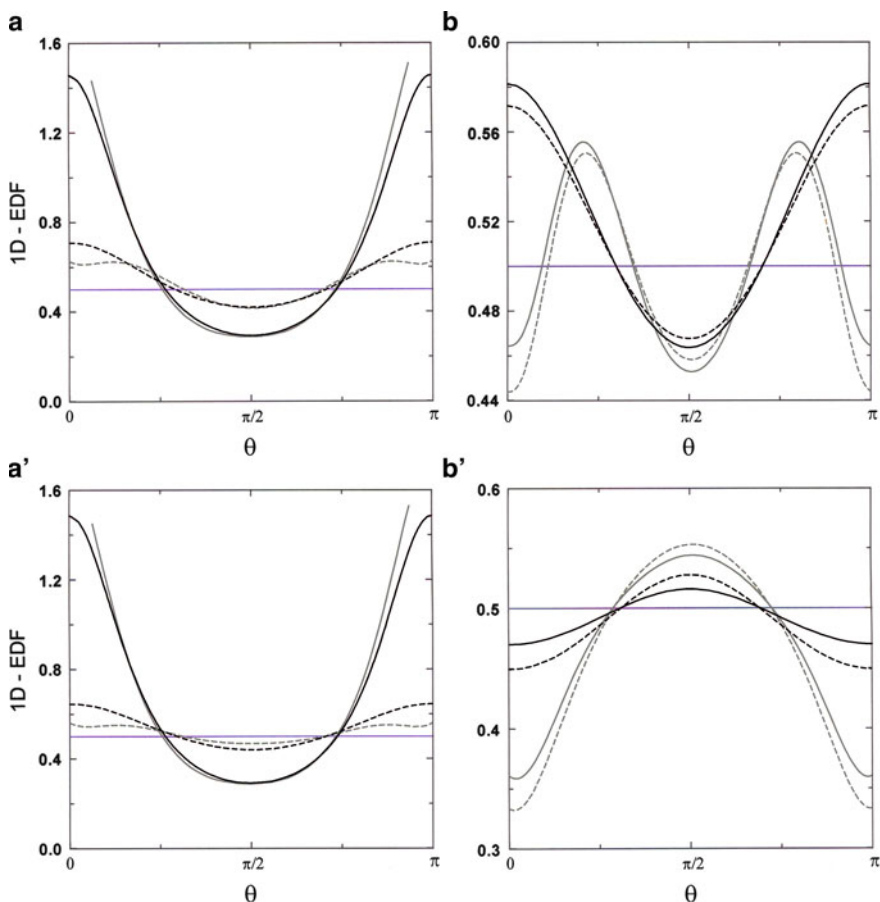


Fig. 10.9 As in Fig. 10.8 with $R_0 = 11.88$; $a_0 = 2$

degrees of freedom. The joint action of both e-i and e-e collisions yields a more structured EDF, with evolving shape and lobes.

10.6 Conclusions

In this chapter, we have reported on the most significant available information concerning the plasma electron kinetics, the distribution function and heating for several physical conditions of LPI. The considered plasma is homogeneous and non-relativistic the laser is single-mode. Appearance of anisotropy of varying form in different physical quantities (in the velocity and energy spaces) as a result of strong

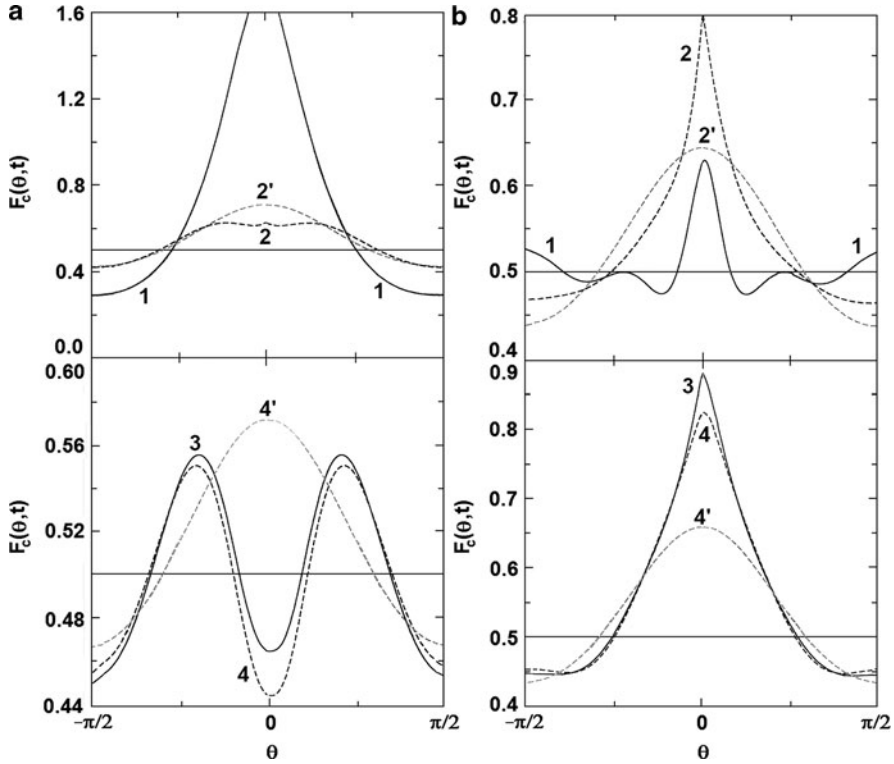


Fig. 10.10 Shape of angular EDF $F_C(\vartheta, t)$ vs θ at four different interaction times (in units of the field period, T) in the angular interval from $\theta = -\pi/2$ to $\theta = \pi/2$. 1– 1T; 2 – 10T; 3 – 30T; 4 – 50T; curves 2' and 4' – shapes of the angular bi-Maxwellian f_{BM} with the same temperatures of the calculated $F_C(\vartheta, t)$ at, respectively, $t = 10T$ and $50T$. (a) $Z = 10$, $R_0 = 11.88$, $a_0 = 2$; (b) $Z = 10$, $R_0 = 4.15$, $a_0 = 1$. The line at 0.5 in the ordinate corresponds to the constant value of a Maxwellian, (10.50) of the main text. The laser field direction corresponds to $\theta = 0$

LPI is, perhaps, the most significant feature brought about by a strong field, capable of far-reaching effects.

The theoretical investigations are based on a kinetic equation that accounts for the electron distribution function evolution on the basis of three kinds of electron interactions: (1) with the laser field, (2) with the plasma ions and (3) with themselves.

The known behaviour of the above interactions in different ranges of process parameters allows a clear understanding of the obtained results and gives a transparent physical picture of all the considered stages of LPI.

Of course, real plasmas and real laser systems may significantly depart from the “ideal” models chosen here which, by the way, are used in most of the investigations. In real physical conditions, some of the reported features may be more or less

altered. Existing experimental evidence, however, lend essential support to the basic results obtained in the important subject of EDFs in strong LPI.

Practically unanswered in this overview remains the question of the final EDF isotropization in a strong field, due to the limitations in our calculations concerning the LPI times (as a rule, 50 field periods). In any case, isotropization will be approached from an anisotropic, self-similar shape elongated in the laser field direction. The issue is complicated by the circumstance that at large LPI times, other interaction mechanisms enter into play, making the present theoretical framework inadequate. The onset of Weibel instability is the most significant among them.

In the first few periods of interaction, a strong rearrangement takes place in the EDF, mostly concerning slow electrons. e-i collisions alone are found to favour, with time, the establishment of two-temperature EDFs, which under broad conditions, may be approximated by an analytical bi-Maxwellian. e-e collisions are found to play an enhanced role in LPI. They accelerate considerably the heating process and make it more effective especially along the field, removing the bottleneck in the absorption observed when e-i collisions dominate. Consequently, they accelerate the EDF evolution without, however, suppressing the reversals of the EDF shape from elongated to squeezed and viceversa. A peculiar feature is that, with time, the heating weakens the e-e collisions role and restores the conditions $v_{ei}^{//} > v_{ei}^{\perp}$; as a result, EDF evolves towards randomization from the elongated shape. In the presence of e-e collisions, the angular EDF is more structured, exhibiting in some cases lobes symmetrically placed in the polar plane. It suggests that the usual definition of the temperatures T_Z and T_{\perp} may become inadequate.

Acknowledgements One of the authors (G.F.) wishes to acknowledge the fruitful collaborations and discussions with S.A. Uryupin (Lebedev Physical Institute, Moscow), M. Zarcone (Palermo University), P.I. Porshnev and O.V. Petrova (Minsk University). R.L.O. acknowledges the financial support by the Palermo University. This work is part of the research program of Italian-Russian Forum for Laser Physics and Technologies.

References

1. Ferrante G, Zarcone M and Uryupin S A (2001) *Plasma Sources Sci. Technol.* **10** 318
2. Kortshagen U (1995) *Plasma Sources Sci. Technol.* **4** 172
3. Batani D, Freeman R R and Baton S (2008) Chapter 13 in “*Progress in Ultrafast Laserscience III*”, Springer-Verlag, New York, p. 265
4. Lontano M and Passoni M (2007) Chapter 17 in “*Progress in Ultrafast Laserscience II*”, Springer-Verlag, New York, p.341
5. Pert G J (2001) *J. Phys. B At. Mol. Opt. Phys.* **34** 881
6. Langdon A B (1980) *Phys. Rev. Lett.* **44** 575
7. Balescu R (1982) *J. Plasma Phys.* **27** 553
8. Mora P and Yahi H (1982) *Phys. Rev. A* **26** 2259
9. Albritton J R (1983) *Phys. Rev. Lett.* **50** 2078
10. Albritton J R, Williams E A, Bernstein I B and Swartz K P (1986) *Phys. Rev. Lett.* **57** 1887
11. Deck D (1987) *Laser Part. Beams* **5** 49
12. Dyson A, Dangor A E, Dymoke-Bradshaw A K L and Evans R G (1988) *Plasma Phys. Controlled Fusion* **30** 1259

13. Matte J P, Lamoureux M, Moller C, Yin R Y, Delettrez J, Virmont J and Johnston T M (1988) *Plasma Phys. Controlled Fusion* **30** 1665
14. Ovchinnikov K N, Silin V P and Uryupin S A (1991) *Sov. J. Plasma Phys.* **17** 748
15. Jones R D and Lee K (1982) *Phys. Fluids* **25** 2307
16. Porshnev P I, Ferrante G and Zarcone M (1993) *Phys. Rev. E* **48** 2081
17. Uryupin S A, Kato S and Mima K (1995) *Phys. Plasmas* **2** 3100
18. Ferrante G, Porshnev P I, Uryupin S A and Zarcone M (1996) *Phys. Scr* **54** 627
19. Fourkal E, Bychenkov V Y, Rozmus W, Sydora R, Kirkby C, Capjack C E, Glenzer S H and Baldi H A (2001) *Phys. Plasmas* **8** 550
20. Bochkarev S G, Bychenkov V Y and Rozmus W (2004) *Phys. Plasmas* **11** 3997
21. Su-Ming W, Zheng-Ming S, He M, Hui-Chun W, Quan-Li D and Jie Z (2006) *Phys. Plasmas* **13** 113302
22. Su-Ming W, Zheng-Ming S and Jie Z (2008) *J. Phys. Conf. Ser.* **112** 022039
23. Rosen M D (1990) *Phys. Fluids B* **2** 1461
24. Chichkov B N (1990) *J. Phys. B At. Mol. Opt. Phys.* **23** 103
25. Glover T E, Crane J K, Perry M D, Lee R W and Falcone R W (1995) *Phys. Rev. Lett.* **75** 445
26. Kieffer J C, Matte J P, Chaker M, Beaudoin Y, Chien C Y, Coe S, Mourou G, Dubau J and Inal M K (1993) *Phys. Rev. E* **48** 4648
27. Silin V P and Uryupin S A (1997) *JETP* **84** 59
28. Bendib A, Bendib K and Sid A (1997) *Phys. Rev. E* **55** 7522
29. Liu J M, De Groot J S, Matte J P, Johnston T W and Drake R P (1994) *Phys. Rev. Lett.* **72** 2717
30. Glenzer S H, Rozmus W, MacGowan B J, Estabrook K G, De Groot J D, Zimmerman G B, Baldi H A, Harte J A, Lee R W, Williams E A and Wilson B G (1999) *Phys. Rev. Lett.* **82** 97
31. Chichkov B N, Shumsky S A and Uryupin S A 1992 *Phys. Rev. A* **45** 7475
32. Porshnev P, Bivona S and Ferrante G (1994) *Phys. Rev. E* **50** 3943
33. Porshnev P, Khanevich E, Bivona S and Ferrante G (1996) *Phys. Rev. E* **53** 1100
34. Ferrante G, Porshnev P I, Uryupin S A and Zarcone M (1998) *Laser Phys.* **8** 150
35. Ferrante G, Zarcone M, Basile S, Petrova O and Porshnev P I (2000) *Laser Phys.* **10** 246
36. Ferrante G (2007) "Strong Field Phenomena in Laser-Plasma Interaction" *ISUILS Conference*, 23–27 September, Pisa, Italy
37. Ferrante G, Oliveri R L and Petrova O (2008) "Strong Laser Field Effects in Plasma Electron Kinetics and Heating" *ISUILS Conference*, 24–28 November, Kyoto, Japan
38. Silin V P (1965) *Sov. Phys. JETP* **20** 1510
39. Ferrante G, Uryupin S A, Zarcone M and Porshnev P I (1997) *J. Opt. Soc. Am. B* **14** 1716
40. Ferrante G, Uryupin S A and Zarcone M (2002) *Laser Part. Beams* **20** 177
41. Ferrante G, Zarcone M and Uryupin S A (2003) *Proc. SPIE* **5228** 498
42. Ferrante G, Zarcone M and Uryupin S A (2001) *Phys. Plasmas* **8** 4745
43. Romanov A Y, Silin V P and Uryupin S A (1997) *JETP* **84** 687
44. Ferrante G, Zarcone M and Uryupin S A (2000) *Phys. Plasmas* **7** 4273
45. Ferrante G, Zarcone M and Uryupin S A (2001) *Laser Phys.* **11** 183
46. Bychenkov V Y, Rozmus W and Capjack C E (2003) *JEPT Lett.* **78** 119
47. Ferrante G, Zarcone M and Uryupin S A (2002) *Eur. Phys. J. D* **19** 349
48. Ferrante G, Zarcone M and Uryupin S A (2003) *Eur. Phys. J. D* **22** 109
49. Ferrante G, Zarcone M and Uryupin S A (2003) *Phys. Rev. Lett.* **91** 085005
50. Ferrante G, Zarcone M and Uryupin S A (2003) *Laser Phys.* **13** 275
51. Ferrante G, Zarcone M and Uryupin S A (2005) *J. Phys.* **11** 14
52. Ferrante G, Zarcone M and Uryupin S A (2006) Chapter 11 in "Progress in Ultrafast Laserscience I", Springer-Verlag, New York, p. 187
53. Yoneda H, Hasegawa N, Kawana S and Ueda K (1997) *Phys. Rev. E* **56** 988
54. Nishimura H, Inubushi Y, Fujioka S, Kawarama T, Shimizu S, Hashida M, Sakabe S, Koike F, Johzaki T, Nagatomo H and Mima J (2007) Chapter 10 in "Progress in Ultrafast Laserscience II", Springer-Verlag, New York, p. 199
55. Inubushi Y, Nishimura H, Ochiai M, Fujioka S and Izawa S (2004) *Rev. Sci. Instrum.* **75** 3699
56. Maximov A V, Ovchinnikov K N, Silin V P and Uryupin S A (1998) *JETP* **86** 710
57. Ferrante G, Zarcone M and Uryupin S A (2001) *Phys. Rev. E* **64** 046408

58. Silin V P (1994) *JETP* **79** 756
59. Ferrante G, Zarcone M, Basile S, Petrova O and Porshnev P (2000) *Proc. Second Italian-Russian Symp. on Ultrafast Optical Physics*, ed G Ferrante, M Vaselli and A Zheltikov, Intellect-Tsentr, Moscow, pp. 47–64
60. Ferrante G, Oliveri R L and Petrova O “Evolution of Plasma Electron Distribution Functions in the Presence of Two Laser Fields” (to be published)
61. Weyl G M and Rosen D (1985) *Phys. Rev. A* **31** 2300

Chapter 11

Ion Acceleration by Ultra-Intense Lasers: Analysis of Contrast Effects

Alessandro Flacco and Dimitri Batani

Abstract The temporal profile of a intense laser pulse impacts in various ways the physics and the evolution of the ion acceleration process. In most experimental cases, the amount of light that precedes the main intensity peak gets intense enough to initiate the ionization of the target; among the consequences, the modification of the target structure, the laser-plasma interaction and the dynamics of ion acceleration have been extensively investigated. In this contribution, we discuss the most important effects related to ion acceleration with ultra-intense, sub-picosecond laser pulses.

The production of accelerated proton beams from laser-matter interaction has been firstly obtained by Gitomer [1], after the growing interest in the late seventies on the presence of ion signals of various species during the expansion of laser produced plasmas (see for instance [2]). Further studies have shown the presence of protons among the set of accelerated species, independently of the type of target material. In forthcoming decades, interest increased on the use of laser matter interaction at relativistic intensities as a way to produce accelerated bunches of charged particles. The main interest in the feasibility of plasma based accelerating structures resides in the fact that very high transient electrostatic fields can be held by the plasma medium (exceeding several TV/m), possibly opening the way to a new approach to the production of particle beams.

The techniques for accelerating particle beams by laser interaction with solid targets have received a huge improvement during the past decade, made possible by the introduction and technological development of Ti:Sa (Titanium doped Sapphire

¹Chirped Pulse Amplification [3].

A. Flacco (✉)

Laboratoire d'Optique Appliquée (ENSTA-ParisTech, CNRS, École Polytechnique), Chemin de la Hunière, 91761 Palaiseau, France

e-mail: alessandro.flacco@polytechnique.edu

D. Batani

Università degli Studi di Milano-Bicocca, Piazza della Scienza 3, 20133 Milano, Italy

e-mail: batani@mib.infn.it

crystal)-based CPA¹ laser systems. Ti:Sa crystals support a broader spectrum, which therefore enables the creation of shorter laser pulses. Commercially available Ti:Sa oscillators produce trains of laser pulses with FWHM² durations as short as several femtoseconds. High-power (>100 TW) commercial laser systems can deliver pulses at a repetition rate of several Hz with a per-pulse FWHM duration of 20–30 fs. The benefits of using shorter laser pulses reside in the fact that higher peak intensities can be reached with limited energy content. Laser systems with reduced energy are smaller and can work at higher repetition rates. These features go in the direction of the production of laser-based particle accelerators.

In this contribution, we review some of the effects that can be triggered by the spatial and temporal features of the laser pulse during the interaction with thin solid targets.

11.1 Laser Proton Acceleration

In the following scenario of laser particle acceleration, the laser pulse interacts with an overdense micrometric target, $\omega_{pe} > \omega_{laser}$, being $\omega_{pe} = \sqrt{n_e e^2 / (\epsilon_0 m_e)}$ the electron plasma frequency of the target material and $\omega_{laser} = 2\pi c / \lambda$ the pulsation of the incoming laser radiation.

The laser starts to ionize the material as its intensity increases over a certain threshold, depending on the material and the nature of the laser beam (see Sect. 11.2): during the forthcoming interaction between the laser and the plasma, the freed electrons start quivering in the laser field, and important collective mechanisms are set up.

As the normalized potential of the laser field approaches the relativistic limit of $a_0 = eA/mc = 1$, at intensities in the order of $I \sim 10^{18} \text{ W cm}^{-2}$, the temperature of heated electrons strongly increases. Different mechanisms have been recognized that produce an energy transfer between the laser field and the electrons in the plasma (see [4–6] and references therein). This last is usually modelled as a two temperature plasma, where two maxwellian electron populations do exist, a colder one (density n_c , temperature T_c) that remains in equilibrium with the ions of the material and a hotter one (n_h , T_h) that gains energy from the laser field [7,8]. The relative importance of the various heating mechanisms, in terms of number of heated electrons and temperature of the hot electron population, depends on the interaction parameters, including the angle of incidence, the duration of the laser pulse, the density profile of the expanding plasma and the length of the density gradient. This last parameter, in particular, has been observed to be very important.

As an upper cut-off to the maximum temperature electrons can reach, it should be considered the energy they acquire in their quivering motion, i.e. their energy in the laser electromagnetic potential. According to [9]:

² Full width at half maximum.

$$\varepsilon_h = m_e c^2 \left(\sqrt{1 + a_0^2} - 1 \right) \quad (11.1)$$

As an example, an electron quivering in a field of $10^{18} \text{ W cm}^{-2}$ acquires a kinetic energy of $\varepsilon_h = (\sqrt{2} - 1)m_e c^2 \approx 200 \text{ keV}$.

The use of laser produced plasmas as a source of accelerated ions originates in the separation of charges that is set at the plasma-vacuum boundary of the expanding plasma. The problem of a two-temperatures plasma expansion in the vacuum has been addressed analytically and numerically in a wide set of works, see for example [10–13].

In most of the experimental cases, the plasma is created by focusing the laser beam to a tiny spot on a thin solid foil. The hot plasma is then created on the illuminated surface; the hot electrons drift through the thickness of the target, filling the volume. The use of very thin (micrometric or nanometric) targets reduces the dilution of the hot electron current that travels to the back surface. The drift current exceeding the Alfvén's limit of the material is responsible for the ionization of the remaining part of the bulk, with the consequent expansion in the vacuum.

The scientific community has been discussing for a long time about the different scenarios of ion acceleration during the laser interaction with the target and during the subsequent plasma expansion in the vacuum. A deeper discussion of the subject goes beyond the scope of this contribution. As a matter of fact, three families of accelerated ions can be isolated emerging from the shot target, after the interaction with the laser. A first is accelerated by the laser pulse itself during its interaction with the created plasma: this is due to the electrostatic gradient that can be created by the laser's strong longitudinal (temporal) and transversal (spatial) ponderomotive force on electrons, pushing the positively charged ions deep in the bulk [14, 15]. A second population is accelerated by the charge separation on the plasma vacuum boundary of the non-illuminated (back) surface of the target, far from the laser source: the process is called target normal sheath acceleration (TNSA) and is recognised to be the source of the most energetic ions produced in the interaction (see [16, 17] and references therein). The TNSA can be active also on the illuminated surface, where the plasma expansion can accelerate ions in the *backward* direction (towards the laser). This last phenomenon (third population) can be observed only when the laser interaction with the target has not broken the symmetry of the created plasma expansion, which is normally the case with ultra-high contrast lasers (see [18] for details). An exhaustive review of all of the mentioned processes can be found in [19].

11.2 Laser Interaction with the Solid: Creation of a Preplasma

Upon the interaction between an intense electromagnetic wave and overdense matter, several mechanisms are put in place that act on the physical state of the irradiated surface and of the surrounding bulk.

Different effects, depending on the intensity of the incoming wave, act at the atomic and molecular level, which result in the ionization of the irradiated amount of matter. As a general rule, the quantity of matter that is involved in the process is limited by the surface extension of the illuminated area and the skin depth of the considered radiation in the material. The relationship

$$\delta_s = \frac{c}{\omega_{pe}} |1 + i\nu|^{1/2}, \quad (11.2)$$

where $\omega_{pe} = \sqrt{n_e e^2 / m_e \epsilon_0}$ is the electron plasma frequency and ν the collision frequency, gives the effective (collisional) skin depth in the material (see [8] and references therein).

The laser pulses that are produced by CPA chains are very likely to be preceded by a certain amount of light (*pedestal*). This pedestal normally starts in the range of *nanoseconds* before the main pulse; its intensity can considerably increase approaching the peak, on the timescale of tens or hundreds of *picoseconds* before it. The pedestal, or amplified spontaneous emission (ASE), normally results from the amplification of the light produced by spontaneous emission in charged crystals. The effect is mostly important at the very first stages of the amplification chain [20, 21], where multiple orders of magnitude in amplification rely on a single crystal and where low intensity seeds have to be used. The contrast ratio between the peak and the pedestal is then conserved (or worsened) in the remaining part of the laser system.

Attenuated replicas of the main intensity peak (*prepulses*), which propagate temporally in advance with respect to it, can also be present.

Considering the very high (relativistic) intensity of the main laser peak ($I > 10^{18} \text{ W/cm}^2$) the irradiated target surface can be therefore ionized prior to the arrival of the main pulse by the pedestal or prepulses. In the case of a target material where no level that is resonant with the laser wavelength exists, the direct, single-photon, ionization is not permitted. However, at sufficiently high intensities, non-linear ionization mechanisms gain importance. In the intensity range under examination, effects such as multiphoton ionization [22–28], tunnel ionization [29] and barrier suppression are dominant. Important multiphoton ionization starts at intensities of $10^{10} \div 10^{14} \text{ W cm}^{-2}$. As the first electrons are extracted, they start freely quivering in the laser oscillating field, eventually producing secondary ionizations by collisions. Once the avalanche process has started, the created plasma on the illuminated surface increases the energy absorption. In dielectrics, the transparency is lost as the first electrons are freed and promoted to the conductivity band.

Experimental measurements supported by modelling set the ionization threshold for a pedestal of 1 ns in 1.5 J cm^{-2} for a metal (gold) and 35 J cm^{-2} for a dielectric (fused silica) targets [30]. For pulses with durations of tens of picoseconds, the ionization threshold is lowered to 0.5 J cm^{-2} in gold and 4 J cm^{-2} for fused silica.

The impact of the laser pulse pedestal on the target have to be taken into account when the intensity of the leading edge increases over the ionization threshold of the material.

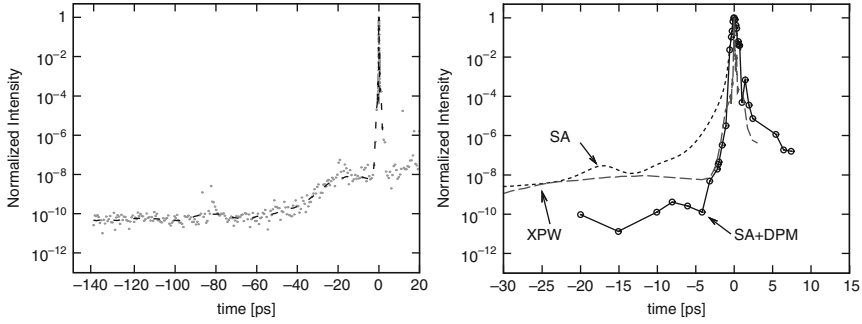


Fig. 11.1 Renormalized intensity plots obtained with a 3ω cross-correlator showing the temporal profile of a *femtosecond* pulse. (*Left*): Relative intensity of the pedestal up to $t = -200$ ps before the *femtosecond* peak on a XPW filtered laser system. (*Right*): Comparison of the pedestal on the timescale of some tens of *picoseconds* obtained with different filtering techniques (SA: Saturable Absorber, XPW: X-Polarized Wave Generation [31], DPM: Double Plasma Mirror [32])

An example of laser pedestals from two different multi-terawatt laser installations is shown in Fig. 11.1. The figure also shows the capabilities of the most common technologies nowadays used to improve the temporal contrast of CPA laser system in the front-end or in the first amplification stages (XPW [33], saturable absorbers [20]) or after the compression of the pulse, just before the interaction (plasma mirrors [32]).

The interaction of the laser pedestal with the solid target can trigger different phenomena on the illuminated (front) or not illuminated (back) surface. The final effect on the generation of accelerated ions is presented more in detail in following sections.

11.3 Effects Induced on the Front Surface

The characteristics of the density gradient on the front (illuminated) surface of the target is a key parameters of the interaction between the incoming laser radiation and the electrons in the plasma. Many previous theoretical and numerical works have discussed about the correlation between the angle of incidence, the length of the existing gradient and the efficiency of the different absorption mechanisms. Moreover, as the laser peak intensity is being increased, even the leading edge of the laser pulse can be active in defining the plasma gradient length, which adds a previously neglected correlation between the duration of the laser pulse and the amount of absorbed energy (on this topic, see [34, 35]).

At relatively short density gradients, the most active mechanisms are the resonant absorption [5] and the vacuum heating [4]. In particular [36], this last is known to produce the highest electron temperature but is active only when a p-polarized component impinges on very short density gradients ($L_{\text{grad}} \sim v_{\text{osc}}/\omega$, which

corresponds to $L_{\text{grad}} \sim 0.1\lambda$ at $10^{17} \text{ W cm}^{-2}$ and $\lambda = 1\mu\text{m}$). At longer density gradients ($L \sim \lambda$), the JxB heating mechanism [6] gains in importance.

Finally, the presence of a laser pedestal can result in the production of a long, sub-critical, plasma in front of the target. The interaction between the laser beam and such a plasma can accelerate electrons out of it, via various non-linear mechanisms (the most important one being stimulated Raman scattering). However, the overall efficiency on the heated electrons is definitely lower than the others presented before.

The realization of laser technologies, such as those mentioned in the previous section, capable of decreasing the pedestal level to below the damage threshold of the solid target, has opened the possibility to gain a deeper insight in the laser target interaction process. An important set of theoretical and experimental studies have been dedicated to the search and realization of the ideal conditions for laser target interaction, aimed to ion acceleration. Recent studies realized with particle-in-cell (PIC) codes show in fact that the complete absence of a plasma gradient limits the ratio of absorbed energy. In [37], hydrogen targets at $n_e = 2n_c$ are simulated by 2.5D-PIC, and it is found that the maximum ion energy would be obtained for a gradient length of $L_{\text{grad}} = 4\lambda$, foreseeing an energy increase of $\sim 50\%$ for protons accelerated in the forward direction.

Studies of this kind are not often realized experimentally, as they require the capability of varying the parameters of the laser pedestal on a temporal scale that is not easily accessible. To control the density gradient length on the scale of several hundreds of nanometers, it would be necessary to cut the laser pedestal in a range of several tens of picoseconds before the main peak, which cannot be accomplished in simple way.

An alternative approach, used by some teams, is instead the realization of a two pulse laser target interaction. In this scheme (see for example [38–40]), a first laser pulse with lower intensity is used to *prepare* the target condition some time before the arrival of the main, high power, beam. The evolution of the plasma created by the pre-heating laser pulse can be very precisely characterized by interferometric measurements and hydrodynamic simulations (Fig. 11.2 left, [41]); this, in conjunction with the delay between the two laser pulses, which can be set with an uncertainty lower than hundreds of *femtoseconds*, enables the creation of very precise interaction conditions. Preliminary studies also need to be performed on the possibly destructive effects that the pre-heating pulse might have on the rear surface of the target, especially when using thin target foils. This is due (see later) on the shock wave that is produced at the interaction interface, propagates in the target and whose reflection on the back surface may be capable to produce a preliminary expansion of it (see for example the simulation in Fig. 11.8). As an example, Fig. 11.2 shows the correlation between the plasma gradient that is created on the illuminated surface (left) and the position, in the target bulk, of the created shock wave (right), after the pre-heating pulse has interacted. The aluminium target has been illuminated by a single $I = 4 \times 10^{15} \text{ W cm}^{-2}$ pulse, with a FWHM duration of $\tau_L = 150 \text{ fs}$. The dashed curve in Fig. 11.2 left shows the displacement of the surface at a critical density (thus opaque to the incoming laser radiation) as a consequence of the plasma expansion. On the right side of the figure, the displacement of the shock wave inside

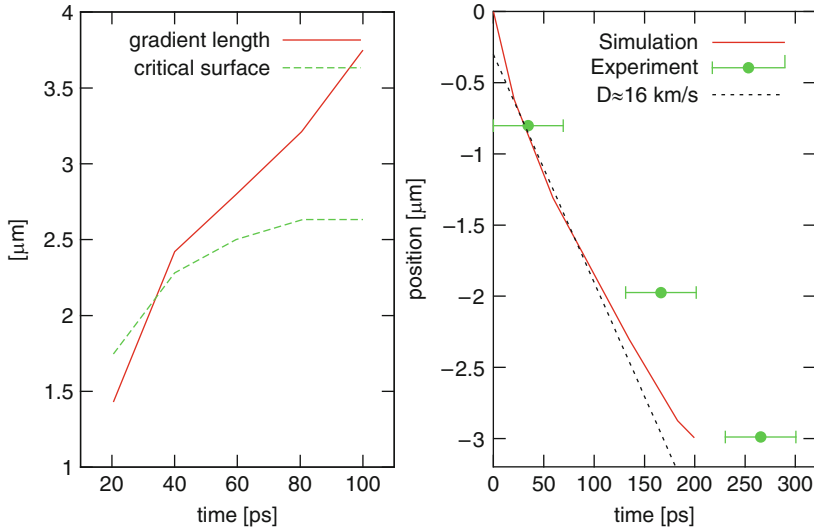


Fig. 11.2 Correlation between the plasma condition on the illuminated surface and the timescale of shock breakout for aluminum targets of varying thickness after being irradiated at $I = 4 \times 10^{15} \text{ W cm}^{-2}$ for $\tau_L = 150 \text{ fs}$ [41]. *Left*: the evolution in time of the density gradient length and the position of the surface at critical density; experimental confirmation has been obtained by interferometric measurements. *Right*: temporal displacement of the created shock in an infinite aluminum bulk. The experimental points are obtained by measuring the shock breakout time on targets of different thicknesses (excerpt from [40])

the target bulk is shown. The experimental points have been obtained by looking at the decrease of reflectivity, which indicates a rise in the electron temperature of the metal, on the non-illuminated surface of the target, after the interaction with the pre-heating laser pulse. The solid line on Fig. 11.3 shows the upper limit of the delay between the two pulses, before any destructive effect on the back surface. The fit (dotted line) shows an average shock speed of $D \sim 16 \text{ km s}^{-1}$ (Fig. 11.2 right).

Some experimental measurements realised in LOA by Flacco, A. and coworkers show an increase in the proton cutoff energy when the surface of a $6 \mu\text{m}$ Aluminum target is pre-heated by a 30 fs laser pulse at $\sim 10^{16} \text{ W/cm}^2$, temporally in advance with respect to the main laser pulse. The best interaction condition was observed with a delay of 100 ps , and produced a kinetic energy increase of $\sim 15\%$ (Fig. 11.3).

McKenna and coworkers [39] have reported the experimental observation of protons with higher energy when the target was pre-heated by pulses with intensities in the range of some $10^{12} \text{ W cm}^{-2}$. The maximum energy conversion efficiency was observed with a density gradient length of $\sim 50 \mu\text{m}$, and it produced a gain of $\approx 40\%$ in proton kinetic energy. Interferometric measurement (Fig. 11.4 right) shows, however, that in the used experimental condition, the long gradient pre-plasma is producing a filamentation of the incoming high power beam, possibly tightening its focusing and thus increasing the on-target peak intensity (see Fig. 2c in [39]).

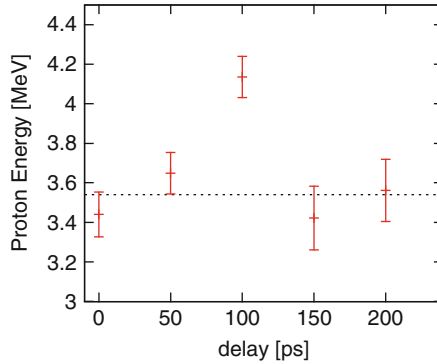


Fig. 11.3 Enhancement of the proton cut-off energy vs. the delay between a pre-heating and a pump laser pulse in the two beam proton acceleration scheme, using aluminium targets of $6\mu\text{m}$ in thickness [41]. The pre-heating pulse complies with the scenario showed in Fig. 11.2. The maximum proton energy is observed for a delay of $\Delta t = 100\text{ps}$, which corresponds to a gradient length on the illuminated surface of $L_{\text{grad}} \simeq 3.5\mu\text{m}$. The dashed line indicated the energy observed without the pre-heating beam

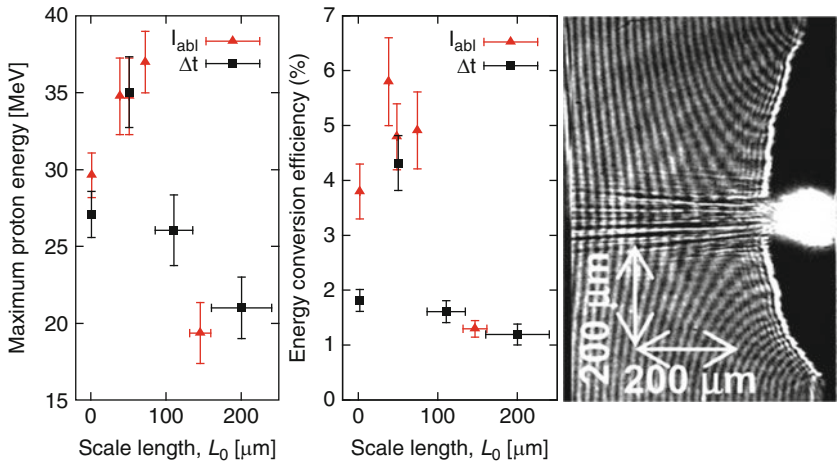


Fig. 11.4 Maximum proton energy (*left*) and energy conversion efficiency (*center*) as functions of the scale length on the illuminated surface of a solid aluminium target. On the *right*, an interferometric image of the state of the plasma in front of the target right after the pump beam propagation shows the presence of filaments (excerpt from [39])

11.4 Effects Induced on the Back Surface

In the context of proton generation by irradiation of foil targets with ultra-high-intensity laser pulses, it is predicted that the use of very thin targets gives higher proton energies. Indeed, this expectation is somewhat met in several experiments including the experimental results by Kaluza et al. [42]. Figure 11.5 shows the

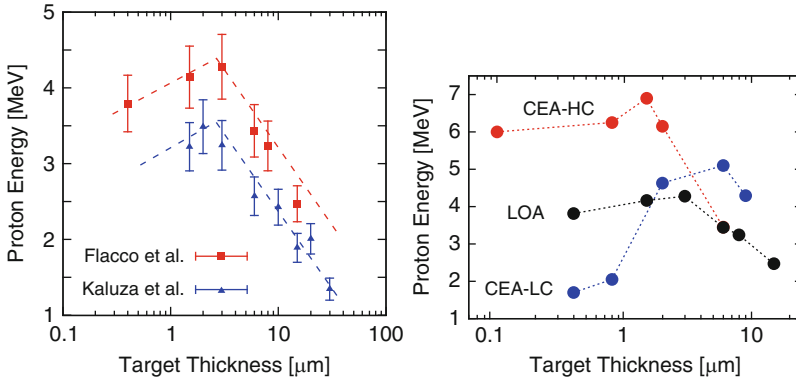


Fig. 11.5 Correlation between proton cut-off energy and target thickness obtained at $I > 10^{19} \text{ W cm}^{-2}$ on thin aluminium targets with different laser pedestal conditions. (*Left*): Points obtained at $I \sim 10^{19} \text{ W cm}^{-2}$ with $\approx 0.5 \text{ ns}$ (Kaluza et al. [42]) and at $I \approx 5 \times 10^{19} \text{ W cm}^{-2}$ with a small picosecond pedestal (Flacco et al.). (*Right*): Data obtained on different laser facilities showing the effects of various contrast enhancement techniques (CEA-LC: saturable absorber, CEA-HC: double plasma mirror, LOA: XPW, excerpt from [45])

results by Kaluza et al., i.e., the correlation between proton cut-off energy and target thickness at $I \approx 10^{19} \text{ W cm}^{-2}$ and with a prepulse duration $\approx 0.5 \text{ ns}$, together with more recent measurements done by Flacco et al. at LOA at larger intensity ($I \approx 5 \times 10^{19} \text{ W cm}^{-2}$). There is a clear trend towards increasing proton energy when the target thickness is reduced. The simplest explanation of this trend correlates the higher proton cut-off energies obtained from thin targets to the higher hot electron density created, due to the reduced dispersion of hot electrons drifting through the bulk [43]. When approaching very thin (sub-micrometric) targets, other mechanisms may be active in increasing the final accelerating field (see for example recirculation effects in [44]).

However, below a certain thickness, the trend is reversed due to prepulse effects breaking the target (let's notice that the inversion point is practically the same for the two sets of points, despite the larger intensity used by Flacco et al., a result which was possible thanks to the improvements in laser contrast). In such results, the trend is reversed below a certain thickness, which is related to the duration of the laser prepulse. This is a clear indication that below a certain thickness, the effects of laser prepulse destroy the targets themselves creating a plasma on the rear side with a long plasma scale-length, which reduces the process of proton acceleration. Generally, the effects of laser prepulse are related to the fact that the laser pedestal, with ns duration, launches a shock wave in the material (see later): its breakout on target rear side may create a long plasma, which is detrimental to acceleration, affecting the mechanism of TNSA. In principle, X-ray pre-heating from the X-rays emitted by the hot plasma corona may induce the same problem. However, this is indeed important only for very thin targets of relatively high-Z (larger X-ray generation and harder X-rays) irradiated at relatively high irradiances.

In this section, we do concentrate on shock-induced effects only. We will show how, depending on target thickness and prepulse intensity, three different regimes can be obtained. The first two are well known in the literature:

1. For “thick” targets and at low pedestal intensities, the shock is very weak and travels slowly in the material. Thereby, it has no time to break out on target rear side before the arrival of the main laser pulse (ps duration) accelerating the energetic proton beam.
2. For “thin” targets and high pedestal intensities, a strong shock is launched in the material and travels quickly. Thereby, it has the time to break out on target rear side and induces a vaporization of the material (plasma formation) with the creation of a long gradient scale-length, which prevents significant proton acceleration.
3. Finally, there is an intermediate regime, in which the shock breaks out on target rear side, but it is so weak that it just produces a deformation of the target surface but not its vaporization. This may produce deformation of target rear side and therefore interesting effects consisting in the deflection of the laser beam, which indeed could even be controlled.

Let’s also notice that a thin foil target can also be displaced as whole by the effect of ablation pressure thereby strongly affecting focusing conditions (especially because in this kind of experiments, tight focusing is used to achieve large intensities on target).

11.5 Laser-Produced Shocks and Proton Generation

The interaction between the nanosecond part of the laser pedestal and the target can produce a shock wave. This is due to heating and expansion of the plasma, created on the illuminated surface, and the interaction of the laser pedestal with it. After the plasma expansion has begun and a density gradient has developed on the target, a quasi-stationary configuration is reached. The laser penetrates up to the surface at critical density, where it deposits its energy; at intensities $I < 10^{14} \text{ W cm}^{-2}$, electrons are mostly heated by collisional absorption [46]. Heat is transported by electrons behind the critical surface towards the colder parts of the target. The conservation of the momentum at the ablation front, where previously unperturbed material is heated and removed, produces a rise in pressure, which propagates at a given speed towards the back surface of the target [47].

The effects related to the shock induced by the laser prepulse depend on

1. Shock pressure (which increases with laser intensity): At high pressure, the shock will produce vaporization of the target rear side and plasma formation;
2. Target thickness and pedestal duration: To avoid breakout, we need the target thickness d to satisfy the relation,

$$d > D\tau, \quad (11.3)$$

where D is the shock velocity and τ the duration of the laser prepulse (before the arrival of the main laser pulse). The shock velocity is related to shock pressure by the relation [47]:

$$D = \sqrt{\frac{\gamma + 1}{2} \frac{P_s}{\rho_0}}, \quad (11.4)$$

where P_s is the shock pressure, γ the adiabatic constant of the material, ρ_0 its initial density. In principle, (11.4) is strictly valid for a perfect gas only. Nevertheless, in the high pressure range (Megabar), all materials approach the perfect gas state, so the relation (11.4) is qualitatively true and quantitatively quite close to the real numbers.

Finally, the shock pressure is given by [48]

$$P_s \text{ (Mbar)} = 8.6 \left(\frac{I}{10^{14}} \right)^{2/3} \lambda^{-2/3} \left(\frac{A}{2Z} \right)^{1/3}, \quad (11.5)$$

where the intensity I is measured in W cm^{-2} , the laser wavelength λ in μm , and A and Z are the atomic weight and number of the irradiated material. According to (11.5), at $5 \times 10^{12} \text{ W cm}^{-2}$, we produce a pressure of the order of 1.2 Mbar, while at $10^{13} \text{ W cm}^{-2}$, we get 2 Mbar. Using the Sesame equation of state tables for Al [49], we can see that these respectively correspond to shock velocities of about 10 and 13 km s^{-1} (i.e. $\mu\text{m/ns}$). Therefore, if for instance we consider a prepulse duration of 1 ns, we see that the shock does not have the time to break out for Al targets thicker than $13 \mu\text{m}$. Indeed the two velocities are not so different due to the weak dependence of velocity on pressure and to the weak dependence of pressure on intensity. However, in order to assess the real effects of shock breakout, we must locate the created conditions in the high-pressure phase diagram of Al [50], shown in Fig. 11.5. Here, we can notice the melting temperature of Al at standard pressure ($T \approx 933 \text{ K}$), the melting point along the Hugoniot of the material ($T \approx 5,000 \text{ K}$) and the boiling temperature at standard pressure ($T \approx 2,500 \text{ K}$). The Hugoniot curve is the set of states in a material, which can be reached by shock compression. This is named as shock *adiabat* in Fig. 11.5.

We must also consider the fact that, as described in [47], at the time the shock breaks out on the target rear side, the shock pressure is not maintained, for the shocked material does face vacuum (or a gas at very low pressure). This causes the motion of the material in the forward direction (i.e. the direction of the shock front), while at the same time, a relaxation wave is created. If the shock is not too strong, it can be shown that the velocity of the free surface of the material is about $2U$ (where U is the fluid velocity in the material behind the shock front moving with velocity D), while the relaxation wave, virtually decompressing the material to zero pressure, travels back in the material at the corresponding sound velocity C_s . Whether we get vaporization of the material on target rear side or not, it depends on the final state of the material after decompression. In principle, we must then draw the relaxation curve and superimpose it to the phase diagram in Fig. 11.6. If

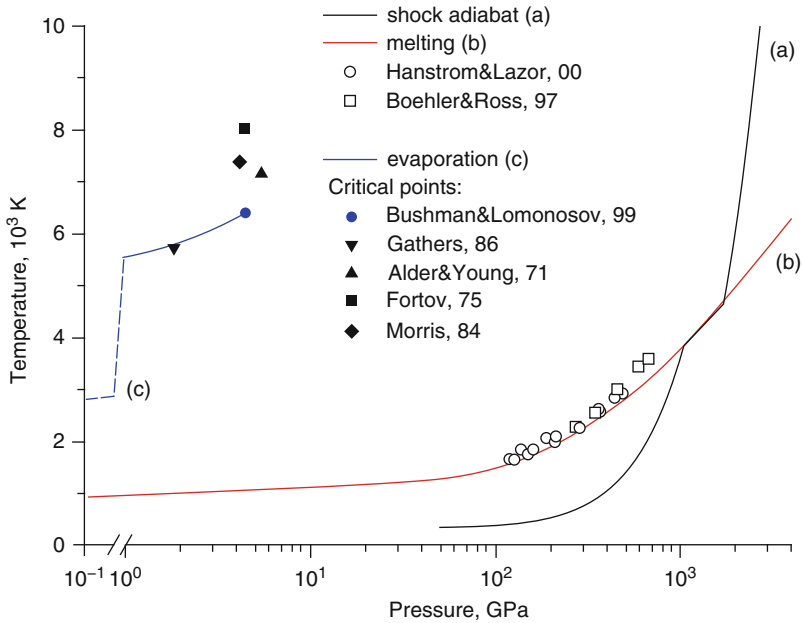


Fig. 11.6 High-pressure phase diagram of Al [50] ($1 \text{ Mbar} = 100 \text{ GPa}$) showing the melting curve, the vaporization curve, and the shock *adiabat*, together with experimental data

we do so, we discover that the shock compression of Al to 2 Mbar would bring to an unloading that ends at zero pressure above the evaporation curve of Al (curve (c) in Fig. 11.6). Shock compression of Al to 1.2 Mbar would instead bring to an unloading that ends at zero pressure below the evaporation curve of Al. Despite the small difference in pressure, the two shocks therefore produce dramatically different effects and may therefore be termed as cases of strong and case of weak shock pressures.

11.6 Detailed Hydrodynamics Simulations

In order to get a more quantitative description of the involved phenomena, one needs to perform numerical simulations. Here we show what we got using the hydrodynamics codes MULTI [51] and MULTI 2D [52]. Figure 11.7 shows the typical density profiles obtained in a $6 \mu\text{m}$ thick Al-target irradiated at various pedestal laser intensities (in all cases, the temporal laser profile is flat-top). Figure 11.8 shows a time-position plot of the results of the simulation at a laser intensity of $5 \times 10^{12} \text{ W cm}^{-2}$ (case with no plasma creation on target rear side). We see indeed that the density profile on rear side remains steep (unlike front side). However, the simulation in Fig. 11.8 shows another effect related to laser prepulse: after the

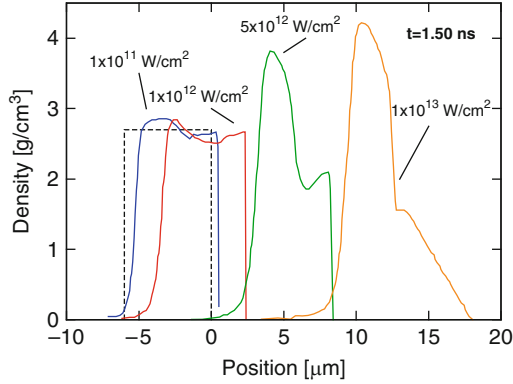


Fig. 11.7 Density profile of a 6 μm thick aluminum target after 1.5 ns for different laser intensities. The *dotted line* shows the unperturbed density profile. At $10^{12} \text{ W cm}^{-2}$, laser ablation generates a relatively cold and plastic deformation of the target. Increasing the intensity one order of magnitude heats the shocked material and creates a density ramp at the rear surface. Such a ramp has been shown to decrease the maximum proton energy

breakout of the shock (here taking place about 0.6 ns after the beginning of irradiation with the 1.5 ns long laser pedestal), the whole target begins to move with a velocity of about $2U$ (as we said before). 1 ns after shock breakout, the target has already moved almost by 10 μm . Of course, the displacement will be larger for higher laser intensities (larger shock pressures) and for thinner targets (earlier shock breakout time, less mass to be moved). Often a very tight focus is realized in this kind of experiments, in order to get a larger intensity, which usually implies a very short depth of focus. Therefore, in similar cases, the target may go out of focus due to its motion, and this can be a further cause for inefficient proton generation.

We notice that the target motion, as shown in Fig. 11.8, is characterized by a series of accelerations every time the shock breaks on target rear. It is also clear that the overall motion, on a longer time-scale, has a parabolic trend, which is characteristics of a constant acceleration. It can be shown that the target displacement is approximately given by

$$x = \frac{1}{2} \frac{P}{\rho_0 d} \tau^2 \quad (11.6)$$

a distance, which must be compared with the typical depth of focus:

$$l \approx \pm 2F^2 \lambda \frac{\theta}{\theta_{\text{DL}}}, \quad (11.7)$$

where we have introduced the F-number of the system, the divergence of the laser beam and the diffraction-limited divergence.

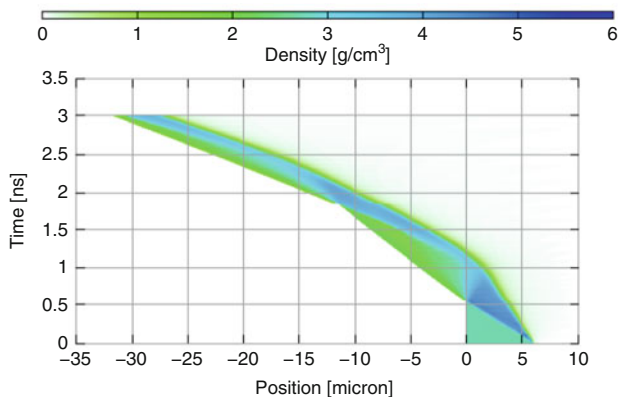


Fig. 11.8 Time-position plot of the 1D hydrodynamics of a $6\mu\text{m}$ Al foil irradiated by a flat-top laser intensity of $5 \times 10^{12} \text{ W cm}^{-2}$. Scale in false colors (see *top* of the figure) shows material density

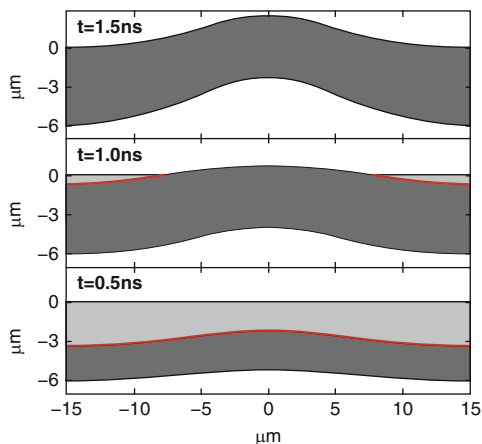


Fig. 11.9 Propagation and breakout of a shock wave driven in a $6\mu\text{m}$ Al target by a $10^{12} \text{ W cm}^{-2}$ pedestal with $10\mu\text{m}$ diameter focal spot. The *red line* represents the position of the shock front. The *light grey* region is unperturbed Al. *Darker grey* is the shocked Al (at the edge of the spot the shock is very weak, or negligible, the shock velocity corresponds to the sound velocity in unperturbed Al, and the degree of compression approaches 1). Along the axis of the laser beam instead shock compression and shock velocity reach their maximums

11.7 Two-Dimensional Effects and Proton Beam Deviation

Until now, we have only considered 1D hydrodynamics effects. These may bring to the formation of a plasma gradient on target rear side and also to target defocusing (due to target displacement after shock break out). In reality, due to the small lateral size of the laser focal spot, 2D effects in shock propagation and in target deformation are very important. Figure 11.9 shows the propagation and breakout of a shock

wave driven in a $6\text{ }\mu\text{m}$ Al target by a 10^{12} W cm^{-2} pedestal with $10\text{ }\mu\text{m}$ diameter focal spot. The simulations are realized with the hydrodynamic code MULTI 2D [52]. Here the intensity on target varies with the (radial) position. Therefore, shock pressure and velocity are different in each point on the surface, resulting in a different shock breakout time. Moreover, after shock breakout, the local displacement velocity ($2U$) of the target rear side is different, because the local fluid velocity is larger at the center and smaller at the edges of the spot. 2D effects in hydrodynamics bring to a deformation of the target. This is particularly interesting in the case of weak shocks, which do not bring to the formation of a plasma phase on target rear side. In this case, the local deformation acts to change the local target normal and thereby may produce a deviation of the accelerated proton from the perpendicular to the “unperturbed” target surface. If the fast electrons travelling in the material, and creating the space charge at target rear side, are directed along the normal to the target surface, this may only result in an increased divergence of the proton beam. In many cases, however, the fast electrons are not travelling along the normal, but rather along the laser beam axis. For instance if a laser beam (main ps pulse) is incident at an angle on the target surface, then fast electrons may still be produced normally to the surface or along the laser beam axis depending on the particular generation mechanism that is dominant in the experiment. In the case of resonant absorption, fast electrons will be mainly directed along the target normal. If instead ponderomotive effects are dominant, fast electrons will be mainly directed along the laser beam axis. In general, the two absorption mechanisms may be acting at the same time and will bring to the generation of different fast electron populations (in this context see also [53]). Figure 11.10 shows the sequential illustration of proton acceleration in a shocked target following the general scheme we have just described. Let’s

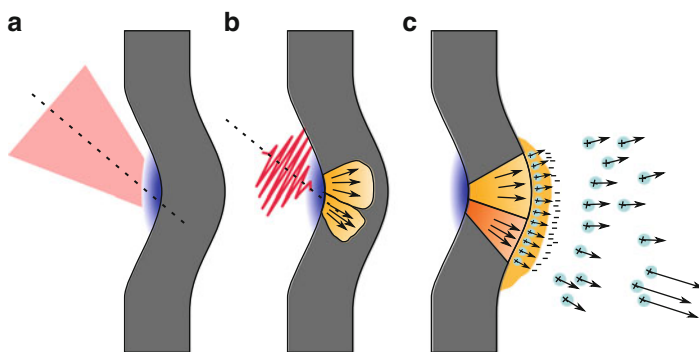


Fig. 11.10 Sequential illustration of proton acceleration in a shocked target. (a) before main pulse arrival, the ablation pressure induced by the ASE deforms the target. (b) The main pulse arrives under oblique incidence and generates a population of hot electrons. (c) The most energetic electrons traverse the target and sets up a strong electric field in an area where the local target normal is shifted towards the laser axis, away from the global target normal. Consequently, during the plasma expansion, the most energetic protons are accelerated in a direction that is shifted towards the laser axis, with an angle that increases with the magnitude of the local deformation

also notice that interesting features are expected to appear in the case of stronger shocks, which may vaporize the material near the centre of the shock front but not at the edges. In this case, acceleration of protons may be completely prevented from the central region. Nearby, however, the shock will be weaker and the target will be deformed but not vaporized. Proton acceleration may still be produced here bringing to the formation of an annular emission region.

11.8 Experimental Results

Experimental results obtained with the Lund laser system [54, 55] do indeed show all the features previously described. The diagnostics simply consisted in CR-39 detector plates with an aluminum filter mask placed before it to enable measurement of both the proton spatial and energy distributions. This is shown together with the expected proton pattern in Fig. 11.11a (assuming a beam directed along

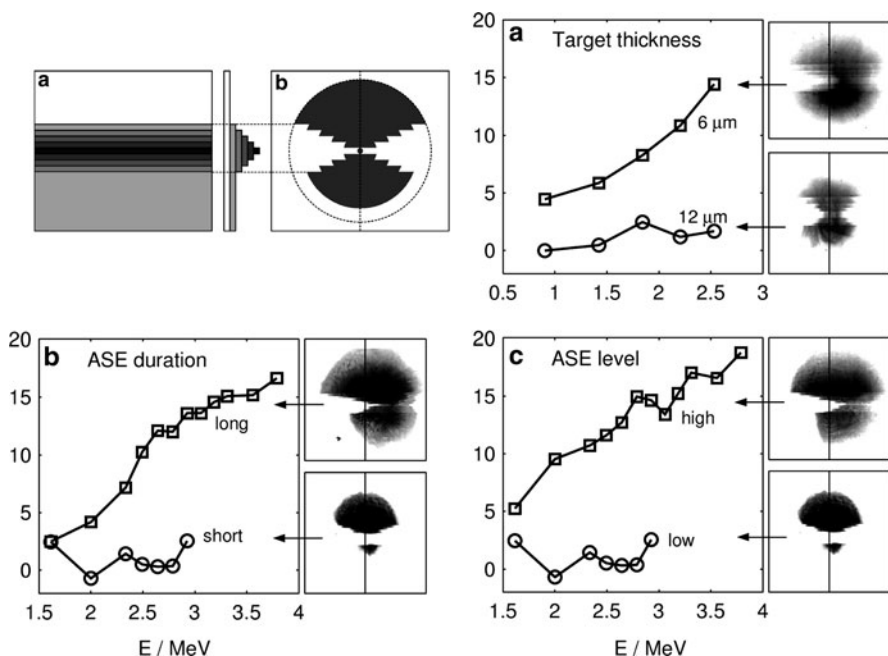


Fig. 11.11 Deviation from target normal to laser direction vs. proton energy (degrees vs. MeV) for protons above different threshold energies. The *lines* through the images on the *right* indicate target normal direction. With the pedestal duration increased by 1 ns from its minimum value and a contrast of 3×10^7 , the target thickness is varied in (a) from 12 μm to 6 μm. With 6 μm target and a minimum pedestal duration (≈ 1 ns) and a contrast of 3×10^7 , (b) illustrates the effect of increasing the pedestal duration by 1 ns and (c) of decreasing the contrast (increasing the ASE level to 6×10^6), corresponding to an estimated ASE intensity of $5 \times 10^{12} \text{ W cm}^{-2}$ (excerpt from [54])

the target normal and with divergence decreasing with increasing proton energy). Figures 11.11b–d show examples of the actual patterns observed in the experiments, together with plots of the deviation from target normal to laser direction vs. proton energy (degrees vs. MeV) for different parameters of the experiment (target thickness, pedestal level, pedestal duration). We see that deviation is larger when we expect so, according to the physical picture described in the previous paragraphs, i.e. when the target is thin and the laser pedestal is intense or long. In all these cases, the shock has the time to burn through and deform the rear surface of the target, while the shock itself remains low enough not to cause the vaporization of the material and the formation of a plasma with sufficient extension on the rear side. Results obtained changing the target material confirm the effect. For instance, we have compared 6 μm targets of Cu and Al. The shock speed is increasing with laser intensity but is lower in Cu than in Al, due to the larger density of Cu as shown by (11.4). The lower shock speed in Cu makes shock-effects less important. Indeed, experimental results in Fig. 11.12 show that, in comparable conditions, deviation is smaller for Cu than for Al. Finally, the shock model also allows to calculate the beam deviation

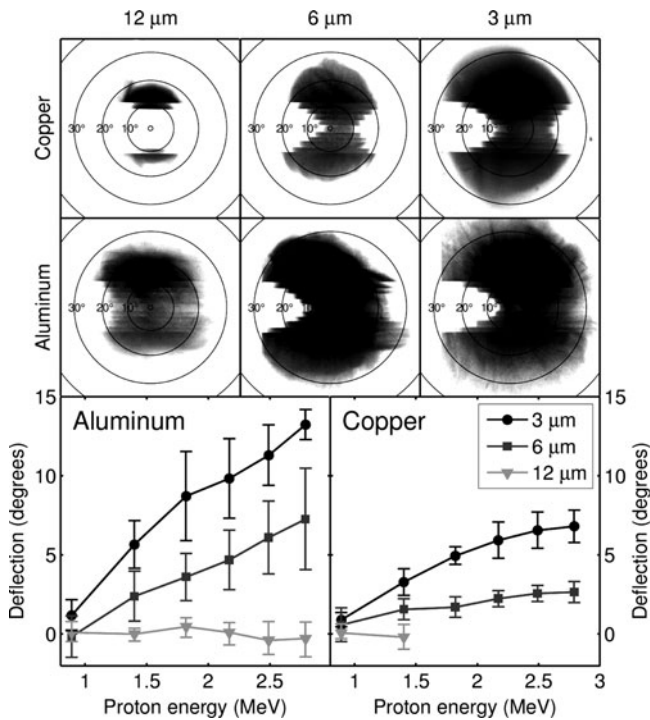


Fig. 11.12 Influence of target properties on the energy dependent emission direction for Cu and Al foils of different thickness. The pedestal intensity and duration were $2 \times 10^{12} \text{ W cm}^{-2}$ and 1.0 ns. The *top* and *middle rows* show representative proton beam patterns. The complete dataset is compiled in the two bottom diagrams where the error bars denote the standard deviation, taken over three consecutive shots (excerpt from [55])

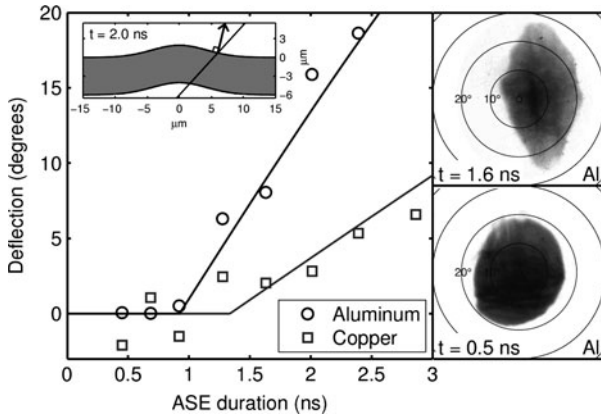


Fig. 11.13 Comparison of the prediction of the shock model and experimental results: proton deflection vs. pedestal duration. Targets were $6\text{ }\mu\text{m}$ Al and Cu at pedestal intensity $2 \times 10^{11}\text{ W cm}^{-2}$. The proton beam stays on the target normal for the shortest pedestals (*bottom right panel*). After shock breakout, the beam is steered towards the laser axis (*top right panel*). The inset shows the calculated shape of the foil for a 2.0 ns pedestal. Emission direction (*solid lines*) is calculated as the local target normal where the laser axis intersects the rear surface (excerpt from [55])

for higher energy protons, those related to the faster electrons (generated by ponderomotive forces and directed along the laser beam axis). Indeed, we can simply calculate the emission direction as the target normal at the point where the laser axis intersects the rear surface. Figure 11.13 compares the prediction of the model with experimental results showing the proton beam deflection vs. pedestal duration. The possibility of controlling the direction of the various spectral components of the accelerated ion beam by acting on optical parameters of the pumping laser is intriguing and might have interesting applications in a future. Moreover, it does suggest a new instrument to study the correlation between the energy of a component of the spectrum and the position on the target surface where it was originated. At present, this deviation adds an unknown on the experimental procedure (possibility of missing the ion peak energy), which can void the experimental measurements.

11.9 Conclusions

As shown in this paper, the pedestal of a laser pulse can have an intensity large enough to influence the acceleration process, possibly impacting the irradiated and the non-irradiated surfaces of the target. Their importance increases as the target thickness is reduced. As the pedestal gets intense enough to ionize the target surface, a plasma is formed. The interaction between the laser and the plasma governs the following acceleration process. The pedestal gains in intensity during the amplification process in the laser chain: some techniques capable of increasing the contrast

and cleaning the temporal profile of the laser pulse have been mentioned in previous sections. These techniques are required to be able to increase the ion peak energy by decreasing the thickness of the target.

The state of the plasma in front of the target at the time when the main intensity peak arrives defines the efficacy and the mechanisms responsible for electron heating, in particular the hot electron temperature and the hot electron number. The presence of a very long, low density, plasma corona may reduce laser-plasma coupling and reduce the hot electron temperature. On the other side, Simulations and some preliminary experiments do suggest that the complete absence of any plasma on the surface reduces the efficiency of the laser energy absorption and that the optimal laser-target interaction for ion acceleration happens in presence of a certain density gradient on the front side. This configuration has been realized in some experimental campaigns.

The interaction of the pedestal with the front surface can also impact on the condition of the target by deforming it on the non-illuminated surface (ionization and expansion). All of the effects produced on the non-illuminated surface, where the most energetic ions are extracted and accelerated are detrimental. The creation, by shock wave or by heating due to hot electrons and photons, of a density gradient on this surface before the arrival of the high intensity peak reduces the accelerating potential and results to be detrimental to the TNSA mechanism. An exception is represented by the cases where the pedestal is intense only enough to deform the target, without destroying it. This effects may open the interesting possibility to control the beam emission angle and the spatial distribution of its spectral components.

Acknowledgements The authors wish to acknowledge contributions and/or collaboration from: D. C. Carrol, M. N. Quinn and P. McKenna (SUPA, Department of Physics, University of Strathclyde, Glasgow, G4 0NG, UK); D. Neely (STFC, Rutherford Appleton Laboratory, Didcot OX11 0QX, UK); T. Ceccotti, F. Réau, P. Monot and Ph. Martin (PHI/IRAMIS/SPAM, CEA-Centre de Saclay, 91191 Saclay, France); F. Sylla, M. Veltcheva and V. Malka (LOA, ENSTA/CNRS/École Polytechnique, Chemin de la Hunière, 91761 Palaiseau, France); F. Lindau, O. Lundh and Claes-Göran Wahlström (Department of Physics, Lund University, P. O. Box 118, S-221 00 Lund, Sweden); M. Roth (Technische Universität Darmstadt, Institut für Kernphysik, Schlossgartenstr.9, 64289 Darmstadt, Germany); R. Jafer (Dipartimento di Fisica, Università di Milano Bicocca, 20126 Milano, Italy)

References

1. S.J. Gitomer, R.D. Jones, F. Begay, W. Ehler, J.F. Kephart, R. Kristal, *Phys. Fluid* **29**, 2679 (1986)
2. W. Ehler, W. Linlor, *J. Appl. Phys.* **44**, 4229 (1973)
3. D. Strickland, G. Mourou, *Opt. Commun.* **56**, 219 (1985)
4. F. Brunel, *Phys. Rev. Lett.* **59**(1), 52 (1987)
5. J.P. Freidberg, R.W. Mitchell, R.L. Morse, L.I. Rudinski, *Phys. Rev. Lett.* **28**, 795 (1972)
6. W.L. Kruer, K. Estabrook, *Phys. Fluid* **28**(1), 430 (1985)
7. K. Estabrook, W.L. Kruer, *Phys. Rev. Lett.* **40**(1), 42–45 (1978)
8. P. Gibbon, *Short Pulse Laser Interactions with Matter*. (Imperial College Press, London, 2005)
9. S.C. Wilks, W.L. Kruer, M. Tabak, A.B. Langdon, *Phys. Rev. Lett.* **69**(9), 1383 (1992)

10. L.M. Wickens, J.E. Allen, P.T. Rumsby, *Phys. Rev. Lett.* **41**(4), 243–246 (1978)
11. A. Gurevich, D. Anderson, H. Wilhelmsson, *Phys. Rev. Lett.* **42**(12), 769–772 (1979)
12. V.F. Kovalev, V.Y. Bychenkov, V.T. Tikhonchuk, *JETP Lett.* **74**, 10–14 (2001)
13. P. Mora, *Phys. Rev. Lett.* **90**(18), 185002 (2003)
14. Y. Sentoku et al., *Phys. Plasmas* **10**, 2009 (2003)
15. M. Zepf et al., *Phys. Rev. Lett.* **90**, 064801 (2003)
16. J. Fuchs, Y. Sentoku, S. Karsch, J. Cobble, P. Audebert, A. Kemp, A. Nikroo, P. Antici, E. Brambrink, A. Blazevic, E.M. Campbell, J.C. Fernández, J.C. Gauthier, M. Geissel, M. Hegelich, H. Pépin, H. Popescu, N. Renard-LeGalloudec, M. Roth, J. Schreiber, R. Stephens, T.E. Cowan, *Phys. Rev. Lett.* **94**(4), 045004 (2005)
17. A.J. Mackinnon, M. Borghesi, S. Hatchett, M.H. Key, P.K. Patel, H. Campbell, A. Schiavi, R. Snavely, S.C. Wilks, O. Willi, *Phys. Rev. Lett.* **86**(9), 1769–1772 (2001)
18. T. Ceccotti, A. Lévy, H. Popescu, F. Réau, P. D'Oliveira, P. Monot, J.P. Geindre, E. Lefebvre, P. Martin, *Phys. Rev. Lett.* **99**(18), 185002 (2007)
19. H. Habara, *Phys. Rev. E* **69**(3), 036407 (2004)
20. J. Itatani, J. Faure, M. Nantel, G. Mourou, S. Watanabe, *Opt. Comm.* **148**, 70 (1998)
21. M. Nantel, J. Itatani, A.C. Tien, J. Faure, D. Kaplan, M. Bouvier, T. Buma, P. Van Rompay, J. Nees, P. Pronko, D. Umstadter, G. Mourou, *J. Sel. Topics Q. Electr.* **4**, 449 (1998)
22. Keldysh et al., *Sov. J. Exp. Theor. Phys.* **20**, 1307 (1965)
23. V. Popov, *Phys. Lett. A* **358**(1), 21 (2006)
24. V.S. Popov, *Phys. Usp.* **47**(9), 855 (2004)
25. G.S. Voronov, N.B. Delone, *Sov. Phys. JETP Lett.* **1**, 66 (1965)
26. P. Agostini et al., *IEEE J. Quant. Electron.* **QE-4**, 667 (1968)
27. P. Agostini et al., *Phys. Rev. Lett.* **42**, 1127 (1979)
28. Mainfray et al., *Rep. Prog. Phys.* **54**, 1333 (1991)
29. A.C. Tien, S. Backus, H. Kapteyn, M. Murnane, G. Mourou, *Phys. Rev. Lett.* **82**(19), 3883–3886 (1999)
30. E.G. Gamaly, V. Tikhonchuk, *Phys. Plasma.* **9**(3), 949 (2002)
31. A. Jullien, O. Albert, G. Chériaux, J. Etchepare, S. Kourtev, N. Minkovsky, S.M. Saltiel, *Opt. Express* **14**(7), 2760 (2006)
32. G. Doumy, F. Quéré, O. Gobert, P. Martin, P. Audebert, J.C. Gauthier, J.P. Geindre, T. Wittman, *Phys. Rev. E* **69**(2), 026402 (2004)
33. A. Jullien, O. Albert, F. Burgy, G. Hamoniaux, J.P. Rousseau, J.P. Chambaret, F. Augé-Rochereau, G. Chériaux, J. Etchepare, N. Minkovski, S.M. Saltiel, *Opt. Lett.* **30**(8), 920 (2005)
34. M. Carrié, E. Lefebvre, A. Flacco, V. Malka, *Phys. Plasma* **16**, 053105 (2009)
35. A. Flacco, F. Sylla, M. Veltcheva, M. Carrie, R. Nuter, E. Lefebvre, D. Batani, V. Malka, *Phys. Rev. E* **81**, 036405 (2010)
36. P. Gibbon, A.R. Bell, *Phys. Rev. Lett.* **68**, 1535 (1992)
37. A.A. Andreev, R. Sonobe, S. Kawata, S. Miyazaki, K. Sakai, K. Miyauchi, T. Kikuchi, K. Platonov, K. Nemoto, *Plasma Phys. Contr. Fusion* **48**(11), 1605 (2006)
38. R. Nuter, L. Gremillet, P. Combis, M. Drouin, E. Lefebvre, A. Flacco, V. Malka, *J. Appl. Phys.* **104**(11), 103307 (2008)
39. P. McKenna, D. Carroll, O. Lundh, F. Nürnberg, K. Markey, S. Bandyopadhyay, D. Batani, R. Evans, R. Jafer, S. Kar, D. Neely, D. Pepler, M. Quinn, R. Redaelli, M. Roth, C.G. Wahlström, X. Yuan, M. Zepf, *Laser Part. Beams* **26**(04), 591–596 (2008)
40. A. Flacco, Experimental Study of Proton Acceleration with Ultra-High Intensity, High Contrast Laser Beam. PhD thesis, École Polytechnique, <http://pastel.paristech.org> (2008)
41. A. Flacco, A. Guemnie-Tafo, R. Nuter, M. Veltcheva, D. Batani, E. Lefebvre, V. Malka, *J. Appl. Phys.* **104**, 103304 (2008)
42. M. Kaluza, J. Schreiber, M.I.K. Santala, G.D. Tsakiris, K. Eidmann, J. Meyer-ter Vehn, K.J. Witte, *Phys. Rev. Lett.* **93**(4), 045003 (2004)
43. J.J. Santos, A. Debayle, P. Nicolai, V. Tikhonchuk, M. Manclossi, D. Batani, A. Guemnie-Tafo, J. Faure, V. Malka, J.J. Honrubia, *Phys. Plasma* **14**(10), 103107 (2007)

44. A.J. Mackinnon, Y. Sentoku, P.K. Patel, D.W. Price, S. Hatchett, M.H. Key, C. Andersen, R. Snavely, R.R. Freeman, *Phys. Rev. Lett.* **88**(21), 215006 (2002)
45. A. Flacco, T. Ceccotti, H. George, P. Monot, P. Martin, F. Réau, O. Tcherbakoff, P. d'Oliveira, F. Sylla, M. Veltcheva, F. Burgy, A. Tafzi, D. Batani, V. Malka, *NIM A* **620**(1), 18–22, DOI: 10.1016/j.nima.2010.01.053
46. C. Garban-Labaune, E. Fabre, C.E. Max, R. Fabbro, F. Amiranoff, J. Virmont, M. Weinfeld, A. Michard, *Phys. Rev. Lett.* **48**(15), 1018–1021 (1982)
47. Y.B. Zeldovich, Y.P. Raizer, *Physics of Shock Waves and High Temperature Hydrodynamic Phenomena* (Academic, New York, 1967)
48. J. Lindl, *Phys. Plasma* **2**, 3933 (1995)
49. Sesame tables 3712 and 3717 for Al, from t4 group lanl, sesame report on the los alamos equation of state library, report no. lalp-83-4, 1983. Technical report
50. A.V. Bushman, G.I. Kanel, A.L. Ni, V.E. Fortov, *Intense Dynamic Loading of Condensed Matter*. (Taylor and Francis, London, 1993)
51. R. Ramis, R. Schmalz, J. Meyer-ter Vehn, *Comput. Phys. Commun.* **49**, 475 (1988)
52. R. Ramis, J. Meyer-ter Vehn, Report no. mpq174. Technical report, Max-Planck-Institut für Quantenoptik (1992)
53. H. Popescu, S.D. Baton, F. Amiranoff, C., Rousseaux, M.R. Le Gloahec, J.J. Santos, L. Gremillet, M. Koenig, T. Hall, D. Batani et al., *Phys. Plasma* **12**, 063106 (2005)
54. F. Lindau, O. Lundh, A. Persson, P. McKenna, K. Osvay, D. Batani, C.G. Wahlström, *Phys. Rev. Lett.* **95**, 175002 (2005)
55. O. Lundh, F. Lindau, A. Persson, C.G. Wahlström, P. McKenna, D. Batani, *Phys. Rev. E* **76**, 026404 (2007)

Index

- Ablation front, 220
- Above-threshold ionization (ATI), 96
- Adiabatic constant, 221
- Alignment, 45, 47, 53, 55–57, 62, 63, 65, 69
 - field-free, 47, 55, 62
 - impulsively, 47
 - revivals, 56, 63
 - rotational wave packet, 63
- Ammosov–Delone–Krainov (ADK) model, 92
- Amplified spontaneous emission (ASE), 214
- Angular electron distribution function, 203
- Angular momentum, 22
- Anisotropic bi-Maxwellian, 184
- Anisotropic heating, 185
- Anisotropy parameter, 196
- Atom, 77
 - excited, 77
 - hydrogen, 78, 79
- Attosecond pulses, 75, 78, 86, 113
 - extreme ultraviolet (XUV), 113
 - isolated, 113, 114, 119
- Attosecond pulse train, 91
- Attosecond streak camera, 98–100

- Barrier suppression, 214
- Beam shapers, 173
- Bessel–Gaussian, 107, 108
- Bi-Maxwellian in spherical coordinates, 203
- Biot–Savart law, 21, 31
- Birefringent scattering damage, 166
- Bow-tie element, 130
 - thermal threshold, 141
- Bremsstrahlung, 79
- BSI, 76

- Carrier-envelope phase (CEP), 90, 96–99, 103, 104, 124, 125
- CEP, *see* Carrier-envelope phase

- Charge circulation, 22
- Charge resonance enhanced ionization, 3, 4, 9–13, 17
- Chirped mirrors, 97
- Chirped pulse amplification, 211
- Chirped-pulse amplifier, 98
- Clusters
 - carbon, 22
- Collision frequency, 214
- Color-centers, 164
- Complete reconstruction of attosecond bursts (CRAB), 100, 103–107, 109
- Computer-generated hologram, 173
- Control
 - active, 24
 - optimal, 23
 - quantum, 24
- Conversion efficiency, 122, 124
- Coulomb explosion, 1–3, 6, 13, 15, 16
- Couplers
 - directional couplers, 170
 - multimode interference coupler, 171
- Covariance, 3, 6, 10, 15
- CR 39 detector, 226
- Critical density, 216, 220
- Cross correlator, 215
- Crystal, 121
- Cutoff energy, 114, 124

- Deformation, 220, 225
- Densities, 22
 - current, 22, 30
 - flux, 22
 - gradient, 215
 - time-dependent, 22
 - toroidal shape, 22
- Depth of focus, 223
- Different frequency generation (DFG), 121

- Diffraction, 46
 - electrons, 46
 - X-ray, 46
- Diffractional lenses, 173
- Diffractional optical elements, 174
- Dipole
 - operator, 26
 - semi-classical approximation, 26
 - transition, 29
- Distribution function, 187, 194
- Double ionization, 4, 9–11, 13, 17
- Double optical gating (DOG), 91, 94, 99
- Double optical gating fields, 101
- Double plasma mirror, 215
- Driving field, 91–95, 99
- Dynamic imaging, 87
- EDF, *see* Electron distribution functions
- Effective collision frequencies, 198
- Eigenfunction, 22, 26
 - complex, 22
 - real, 22
 - symmetry-adapted, 22
- Eigenstate
 - bending, 28
 - complex, 27, 28
 - degenerate, 21, 27, 28, 32
 - near-degenerate, 22
 - pseudorotational, 27, 28, 32
 - real, 28
 - toroidal, 27
- Electric field, 25
- Electron, 77
 - bound, 77
 - free, 77
- Electron distribution functions (EDF), 183
 - shape reversal, 185
- Electron–electron collision integrals, 186
- Electron–ion collision integral, 186
- Electron trajectory, 117
 - long trajectory, 115
 - short trajectory, 115
- Enantiomers, 24
- Few-cycle, 17
- Few-cycle pulses, 11, 17
- Filamentation, 161, 217
- Finite difference time domain (FDTD)
 - analysis, 131
 - modified Debye model, 131
- Flux
 - stationary, 24
- Fourier transform spectral interferometry, 97
- Four-lobe shape, 205
- Frequency
 - degenerate, 27
 - near-resonant, 27
 - resonant, 27
 - transition, 27
- F-to-2f, 96, 97
- F-to-2f interferometer, 124
- Gate width, 91, 92, 95
- Gating
 - amplitude gating, 90
 - DOG/GDOG, 106
 - double optical gating (DOG), 90, 93, 98, 108
 - generalized double optical gating (GDOG), 90, 94, 103
 - polarization gating (PG), 90, 91, 93
 - two-color gating, 90, 91, 93
- Gating field, 92, 93, 95, 99, 101
- Grating, 172
 - Dammann grating, 172
 - volume grating, 172
- Group delay dispersion, 138
 - phase mismatch, 141
- Group velocity, 92
- Hamiltonian, 26
- Harmonic generation, 146, 147, 153
 - fullerenes, 146, 153
 - nanoparticles, 147, 151
 - in plasmas, 185
- H atom, 22
- Heating equations, 195
- Helicity, 24, 37
- Hexapole, 45, 50–52, 59, 62
 - focusing, 50–52
 - low-field seeking, 50, 51, 61, 62
 - state selection, 45, 50, 52
 - state selector, 50
 - state-selected, 45, 52, 53
- High harmonic generation (HHG), 75, 91, 100, 101, 117, 125, 129, 131, 133, 135, 137, 139, 141, 143, 145, 151
 - comb structure, 140
 - conversion efficiency, 140
 - CPA, 129
 - cut-off frequency, 141
 - gases, 145
 - laser-produced plasmas, 145
 - solid surfaces, 146

- H₂⁺ ion, 81
- Hollow-core fiber, 96–99
- Hot electron population, 229
- Hugoniot, 221
- Hybrid states, 22
- Hydrodynamics simulations, 222
- Hydrogen
 - atom, 22
 - bond, 32
- Interference, 76
 - fringes, 83
 - maximum, 86
 - two-center, 81
 - two-slit, 81
- Interferometry, 217
- Inverse bremsstrahlung absorption, 183
- Inverse Faraday effect, 23
- Ionization ratio, 117, 118
- Ions
 - atomic, 21, 22, 32
 - FHF[−], 27, 32, 34, 37
 - He⁺, 33, 34, 37
 - molecular, 32
 - triatomic, 27
- Isomerization, 24
- Isotropic function, 188
- Isotropization, 185
- JxB heating, 216
- Kinetic energy, 118
- Kinetic equation, 185
- Langdon parameter, 189
- Laser–plasma interaction, 183
- Laser prepulse, 219
- Laser pulses, 121
 - CEP stabilized, 124
 - cosⁿ envelope, 25
 - detuned, 113–115
 - duration, 28
 - few-cycle, 25
 - frequency-doubled, 115, 120
 - Gaussian envelope, 25
 - intensity, 25
 - mid-infrared, 122
 - optimal, 21
 - phase, 25
 - π, 21, 24, 39
 - pump-dump, 24, 36, 38
 - series of, 24
 - spectral width, 26, 28
 - tunable, 122–124
 - two-color, 113, 117, 120
- Lifetimes, 14
- Local target normal, 228
- Low-field seeking, 50
- Mach–Zehnder interferometer, 100
- Magnetic field, 21, 25, 31, 33, 39
 - direction, 36, 37
 - external, 21
 - induced, 21, 34, 38
 - stationary, 22
 - time-dependent, 22
- Maxwellization time, 189
- Melting curve, 222
- Melting point, 221
- Micromachining, 169
- Molecule, 21, 48, 81
 - aromatic, 40
 - benzene, 22
 - CdH₂, 27, 32, 34, 35
 - diatomic, 32
 - ethylene, 22
 - linear, 22, 27, 28, 32
 - Mg-porphyrin, 22, 28, 32–34
 - polar, 26
 - polyatomic, 32
 - pseudorotating, 31
 - stretched, 83, 87
 - tetrahedral, 38
 - triatomic, 27, 28
 - UH₄, 39
- Mo/Si mirror, 100, 103, 105
- Multiphoton ionization, 2, 214
- Multiple filaments, 162
- Multiple ionization, 2, 4, 16
- Nanofabrication, 134
 - focused ion beam, 136
- Nanoring, 22
- Nanotubes, 22
- Neutrons, 21
 - scattering, 40
- NO, 48, 49, 62
 - dipole moment, 62
 - Hund's case, 48
- NO molecules, 48, 61
 - dipole moment, 62
 - Hund's case, 49

- L-type splitting, 49
 - rotational states, 49
- Normalized laser field potential, 212
- Nuclear magnetic resonance, 40
- Optical breakdown, 166
- Optical vortex, 173
- Optimal control, 69
- Optimization, 69, 71
 - evolutionary algorithm, 69
- Orientation, 45, 47, 53–57, 65–69
 - field-free, 45, 47, 55, 65, 66
 - impulsive, 45, 53, 65, 66
 - impulsively, 47
 - revivals, 56, 66
 - rotational wave packet, 53, 54, 65
- Oscillating system, 194
- Particle in Cell Code (PIC), 216
- PCGPA, 106
- Pedestal, 214, 222
- Phase diagram, 221
- Photon energy, 120
- Photonic devices, 169
- Plasma, 183
 - corona, 229
 - frequency, 212
 - heating, 184
 - with unusual optical properties, 185
- Polarization
 - circular, 21, 38, 39
 - linear, 27
- Polarization gating (PG), 91, 94, 101
- Ponderomotive effects, 228
- Ponderomotive potential, 141
- Population transfer, 29
- Power-locking, 97
- Pre-alignment, 24
- Pre-orientation, 24
- Pre-/post-pulses, 90, 105
- Proton cut-off energy, 219
- Pulse shaper, 59, 60, 70
 - spatial light modulator (SLM), 69
- Pulse shaping, 69
- Pump-probe, 1, 17, 98, 109
- Quantum dots, 37
- Quivering motion, 212
- Quiver velocity, 186
- Radiation flux density, 186
- Randomization, 201
- Recollision, 81
- Recombination, 79
- Recombination time, 117
- Refractive index changes, 164
- Rescattering, 2, 9–13
- Rescattering double ionization, 4
- Residual electron heating, 195
- Resonant absorption, 215
- Reversal of EDF shape from squeezed to
 - elongated, 199
- Revival
 - rotational, 26, 37
- Ring current, 25, 30, 38
 - charge, 31, 32
 - direction, 33, 36
 - electronic, 21, 30, 33
 - frequency, 31, 32
 - loop model, 31
 - nuclear, 21, 31, 34, 39
 - partial, 31
 - period, 31
 - radius, 31
 - stationary, 22
 - toroidal, 34
- Rotating wave approximation, 29
- Rotational state, 49
- Rydberg state, 22
- Scattering damage, 164
- Schrödinger equation, 35
 - time-dependent, 26
 - time-independent, 26
- Second harmonic (SH), 90, 91, 94
- Self-focusing, 161
- Self-similar EDF, 192
- Self-similar evolution, 204
- Semi-classical approximation
 - dipole, 26
- Shock adiabat, 222
- Shock breakout, 217
- Shock front, 226
- Shock pressure, 220
- Shock speed, 217, 227
- Shot noise, 106
- Single filament, 162
- Single isolated attosecond pulses, 89, 90, 92, 109
- Skin depth, 214
- Slow electron depletion, 184
- Spectrometer
 - time-of-flight (TOF), 100
 - XUV-grating, 98, 99, 101

- State
 - pseudorotational, 34
- Stimulated Raman Scattering, 216
- Strong field, 194
- Supercontinuum, 116, 119
- Supercontinuum generation, 161
- Suprathermal electrons, 188
- Surface plasmon, 130
 - field enhancement, 130
 - localized surface plasmon, 130
 - ringing-down oscillation, 134
 - temporal variation, 134
- Switches, 37
- Switching, 21, 25, 36, 38, 39
- Target normal sheath acceleration (TNSA), 213
- Target thickness, 219
- TDSE, 77
 - numerical solution, 78
- Thermal, 188
- Time-dependent ellipticity, 92
- Time-frequency distributions, 120
- Time reversibility, 24, 37
- Ti:sapphire femtosecond laser, 131
- Titanium sapphire, 211
- Transition, 76
 - bound-bound, 77
 - continuum-bound, 77, 78
 - continuum-continuum, 77, 78
- Transverse and longitudinal effective temperatures, 195
- Tunnel ionization, 2, 214
- Two color, 94
- Ultrafast, 1
- Ultrafast imaging, 4
- Unloading, 222
- Vacuum heating, 215
- Vaporization, 220
- Vaporization curve, 222
- Vector field, 25
- Velocity map imaging spectrometer (VMIS), 59, 60
- Void
 - self-organized void array, 168
 - void array, 168
- Water window, 84, 113
- Waveform, 81
- Waveguides, 169
- Wave packet, 76
 - dissociative, 76, 86
 - evolution, 85, 87
 - free-electron, 76, 83, 85
 - rotational, 76, 86
 - spreading, 76
 - vibrational, 76, 86
- Weak field, 187
- Weibel instability, 185
- Welding/joining, 174
- White light continuum (WLC), 121
- X-polarized wave generation (XPW), 215